Characterisation of photoconvertible fluorescent proteins for single-molecule localisation microscopy

Daniel Thédié

Communauté
UNIVERSITÉ Grenoble Alpes

THÈSE

Pour obtenir le grade de

DOCTEUR DE LA COMMUNAUTÉ UNIVERSITÉ GRENOBLE ALPES

Spécialité : **Biologie Structurale et Nanobiologie**

Arrêté ministériel : 25 mai 2016

Présentée par

Daniel THÉDIÉ

Thèse dirigée par **Dominique BOURGEOIS**

préparée au sein de **l'Institut de Biologie Structurale**
dans **l'École Doctorale Chimie et Sciences du Vivant**

Caractérisation de protéines fluorescentes photoconvertibles pour la microscopie super-résolution par localisation de molécules uniques

Characterisation of photoconvertible fluorescent proteins for single-molecule localisation microscopy

Thèse soutenue publiquement le **25 novembre 2019**,
devant le jury composé de :

Monsieur Guy Royal
Professeur des Universités, Université Grenoble Alpes, Président
Madame Aleksandra Radenovic
Professeur associé, Ecole Polytechnique Fédérale de Lausanne, Rapporteur
Monsieur Jean-Baptiste Sibarita
Ingénieur de Recherche, Institut Interdisciplinaire pour les Neurosciences, Rapporteur
Madame Ilaria Testa
Professeur assistant, KTH Royal Institute of Technology, Examinateur
Monsieur Emmanuel Margeat
Directeur de Recherche, Centre de Biochimie Structurale, Examinateur
Monsieur Dominique Bourgeois
Directeur de Recherche, Institut de Biologie Structurale, Directeur de thèse

Contents

Abstract

Abstract in English

Fluorescence microscopy is a powerful tool for the observation of biological specimens and the understanding of molecular processes. The last two decades have seen tremendous advances in the field, notably with the development of super-resolution techniques, which allow the observation of structures smaller than the diffraction limit of visible light (∼200 nm). One of the most popular of these techniques is Photoactivated Localisation Microscopy (PALM), which uses Phototransformable Fluorescent Proteins (PTFPs) to image single molecules and localise them with 10-20 nm precision. PTFPs are proteins from the Green Fluorescent Protein (GFP) family, which not only produce fluorescence, but can also undergo light-induced reactions such as fluorescence activation or change in emission color. These specific properties are at the base of PALM, since they allow stochastic temporal separation of the fluorescence events and imaging of sparse single-molecules. The fact that PALM deals with single molecules prompted the development of a variety of applications, among which single-particle tracking PALM (sptPALM) and quantitative PALM (qPALM). These advanced applications already provide amazing insights into biological phenomena, but their use remains challenging. One of the reasons for this is the complex photophysical behaviour of PTFPs, beyond the transormations that are useful for PALM imaging.
Therefore, this thesis focused on characterising the light-induced reactions occurring in Photoconvertible Fluorescent Proteins (PCFPs, some of the most popular PALM markers) with the aim of improving single-particle tracking and quantitative approaches in PALM. In particular, the work was directed to the understanding of transient losses of fluorescence, known as blinking, that are detrimental to PALM experiments. After a thorough characterisation of light-induced reactions in both the green and the red form of the investigated PCFPs, a strategy was proposed to alleviate blinking and the artefacts it produces. Finally, insights were given into the application of this strategy to improve a qPALM experiment.
This work constitutes an further step towards a better understanding of PCFPs photophysics, and improved extraction of quantitative information from PALM datasets.

Résumé en français

La microscopie de fluorescence est une puissante technique pour l'observation d'échantillons biologiques et la compréhension de processus moléculaires. Les deux dernières décennies ont été témoins de grandes avancées dans ce domaine, notamment avec le développement des techniques de "super-résolution", qui permettent l'observation de structures plus fines que la limite de diffraction de la lumière visible (∼200 nm). Une de ces techniques les plus populaires est le PALM (Photoactivated Localisation Microscopy, microscopie par localisation photoactivée), qui utilise des protéines fluorescentes phototransformables (PTFPs) pour observer des molécules uniques, et les localiser avec une précision de 10-20 nm. Les PTFPs sont des protéines de la même famille que la GFP (Green Fluorescent Protein, protéine fluorescente verte), qui non-seulement produisent de la fluorescence, mais peuvent aussi subir des réactions photo-induites, comme l'activation de fluorescence ou le changement de couleur d'émission. Ces propriétés sont à la base du PALM, puisqu'elle permettent la séparation temporelle stochastique des émissions de fluorescence, et l'imagerie de molécules uniques. Le fait que le PALM détecte des molécules uniques a conduit au développement d'un grand nombre d'applications, dont le sptPALM (single-particle tracking PALM, suivi de molécules uniques en PALM) et le PALM quantitatif (qPALM). Ces applications avancées permettent déjà d'acquérir des informations précieuses sur le fonctionnement des systèmes biologiques, mais leur utilisation reste difficile. Une des raisons en est le comportement photophysique complexe des PTFPs, qui va au-delà des transformations utiles pour l'imagerie PALM.
L'objet de cette thèse était donc de caractériser les réactions photo-induites subies par les protéines fluorescentes photoconvertibles (PCFPs, qui sont parmi les marqueurs les plus populaires en PALM), dans le but d'améliorer les approches de suivi de molécules uniques et quantitatives en PALM. En particulier, ce travail cherchait à comprendre les pertes transitoires de fluorescence, connues sous le terme de scintillement (blinking en anglais), qui sont détrimentales aux expériences PALM. Une caractérisation poussée des réactions photo-induites ayant lieu dans les formes verte et rouge de la PCFP étudiée nous a suggr une stratégie pour réduire l'influence du scintillement, et des artéfacts qu'il produit. Enfin, cette stratégie a été appliquée à une expérience de qPALM.
Ce travail constitue un pas en avant vers une meilleure compréhension de la photophysique des PCFPs, et une meilleure extraction d'informations quantitatives des données PALM.

Rezumo en Esperanto

Fluoreska mikroskopio estas potenca tekniko por observi biologiajn specimenojn kaj kompreni molekulajn procezojn. En la pasintaj du jardekoj, grandajn progresojn okazis en fluoreska mikroskopio, ĉefe kun la elvolvo de "super-solvopova" teknikoj, kiuj permesas observi strukturojn pli malgrandajn ol la difraktolimo de videble lumo. Unu el la pli populara el ĉi tiuj teknikoj estas PALM (angle *Photoactivated Localisation Microscopy*, fotoaktivigita lokalizado mikroskopio), kiu uzas fototransformeblajn fluoreskajn proteinojn (PTFP) por observi solajn molekulojn, kaj lokalizi ilin kun 10-20 nm precizeco. PTFP-ojn estas proteinoj el la sama familio ke GFP (angle *Green Fluorescent Protein*, verda fluoreska proteino), kiuj ne nur produktas fluoreskon, sed konas ankaŭ sperti lumoinduktitajn reagojn, kiel aktivigo de fluoresko aŭ ŝanĝo de emisiokoloro. Tiuj ecoj estas la bazo de PALM, ĉar ili permesas hazarde apartigi la fluoreskajn emisiojn en tempo kaj observi solajn molekulojn. La fakto ke PALM bildigas solajn molekulojn instigis la elvolvon de multe da aplikaĵoj, inkluzive sola ero spurado (sptPALM) kaj kvantiga PALM (qPALM). Ĉi tiuj kompleksaj aplikaĵoj jam produktas mirigajn enrigardojn al biologiaj fenomenoj, sed ilia uzo ankoraŭ estas defia. Unu el la kialoj estas la kompleksa fotofiziko de la sondiloj, kio estas pli komplika ol sole la utilaj transformoj por PALM bildigo.
La subjekto de ĉi tiu tezo do estis la karakterizado de la lumoinduktitaj reagoj en fotokonverteblaj fluoreskaj proteinoj (PCFP-oj, kiuj estas inter la pli populara sondiloj en PALM), ĉelante plibonigi la spurado kaj kvantigo aplikaĵojn en PALM. Precipe, ĉi tiu verko provis kompreni la pasemajn perdojn de fluoresko, konata kiel briletado (angle *blinking*), kiuj malutilas PALM eksperimentojn. Post ĝisfunda studo de la okazantaj lumoinduktitaj reagoj en verda kaj ruĝa formoj de la esploritaj PCFP-oj, strategio estis proponita por mallongigi briletadon, kaj redukti ĝian influon sur PALM eksperimentoj. Fine, ekzemplo por aplikiĝo de ĉi tiu strategio al kvanta PALM estis donita.
Ĉi tiu verko estas antaŭenpaŝo al plibona kompreno de la fotofiziko de PCFP-oj, kaj plibona eltiro de kvantigaj informacioj de PALM datumoj.

List of Figures

List of Tables

Glossary

AOTF acousto-optic tunable filter.

APS ammonium persulfate.

APTES (3-Aminopropyl)triethoxysilane.

AUC Analytical Ultracentrifugation.

DSS Disuccinimidyl suberate.

EM Electron Microscopy.

EMCCD electron multiplying charge-coupled device.

ESPT excited-state proton transfer.

FBS Fetal Bovine Serum.

FP fluorescent protein.

FRAP Fluorescence Recovery After Photobleaching.

FRET Förster Resonance Energy Transfer.

GFP Green Fluorescent Protein.

GPCR G-protein coupled receptor.

HBDI HydroxyBenzylideneDimethylImidazolinone.

IPTG Isopropyl β-D-1-thiogalactopyranoside.

LdcI inducible lysine decarboxylase.

MSD mean square displacement.

NA Numerical Aperture.

NMR Nuclear Magnetic Resonance.

NPC Nuclear Pore Complex.

NSOM Near-Field Scanning Optical Microscopy.

PAA polyacrylamide.

PAFP PhotoActivatable Fluorescent Protein.

PAINT Point Accumulation for Imaging in Nanoscale Topography.

PALM PhotoActivated Localisation Microscopy.

PCFP Photo-Convertible Fluorescent Protein.

PCR polymerase chain reaction.

PLP Pyridoxal 5-phosphate.

PSF point-spread function.

PTFP PhotoTransformable Fluorescent Protein.

PVA polyvinyl alcohol.

qPALM quantitative PALM.

QY Quantum Yield.

RSFP Reversibly Switchable Fluorescent Protein.

sCMOS scientific Complementary Metal Oxide Semiconductor.

SIM Structured Illumination Microscopy.

SMLM Single-Molecule Localisation Microscopy.

SNR signal-over-noise ratio.

sptPALM single-particle tracking PALM.

STED Stimulated Emission Depletion.

STORM Stochastic Optical Reconstruction Microscopy.

TEMED tetramethylethylenediamine.

TIRF Total Internal Reflection Fluorescence.

XFEL X-Ray Free Electron Laser.

Part I

Introduction

Looking at biological objects

The last century has seen a spectacular advancement of knowledge in biological sciences, driven by important technical progress. Many techniques are used nowadays to understand biological phenomena, but one of the most basic and powerful ways to learn about a subject, is to *look at it*. For objects smaller than the resolution limit of the human eye ($\sim$ 50 µm), it was made possible by the use of optical microscopes, which became widely used in the 19th century. These rather simple apparatus allowed ground-breaking discoveries, including the first observations of cells, bacteria, and microscopic processes such as gamete fertilisation and mitosis. These and similar observations laid the base of modern cell biology. Across the 19th and 20th centuries, progressively smaller and finer structures could be observed thanks to technical improvements such as phase contrast, or confocal microscopy.
However, despite these constant improvements, optical microscopy has intrinsic limitations. First of all, its resolution is limited by the diffraction of light, according to Abbe's law:[1]

$$d = \frac{\lambda}{2.NA}$$

with d, the smallest distance between two resolvable objects, λ the wavelength of the light used for the observation, and NA the Numerical Aperture of the microscope.
Furthermore, biological systems such as cells are extremely complex, and composed of a very large number of elements. Therefore, visualising an unlabelled object in a cell can prove difficult. Fluorescence microscopy brought a solution to that issue by highlighting structures of interest using fluorescent dyes, or immunostaining.

Purified biological components (e.g. proteins) can now be visualised at near-atomistic resolution using techniques such as protein crystallography, Electron Microscopy (EM) or Nuclear Magnetic Resonance (NMR). There is therefore a gap to be filled, between high-resolution information obtained on isolated components, and medium-resolution images of organisms, cells and organelles obtained by optical microscopy. Furthermore, a great deal of insight can be gained by visualising the distribution, interactions and dynamics of particular components directly in their native, cellular environment. Several techniques such as electron tomography, X-ray tomography or atomic force microscopy have allowed to bridge this resolution gap. Fluorescence microscopy is one of them, and presents the combined advantages of allowing specific labelling and imaging of living specimens for prolonged periods. The technique has been made possible by the use of fluorescent dyes, among which fluorescent proteins, which brought unprecedented possibilities to fluorescence microscopy.

Chapter 1

Fluorescent proteins

1.1 Preliminary remarks on fluorescence emission

Fluorescence is a process by which a molecule absorbs light of a given wavelength, and emits light of a longer wavelength. As shown on Figure 1.1, when a molecule (e.g. a fluorescent protein (FP)) in the electronic ground state absorbs a photon, it accesses the first excited state. This state is typically short-lived (a few nanoseconds), and rapidly decays back to the ground-state, either through the emission of a photon, or by non-radiative relaxation. Alternatively, the singlet excited state can undergo inter-system crossing to the triplet state, which will relax back to the singlet ground-state on a millisecond timescale.[2] Inter-system crossing causes relaxation to the singlet ground state without fluorescence emission, and is also an important entry point to chemical reactions affecting the chromophore.[3]

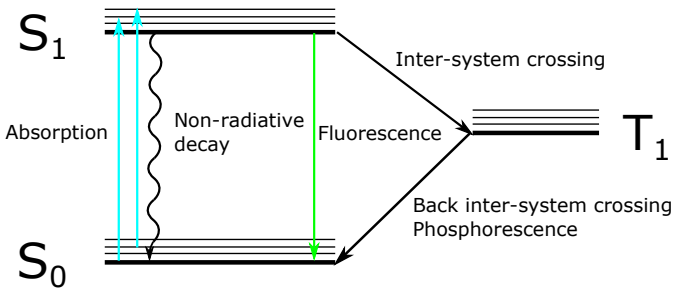

Figure 1.1: Jablonski diagram of fluorescence emission. Upon absorption of a photon, the S_0 ground-state enters the S_1 excited state. From there, it can return to the ground-state by non-radiative decay, emission of a fluorescence photon, or through the triplet state T_1. In each state, the fluorophore can enter vibrationally excited states, from which it can also be excited.

The fluorescence Quantum Yield (QY) is defined as the probability of emitting a fluorescence photon upon absorption of a photon. For example a quantum yield of 0.77 means that on average for 100 absorbed photons, 77 fluorescence photons are emitted.

The extinction coefficient (ε, expressed in $M^{-1}.cm^{-1}$) represents the capacity of a molecule to absorb incoming photons at a given wavelength. The higher the extinction coefficient, the more often the molecule will absorb photons, and thus enter the excited state.

Brightness is defined as the product of the QY and extinction coefficient, and therefore represents the number of photons emitted by a fluorescent molecule under a given intensity of excitation light.

1.2 The Green Fluorescent Protein (GFP)

1.2.1 Discovery

In 1962, while trying to isolate the bioluminescent protein aequorin from the jellyfish *Aequorea victoria*, Japanese researcher O. Shimomura discovered the first known FP: the Green Fluorescent Protein (GFP).[4] In the jellyfish, aequorin uses calcium ions to produce blue light, which excites the green fluorescence of GFP,[5] giving *Aequorea victoria* its color (as shown on Figure 1.2).

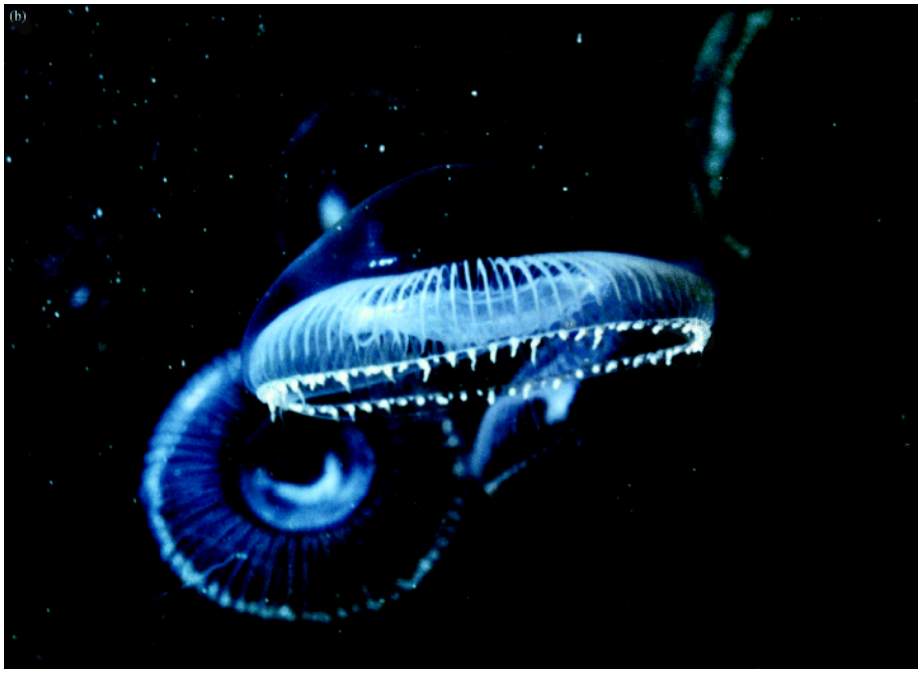

Figure 1.2: The bioluminescent jellyfish *Aequorea victoria*. The bioluminescent cells containing aequorin and GFP are visible at the edge of the umbrella. Adapted from ref.[4]

In 2008, the Nobel prize in chemistry was awarded to O. Shimomura, M. Chalfie and R. Tsien "for the discovery and development of the green fluorescent protein, GFP".

1.2.2 Structure

The first structure of the GFP was obtained in 1996,[6,7] and is shown on Figure 1.3. The protein is made of 238 amino-acids, and measures approximately 40 by 20 Å. It is composed of 11 beta-strands arranged as a barrel, inside which an alpha helix bears the three amino-acids of the chromophore (Ser65-Tyr66-Gly67). After maturation, these three amino-acids form a p-HydroxyBenzylideneDimethylImidazolinone (HBDI) structure, responsible for the light absorption and emission properties of the protein.

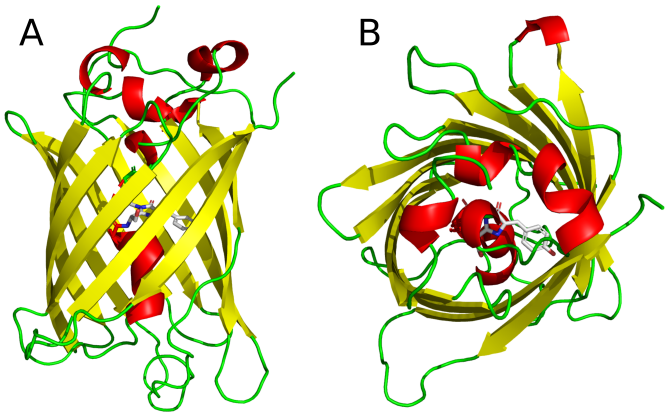

Figure 1.3: (A) Side view of the structure of the GFP. β-strands are colored green, α-helices red. (B) Top view showing the chromophore inside the barrel structure. PDB: 1emb.[8]

The β-barrel structure produces a very tight packing of the interior of the protein, so that the chromophore and water molecules are fixed into place by hydrogen bonds, with limited diffusion of ions or small molecules. This constraining of the chromophore is essential for fluorescence; the isolated p-HBDI is very weakly fluorescent, due to its high flexibility.[9]

1.2.3 Chromophore properties

One of the most interesting features of the GFP chromophore is that it does not require a catalytic system to be formed, but is autocatalytically assembled after protein production, and requires only oxygen as a cofactor for its full maturation, as shown on the scheme of Figure 1.4. The maturation is initiated thanks to the protein environment, which constrains the three amino-acids of the chromophore (Ser, Tyr, Gly) in a sharp turn. This strongly favors a nucleophilic attack of the nitrogen of Gly67 on the carbonyl of Ser65.[10,11] This is followed by an oxidation of the newly formed ring, and finally a dehydration connecting its electron-conjugation system with that of Tyr66. Whereas Tsien originally proposed that the maturation process should feature dehydration followed by oxidation,[12,13] a more recent study proposed that the dominant pathway would in fact be oxidation followed by dehydration.[14] In both models, oxidation is described as the rate-limiting step of the reaction, with full maturation occuring in 2 to 4 hours at 37°C.

Of note, while Gly67 is essential for chromophore formation, the other two amino-acids (Ser65 and Tyr66) can be substituted, the effect of which will be discussed in section 1.3.

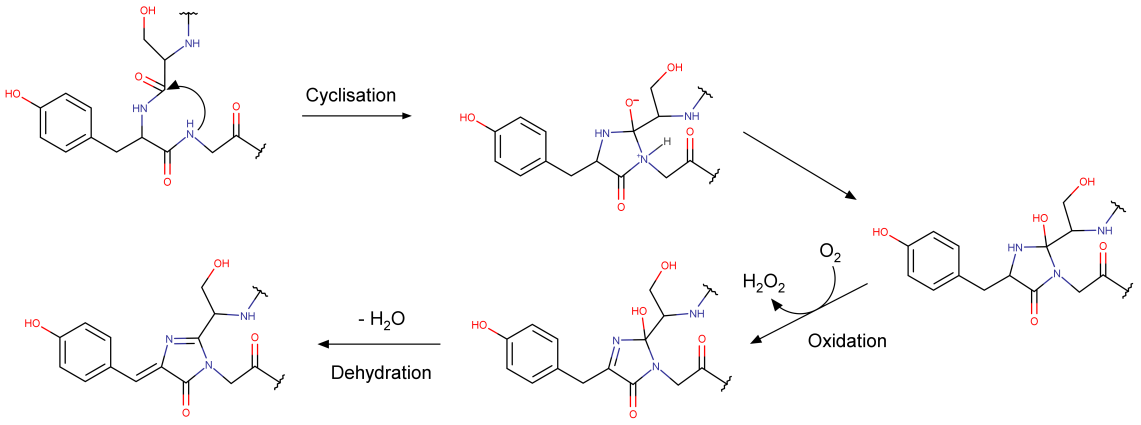

Figure 1.4: Maturation of the GFP chromophore. The four steps of the maturation process are autocatalytic, and require only oxygen as a cofactor. The matured chromophore possesses an extended π-electron conjugation system, responsible for light absorption and emission. Figure based on ref.[14]

The excitation spectrum of GFP (shown on Figure 1.5) features a main peak at 395 nm, and a minor peak at 475 nm. These have been found to correspond respectively to the protonated and anionic forms of the chromophore.[8] Excitation in the main absorbance peak around 395 nm induces an excited-state proton transfer (ESPT) on the tyrosine of the chromophore, and fluorescence emission peaking at 508 nm.[15] Excitation in the anionic absorbance peak is also possible, but yields lower fluorescence due to the low population of anionic chromophores.

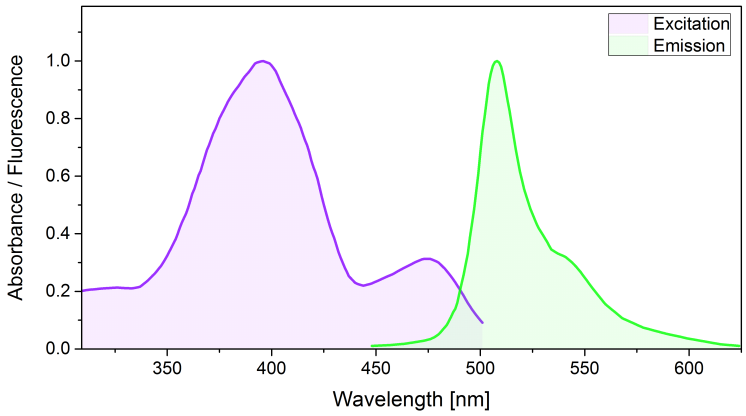

Figure 1.5: Excitation and emission spectra (violet and green, respectively) of wild-type GFP from *Aequorea victoria*. Adapted from ref.[13]

1.2.4 Fluorescent proteins from other organisms

After the discovery of GFP, other organisms were searched for protein homologs. This resulted in the discovery of a number of FPs in organisms such as anemones and stony corals.[16] Among these discoveries were the first red-emitting FP DsRed, as well as the different PhotoTransformable Fluorescent Proteins (PTFPs), which will be described in chapter 3.
Interestingly, it appeared that not all organisms expressing FPs did so for bioluminescence purposes. Some marine organisms growing in shallow water use them for protection against short-wavelength irradiation,[17] whereas others growing in deeper water (where mostly blue light is available) use them to produce longer-wavelength light for their photosynthetic symbiotes.[18,19]

1.3 Important fluorescent protein properties

Following the discovery of GFP, it has quickly become clear that the large number of applications and techniques derived from it could benefit greatly from variant proteins with improved or different properties. This has been achieved either by mutations, or by isolating GFP homologs from diverse marine organisms such as jellyfish, anemones or corals. This section aims at summarising the main properties of FPs, and how they have been engineered to make better fluorescent probes.

1.3.1 Mutating FPs to change their properties

Engineering of FPs by introducing mutations in their amino-acid sequence can be done by directed or random mutagenesis, or a combination of both.

Directed mutagenesis is used to affect a defined characteristic, based on mechanistical studies. It is a high-risk/high-gain approach: even though rational design can enhance a property of interest, its overall effects are difficult to predict. It can often result in the modification of other properties of the protein, or even annihilate its fluorescence.

Random mutagenesis on the other hand can prove a more cost- and time-effective solution. It can be used to find FP variants with new or improved properties, or applied after directed mutagenesis to rescue lost properties. However, it is not always easy to implement, since it requires a high-throughput screening method for the characteristic of interest.

An intermediate solution can be performing semi-rational engineering, for example by using random mutagenesis on a single residue of interest.

1.3.2 Photobleaching

Photobleaching is the irreversible loss of fluorescence, due to the destruction of the chromophore or to a permanent modification of its conformation. The photobleaching rate of an FP therefore determines the total number of photons it can emit.
It has been reported that at equal illumination intensities, different FPs could have very different bleaching half-times.[20] Furthermore, the same study showed that for all tested FPs the photobleaching rate was not linearly correlated to illumination intensity, but had a "supralinear" (or accelerated) behaviour. As a consequence, FP photobleaching is faster under high illumination

intensities than would be expected from a linear dependence. Even though the reason for this behaviour has not been elucidated, it could arise from photon absorption in the excited state of the protein, or from two co-existing photobleaching pathways.

In this manuscript, FPs of anthozoan origin will be of particular interest. IrisFP (see section 3.2.2) is part of this family. For this protein, two major photobleaching pathways have been characterised at the structural level, depending on the intensity of the excitation light.[21]

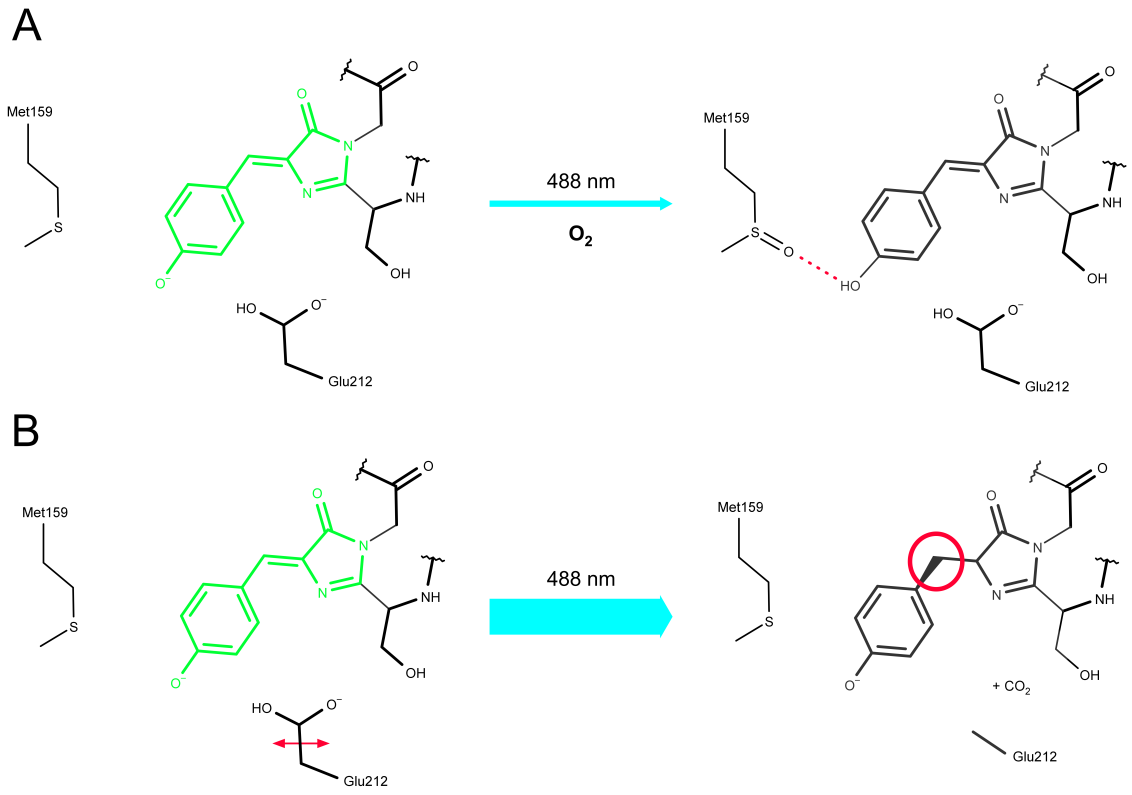

Figure 1.6: Main photobleaching pathways in IrisFP. (A) Under low illumination power (< 100 W/cm^2), an oxygen-dependent pathway takes place, with sulfoxidation of Met159 and trapping of the chromophore in the protonated state. (B) Under higher illumination power (> 100 W/cm^2), an oxygen-independent pathway predominates, where decarboxylation of Glu212 leads to an hybridisation change, breaking chromophore planarity. Adapted from ref[22]

Low intensity photobleaching. At low excitation light intensities (< 100 W/cm^2), an oxygen-dependent photobleaching mechanism takes place, with the sulfoxidation of Met159, located in the chromophore pocket. This results in a locking of the chromohore in the non-fluorescent protonated form. This sulfoxidation is caused by singlet oxygen generated in the quenching of the triplet state.[3]

High intensity photobleaching. At higher excitation light intensities (> 100 W/cm^2), which are typically used in super-resolution microscopy, another, oxygen-independent mechanism predominates. In this pathway, Glu212 undergoes decarboxylation, resulting in a modification of the hydrogen-bond network around the chromophore, and an sp^2 to sp^3 hybridisation change of the α carbon of the chromophore Tyrosine. This hybridisation change breaks the electron-conjugation system, and therefore prevents fluorescence emission.

1.3.3 Brightness

As mentioned above, the brightness of an FP depends on its quantum yield and extinction coefficient (ε). Modification of either of these two properties will change the brightness.

The QY is changed with the mechanical constraints on the chromophore. The more constrained the chromophore is, the less non-radiative relaxation will occur, and the higher the QY. Of note, this is one of the main roles of FPs β-barrels, which place the chromophore in a tightly packed environment, allowing them to have a much higher QY than when isolated in solution.

One of the major flaws of wild-type GFP is its limited brightness when excited at 488-nm, due to a large part of the chromophore being in the neutral state (395-nm absorption peak on Figure 1.5). Even though bright fluorescence could be obtained by excitation at 400-nm, this wavelength is phototoxic, and few microscopes are equipped with the appropriate filter sets. One of the very first published engineering of GFP was therefore the S65T mutation, which by replacing the Serine of the chromophore with a Threonine, completely abolished the neutral form, to the benefit of the anionic one.[23] The resulting protein was called EGFP, for enhanced GFP, and was highly fluorescent when excited at 488-nm. This was a decisive step in making GFP the powerful and widely used marker that it is now.

The S65T mutation has succesfully been applied to different GFP mutants with the same effect,[24] and to a humanised version of GFP designed for transfection into human cells.[25]

20 years after the first introduction of the S65T mutation, brighter FPs are still being developed, such as the recent red FP mScarlet,[26] and brightness continues to be a major concern for microscopists.

1.3.4 Color

The first color variations of fluorescent proteins came from the team of R. Tsien in 1994, from mutations of the chromophore's Tyrosine.[27] Mutating this residue changes the length of the electron-conjugation system, and therefore the absorption and emission properties: the GFP Y66H mutant emits blue light, and the Y66W cyan light. A few GFP variants were also proposed that had slightly red-shifted emission.[6]

Even though new FP colors were accessible by then, they were still limited to the blue to yellow part of the visible spectrum. This changed in 1999 when the first coral FP was discovered: DsRed.[16] Although this protein, being an obligate tetramer, was of limited use in biology, its later engineering

into the monomeric mRFP1 opened the way to a broader use.[28]

Later on, mRFP1 was further engineered to yield the mFruit collection of fluorescent proteins, a set of monomeric FPs covering a broad range of colors.[29]

The first and most obvious use of different colors of FPs is to perform multi-color imaging. Well-distinct emission peaks allow simultaneous tagging of several proteins of interest, and opens the way to colocalisation studies. Different colors also open more possibilities for the study of protein-protein interactions using Förster Resonance Energy Transfer (FRET), which will be described in section 1.4.2.

Finally, using FPs with red-shifted excitation can prove useful for imaging of living cells, since longer wavelengths are less phototoxic. It would also constitute an advantage for imaging at the tissue or organism level, since red light penetrates better in biological tissues. Therefore, efforts have been put in developping bright, near-infrared emitting FPs.[30,31]

1.3.5 Monomericity

Due to its compact shape, and to the presence of aliphatic residues at its surface, GFP has a tendency to dimerise at high concentration, as suggested by its dimeric crystal structure.[7] The dissociation constant (K_d) for the dimer was found to be 0.11 mM for the YFP variant by Analytical Ultracentrifugation (AUC).[32] Such dimerisation tendency can be responsible for a large number of artefacts in in-vivo studies, especially when looking at abundant proteins, or membrane proteins for which diffusion is constrained in a 2D space. Therefore, Zacharias et al. introduced the S206K mutation in GFP, which allowed breaking the dimerisation interface by introducing a positive charge in it.[32]

A similar, though more difficult problem came up with the discovery of DsRed, which was an obligate tetramer in its wild-type form. Introduction of arginines at its surface succesfully converted the tetrameric protein to a dimer, and then to a monomer, but destroyed its fluorescence properties. These could be rescued by extensive random and directed mutagenesis to generate the first monomeric red FP, mRFP1.[28] Of note, the dimeric intermediary generated during the process was further developed as a genetic dimer, which gave rise to tdTomato, still one of the brightest existing FPs.

Monomerisation has since then been applied to a large number of newly discovered or engineered FPs, and is still one of the prime concerns when generating new FP variants.

1.4 Use in biology

Even though GFP was discovered in 1961, 30 years passed before it started being applied in biological research. This begun in 1992, when Prasher cloned the gfp gene,[33] and M. Chalfie introduced it in the nematode *C. elegans*.[34] This was a new breakthrough: it showed that GFP could be expressed in foreign organisms, and contributed to demonstrate that the protein was able to mature without the intervention of a specialised enzymatic complex. Finally, they showed that fusing GFP to a protein of interest did not impair GFP fluorescence, nor the function of the target protein.

Although this last point varies depending on the targeted protein, and should always be a matter of concern when producing new GFP fusions, this finding made GFP a tag of choice for a growing number of applications. This section will give an overview of some of the popular uses of FPs in biological research.

1.4.1 First imaging applications

Fusing GFP to different target proteins greatly improved the imaging of cellular processes. Thanks to the specific fluorescence emission, the distribution of small and previously undetectable particles could be probed. Furthermore, the genetic encoding and auto-catalytic maturation of GFP make it an outstanding tool for live-cell imaging. This, combined with specific techniques based on GFP properties, such as Fluorescence Recovery After Photobleaching (FRAP), 2-color imaging, or two-photon excitation, enabled the imaging of dynamic cellular processes; for example, secretory and endocytic vesicle trafficking,[35] or bacterial division.[36]

At the time of these first studies, a major bottleneck of protein-tagging with GFP was the insertion of the gfp gene in the cells or organism of interest. The easiest and most common approach was transient transfection, which has the major inconvenient of expressing the protein of interest above the endogenous level. However, recent progresses in molecular biology have made it more and more accessible and cost-effective to perform genome-editing, enabling endogenous labelling of proteins. Although such a modification still requires a lot more work than a simple transfection, it constitutes an invaluable tool for the study of proteins in-vivo, in *physiological* conditions.

1.4.2 FP-based biosensors

The fluorescence of GFP constitutes not only a potent marker for biological imaging, but also a useful reporter for different cellular processes and properties. This section will present some of the reporting applications that use FPs.

Gene expression

It is arguably the most straightforward application of GFP to probe the production of specific proteins by fusing the gfp gene with a gene of interest. This can give valuable information on the temporality of gene expression (e.g. during embryonic development), its localisation (specific tissues within an organism, or cells within tissues), or its response to external factors (environmental stress, ingestion of a drug...).[37]

Protein-protein interactions

The discovery and engineering of FPs of different colors made possible their use as probes of protein-protein interactions. A basic way of assessing such interactions would be to fuse each protein of interest to a different-colored FP, and estimating colocalisation of the fluorescence signals. Such a technique however does not allow differenciating protein colocalisation and interaction, and can be challenging if the proteins of interest are present at high concentrations in small volumes. This method can therefore be suitable to show colocalisation of proteins within a region of interest (e.g. an organelle), but not to probe direct interaction between them.

This last point has been considerably facilitated by the development of Förster Resonance Energy Transfer (FRET).[38,39] FRET relies on the overlap between the excitation and emission spectra of two fluorescent emitters. If the overlap is sufficient, one fluorophore can excite the other through a resonance process, which depends on the inverse of the 6-th power of the distance between the two probes. Therefore, the FRET signal is maximal when the two fluorophores are in close proximity (< 10 nm), and quickly decays if they are further apart. This makes it a great tool to track close interactions of proteins within living cells, and under different stimuli. Two main types of FRET experiments can be distinguished: intermolecular FRET probes the interaction between two proteins by tagging one with the acceptor, and the other with the donor (Figure 1.7); intramolecular FRET probes conformational changes of a protein by labelling it with both acceptor and donor. Intramolecular FRET is however rarely performed using FPs due to their size, and difficulty to label different sites within a protein without altering its function.

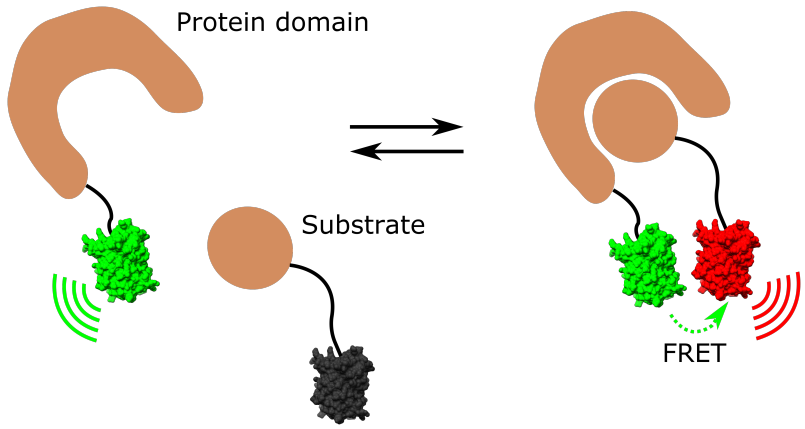

Figure 1.7: Schematic representation of intermolecular FRET between a protein domain and its substrate. The association brings the two FPs in close proximity, which generates a FRET signal.

Calcium concentration

Calcium is a major cofactor in biological systems, implicated in the regulation of a large number of cellular processes.[40] Hence, probing calcium concentration inside tissues, cells or organelles is of general interest to the scientific community.
Some of the first calcium sensors used the calcium-sensitivity of aequorin, and led to a number of discoveries.[41] The calcium-sensing abilities of aequorin are however limited: first by its defined sensitivity range ($\sim$ 100 nM to 10 µM), and secondly by its unsuitability to be targeted to certain compartments, such as the endoplasmic reticulum (one of the major calcium-regulating organelles in the cell). Thus alternatives were sought, and one of the most used system has been a protein fusion between a blue- or cyan-emitting FP, calmodulin, the calmodulin-binding peptide M13, and a green- or yellow-emitting FP. Upon calcium binding, calmodulin undergoes a conformational change, and wraps around the M13 peptide, bringing the two FPs close together, which produces a FRET signal. This system has proved to be reliable, and usable in different organelles, with a broad calcium-sensitivity range (10 nM to 10 mM).[42] Since then, calcium sensors have continuously been improved, and applied to biological research.[43,44]

pH

The Tyrosine of the GFP chromophore exists in two forms, anionic and neutral, which are visible as the two peaks of the absorption spectrum of GFP (Figure 1.5). The extended electron-conjugation system in the anionic form results in a lower $S_0 \rightarrow S_1$ transition energy, and therefore to a red shift in absorbance. Furthermore, the two states have different brightnesses. This feature has been exploited to design in-vivo pH sensors.
Such a sensor needs to have a pK within the range of pH studied, and detectable fluorescence emission from both the neutral and anionic states of the chromophore. If these conditions are fulfilled, the pH of diverse cellular compartments can be inferred by calculating the ratio of the fluorescence produced under excitation in each absorption band of the chromophore.[45]

As a genetically encoded fluorescent marker, GFP opened up many possibilities in biological research, as exemplified above, and fluorescence microscopy became a routine technique in many laboratories. The next chapter aims at describing the basic elements constituting a fluorescence microscopy setup.

Chapter 2

Fluorescence microscopy

2.1 Principle

Fluorescence microscopes are composed of a light source, a microscope body (containing the objective), and a detection apparatus (Figure 2.1). The design allows excitation of a fluorescent probe, and observation of a magnified fluorescence image through the objective, on the camera.

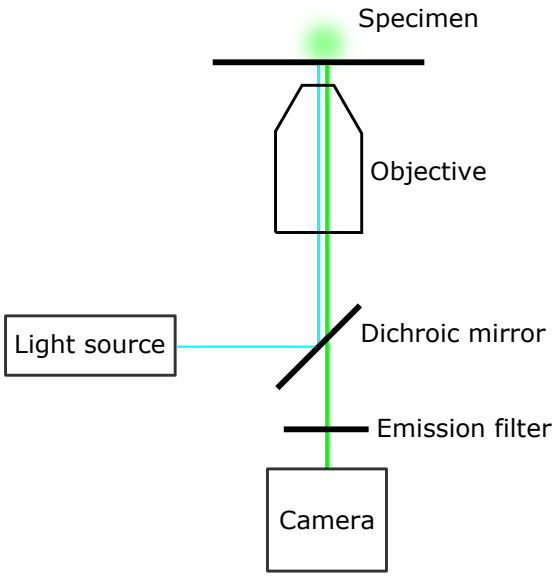

Figure 2.1: Schematic representation of an epifluorescence microscope.The dichroic mirror allows separating the excitation light and the emitted fluorescence. The emission filter selects the wavelength range of interest for detection on the camera.

The light source can be a laser, or a lamp, in which case an excitation filter is needed to select the wavelengths of interest for fluorescence excitation. Even though a laser source delivers more power,

lamps are more versatile in terms of excitation wavelengths.

The main elements in an epifluorescence microscope body are the dichroic mirror and the objective. The dichroic mirror reflects light of certain wavelengths, and is transparent to lights of other wavelengths. It is used to separate the co-aligned excitation and emission lights. The objective is a central part of the setup, since it provides the magnification of the image, and the resolution of the observed features. It is defined by several characteristics:

- Numerical Aperture (NA): defines the maximum angle with which light coming from the specimen can be detected. The greater the NA, the more light can be collected, and as shown by Abbe's law (chapter 1), the better the resolution. The greatest NA currently attainable by objectives without introducing significant aberrations is $\sim$1.6.

- Magnification: factor by which the image of the observed specimen will be enlarged. Magnification should be chosen in accordance with NA, so that resolved features are magnified enough to be visible, but unresolved ones are not uselessly enlarged.Typical magnifications range from x1 or x4 for low NAs, to x100 for high-NAs.

- Aberration correction: image magnification through a set of lenses produces different types of aberrations, that can be corrected for within the objective. Different types of corrections exist, the most commonly used being the plan achromat objectives, which are optimised to correct both spherical and chromatic aberrations.

- Depth of field: the axial range over which the objective can be focused without altering image sharpness. It tends to decrease with increasing NA, down to approx. 0.5 µm.

Basic fluorescence microscopy setups use an eyepiece to allow the user to look at the image. However, applications dealing with weak fluorescent signals require more sensitivity, and therefore use signal-amplifying cameras for fluorescence detection. Two types of such cameras exist and are commonly found on microscopes. Although electron multiplying charge-coupled device (EMCCD) cameras have long been the most sensitive ones available, the scientific Complementary Metal Oxide Semiconductor (sCMOS) technology has greatly progressed in the past years, and achieved a similar sensitivity. sCMOS cameras have the advantage of being much faster, and providing a larger field of view than EMCCDs.

2.2 Widefield and confocal microscopy

The two main categories of fluorescence microscopes available are widefield and confocal microscopes. Both provide similar resolution, but differ in their functionning, as shown on Figure 2.2. In short, whereas widefield microscopes illuminate the whole field of view with the light source to record the fluorescence image, confocal systems successively illuminate small subregions, and record the fluorescence intensity in each of them to build a full image.

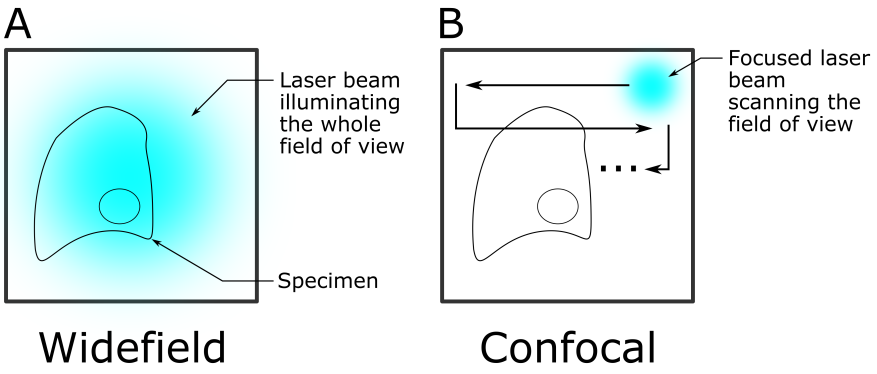

Figure 2.2: (A) In a widefield fluorescence microscopy scheme, fluorescence is excited and recorded from the whole field of view simultaneously. (B) In a laser-scanning confocal microscope, a focused laser beam scans the field of view, and the fluorescence intensity is recorded independently for each point.

The main advantage of confocal microscopes is their strong reduction of background arising from out-of-focus fluorescence. This comes at the cost of an increased acquisition time, which can be a disadvantage for the observation of living material; however, spinning-disk microscopes have largely solved this problem by parallelising signal acquisitions on different parts of the field of view.

On widefield microscopes, the problem of background from out-of-focus fluorescence is usually solved by using Total Internal Reflection Fluorescence (TIRF) illumination. TIRF relies on the fact that when a light beam bounces-off a glass surface, it generates an evanescent light wave. This evanescent wave is powerful near the glass surface, but rapidly decreases away from it. This allows imaging a thickness of ~ 200 nm, but cannot be used for thicker samples, or to image features that stand further away from the glass.

2.3 Fluorescent proteins or organic dyes?

In parallel to FPs, organic dyes have been developed and used for fluorescence microscopy. These small molecules are not genetically encoded, but they are extremely bright due to high extinction coefficients and QY. Furthermore, they are usually more resistant to photobleaching. So, why still use FPs?

The fact that FPs are genetically encoded constitutes a very big advantage for all in-vivo applications, and is almost indispensable for imaging on whole organisms or tissues. Using organic dyes often requires permeabilising the cells, and using specific buffers that are not always compatible with living cells. Finally, organic dyes do not provide the very high specificity and one-to-one labelling that FPs do.

In conclusion, although organic fluorophores combine very good imaging characteristics with a wealth of tunable properties, FPs remain markers of choice for labelling of living material, and applications where labelling specificity is crucial. It is therefore expected that FP development will

be of major interest to the fluorescence microscopy community in the coming years.

2.4 Limitations

Although fluorescence brought unprecedented contrast to microscopy images, it was still subject to the resolution limit described by Abbe's law, limiting the lateral resolution of fluorescence images to $\sim$ 200 nm. If anything, this limit was even more acutely perceived, since better objectives and cameras allowed detecting extremely small fluorescent objects, down to the single molecule. Thus image quality was not limited by sensitivity, or magnification, but by resolution.

However, this historical limitation was overcome by super-resolution techniques, including Single-Molecule Localisation Microscopy (SMLM) (described in chapter 4). One of the main tools that made SMLM possible were a novel class of FPs: PTFPs.

Chapter 3

Phototransformable fluorescent proteins (PTFPs)

PTFPs are GFP-like fluorescent proteins that display photochromism properties, meaning that their spectral properties can change under specific illumination. Three main types of PTFPs are known to date:[22]

- PhotoActivatable Fluorescent Proteins (PAFPs) irreversibly change from a non-fluorescent to a fluorescent state
- Reversibly Switchable Fluorescent Proteins (RSFPs) reversibly switch between a fluorescent and a non-fluorescent state
- Photo-Convertible Fluorescent Proteins (PCFPs) irreversibly convert between fluorescent states with different emission colors

This chapter will try to give an overview of the basic characteristics of PTFPs from these three classes, and the approaches taken to engineer new variants with different, or improved properties.

3.1 The different types of PTFPs

3.1.1 Discovery

Photochromism in FPs was first observed in the early times of GFP development. In 1997, "blinking" of fluorescence emission was observed on yellow FPs at the single-molecule level.[46] The protein was shown to repetitively switch between emitting and non-emitting states, and could be rapidly brought back from dark states using 405-nm illumination. In the same year, it was shown that under anaerobic conditions and blue light excitation, GFP changed its emission color from green (508 nm) to red (600 nm).[47] A similar process termed oxidative redding was later reported, where green-to-red photoconversion occured in the presence of oxidant molecules.[48]

Despite these early findings, photochromism was still rarely studied, and perceived more as a nuisance than an asset. However, a few years later, the discovery of coral and anemone FPs with

photochromism properties, and the first engineering of PTFPs, changed the situation.

Among these new FPs were the first RSFPs, asFP595 and 22G (then engineered to Dronpa),[49] as well as the PCFPs Kaede and EosFP.[50,51] Around the same time, GFP was engineered to make the first PAFP, PA-GFP (Photo-Activatable GFP).[52] This, together with the first applications in super-resolution microscopy (discussed in the next chapter) gave a start to a broader interest in PTFPs and their engineering.

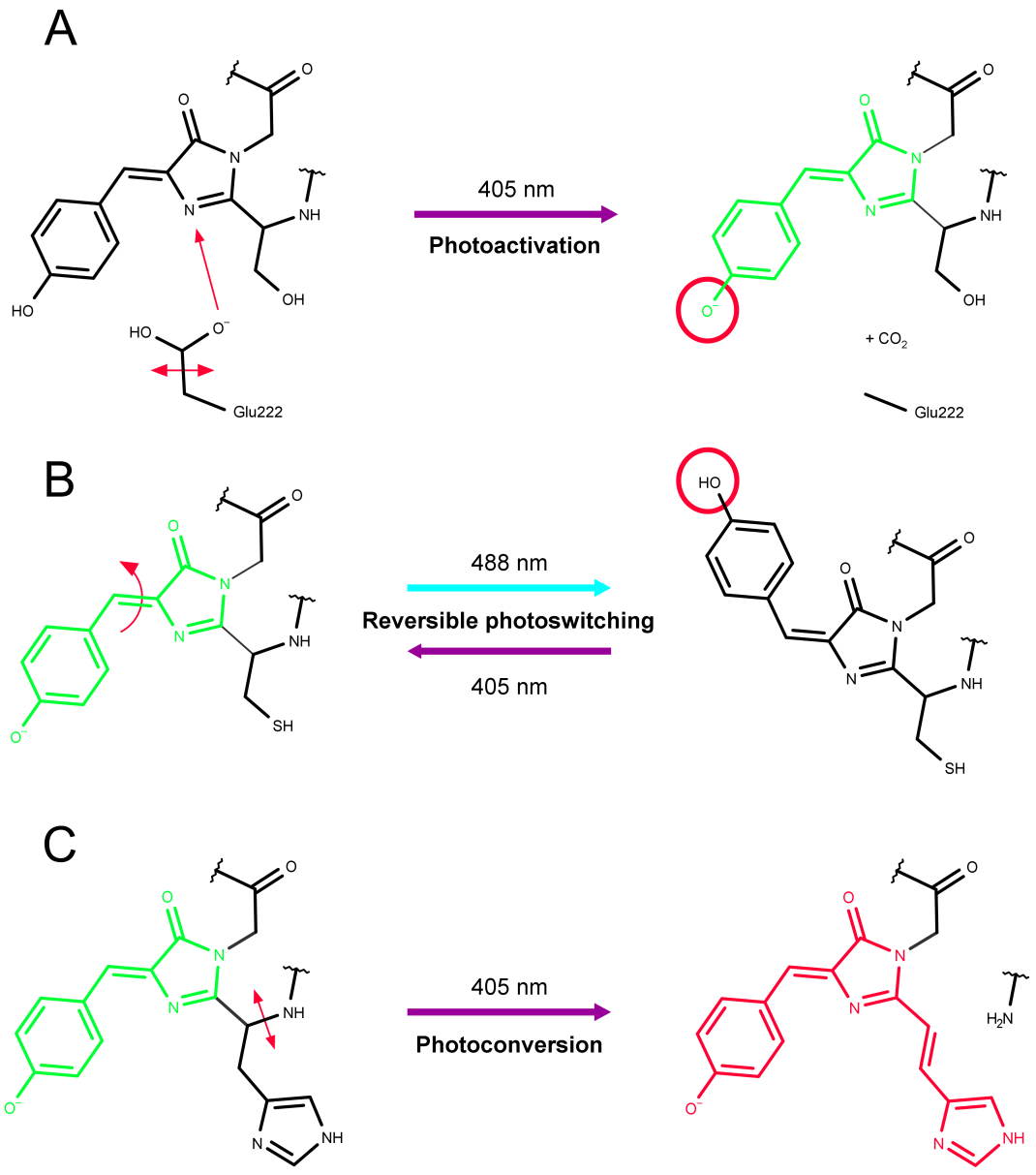

Figure 3.1: Categories of PTFPs according to their photochromism. (A) Photoactivatable FPs undergo decarboxylation of Glu222 under illumination at 405 nm, which favors the anionic, fluorescent form of the chromophore over the neutral, non-fluorescent form. (B) Reversibly switchable FPs undergo reversible switching between the fluorescent *cis* anionic conformation of the chromophore Tyrosine, and a non-fluorescent *trans* protonated conformation. The reaction shown here corresponds to a negative photoswitcher (e.g. Dronpa). (C) In photoconvertible FPs, breakage of a peptide bond under 405-nm illumination results in the extension of the electron-conjugation system to the histidine of the chromophore, and thus to a shift in emission colour. Adapted from ref.[22]

3.1.2 Photoactivatable fluorescent proteins (PAFPs)

The design of the first PAFP was based on the observation that wild-type GFP possessed two main absorbance peaks corresponding to the neutral and anionic chromophore, as shown on Figure 1.5. Upon UV-irradation however, the neutral form would convert to anionic, giving rise to an approximately 3-fold increase in fluorescence upon 488-nm excitation. Furthermore, it had been previously reported that mutation of Threonine 203 affected the equilibrium between the neutral and anionic peaks.[27] Therefore, G. Patterson and J. Lippincott-Schwartz conducted random mutagenesis at this position, seeking to amplify this behaviour. The result of this study was the GFP T203H mutant, termed PA-GFP, which was almost completely non-fluorescent when produced, and underwent a 100-fold increase in fluorescence upon UV-irradiation.

Some years later, the first photoactivatable red fluorescent protein was engineered from mCherry using a combination of saturated mutagenesis at a few sites of interest, random mutagenesis, and extensive screening of the produced variants.[53] The resulting protein was called PA-mCherry, and enabled two-color applications with PAFPs.

PA-GFP and PA-mCherry have partially similar activation processes, where absorption of near-UV light induces decarboxylation of Glu222, and deprotonation of Tyr66 to form the fluorescent anionic chromophore (Figure 3.1, panel A).[22,53] This process is irreversible, and once activated, the protein cannot go back to its inital dark state (but will eventually photobleach).

3.1.3 Reversibly switchable fluorescent proteins (RSFPs)

Unlike photoactivation, photoswitching is a reversible process. It relies on the combined isomerisation and (de)-protonation of the chromophore, to switch the protein between a non-fluorescent and a fluorescent state (Figure 3.1, panel B). The fluorescent state is the *cis* anionic state, whereas the *trans* protonated state is non-fluorescent. Different categories of RSFPs exist depending on whether photon absorption at the peak excitation wavelength induces:

- off-switching (negative switchers such as Dronpa[49])
- on-switching (positive switchers such as Padron[54])
- has no switching effect (decoupled switching as in Dreiklang[55])

Important engineering efforts have been made to improve RSFPs, in terms of brightness, switching efficiency, switching contrast (the ratio between the maximum and minimum fluorescence attainable upon on- and off-switching, respectively), and folding properties.[56–58]

3.1.4 Photoconvertible fluorescent proteins (PCFPs)

The first PCFPs discovered were Kaede[50] and EosFP,[51] from the stony corals *Trachyphyllia geoffroyi* and *Lobophyllia hemprichii*, respectively. Both of these proteins, upon near-UV illumination, undergo cleavage of a peptide bond linking the chromophore to the protein backbone, which results in an extension of the electron-conjugation system of the chromophore, shifting the main absorbance peak from blue to yellow, and the fluorescence emission from green to red (Figure 3.1, panel C). This is made possible by the composition of the chromophore, which features the amino-acids His-Tyr-Gly in all known green-to-red PCFPs. Like photoactivation, photoconversion is an irreversible

process, and photoconverted proteins cannot return to the green-emitting state.

A historical inconvenient of PCFPs was their obligate tetrameric state; however, this initial hurdle was overcome by several rounds of mutagenesis, successively breaking the tetramers into dimers and monomers. Of note, because of this initial tetrameric assembly, some of the monomerised PCFPs kept a tendency to oligomerise at high concentrations. Therefore, some of the subsequent studies focused on designing truly monomeric PCFPs.[59]

Popular PCFPs include mEos2,[60] Dendra2,[61] Kaede[50] and mMaple.[62]

Role in nature

Interestingly, photoconversion in PCFPs seems to be an evolved process, and to be playing a role in stony corals - contrarily to PAFPs and RSFPs, which rather result from the engineering of properties largely shared by the different FP families.

Stony corals are symbiotic organisms, made from the association of a cnidarian host, and a unicellular algae. They grow in shallow waters, which means they are exposed to strong sunlight irradiation. In this context, PCFPs would be produced as a means to protect the algae's photosynthetic system from strong irradiation.
The tetrameric structure has an important role here: under the natural UV exposition from sunlight, some of the proteins in the tetramer convert to the red-emitting form, and can thus serve as FRET acceptors for the green-emitting proteins. This has the net effect of absorbing the high-energy and potentially harmful blue light, and re-emitting red light, which is less damaging and more useful for photosynthesis.

3.1.5 Understanding the molecular mechanisms underlying phototransformations

The study of photochromism brought renewed interest to structural studies on fluorescent proteins. Solving the structure of new FPs and their different states by crystallography helped understand how light-induced structural modifications could lead to reversible and irreversible spectral changes. More recently, setups have been designed to record absorbance and fluorescence spectra on protein crystals, thus directly correlating spectroscopically observed changes with differences in protein structure.[63] Finally, time-resolved crystallography allowed deciphering the dynamic processes behind photochromic behaviours, and was recently pushed to the picosecond timescale using X-Ray Free Electron Lasers (XFELs).[64] Such studies are still ongoing, and will surely bring more insights into the functionning of PTFPs, and clues for their improvement.

3.2 The EosFP family

3.2.1 Discovery and developments

As mentioned previously, EosFP was one of the first discovered PCFPs, and was rapidly engineered to a monomeric form called mEosFP.[51] However, mEosFP still suffered from improper folding at 37°C, which practically prevented its use in mammalian cells. This prompted the development of

mEos2, which folded properly at 37°C, while correctly targeting various cellular structures of interest (e.g. tubulin, histones, or intermediate filaments).[60] The next development was introduced when it became apparent that mEos2 was not fully monomeric and still induced protein aggregation, in particular in the limited space of membrane-anchored proteins.[59] This led to the design of mEos3.1 and mEos3.2, two truly monomeric variants. Finally, the most recent step came when researchers tried to use Eos proteins in correlative light and electron microscopy, where the FPs need to resist to resin embedding and OsO_4 fixation. This was achieved starting from mEos3.2, and without damaging other properties such as maturation rate, folding properties or brightness. The resulting protein was named mEos4b.[65] This line of engineering, as well as other developed variants, are summarised on Figure 3.2.

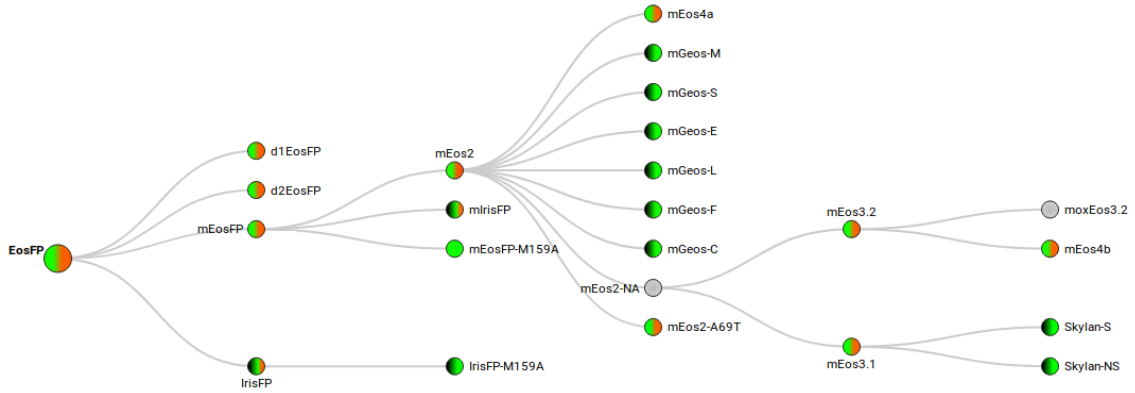

Figure 3.2: Summary of the FP variants engineered from EosFP. Colors indicate the phototransformations undergone by the corresponding FP: green-to-red photoconversion, photoswitching, or a combination of both. Figure adapted from FPbase (fpbase.org).

All along their development, Eos proteins have been very popular for microscopy, and especially super-resolution approaches (as discussed in the next chapter). This is mainly due to the fact that they are brighter than PAFPs and other PCFPs (as shown on table 3.1 for a few popular PA- and PCFPs). Moreover, their green fluorescence can be used to locate features of interest before imaging of the red state, which is an advantage over PAFPs. As a result, mEos2, and now its derivatives, have been extensively used in diverse microscopy experiments requiring photochromism.

FP	Extinction coefficient ($M^{-1}.cm^{-1}$)	Fluorescence QY	Brightness
mEos2 (red)	46000	0.66	30.36
mEos3.2 (red)	32200	0.55	17.71
mEos4b (red)	55500	0.71	39.41
PA-GFP	17400	0.79	13.75
PA-mCherry2	24000	0.53	12.72
Dendra2 (red)	35000	0.55	19.25
Kaede (red)	60400	0.33	19.93
mMaple (red)	30000	0.56	16.8

Table 3.1: Comparison of FP brightnesses between Eos variants, PAFPs and other PCFPs. For PCFPs, numbers are given for the red form, which is the one typically imaged in super-resolution (see chapter 4). Data obtained from FPbase (fpbase.org). QY: Quantum Yield.

3.2.2 IrisFP: combining properties

IrisFP, designed from EosFP (see Figure 3.2), was the first engineered biphotochromic protein. On top of retaining the photoconversion ability of its parent, it was also able to undergo efficient reversible switching, in both its green and red form. This was made possible by the F173S mutation, which resulted in the creation of two cavities near the chromophore, and thus allowed its isomerisation.[66] This protein however retained its tetrameric character, until a variant with similar properties was engineered directly from mEosFP, and named mIrisFP.[67]

Interestingly, another biphotochromic variant (pcDronpa) was later designed using the RSFP Dronpa as a template and enabling it to photoconvert to a red-emitting state.[68] Like IrisFP, it is tetrameric, but a noteworthy difference is that is does not photoswitch in the red state.

3.3 PCFPs display complex photophysical behaviours

As stated previously, PCFPs such as mEos2 or mEos4b are widely used in microscopy experiments. However, their photophysics is in fact not as straightforward as was initially thought, and it appeared that other light-induced processes occurred than green-to-red photoconversion. Understanding these processes can help to better delimitate their effects, and to avoid related artefacts. This section aims at giving an overview of such behaviour in PCFPs of the Eos family, including incomplete photoconversion, blinking, and conversion to the triplet state.

3.3.1 Incomplete photoconversion

A commonly reported issue with PCFPs is the incomplete photoconversion of the protein, which results in a fraction of the labels missing from fluorescence images. For example, a measure of this phenomenon on the mEos2 protein showed a photoconversion efficiency of $\sim 60\%$; meaning 40% of the FP labels are not seen.[69] Reasons for this include incorrect folding of the FP, non-maturation of the chromophore, or pre-mature photobleaching in the green or red state (i.e. before the protein has emitted enough red photons to be detected).

3.3.2 Blinking

Blinking is defined as the transient loss of fluorescence of a fluorophore. It is commonly observed when imaging single FPs, and was first reported by Dickson et al. in 1997, in their observation of single GFP molecules.[46] From their observations they proposed a model (shown on Figure 3.3) showing the energy landscape of a blinking protein. Typically, FPs can transition to different non-emissive states, from which they recover either thermally (e.g. the I state in Figure 3.3) or in a light-induced manner (like the N state).

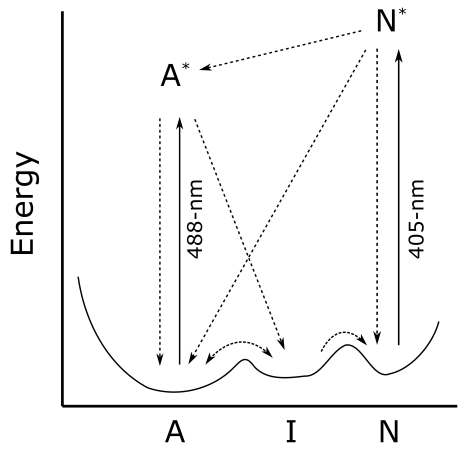

Figure 3.3: Schematic representation of the blinking states of GFP (adapted from ref[46]). The fluorescent state A, upon excitation at 488-nm, can transition to the I intermediate state, which is not fluorescent. From there, it can either spontaneously recover to A, or transition to N, from where it can be re-excited with 405-nm light.

Blinking has since then been observed in different fluorescent proteins,[70,71] including PCFPs such as mEos2 and Dendra2.[72–74] In PCFPs, two blinking regimes have been characterised: a short-lived one, with durations up to $\sim$ 100 ms, and a longer-lived one, which can last for several seconds. The corresponding photophysical model is depicted on the scheme of Figure 3.4. The short-lived dark-state is thought to be a non-absorbing radical state, and therefore recovers to the fluorescent state by thermal relaxation, with a rate constant of 15-20 s^{-1}.[75,76] The nature of the long-lived dark-state, on the other hand, is not known, but it has been reported to be sensitive to 405-nm illumination.[73,74]

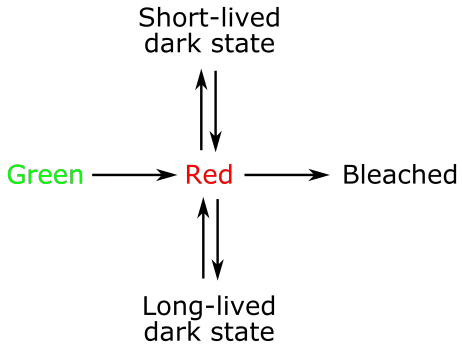

Figure 3.4: Basic photophysical scheme for blinking in PCFPs (adapted from ref[74]). Once photoconverted to the red state, the protein can enter a short-lived dark-state (responsible for fast blinking), a long-lived one (responsible for slow blinking), or irreversibly photobleach.

Interestingly, the photophysical models for blinking in GFP and in PCFPs (Figures 3.3 and 3.4 above) are slightly different. In GFP, the short-lived dark-state I can relax thermally to either the fluorescent state A, or the long-lived dark-state N. In the current view of PCFP photophysics however, the short- and long-lived dark-states are independent, and both relax only to the fluorescent state. These different behaviours could be due to the different origins of the studied FPs; but it might also point to an incomplete understanding of the photophysics of either or both types of proteins. Better understanding the nature of the long-lived dark-state of PCFPs would provide some insight as to whether it could be populated from the short-lived dark-state, as proposed for GFP.

Different PCFPs have different blinking properties

Although few comparative studies exist, previous work in the lab by former PhD student Romain Berardozzi has shown that different PCFPs could have different blinking behaviours, like in the case of Dendra2 and mEos2.[74] These two proteins were found to be different in that respect: while both showed blinking, mEos2 had a high blinking propensity with long-lived dark states, and was relatively resistant to photobleaching, and Dendra2 was more prone to photobleaching, which resulted in a lower apparent blinking propensity.

Interestingly, another finding in that project was that a single point mutation (A69T in mEos2 or T69A in Dendra2) was enough to invert the properties of both proteins, reducing blinking and increasing photobleaching in mEos2 while increasing blinking and decreasing photobleaching in Dendra2.

Dependence of blinking on the experimental conditions

Not only the intrinsic properties of the fluorophores, but also the experimental conditions have been reported to affect blinking of FPs, the main factors investigated being illumination intensity (at different wavelengths) and chemical environment.

Light-sensitivity of blinking. Several blinking processes in different FPs have been reported to be light-induced, including recovery from dark-states and transition from the fluorescent to blinked states.[46,73,74,77]

This light sensitivity arises from the fact that non-emissive states are typically reached through the S_1 excited state (see section 1.1, Figure 1.1). Recovery to the fluorescent state can happen thermally if the dark state is non-absorbing, and of higher energy than the S_0 ground state. If the dark state absorbs light, its transition to an excited state can speed up its recovery to the fluorescent state.

The rate of transition from one state to another will depend on:

- Illumination intensity
- Absorbance of the starting state at the illumination wavelength
- Probability of the transition occuring per absorbed photon (also called reaction quantum yield, not to be confused with the fluorescence quantum yield described in section 1.1).

In analogy to the brightness of a fluorophore, one can refer to the reaction brightness, which is the product of the absorption coefficient at the illumination wavelength, and the reaction quantum yield ($B = QY_{reac} \times \varepsilon$).

Sensitivity to the chemical environment. Some studies have probed the behaviour of FPs in buffers with different chemical compositions. Notably, reducing agents have been found to increase blinking in mEos2 and mEos3.2.[78,79] Even though only small molecules are able to diffuse in the β-barrel of FPs to directly interact with the chromophore, bigger molecules can initiate electron-transfer reactions, thus also affecting FPs photophysical behaviour. Further studies of the influence of buffer composition on FPs could however be of interest, given the strong dependence of organic dyes photophysics on these parameters.[80,81]

3.3.3 Conversion to the triplet state

As mentioned in section 1.1 and shown on Figure 1.1, FPs can undergo inter-system crossing from the S_1 singlet excited state to the T_1 triplet state. Differing values have been reported for the yield of inter-system crossing (0.1%[82] to 1%[3]), as well as for the lifetime of the triplet state (from µs[82] to ms[3]). In any case, the lifetime is much shorter than typical exposure times in fluorescence microscopy, meaning transition to the triplet state is not directly observed as intermittencies in fluorescence emission, like in the case of blinking.

Even though this process is not directly observable in microscopy experiments, it can still be detrimental. Its most straightforward consequence is the reduction of the total number of photons emitted by a protein during a single camera exposure, reducing the apparent brightness of the fluorophore. A recent study in the lab has furthermore proposed that the triplet state could serve as an entry point for further chemical reactions, including photobleaching and blinking: the findings suggest that electron acceptors can abstract an electron from the chromophore in the triplet excited state, yielding a chromophore radical that does not absorb at 488 nm.[3] Such a radical state was previously proposed to be at the source of short-lived blinking in PCFPs.[76]

However, triplet-mediated photochemistry is not necessarily detrimental to microscopy experiments. In 2015, a study demonstrated the possibility to photoconvert the Dendra2 PCFP by using a combination of 488- and 642- or 730-nm light instead of the traditional 405-nm light.[83] This technique, called "primed photoconversion", allows photoconverting certain PCFPs without using potentially phototoxic 405-nm light. A later study by the same authors showed that primed photoconversion proceeds from a triplet state.[84]

The discovery of PTFPs and the progressive understanding of their photophysics opened the way to the use of FPs in SMLM, a category of super-resolution techniques which will be described in the following chapter.

Chapter 4

Single-Molecule Localization Microscopy (SMLM)

4.1 Beating the light-diffraction limit

As stated in the introductory section of this manuscript, the resolution of images obtained with an optical microscope is limited by light diffraction. According to Abbe's law, the resolution of fluorescence images cannot be improved beyond $\sim$ 200 nm. Furthermore, this limit applies equally to fluorescence emission from molecules, as to a focused laser beam; therefore, simple confocal schemes cannot alone surpass it. However, a number of developments introduced in the 1990s and 2000s managed to address this challenge: the *super-resolution* techniques.

The first super-resolution technique to beat the diffraction limit was Near-Field Scanning Optical Microscopy (NSOM), developed in the lab of E. Betzig. The method used no objective lens, but light coming from a very thin aperture. This light would generate an evanescent wave of sub-diffraction size ($\sim$ 20 nm laterally and axially).[85] Although this technology provided unprecedented possibilities, it was still difficult to implement, and found only few applications.
Some years later, Structured Illumination Microscopy (SIM) was developed. This technique used interferences between two beams to generate a sinusoidal pattern in the illumination light. Analysis of the interaction of such a structured illumination with the sample allowed retrieving structural features up to twice smaller than the light diffraction limit.[86,87]

These were the first breakthroughs in the field of super-resolution; however, the real revolution occured with the development of two techniques which managed considerable resolution improvements: Stimulated Emission Depletion (STED)[88] and PhotoActivated Localisation Microscopy (PALM).[89,90]
In brief, STED uses the non-linear response of FPs to a fluorescence depletion laser to reduce to an arbitrary size the spot of FPs contributing to the fluorescence signal. For clarity and compactness reasons, the rest of this manuscript will however not deal with this technique and the family of variants and applications that were derived from it. The following sections will only deal with PALM, and more generally the single-molecule imaging techniques.

4.2 First images of single molecules

SMLM relies on the detection of single fluorophores. This was definitely not an obvious option, and it came as a breakthrough when W.E. Moerner imaged single molecules for the first time in 1989,[91] shortly followed by M. Orrit in 1990.[92] The development of single-molecule imaging continued in the 1990s, which eventually led to the publication of the first observation of single GFP molecules in 1997, along with an unprecedented analysis of their photophysics.[46] As expected from Abbe's law, the image of a single-molecule is the convolution of the signal it emits through the point-spread function (PSF) of the microscope, resulting in a $\sim$ 200 nm broad spot.

However, observing single molecules was not yet enough to improve image resolution: although their position could be precisely determined, they had to be separated by more than the diffraction limit. This effectively limited the resolution of any reconstructed structure: the smaller the feature to be resolved, the closer together the fluorescent labels have to be.[93] An insufficient number of fluorophores will result in "undersampling", which will prevent the observation of small structures.

This is where the development of PTFPs came to be of great interest, by enabling the consecutive imaging of sparse subsets of fluorophores in a densely labelled sample.

4.3 Modalities for SMLM

The first SMLM schemes developed were PALM,[89,90] Stochastic Optical Reconstruction Microscopy (STORM),[94] and Point Accumulation for Imaging in Nanoscale Topography (PAINT).[95]

- PALM uses phototransformable fluorescent proteins to image single fluorophores from a densely labelled sample.

- STORM initially reached the same goal using a pair of organic fluorophores (e.g. the Cy3 and Cy5 dyes). One of the fluorophores would be switched to a stable dark-state, that can be rescued when the second dye (called activator) is excited. A few years later, this technique gave rise to dSTORM,[96] which uses either photoswitchable organic fluorophores (such as the ATTO dyes, or the recent photoactivatable Janelia Fluor dyes), or reducing/oxygen-depleting buffers, which induce blinking of the dyes. The advantage of dSTORM over STORM is that it does not require an activator dye. Of note, STORM and dSTORM most often require cell permeabilisation for labelling, which is not compatible with living cells; therefore, cell-permeable organic dyes have been recently developed, which are more suited to in-vivo studies.[97]

- PAINT uses yet another solution, as it relies on diffusing fluorophores binding specifically to a target (e.g. a genetically encoded protein tag). Since freely diffusing fluorophores could create important background in the images, this technique requires either using TIRF imaging with target structures located close to the glass surface, or fluorogenic probes which become fluorescent only when bound to a target molecule. Overall, PAINT presents the significant advantages of allowing multiple binding events to occur on the same target, thus improving the precision of the reconstructed image, and optimising the fraction of labelled targets.

4.4 Principle of single-molecule localisation microscopy (SMLM)

SMLM relies on the temporal separation of fluorescence events to localise single fluorophores with nanometer precision, and reconstruct a high-resolution image. Technically, this makes use of the photochromic properties of the dyes. For each image, a large number of camera frames need to be acquired ($\sim 10^4$ to 10^5), during which a constant fluorescence excitation laser is applied, along with a weak activation laser (typically 405-nm) to prompt the stochastic photoconversion of a small amount of fluorophores per frame. After a few frames of fluorescence emission, the activated fluorophores will be photobleached or switched off, and new ones can be activated (Figure 4.1). For each detected single-molecule, a gaussian function can be used to fit the PSF (Figure 4.2) and determine the position of the molecule with sub-diffraction accuracy.

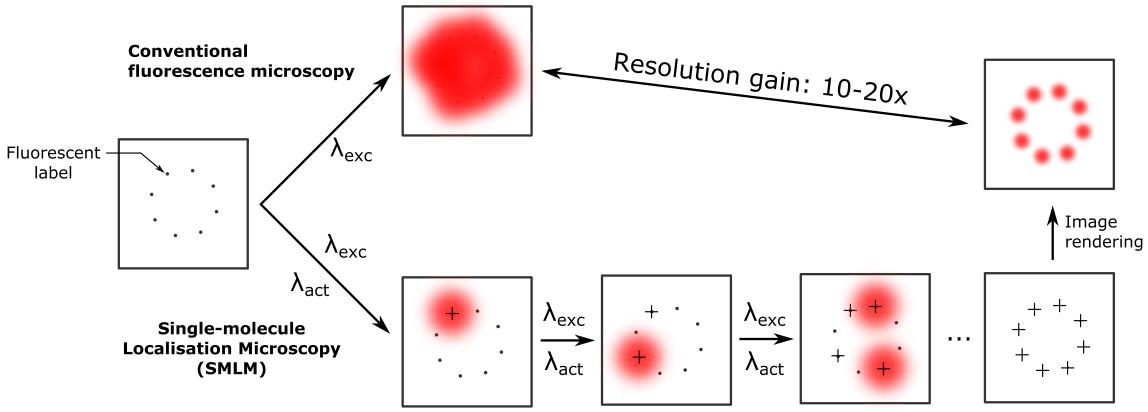

Figure 4.1: Principle of single-molecule localisation microscopy (SMLM). In conventional fluorescence microscopy, fluorescence from all labels is detected at once. Therefore, features smaller than the resolution limit cannot be distinguished. In SMLM, labels are stochastically and sparsely activated over time, and their positions recorded. From the list of localisations, a reconstituted image can be built, with a final resolution of $\sim$ 10 to 20 nm.

4.4.1 Resolution limit in SMLM

Resolution in SMLM depends on two criteria: the precision of the fit used to determine fluorophore position (shown in Figure 4.2), and the density of labelling. Fit precision is itself conditioned by the number of photons collected per localisation, which explains the dependency of image resolution on $1/\sqrt{N}$ (with N the number of photons collected). The density of labelling required to attain a certain resolution is dictated by the Nyquist sampling theorem, which states that to be resolved, a structure of interest should be labelled at intervals at least two times smaller than the smallest feature of the structure. SMLM images typically reach a resolution of $\sim$ 10-20 nm. The main limits to this figure are the number of photons collected per fluorophore, and incomplete labelling (discussed in the case of FPs in chapter 3.3) which limits sampling.

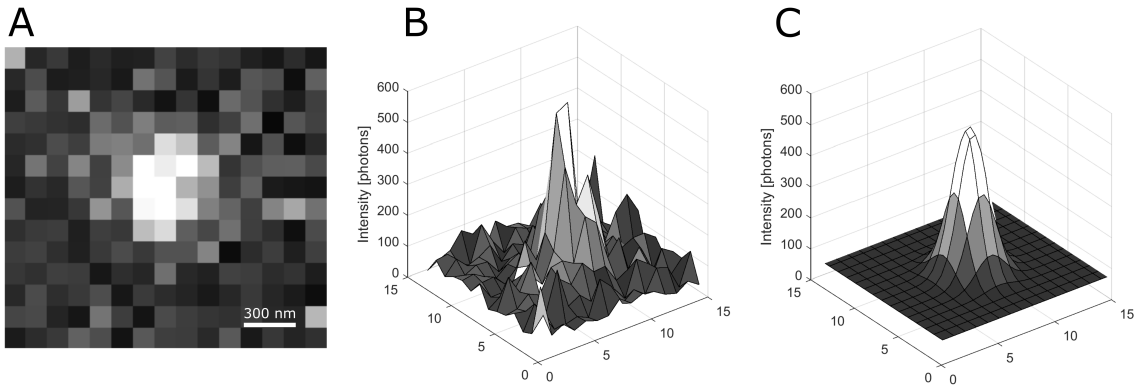

Figure 4.2: Gaussian fitting of the intensity profile of a single emitter. (A) Single molecule detected on an EMCCD camera during a PALM experiment. (B) Surface representation of the intensity profile of the single molecule. (C) Gaussian fit to the intensity profile, from which the position of the molecule can be determined with $\sim$ 20 nm accuracy.

4.4.2 Important parameters to be taken into account during SMLM experiments

Resolution, but also image quality in general depend on specific parameters that are usually assessed and optimised to produce a useful SMLM image. This non-exhaustive list aims at pointing out some of the most important ones.

- **Signal-to-noise.** As mentioned previously, the number of photons collected per molecule will directly influence the resolution of the reconstructed image. More precisely, the key parameter is the signal-to-noise ratio. This ratio can be improved by using brighter, or more photostable probes; but also by reducing background fluorescence in the images. This is particularly important for in-vivo imaging, since cells are known to be auto-fluorescent. One of the commonly used ways to decrease background signal in widefield microscopy is to use TIRF illumination.

- **Localisation density.** By definition, PALM requires that the fluorescent labels are sparsely activated over time, which is not always easily achieved, especially for very densely labelled samples. Overlapping molecules will lead to missed detections, mis-localisations, and decreased resolution. A simple but often unsufficient means of avoiding overlapping molecules is to keep the activation laser at a low power. Alternatively, frames where fluorophore density is too high can be discarded to preserve image quality, at the cost of reduced sampling. Several advanced methods have also been developed until recently to resolve overlapping spots, and reduce the occurence of artefacts.[98–105]

- **Clustering.** Since some molecules stay in the fluorescent state for more than one camera frame, the resulting localisations can be merged in the rendered image. This can avoid artefacts due to stochastic bleaching times of the molecules, and improve localisation precision by adding up the information from several consecutive frames. However, this supposes that close localisations can be unambiguously attributed to the same molecule. Misattributions

will lead to wrong localisations. In the case of clustering or co-localisation analyses, the clustering method is of course of primary importance. Clustering algorithms used in PALM include among others K-means,[106] density-based spatial clustering of applications with noise (DBSCAN),[107] or Voronoi tesselation.[108]

4.4.3 Artefacts due to PCFP photophysics

The complex photophysics of PCFPs described in section 3.3 affects the quality of SMLM images. Incomplete photoconversion results in reduction of the labelling density, and hence of the resolution of the image, according to the Nyquist sampling theorem. It is also very detrimental to co-localisation and FRET studies, by decreasing the degree of labelling of each of the interacting proteins.

Blinking can also be a source of error: whereas in STORM, it is a useful property that is at the base of single-molecule imaging, in PALM it constitutes more of a spurious effect, since temporal separation of fluorescence events is achieved by photoactivation or photoconversion. An example of blinking-induced artefact is the erroneous clustering patterns observed on images of membrane receptors.[109]

Beyond generating images with unprecedented resolution, SMLM approaches have the power of detecting individual molecules rather than an average population. This gives unique information on dynamic processes such as protein diffusion or complex assembly, and allows precise quantification of the number of molecules in a cell or organelle. This is particularly true in the case of PALM, where such approaches benefit greatly from the very high specificity and 1-to-1 labelling provided by FPs. This has led to the development of advanced applications of PALM. Two of them will be described in the next sections that are of particular interest for this thesis: single-particle tracking PALM (sptPALM) and quantitative PALM (qPALM).

Chapter 5

Advanced PALM applications

5.1 Single-particle tracking PALM (sptPALM)

5.1.1 Principle

Classical PALM experiments, due to their temporal separation of fluorescence events, generally require working on fixed samples. sptPALM on the other hand, which was first reported in 2008,[110] is used to observe living - or at least non-fixed - samples, where molecules are diffusing. The main aim of the technique is not anymore to obtain a high resolution image, but rather to use the single-molecule information inherent to PALM datasets to characterise the diffusion behaviour of a protein of interest.

The basic principle of sptPALM is summarised in Figure 5.1. In short, fluorescence events detected close together in consecutive frames are attributed to the same molecule, hence reconstituting its motion over time. From the final tracks obtained, different types of motions can be observed. This can be characterised more quantitatively by different means, either at the single-particle level, or from the total population of tracks recorded.[111] Below are listed some of the most common figures used for sptPALM data analysis.

At the population level

- The **mean square displacement (MSD)** is the average squared distance between two localisations of a molecule separated by a given time (termed lag time). MSDs can be computed for a range of different lag times (as shown on Figure 5.1, panels B and C). Their dependence on lag time reflects the diffusion behaviour of the molecules (free, confined or directed diffusion). Fitting of the MSD vs. lag time curves can also yield diffusion coefficients.[112]
- The **cumulative frequency distribution of diffusion coefficients** can be plotted, which allows distinguishing changes in diffusion regimes between experimental conditions. Figure 5.1 D shows an example of distributions for molecules diffusing in or out of synapses. The shift of the cumulative curve to the left for synaptic molecules shows slower diffusion.
- The **distribution of dwell times** corresponds to the percentage of time spent by a molecule at a specific position (e.g. a synapse or an organelle) over the total duration of the experiment.

An example is shown on Figure 5.1 E, to probe the residence time of molecules in the synapse of a neuron. The dwell time corresponds to the total time spent in the synapse over the course of the experiment. Molecules that remain in the area of interest during the whole experiment are considered immobile. This distribution can be coupled to an analysis of the transition frequencies, i.e. the frequency with which molecules enter and exit the region of interest.

- **Colocalisation times** can be used to detect interactions between diffusing molecules.

At the single-molecule level

- **Instantaneous diffusion coefficients**, represented as a plot of diffusion coefficient (in $\mu m^2/s$) vs. time, can show transitions of a molecule between different diffusion regimes, or binding to molecular partners. However, this requires reliable tracks, with sufficient length to be able to observe changes, and sufficient time resolution to detect fast processes like transient bindings.

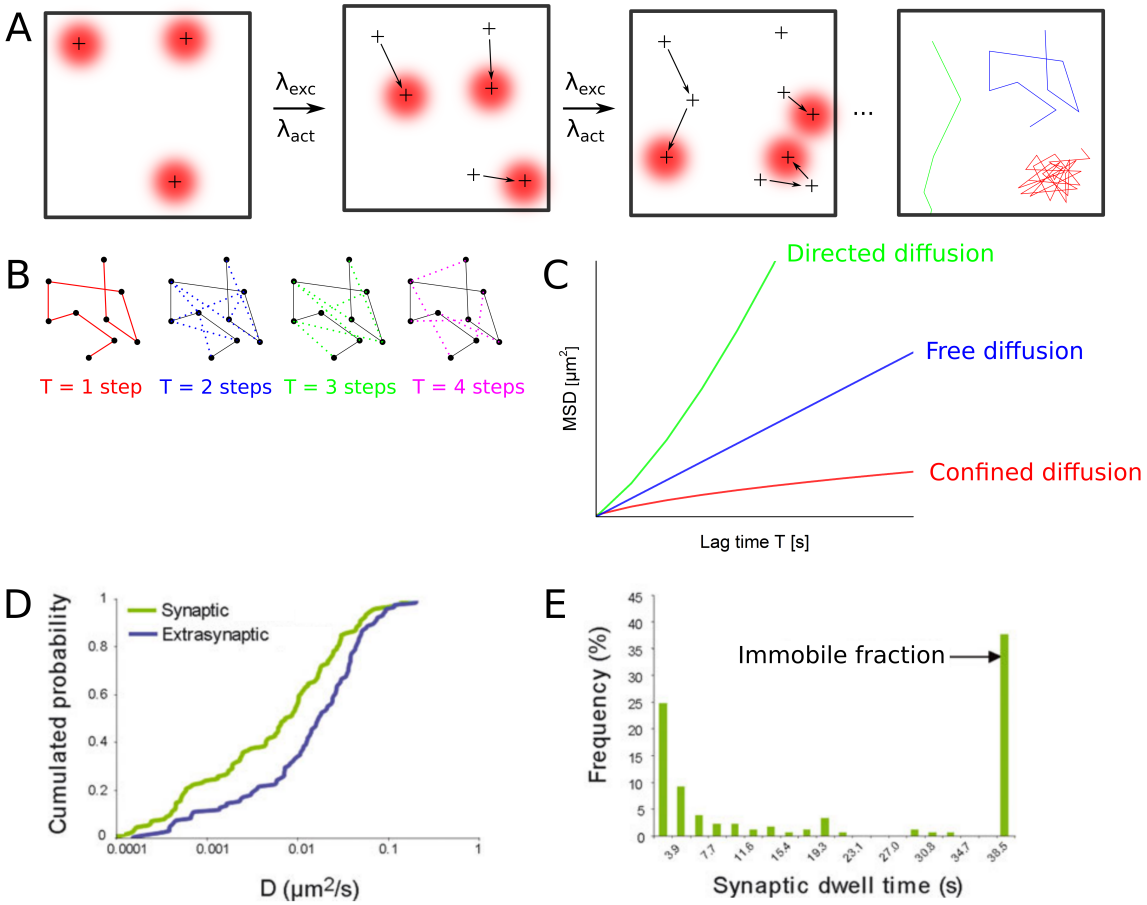

Figure 5.1: (A) Principle of single-particle tracking PALM (sptPALM). Diffusing molecules are localised on consecutive images, allowing the reconstitution of their path along the experiment, and the observation of different diffusion behaviours. (B) From each molecule track, mean square displacements (MSDs) can be calculated for different lag times (here shown for 1, 2, 3 and 4 camera frames). (C) A plot of MSD versus lag time reveals the diffusion behaviour of the molecules: free (straight line), confined or directed. (D) Cumulative frequency distribution of the diffusion coefficient for a protein diffusing in or out of a synapse. The shift of the distribution to the left shows a slowing down of the protein in the synapse. (E) Distribution of a molecules dwell time at synapses. The dwell time is the time spent at the synapse over the total time of the experiment (here 38.5 s). The immobile fraction corresponds to molecules that stayed in the synapse during the whole experiment. Panels D and E were both adapted from ref.[111]

sptPALM offers great possibilities for the study of biological phenomena. It can provide information on dynamic processes in living cells, and its single-molecule sensitivity allows detecting heterogenous behaviours. Hence it becomes for example possible to assess whether a given protein changes diffusion regime in particular organelles, or under specific stimuli.

sptPALM has been extensively used to study diffusion of membrane-bound proteins[113] and effectors in neurons,[111] as well as to characterise G-protein coupled receptors (GPCRs).[114]

5.1.2 Important parameters

At the technical level, several parameters are of importance when performing sptPALM:

- **Label sparsity** As an SMLM technique, sptPALM relies on temporal separation of the fluorophores to obtain single-molecule information. Hence, activation of the probes should be slow enough to maintain this single-molecule regime. Arguably, the sparsity of the labels should be even lower than in normal PALM, since there is the added risk in sptPALM of mixing up the tracks of molecules appearing close together.

- **Acquisition rate** By definition, sptPALM is interested in dynamic processes. Therefore, the acquisition rate of the camera used for recording should be high enough to provide a good sampling of diffusing molecules. A too low acquisition rate will cause blurring of the signal from single molecules, which will result in lower localisation precision and higher risk of erroneous linking of molecules between frames. If the fluorophores are bright enough, stroboscopic illumination can be used to alleviate this effect.[115]

- **Track length** The length of the recorded tracks are of great importance to make sptPALM analyses meaningful and informative. In general, the achieved tracking length determines how many lag times can be used in MSD curves; longer track lengths will provide statistically relevant information up to longer lag times, and therefore a finer distinction between different diffusion regimes. On the contrary, too short tracking times can lead to imprecise MSD curves and erroneous diffusion coefficients. Finally, recording longer tracks can provide superior temporal information, such as repeated changes in diffusion regime over time.

The optimisation of these three parameters is typically achieved by fine-tuning the illumination scheme used for the experiment. Adjusting the activation laser power will allow controlling the rate of activation of the molecules, and therefore their sparsity. Increasing the readout laser power allows the collection of more photons per frame, allowing for higher acquisition rates, but at the cost of increased photobleaching, and therefore shorter track lengths. This tradeoff requires that experimental parameters are adjusted depending on the processes of interest: better time resolution for fast processes, and longer track lengths for slow processes, or to detect subsequent events.

5.1.3 Limitations of the technique

Despite being a very powerful and broadly used technique, sptPALM still suffers from certain limitations, some of which are directly related to the properties of the fluorescent probes used.

Diffusion processes

Some of the most fundamental limits of sptPALM lie in the nature of the observed phenomena. Camera exposition times (when using an EMCCD camera) and brightness of the fluorophores limit the maximum rate at which images can be acquired. Therefore, molecules that are diffusing too fast can generally not be observed. The shortest reported exposure time in single-particle tracking

was 20 µs, using gold beads as markers.[116] This is however far from attainable for most biological studies, and common exposure times are in the tens of milliseconds range.

Another limitation comes from the 3D diffusion of the observed molecules. High-NA objectives used for single-molecule detection have a rather small depth of focus (< 1 µm), so molecules that are freely diffusing will quickly diffuse out of focus. This is an important limitation to sptPALM experiments, and as a consequence, most sptPALM studies focused thus far on membrane proteins, that diffuse slower, and in a two-dimensional space.

Probes used for single-particle tracking

Different probes have been used for single-particle tracking, each bearing different advantages.

- Quantum dots have the advantage of being highly fluorescent, with low photobleaching. However, their large size (10-30 nm) makes it hard for them to enter cells, and to probe confined environments. Given the crowded molecular environment found in cells, their large size could also lead to a modified diffusion behaviour.
- Organic dyes also have good brightness and photostability, while being much smaller than quantum dots (1-2 nm). However, most of them are not compatible with living cells, since they require permeabilisation to cross the plasma membrane. Dyes commonly used for single-particle tracking are the cyanines, and more recently the cell-permeable Janelia fluor dyes, including their photoactivatable versions.[97]
- As stated previously, FPs are tools of choice for in-vivo labelling of proteins, which comes at the cost of a reduced brightness and photostability compared to organic fluorophores. Among the popular FPs used in sptPALM are mEos2, PAmCherry and Dendra2.

FPs photophysics

Knowledge of FPs photophysics helps us understand what are the limiting factors when using these markers in sptPALM experiments.

Blinking can be an extremely detrimental factor: it can lead to mixing up of the tracks of different molecules, or to interrupted tracks. Furthermore, these negative effects are expected to be more pronounced when the duration of the blinks increases. Short blinks of at most a few frames can still be corrected for, since the molecule will not have diffused very far. However, longer blinks systematically cause track interruptions due to the molecule reactivating at a large distance from its last known position. It is interesting to note that in a situation where most molecules blink at least once during their lifetime, blinking - more than bleaching - becomes a limiting factor to the maximum tracking length that can be achieved.

5.2 Quantitative PALM (qPALM)

5.2.1 Purpose

Interactions between proteins and formation of macromolecular complexes are key to a large number of processes in cells. qPALM (or molecular counting) proposes to use the single-molecule informa-

tion in SMLM images to infer the stoichiometry of complexes that are too small to be spatially resolvable. Although many different techniques exist that can give information on the stoichiometry of complexes, qPALM is unique through the combination of several features:

- By definition, it has single-molecule sensitivity, which allows stoichiometry determination from low amounts of proteins. This can be used to perform molecular counting in cells, at endogenous expression levels. Since complex formation largely depends on the concentration of the components, this can be of great importance.
- As mentioned in the previous point, qPALM can be performed in-cellulo, thus accessing protein oligomerisation states in the cellular environment (whereas most other techniques take place in-vitro). This eliminates concentration- or buffer-induced artefacts, yielding more reliable results, and at the same time takes into account specific effects taking place in living cells, such as molecular crowding (the presence of many macromolecules of different size within the cell).
- The fact that qPALM is primarily a (super-resolved) microscopy technique means that on top of oligomeric states, it gives access to localisation information. This can be a valuable characteristic to determine e.g. colocalisation of a complex with another effector protein, or formation/dissociation of protein complexes in different organelles or loci within the cell.
- Finally, qPALM can provide stoichiometry informations on a cluster-by-cluster basis, i.e. retrieve the oligomeric state of each protein complex individually. Such information can provide interesting insight into mixed oligomeric states of proteins.

Despite being a very promising technique, qPALM has scarcely been used in biological studies. Among articles reporting the use of qPALM for stoichiometry determination, most are proofs of concept for new methodologies. Very little consensus exists on the way to best perform molecular counting. One of the major reasons why qPALM is still a challenging technique is the complexity of the fluorophores used. In the case of PCFPs, their photophysical behaviour (notably blinking) complicates the extraction of molecule counts from PALM datasets.

The following sections will give an overview of the main challenges faced in molecular counting, as well as some of the techniques available, along with their advantages and limitations.

5.2.2 PCFPs photophysics complicate qPALM

Let us first consider an ideal FP for PALM: a bright PCFP, with rapid and complete chromophore maturation, and stable fluorescence emission in the activated state (i.e. no blinking, and low photobleaching). Molecular counting using such a hyopthetical marker would amount to counting the number of fluorescence activations within a given cluster. Of note, even in this ideal case, a few parameters would need to be carefully monitored to allow accurate counting:

- Photoconversion of the PCFPs should be slow enough to avoid simultaneous fluorescence emission from two FPs in the same cluster, which would complicate their individual detection.
- Photoconversion should be complete, i.e. no FP should remain in the unactivated state at the end of the experiment, to prevent under-counting. For the same reasons, no FP should be photobleached prior to the experiments, e.g. during the choice of a region of interest.

– Molecular complexes should be sparse enough to allow reliable clustering of the localisations.

– False-positive localisations should be rare enough to be easily filtered, and not be incorrectly interpreted as new molecule activations.

On top of these issues, as described in section 3.3, PCFPs show complex photophysical behaviours, which further hinder qPALM measurements. Incomplete photoconversion reduces the number of events detected per cluster, while blinking causes fluorescence re-activations which can be erroneously registered as new molecules.

Overall, counting errors in qPALM can be classified into two categories: under- and overcounting. Below is a summary of the different causes for each type of counting errors.

Undercounting can be due to:

– Stochastic superposition of fluorescence events.

– Incomplete photoconversion, due for example to poor maturation of the chromophore, photobleaching of the green state, or too short PALM acquisition.

The distribution of the number of FPs observed from an oligomer due to incomplete photoconversion can be described as a binomial distribution:

$$P_{n,N}(s) = \binom{N}{n} s^n (1-s)^{N-n}$$

with N the true number of molecules per cluster, n the observed number of molecules per cluster, and s the photoconversion efficiency (i.e. the proportion of PCFPs that are seen in the red state).[117]

Overcounting can be due to:

– Noise localisations registered as molecules.

– Reactivations due to blinking registered as newly appearing molecules.

In the last ten years, several strategies have been developed to correct for these errors, and infer protein stoichiometries from PALM images. Table 5.1 summarises several of them, along with some of their main characteristics. Some of these techniques require a calibration dataset of known stoichiometry (either monomeric proteins, or multimeric assemblies). On top or instead of this calibration, they might require a priori knowledge of the photophysics of the dye used, such as a photophysical model describing the transitions between fluorescent and dark states undergone by the protein during the experiment. Finally, some of the methods allow determining photophysical parameters such as blinking or photobleaching rates. For each technique, the system used for benchmarking is also mentioned. The various strategies often target different ranges of stoichiometries, from small complexes (< 4 proteins/cluster) to bigger oligomers such as the Nuclear Pore Complex (NPC) or FliM motor proteins (> 30 proteins/cluster). Most of these studies used mEos2 or Dendra2 PCFPs as fluorescent markers.

Ref.	Number of molecules counted	Calibration	Photophysics knowledge required	Photophysics determination	FPs used	Proteins counted
Annibale et al. (2011)[118]	Densities	No	No	No	mEos2, Dronpa, PA-GFP	Beta-2 adrenergic receptor
Coltharp et al. (2012)[119]	Densities	Monomer	No	No	mEos2	FtsZ
Lee et al. (2012)[73]	34	Monomer	Photophysical model	Yes	mEos2, Dendra2	FliM bacterial flagella motor
Puchner et al. (2013)[120]	1-3	mEos2 tandem repeats	Off-times histogram	No	mEos2	Monomer, dimer and trimer mEos2
Avilov et al. (2014)[121]	N/A	No	Photophysical model	Yes	Dendra2	N/A
Rollins et al. (2015)[122]	5-20	No	No	Yes	Dendra2	N/A
Fricke et al. (2015)[117]	1-3	Monomer	No	No	mEos2	CD86, CTLA-4, CD80, VSVG
Thevathasan et al. (2019, bioRxiv)[123]	16, 32	NPC	No	No	mMaple	NPCs

Table 5.1: Comparative table of the different qPALM techniques published for protein stoichiometry determination.

Among these methods, two have generated particular interest: the quantification of the number of blinks per cluster by Fricke et al.[117] and the τ_c splitting developed by Annibale et al.[118] and Lee et al.[73] The next two sections will describe these techniques in more details, and give an overview of their strengths and limitations.

5.2.3 Counting from the number of blinks

Principle

This approach, first described in ref[117] and later used in refs,[124,125] relies on the statistical analysis of the number of blinks per cluster. Therefore, it retrieves an average oligomeric state for the observed protein, without any indication of the cluster-by-cluster stoichiometry. The application of the technique requires a calibration based on a monomeric protein (as shown on Figure 5.2). The distribution of the number of blinks in such a case can be described by a geometric distribution:

$$P_p(N_{blinks}) = p(1-p)^{N_{blinks}}$$

With p, the probability to observe no blinking from the fluorophore. Fitting the N_{blinks} distribution from the monomeric protein with this equation allows retrieving the blinking parameter "p".

Of note, this calibration should be performed for each experiment, since it will vary depending on the label used, the laser intensity, and the fluorophore environment (as described in section 3.3.2). However, since the duration of the blinks does not influence the N_{blinks} distribution, the model does not need to be adapted for multiple dark-states with different lifetimes.

In the case of an oligomeric protein, the N_{blinks} distribution can be generalised as follows:

$$P_{N,p}(N_{blinks}) = \binom{N_{blinks}}{N-1} p^N (1-p)^{N_{blinks}-N+1}$$

This equation is a negative binomial distribution, which describes the number of blinks produced by a number N of identical fluorophores with blinking parameter p. From this distribution, N, the number of fluorophores per cluster, can be fitted.

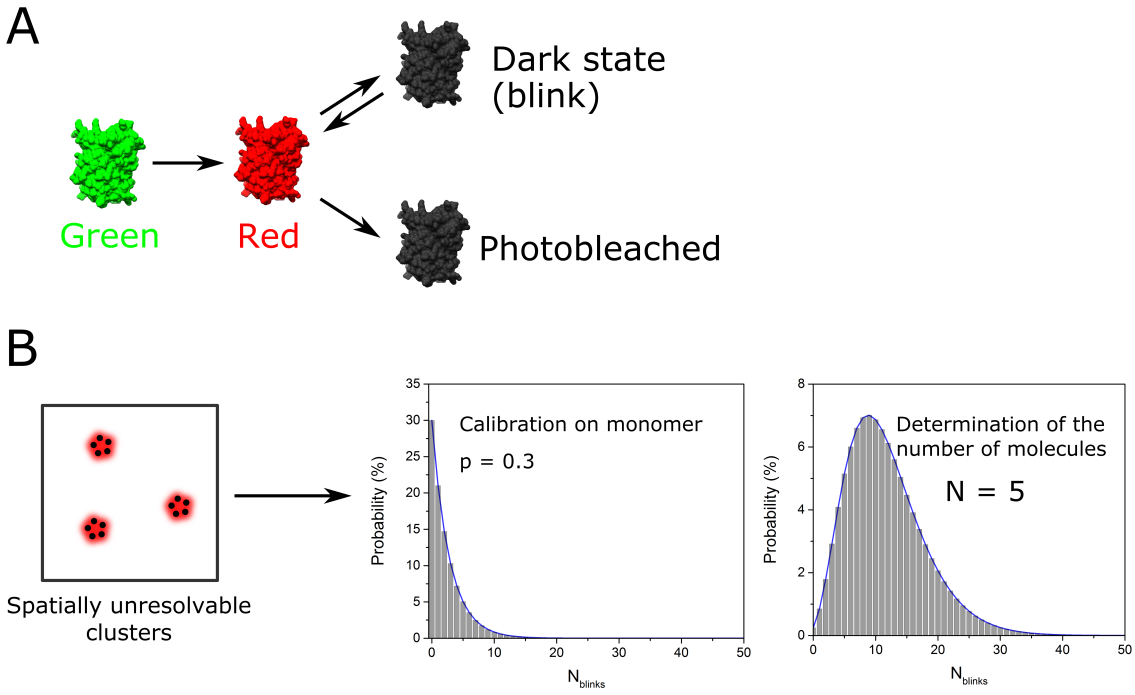

Figure 5.2: Principle of the N_{blinks} approach. (A) Photophysical model used in the method. Since blink duration is not taken into account, the model includes only one dark state, considered responsible for all observed blinking events. (B) Stoichiometry determination. First, the blinking parameter p is retrieved from the N_{blinks} distribution of a monomeric protein. Secondly, this parameter is used to fit the N_{blinks} distribution of the oligomer, and retrieve its stoichiometry (here, a pentamer).

This method has proved very efficient to determine the stoichiometry of small oligomers, such as demonstrated in the original publication,[117] including for mixed oligomeric states such as a

combination of dimers and trimers. However, it also suffers from a number of limitations, as will be described in the next section.

Limitations

Noise sensitivity. Missed detections of molecules might result in an altered shape of the N_{blinks} histograms, and therefore prevent correct fitting by a negative binomial function. Furthermore, false-positive localisations, relatively common in PALM experiments on biological material, will produce an artefactual increase of the first bin of N_{blinks} histograms ($N_{blinks} = 0$). Therefore, in the original study, the authors exclude this first bin from their analyses.

Photoconversion efficiency. As mentioned in sections 3.3.1 and 5.2.2, PCFPs display incomplete photoconversion, leading to part of the labels not being detected in the PALM acquisition. This has important consequences for the technique, since it will tend to shift N_{blinks} histograms towards lower numbers, leading to undercounting of the target stoichiometries. Furthermore, incomplete photoconversion will produce a distribution of apparent stoichiometries, thus broadenning the N_{blinks} histogram and requiring the use of a linear combination of negative binomials for fitting.

Stoichiometries of large complexes. Even though the method is appropriate for stoichiometry determination on small oligomers, it becomes increasingly difficult to apply with increasing complex size. This is due to the effect of limited photoconversion efficiency described above, but also to the fact that differences in N_{blinks} histograms become smaller (and thus harder to detect) in the case of big oligomers.

Finally it should be noted that, like most qPALM techniques, this method requires good separation of protein activations in time, since overlapping activations will give rise to an underestimated blinking behaviour. In conclusion, the N_{blinks} technique is well suited to the study of small oligomers (< 4 molecules/cluster), but cannot be used in its present form for bigger protein complexes, which are nonetheless frequently encountered in biological studies.

The τ_c method described in the next section attempts to provide a more generally applicable approach to molecular counting.

5.2.4 Account for blinking using a threshold dark-time

A rather straightforward idea to account for blinking in qPALM is to consider the time separating fluorescence bursts. If the activation of the FPs is slow enough over time, fluorescence bursts separating different molecules should be longer than those between FP reactivations due to blinking. This was used by Annibale et al.,[118] who used a threshold dark time to differentiate blinks from new molecules. Varying the threshold time, they observed the change in the computed molecule density in the PALM image, and simulated over- and undercounting errors arising at each threshold time. Based on this knowledge, they proposed a model to fit the molecule density vs. threshold time curve, and retrieve the correct number of molecules in the image.

The method however relies on a photophysical model including a single dark-state, whereas it was later shown that red mEos2 was able to enter at least two distinct dark-states.[73] Furthermore, the fitting of the molecule density vs. threshold time curve at low threshold time did not take into account possible missed-counts. Although the authors show that it does not prevent retrieval of the correct number of molecules, this can be expected to reduce the precision of stoichiometry determination.

Soon after this publication, Lee et al. proposed another method relying on a threshold dark-time for stoichiometry determination, as detailed below.

The τ_c splitting technique

The technique proposed by Lee et al.[73] makes use of a photophysical characterisation of the PCFPs used (mEos2 and Dendra2) to determine optimal threshold times τ_c to balance over- and under-counting errors, and retrieve the correct number of molecules.

Quantifying counting errors. First, the authors propose a characterisation of different types of blinking errors. To this aim, they imaged monomeric, purified mEos2 and Dendra2 molecules, and reconstructed emission patterns of oligomeric proteins by concatenating individual emission traces. In that way, the true number of molecules underlying the trace is known, and the different sources of counting errors can be directly quantified.

Two types of counting errors are defined: overcounting due to blinking, and undercounting due to mixing of fluorescence traces (i.e. different FPs activating closer in time than the threshold time τ_c). Of note, the publication does not take into account the undercounting due to incomplete photoconversion. This potential flaw will be discussed below, in section 5.2.4.

The evolution of the counting error was probed for different τ_c values. As τ_c increases, the overcounting error due to blinking decreases, while the undercounting error due to trace mixing increases, and one can find a τ_c value which retrieves the correct number of molecules. It is important to note however that this τ_c does not allow correctly attributing fluorescent bursts to the different molecules, but rather balances under- and overcounting errors to reach the correct solution (as shown in Figure 5.3 A).

Activation pattern. The extent of the undercounting error produced by trace mixing is directly related to the sparsity of activation of the molecules in time. The best way to obtain maximum sparsity is to maintain a constant number of FPs activated per frame. If the activation laser intensity is kept constant, the number of photoconversion events per frame will decrease exponentially, making simultaneous photoconversions within the same complex likely. To obtain an even distribution of photoconversion events, the authors propose that the photoconversion times (i.e. the time between subsequent photoconversions) should follow a Fermi probability density function (p_F) as follows:

$$p_F(t) = \frac{1}{1 + e^{(t-t_F)/T}}$$

with t_F the time for the Fermi function to drop to half of its maximum value, and T the fall-off time of the Fermi function. As a result, photoconversion events should be separated by a large time at the beginning of the dataset (where several FPs might activate simultaneously in the same complex), and a smaller time at the end of the dataset, where only few FPs remain to be activated in each complex. This probability density function can be obtained using the following time-varying activation rate $k_a(t)$:

$$k_a(t) = \frac{1}{T} \frac{e^{-(t-t_F)/T}}{[1 + e^{-(t-t_F)/T}] \ln[1 + e^{-(t-t_F)/T}]}$$

resulting in the profile of Figure 5.3 B, that can be used to modulate the intensity of the activation laser over time.

Varying τ_c according to molecular density. The undercounting error also varies depending on the number of molecules in the cluster. As the number of molecules increases, the frequency of activation also increases, making trace mixing more probable. Therefore, optimal τ_c values have to be computed for each possible number of molecules in the cluster, which can be represented as a curve of τ_c vs. number of molecules (Figure 5.3 C). This curve will be different for each FP used, and can be obtained from concatenated experimental or simulated fluorescence traces from monomeric proteins.

Since the number of molecules is the variable that needs to be determined, an iterative procedure (schematised in Figure 5.3 D) is necessary to find the correct τ_c value. In brief, the number of molecules is first computed with $\tau_c = 0$; then a new τ_c corresponding to this number of molecules is chosen to get a new number of molecules, and the process is repeated until convergence to retrieve the correct number of molecules. Hence, each cluster in the dataset will use a different τ_c value for trace splitting.

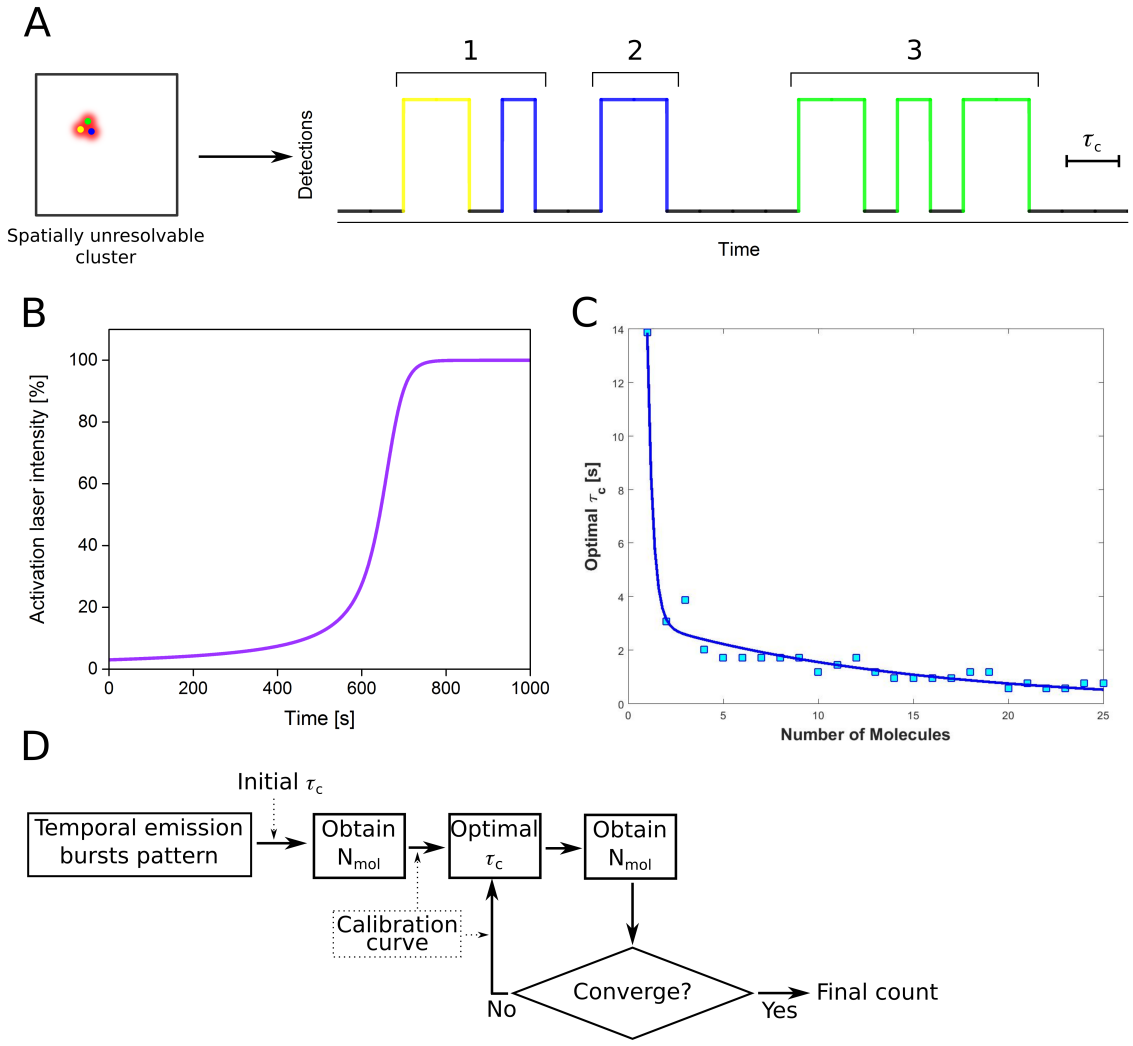

Figure 5.3: (A) For each unresolvable cluster (here a trimer of fluorescent proteins), a fluorescence time trace is built. The trace is split according to a threshold dark-time τ_c, allowing to retrieve the number of molecules in the cluster. Note that here, the correct number of molecules has been retrieved, despite an erroneous assignment of molecules 1 and 2. (B) Fermi profile used to produce an even distribution of photoactivations over the dataset. (C) Example of a calibration τ_c vs. N_{mol} curve obtained from the processing of concatenated simulated fluorescence traces. The optimal τ_c decreases with higher oligomeric states. (D) Iterative τ_c counting algorithm that allows retrieving the correct τ_c and number of molecules (N_{mol}) for each cluster.

In a subsequent work, Avilov et al. proposed a method based on τ_c splitting, that additionaly extracted the parameters of the kinetic model for blinking of the fluorescent protein,[121] allowing a quantitative evaluation of the blinking and bleaching times in different environments, including in-cellulo.

Limitations

Despite being a very elegant technique, τ_c splitting suffers from several flaws that have so far prevented its wide use as a stoichiometry determination method.

Its main weakness is that even though, as described above, the correct assignment of blinks is not required to retrieve the correct number of molecules, it still supposes that blinks are on average shorter than the time between photobleaching of a molecule and photoactivation of another one. If these two processes generate dark times on a similar timescale, the counting accuracy might be largely decreased. In practice, this might happen if:

- There are many molecules per cluster, so photoactivations are close together in time.
- Fluorophores undergo long blinks (i.e. blinking generates long dark times).

A consequence of having similar times for blinking and separation of fluorescence traces is the "flattening" of the τ_c curve. As shown on Figure 5.3 C, τ_c values are largely different for small oligomers, but become extremely similar for bigger oligomers. Therefore, large oligomers will be processed with very similar τ_c values, and the iterative algorithm (Figure 5.3 D) will be more prone to converge to an erroneous number of molecules.

Finally, the method does not take into account undercounting due to incomplete photoconversion. As a result, the stoichiometries retrieved will follow a binomial distribution (described in section 5.2.2). The maturation rate of the FP will then need to be known in the conditions of the experiment to retrieve the underlying stoichiometry of the complex.

5.3 How can we improve advanced PALM experiments?

Performing advanced PALM experiments still represents a challenge, notably due to the photophysical behaviour inherent to the fluorescent probes employed. These techniques are however still young, and can probably be improved to make them reliable, user-friendly, and to fully exploit their potential. More particularly, addressing issues related to fluorophore photophysics could be achieved by a combination of the steps below.

Characterising the mechanisms by which incomplete photoconversion or blinking occur would allow us to better understand the problems we are facing, and provide a solid base for designing new solutions to them. This characterisation can be performed at the structural level by crystallography, at the spectroscopic level by absorption/fluorescence measurements, and by microscopic observation of the behaviour of FPs at the ensemble or single-molecule levels. Furthermore, these informations should be combined to be able to relate phenomena observed e.g. at the single-molecule level in PALM experiments, such as blinking, to spectroscopic and structural changes in the protein.

This fundamental mechanistic knowledge could be used for the design of new FP variants, by a combination of directed and random mutagenesis (as described in section 1.3.1). However, although this approach has been in use for years, it has revealed to be often work-intensive, and yielding uncertain results. Therefore, other approaches might be easier to design and implement: rather than changing the properties of the fluorescent probes, an alternative could be optimising the imaging

conditions, such as buffers, or laser illumination. As mentioned in section 3.3.2, the photophysical behaviour of FPs can be changed by their illumination conditions (intensity and wavelength), and by the chemical composition of their environment (presence of oxygen, reducing agents,...). Such approaches, directed by precise mechanistical knowledge, could substantially improve the quality of PALM images and informations obtained from them, while being easily implemented on different microscopy setups. Not the least important, they could be tested by different labs without having to invest time in molecular cloning to change already existing constructions with other FPs.

5.4 Purpose of the work

The work presented in this manuscript has concentrated on characterising PCFPs of the Eos family through ensemble-level fluorescence and single-molecule localisation microscopy. This allowed better understanding the photophysics of these proteins, and designing experimental conditions that improve advanced PALM techniques such as sptPALM and qPALM.

5.4.1 Photophysics of green mEos2

When performing PALM with mEos2, the red form of the protein yields the super-resolved image. In most experiments, the green form is merely used to locate structures of interest, obtain a diffraction-limited image before single-molecule data collection, or is simply not considered at all. As a result, most photophysical studies on mEos2 (or other PCFPs) have concentrated on studying the red form of the protein, but few got interested in the green form. Our lab got interested in the topic, considering that green state photophysics might partly explain phenomena such as the poor photoconversion efficiency of mEos2, or the common observation in PALM of "readout photoconversion", the photoconversion of molecules to the red state in the sole presence of 561-nm illumination. Therefore, a project of characterisation of green mEos2 photophysics was initiated in the lab by previous PhD student Romain Berardozzi, which aimed at studying the influence of strong 561-nm light (such as used in PALM) on the green state of mEos2. Romain did not have time to fully complete this characterisation within his PhD, and I therefore took over the project when I entered the lab in 2016. Finally, the informations gained from this project were complemented by structural and spectroscopic data obtained on the green state of mEos4b by Elke De Zitter, as explained in the section below in more details.

The first part of the manuscript therefore focuses on this characterisation of green mEos2 (and mEos4b) photophysics, and more particularly on the effects that it can have on PALM experiments.

5.4.2 Blinking of mEos4b

As mentioned previously, blinking in PCFPs is a common issue, and a hindrance to advanced PALM experiments such as sptPALM and qPALM. In this context, our lab set up a collaboration with KU Leuven (Belgium) aimed at investigating mEos4b dark-states at the structural and spectroscopic levels. As part of this collaboration, Elke De Zitter came to the lab in 2015, crystallised mEos4b in the green and red states, and performed ensemble-level photoswitching experiments on the crystals, under spectroscopic control. The double aim of these experiments was to see the spectroscopic signature of the dark states, and to trap them *in-cristallo* by flash-freezing in liquid nitrogen to solve their structure using X-ray diffraction. Elke was able to do this, and obtained crystallographic

structures of mEos4b in the green, red, and dark states accessed from each of the fluorescent states. This work provided unprecedented insight into the mechanistical aspect of PCFP blinking, and initiated a photophysical characterisation of the red state of the protein at the single-molecule level, which was part of my thesis work.

The second part of this manuscript will present the knowledge gained from this study, and more particularly how the illumination conditions in PALM affect blinking, and can be applied to reduce related artefacts in PALM experiments. Finally, it will be shown how the developed illumination strategy can improve sptPALM experiments.

5.4.3 Design of a qPALM experiment

All along my PhD work, the quantitative aspects of PALM have been a central topic, from the influence of readout 561-nm light on the photoconversion efficiency of mEos2 to the characterisation of mEos4b blinking at the single-molecule level. However, I had not yet attempted to perform actual molecular counting by PALM on a protein complex. I therefore set out to investigate whether the photophysical knowledge gained in these previous projects could be applied to design an improved qPALM experiment.

In the last part of the manuscript, the design of this strategy will be shown, followed by a discussion of the pitfalls and challenges that remain to be addressed to perform accurate molecular counting experiments.

Part II

Materials and methods

Chapter 6

Molecular biology and biochemistry

6.1 Cloning of FPs

All the expression plasmids for the FPs used were available in the lab. They were all based on the pRSET-B plasmid, with the gene of interest inserted after the inducible T7 promoter (as schematised on Figure 6.1 for the plasmid containing the mEos4b gene). The constructs were sequenced (GATC) to ensure that the produced protein would be the correct one.

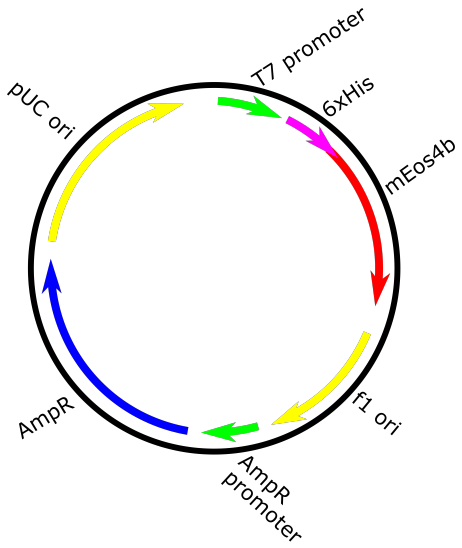

Figure 6.1: Schematic map of the pRSET-B plasmid containing the mEos4b gene. This construct can be used for protein overexpression in E. *Coli* cells.

For the inducible lysine decarboxylase (LdcI)-mEos4b construct, only LdcI fusions with other FPs

were available. Therefore, the LdcI plasmid and the mEos4b gene were amplified by polymerase chain reaction (PCR), and a Gibson assembly[126] was performed so that the mEos4b gene would replace the one of the previous fluorescent protein. The resulting construct was sequenced to confirm the success of the operation.

For amplification, plasmids were transformed into the *E. coli* DH5α strain. The bacteria were grown overnight in 5 mL LB medium supplemented with ampicillin (100 µg/mL) at 37°C, under agitation at 150 rpm. They were harvested the next day by centrifugation for 5 min at 10000 g, and the plasmid DNA was extracted using a miniprep kit (Qiagen). The concentration of the purified DNA was quantified by measure of absorbance at 260 nm, and stored at -20°C.

6.2 Protein expression and purification

6.2.1 FPs

The plasmid encoding the FP of interest was transformed into the E.*Coli* BL21 strain by heat shock at 42°C for 1 min, and spread on an LB-agar plate containing ampicillin (100 µg/mL). The plate was incubated overnight at 37°C. The following day, a single bacterial colony was picked and used to start a pre-culture in 100 mL LB medium supplemented with ampicillin (same concentration as above). The pre-culture was grown overnight at 37°C, 150 rpm. An aliquot of the pre-culture was then used to start a larger culture in 1L LB medium with ampicillin, which was grown to an OD_{600nm} of 0.5-0.6 in LB medium supplemented with ampicillin, and protein expression was induced with 1 mM Isopropyl β-D-1-thiogalactopyranoside (IPTG), for 3 hours at 37°C.

After protein expression, cells were harvested by centrifugation for 20 min at 4000g, and the pellets resuspended in lysis buffer (Hepes 25 mM, NaCl 300 mM, imidazole 25 mM, pH 7.4). Cell lysis was performed by sonication on ice for 2 minutes, followed by removal of cell debris by centrifugation for 1h at 40000g.

After centrifugation, the supernatant was loaded on a Ni-NTA affinity resin, which was washed with 25 and 50 mM imidazole to reduce unspecific binding, and the protein was eluted with 300 mM imidazole. Finally, the imidazole was removed by dialysis overnight against lysis buffer. The purity of the protein was evaluated at each step by loading a small aliquot on SDS-PAGE.

An aliquot of the protein (1 mL) was kept in the fridge as a working stock, and the rest of the purified protein was kept at -80°C.

6.2.2 LdcI

Bacteria carrying the LdcI-mEos4b (pRSET-B) plasmid were grown as described in the section above. Protein expression was induced with 250 µM IPTG, overnight at 20°C.

Cells were harvested by centrifugation for 20 min at 4000g, and the pellets resuspended in lysis buffer (Tris 25 mM, NaCl 300 mM, glycerol 10%, Pyridoxal 5-phosphate (PLP) 0.1 mM, β-mercaptoethanol 2 mM, imidazole 10 mM, pH 7.5). PLP is an essential cofactor for LdcI to form a decamer. Cell lysis was performed by sonication on ice for 2 minutes, followed by removal of cell

debris by centrifugation for 1h at 40000g.

After centrifugation, the supernatant was loaded on a Ni-NTA affinity resin, which was washed with lysis buffer. The protein was eluted in the same buffer supplemented with 250 mM imidazole. The protein was dialysed overnight against the gel filtration buffer (Hepes 25 mM, NaCl 300 mM, glycerol 10%, PLP 0.1 mM, DTT 1 mM, pH7). The pH was lowered to 7 at this step to favour the formation of the decameric form of the protein.

The protein was further purified by gel-filtration on a superose-6 10/300GL column (GE Healthcare), and the fractions corresponding to the decamer (elution volume 11 mL) were isolated. The complex was finally flash-frozen in liquid nitrogen and kept at -80°C. The purity of the protein was checked at all steps of the purification by SDS-PAGE.

Quality control of LdcI assembly by AUC

To check the presence of decameric LdcI in our sample, we performed AUC on the purified protein (as shown in chapter 12). A sedimentation speed experiment was performed on a XLI analytical ultracentrifuge equipped with an Anti-50 rotor (Beckman Coulter, Brea, USA), at 35000 rpm and 20°C. Sedimentation was followed using the green fluorescence of the mEos4b proteins fused to LdcI.

Chapter 7

Microscopy

7.1 Sample preparation for in-vitro imaging of purified proteins

Since this thesis focuses on the *in-vitro* characterisation of FPs, the method of protein immobilisation used for imaging was of importance. Several methods were used during the course of this work.

As a constant for all the methods mentioned below, the glass coverslides were first cleaned for 20 min in a UV-ozone oven (HELIOS500, UVOTECH Systems) to remove any fluorescence contamination. This treatment also makes the glass hydrophilic, which enables better spreading of the different solutions. In all samples prepared for single-molecule experiments, fiducial markers were added (typically fluorescent nanodiamonds, which provide a signal-to-noise ratio relatively close to the studied FPs, and do not photobleach). For ensemble-level experiments, FPs were used at μMfinal concentration, and for single-molecule experiments at nM final concentration.

7.1.1 Poly-vinyl alcohol (PVA)

A 1% stock solution was prepared by dissolving polyvinyl alcohol (PVA) powder in PBS, and stored at room temperature. Samples were prepared by mixing 1μL PVA 1% with 1μL of FP solution. The mixture was spread on a coverslide and let to harden at room temperature for 5 min.

The main advantage of this method is its ease and rapidity of use. Once the PVA stock solution has been made, samples can be prepared in a few minutes. This method has been previously used for photophysical studies of FPs.[127,128] However, doubts persist as to the actual redox environment in the gel (which could notably influence blinking behaviour), the state of hydration of the protein, or oxygen accessibility compared to classical mounting media.[128] Generally, control of the chemical environment in the gel is very limited; for example, PVA polymerisation has been shown to be less efficient at low pH,[129] which is expected to prevent proper immobilisation of FPs.

Immobilisation of FPs in PVA was used for all experiments on mEos2 (chapter 9).

7.1.2 Polyacryamide (PAA)

A 15% polyacrylamide solution was prepared by mixing 50µL acryl/bis-acrylamide stock solution with 50µL Tris (1.5 M, pH 8.8). 1µL of FP solution was added, and gel polymerisation initiated with 1µL ammonium persulfate (APS) 10%, and 1µL tetramethylethylenediamine (TEMED). 5 µL of the solution were spread between two glass coverslides to form a uniform thin layer, and let to harden at room temperature for 5 min.

Like PVA, polyacrylamide (PAA) has previously been used for photophysical studies on FPs,[130,131] but also suffers from limited control of the FP environment. Although small changes in pH can be made, the efficiency of the APS/TEMED catalysis couple is reduced at low pH.[132] In practice, changing pH can therefore prove difficult, and lead to badly immobilised molecules.

FP immobilisation in PAA was used for the photophysical characterisation of red mEos4b, and the *in-vitro* demonstration of blinking suppression by 488-nm light (chapters 10 and 11).

7.1.3 Adsorption on glass

Once treated by UVs, glass coverslides become very hydrophilic (through breakage of the siloxane bridges, forming silanol groups), and acquire very good affinity for proteins. Therefore, one strategy was simply to let FPs adsorb on glass, and cover them with a buffer of choice.

In short, 50µL of FP solution were deposited on a UV-treated glass coverslide, and left to adsorb for 30 min. The coverslide was then rinsed with several mL of buffer, and sealed on a glass slide, with the imaging buffer (typically the purification buffer) in between, covering the FPs.

A big advantage of this method is the complete flexibility in the buffer used. pH, redox conditions, addition of small molecules, can all be achieved easily. However, once adsorbed on the glass, proteins might not be in their native shape.[133] Furthermore, adsorption on glass being non-covalent binding, it is unsure whether some proteins may be able to occasionally detach and diffuse in the imaging buffer, hence perturbing the photophysics analysis.

7.1.4 Disuccinyl-suberate (DSS) cross-linking

An alternative protocol was recently developed in the group for immobilisation of proteins on glass surfaces.[74] This protocol (schematised on Figure 7.1) uses the following steps:

1. Breakage of the siloxane bridges at the surface of the glass to silanol groups, either by heating with a strong acid, or by treatment in a UV-ozone oven.

2. Binding of (3-Aminopropyl)triethoxysilane (APTES) on the silanol, which exposes free amines.

3. Cross-linking of Disuccinimidyl suberate (DSS) on the free amine. Since DSS is a symmetrical molecule, it bears a second reactive group for amine cross-linking.

4. Cross-linking of the protein of interest through its free amine groups (lysines, arginines, or N-terminus) to DSS.

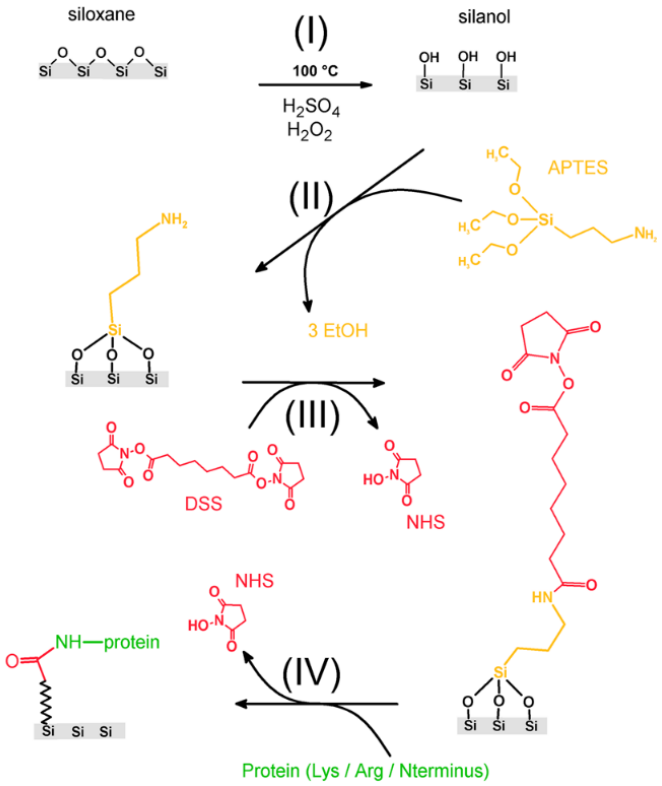

Figure 7.1: Protocol for cross-linking of proteins to a glass surface using disuccinyl-suberate. Proteins are bound to the functionalised glass through their free amines (lysines, arginines, or N-terminus). Figure adapted from ref.[74]

Of note, non-covalent binding of proteins to the glass surface is still possible. To prevent this, the glass slide with bound proteins was incubated 1h at 37°C with Fetal Bovine Serum (FBS). The different-sized proteins in FBS will compete with the adsorbed proteins and detach them. Proteins that were covalently bound by DSS cross-linking will however not be affected.

This technique allows covalent binding of proteins (including FPs) on a glass surface, while preserving their native state. It allows the use of a wide range of buffers, with the exception of amine-containing buffers (e.g. Tris), which would inhibit DSS cross-linking.

DSS immobilisation was used for all qPALM experiments presented in chapter 12, using the detailed protocol presented on the next page.

Detailed protocol for DSS cross-linking of proteins on glass

Material 20x20 mm coverslides (that will be treated will DSS and will carry the proteins).
Reagents: H_2O_2, H_2SO_4, APTES, DMSO, acetone (all stored at ambient temperature), DSS and FBS (both kept frozen at -20°C).
Coupling buffer (no Tris, Hepes, PBS and NaCl can be used).
Cavity microscope slide on which the coverslide will be sealed.
Diluted nanodiamond solution.

Preparation of the coverslide Put the coverslides in the UV-ozone oven for 20 min (the face that will be functionalised should be placed upwards).

APTES binding step Under a fume hood, prepare a 2% solution of APTES in acetone. APTES is sensitive to oxygen, so the solution should be prepared at the last moment. Prepare ∼100 µL solution per coverslide to be treated.
Still under the fume hood, cover the coverslide with this solution, and let it react for 30 seconds.
Rinse the surface with acetone, then water, and air-dry.
Coverslides can be stored for several days at this step.

DSS binding step Prepare a 20 mg/mL stock DSS solution in DMSO (DMF can also be used). This stock solution can be aliquoted and kept at -20°C.
Cover the coverslides with 50 µL of this solution.
Let it react for at least 2 min at ambient temperature, and rince with DMSO (note: longer incubation times will not alter the efficacy of the reaction).
Air-dry the coverslides.

Protein cross-linking Deposit 5 µL of nanodiamond solution at the centre of the coverslide and let dry.
Cover the DSS-modified surface with the protein solution (to observe single molecules with a purified FP, use a protein concentration of ∼1 nM).
Incubate for 30 min at room temperature.
Rinse the surface with the coupling buffer.
Cover the surface with FBS and incubate 1h at 37°C.
Rince with coupling buffer.
Deposite the coverslide on the cavity slide (with the protein in between) with coupling buffer and seal.

7.2 PALM microscopy setup

All microscopy experiments presented in this manuscript were performed on the PALM microscopy setup at IBS, shown on Figure 7.2. This setup was assembled in the lab, which makes it versatile, and allows making modifications and improvements as needed.

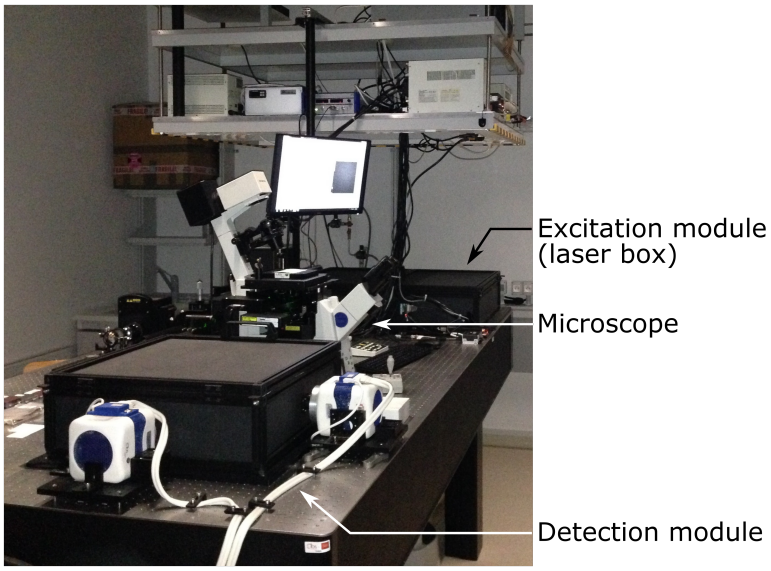

Figure 7.2: The PALM setup at IBS. The three main parts of the setup are labelled (excitation module, microscope, and detection module). All of them rest on an optical table, to prevent vibrations.

Excitation module

Six lasers at different wavelengths (405, 488, 532, 561, 643 and 730 nm) are present in the laser box. They are coaligned using dichroic mirrors, and directed to the microscope through an acousto-optic tunable filter (AOTF) (AA Opto Electronic). This device allows precise control of laser illumination, both in intensity and in time.

Microscope

The microscope is a commercially-available IX-81 inverted microscope, equipped with a 100x 1.49 Numerical Aperture (NA) oil immersion apochromatic objective lens (Olympus). The lasers are focused at the back focal plane of the objective, providing widefield illumination of the sample. The sample is set on a motorised stage (PI) allowing precise movement on the horizontal plane. The microscope also includes a continuous focus system (ZDC, Olympus), used to correct for drift on the vertical axis.

Detection module

The detection module contains two Evolve 512 back-illuminated EMCCD cameras (Photometrics) used for image acquisition. Moreover, additional modules can be added in the detection path, such as a dichroic mirror for 2-colour imaging, or an astigmatic lens for 3D.

Custom Labview software

A custom-made Labview software is used to control both the AOTF and the EMCCD cameras. This allows synchronising laser illumination and camera exposure, as well as designing complex laser pulse sequences. This was used to temporally separate readout and actinic laser illuminations in ensemble-level and single-molecule experiments, and to design a Fermi activation profile for qPALM acquisitions.

I participated to the later development stages of this software, by adding the possibility to input text instructions for changes in the laser illumination scheme over time. This allowed for example to implement the Fermi activation profile, or to perform replicates of experiments in a controlled and reproducible manner (rather than by manual timing). Text files containing the insctructions could be written by hand, generated using a dedicated Matlab script, or directly recorded during a manually executed experiment.

7.3 Determination of laser illumination intensities

Laser powers at the sample were measured using a power-meter (Thorlabs) placed in front of the objective, and beam profiles were recorded by imaging a coverslide covered with fluorescent highlighter (Stabilo). A Gaussian fit was performed on the beam profiles in Matlab, to be able to extrapolate the fraction of laser power that was detected by the power-meter, but outside of the field of view of the camera. Finally, these data were used to retrieve power-densities at all points of the field of view. The power-density measurements given throughout the thesis correspond to the maximum intensity, in the centre of the field of view.

In the case of the 405-nm laser, the beam profile was not Gaussian, but its limits could be clearly seen when acquiring an image on the full camera chip. The total area covered by the beam was therefore manually calculated, and used to retrieve the power-density by dividing the laser power at the objective by the surface covered by the beam. Of note, this calculation is an approximation of the power-density, since it doesn't take into account fine variation in laser intensity over the beam profile.

7.4 Ensemble-level data collection

Ensemble-level fluorescence data were collected on samples containing micromolar concentrations of FPs. In order to study the effect of different wavelengths on FPs photophysics, fluorescence readout was achieved with low laser intensity (typically on the order of a tenth of W/cm^2), for only 5% of the frametime. During 90% of the frametime, an actinic laser was applied, at any wavelength and power-density needed (from W/cm^2 to a few kW/cm^2).

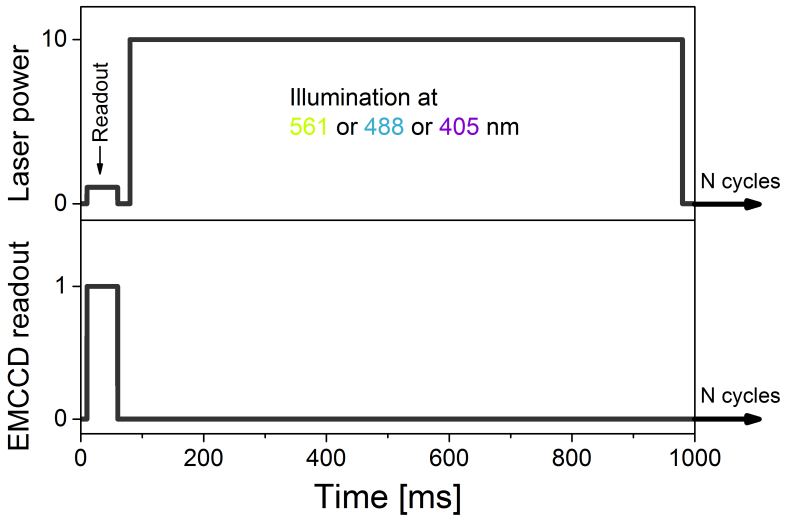

Figure 7.3: Laser illumination and EMCCD acquisition scheme for ensemble fluorescence experiments. Fluorescence readout was achieved by weak illumination at the readout wavelength (488-nm for green fluorescence, 561-nm for red fluorescence) during 50 ms, followed by actinic illumination at either 561, 488, or 405 nm.

7.4.1 Recording of photoswitching cycles

Photoswitching cycles on green FPs were recorded by sequential illumination at 488- or 561-nm (to induce off-switching) and 405-nm (for on-switching).

On red PCFPs, a pool of proteins was first converted to the red state by 405-nm illumination for 10 seconds, off-switching was induced by 561-nm light, and on-switching by 405- or 488-nm light. 405-nm light produces both on-switching and photoconversion, but the latter occurs on a slower timescale, so that the level of fluorescence recovery is not significantly offset by newly photoconverted molecules.

7.4.2 Recording of thermal recovery curves

Measures of thermal recovery rates to the fluorescent state must be performed at very low laser illumination, to avoid light-induced reactions. In the course of this work, thermal recovery kinetics were recorded in two ways, either on the microscope, or on a plate reader.

On the microscope: PAA-embedded green or red mEos4b was photoswitched by illumination at 488- or 561-nm, respectively. It was subsequently left in the dark, and the fluorescence monitored with weak pulses of readout light for 50 ms every 10 min for 10 hours.

On the plate reader: an aliquot of green or red mEos4b in solution was photoswitched by placing the tube in front of a laser source for a few minutes. Photoswitching was visually assessed by observing the clearing of the FP solution. 100 µL of photoswithed FP solution was then transferred

to a 96-well plate, which was set in the plate reader to follow fluorescence. The kinetic was recorded at 37°C to accelerate the process, over 10 hours.

Both systems have flaws and advantages. The main flaw of the plate reader is the absence of control of illumination intensity, which coud be too high and influence the fluorescence recovery. Its main advantages are however the precise control of the temperature, and the possibility to record many samples in parallel. Using the microscope on the other hand allows more precise control of laser illumination, but can be more instable (e.g. drift can shift the sample, creating a bias in the analysis). Furthermore, only one sample can be recorded at a time (the experiment is typically performed overnight).

7.4.3 Experiments on crystalline samples

Protein crystals were mounted in crystallisation solution between two glass coverslides sealed with vacuum grease. Ensemble-level fluorescence data were collected as for *in-vitro* samples, with however higher laser intensities to account for the high optical density of crystals.

7.5 Single-molecule data collection

7.5.1 Photophysics analyses

Single-molecule data were acquired on samples with pico- to nanomolar concentrations of FPs, with laser power-densities ranging from 0.2 to 6 kW/cm^2, using an EM gain of 200 and an exposure time between of 50 (chapter 9) or 70 ms (other chapters). Fluorescence readout was temporally separated from any other laser illumination (e.g. 405- or 488-nm) to avoid background fluorescence, notably due to excitation of green fluorescence which would be slightly visible in the red channel (Figure 7.4, pulsed mode).

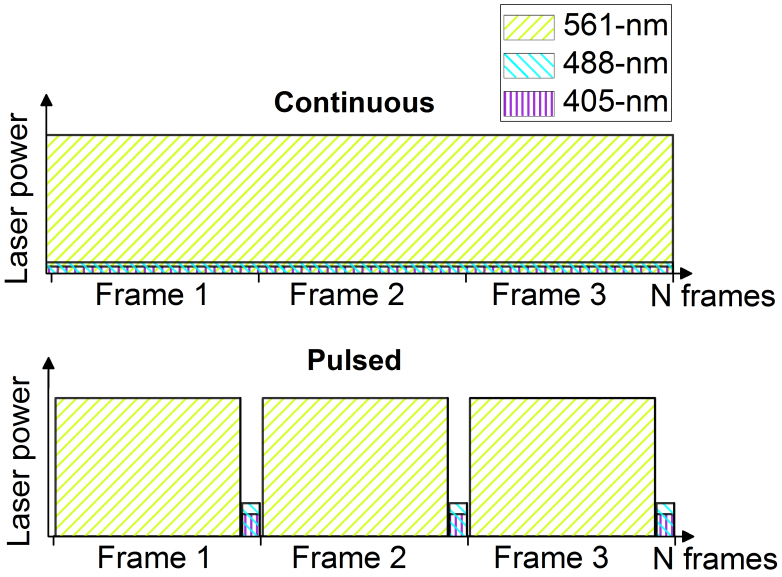

Figure 7.4: Laser illumination schemes used for single-molecule experiments on mEos2 and mEos4b. Fluorescence readout is achieved by strong 561-nm illumination during the exposure time of the EMCCD camera. 405- and 488-nm illuminations were added either continuously or in short pulses between frames, to avoid background signal arising from excitation at either of these two wavelengths. Within this work, only the pulsed mode was used.

7.5.2 qPALM experiments

During qPALM experiments, TIRF illumination was used to limit background fluorescence. Furthermore, for molecular counting by τ_c splitting[73] as described in section 5.2.4, the intensity of the activation laser was tuned according to a Fermi profile, with identical parameters to those proposed in ref[73] and a maximum intensity of 5 W/cm^2.

Finally, the power of the 561-nm readout laser was kept relatively low ($\sim$ 0.5kW/cm^2) to limit photobleaching of the green form of the protein while ensuring reliable detection of the single molecules (for more details on photobleaching of green mEos2 see chapter 9).

Chapter 8

Data analysis

8.1 Ensemble-level data analysis

8.1.1 Analysis sub-region

Since the illumination produced by the laser beams at the sample is not homogeneous but gaussian, FPs situated at different distances from the centre of the beam experience different light intensities. If not accounted for, this would result in a mixing up of kinetic constants for light-induced processes, making their retrieval impossible. The simplest way to correct for this, is to perform ensemble-level data analysis on only a small area of the field of view, near the beam centre, where illumination can be considered homogeneous (Figure 8.1).

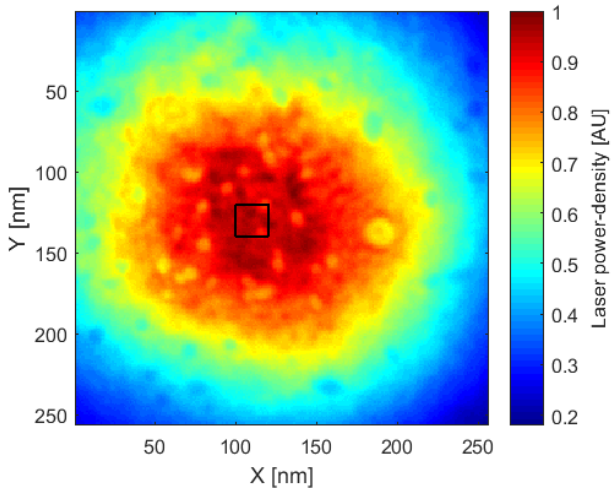

Figure 8.1: Laser intensity profile at the sample, measured using fluorescent highlighter on a coverslide. Black square: typical region used for ensemble-level measurements analysis. The standard deviation of the intensity values in the square (for a maximum intensity normalised at 1) is very reduced (SD = 0.03) as compared to the full field of view (SD = 0.18).

8.1.2 Fitting of kinetic rate constants

On the defined region, the average pixel intensity is plotted over time using ImageJ. The resulting curve (typically off-switching followed by on-switching) is imported in Matlab (The MathWorks) and the off-switching was fitted using a kinetic model implemented within a custom script. The model included a fluorescent state (fitting variable), a bleached state, and one or several dark-states, and could be readily adapted to match different working hypotheses. It also accounted for the anisotropy of the molecules (since immobilised proteins often have a fixed orientation), using the method reported in ref.[134]

A common concern when fitting such complex models is over-fitting. Indeed, increasing the number of fitted parameters adds more degrees of freedom to the fit, which will improve its quality even if the model used is not more relevant. To reduce this risk, we used the additional information provided by the fluorescence recovery under 405-nm light. Considering that after on-switching, all molecules that were shelved in dark-states are brought back to the fluorescent state, the fraction of fluorescence signal that is lost corresponds to photobleaching (as shown on Figure 8.2). The photobleaching rate of the model was then manually adjusted so that the predicted fraction of bleached molecules corresponded to the experimentally observed value, while the other parameters were free fitting parameters (unless otherwise specified). Of note, performing a global fit on the fluorescence decay and recovery phases would allow extracting more informations from the exact recovery kinetics, and take into account any effect of the readout laser on the observed level of fluorescence recovery.

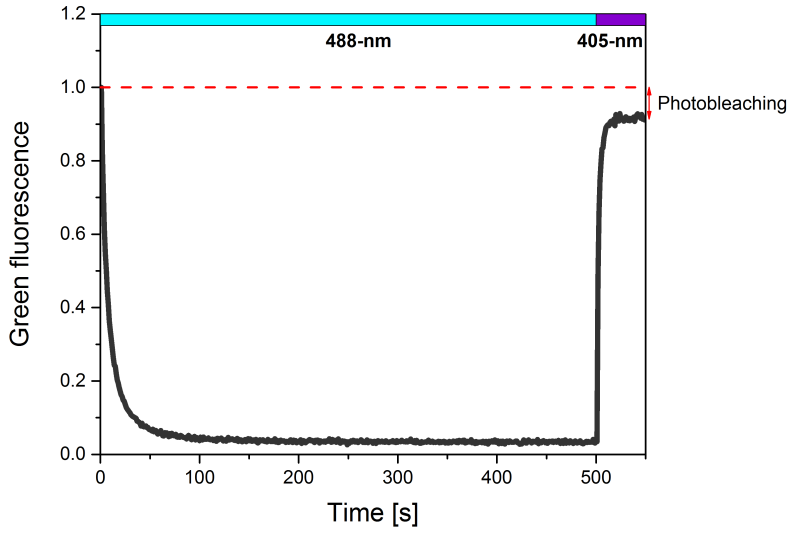

Figure 8.2: Photoswitching of the Dronpa RSFP using 488- and 405-nm light for off- and on-switching, respectively. 405-nm illumination triggers a rapid recovery of fluorescence; the fraction that cannot be recovered (here 10%) can be considered photobleached.

From the fit, on- and off- switching were extracted, and could be compared to those obtained from single-molecule data, or their evolution followed as a function of laser intensity.

The fluorescence recovery kinetics upon 405-nm illumination could also be fitted, using a monoexponential model (which was found sufficient to account for the observed kinetics). The on-switching rate as well as initial fraction of protein in a dark-state were free fit parameters. This same strategy was applied to thermal fluorescence recovery curves, which allowed retrieving a recovery half-time.

From the fitted kinetic rates, reaction quantum yields can be derived using the extinction coefficient of the starting state (ε_λ) and the laser power-density (P_λ), from the following equation:

$$\phi = \frac{k \cdot h \cdot c \cdot N_A}{P_\lambda \cdot \lambda \cdot \varepsilon_\lambda \cdot \ln(10)}$$

where k is the reaction rate (in s^{-1}), h Planck's constant (6.62×10^{-34} $m^2.kg.s^{-1}$), c the speed of light in vacuum (3×10^8 $m.s^{-1}$), N_A Avogadro's constant, and λ the laser wavelength.

8.2 Single-molecule data analysis

8.2.1 General workflow

Localisation of single molecules was performed in ImageJ, using the Thunderstorm plugin.[135] The detection threshold was typically set to 1.2*std(Wave.F1) (i.e. 1.2 times the first wavelet level of the wavelet filter applied by the algorithm). The obtained localisation table was corrected for drift using the fiducial markers present in the field of view, and artefactual localisations were removed based on peak intensity, localisation precision, or broadness of the gaussian fit[i] (0.05% of the localisations). Finally, localisations were clustered in Matlab using a k-means clustering algorithm.

From the table of localisations produced by Thunderstorm, basic statistics can be obtained such as the brightness of the localisations, the background level, or the precision of localisation.

8.2.2 Photophysics analysis

If the processed dataset is composed of sparse enough FP monomers, each cluster obtained in the previous step is expected to correspond to one fluorophore. Using this assumption, all fluorescent signals appearing at the same location can also be attributed to the same molecule, independently of how far apart in time they are situated. Figure 8.3 shows the evolution of the proportion of overlapping molecules as a function of the number of molecules in the field of view (30x30 μm). Our experiments on photophysics had on average of ∼1000 molecules, resulting in about 3% of them overlapping. Furthermore, we checked that there was no visible correlation between the outcome of our experiments (e.g. the fraction of long single-molecule off-times) and the number of molecules in the dataset.

[i] Localisations were filtered out if their characteristics were clearly outside the main distribution, e.g. very high background or localisation precision.

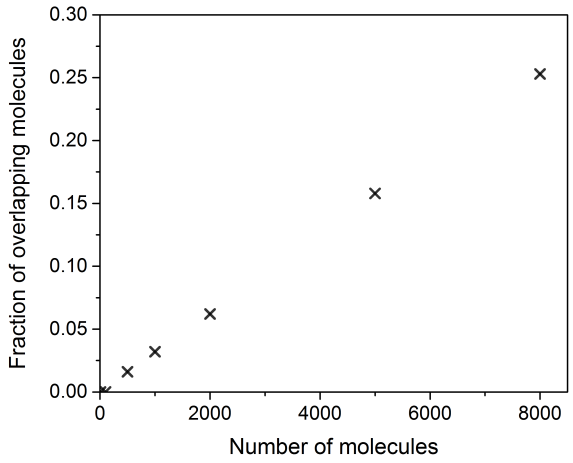

Figure 8.3: Simulation of the number of overlpping molecules in *in-vitro* experiments, as a function of the number of molecules per dataset.

For each cluster of localisations obtained, on-times can be computed (periods during which a molecule is continuously fluorescent), as well as off-times (periods during which a molecule is non-fluorescent between two fluorescence emissions, also called "blink"). These on- and off-times can be represented as histograms for all the molecules present in the dataset, as shown on Figure 8.4.

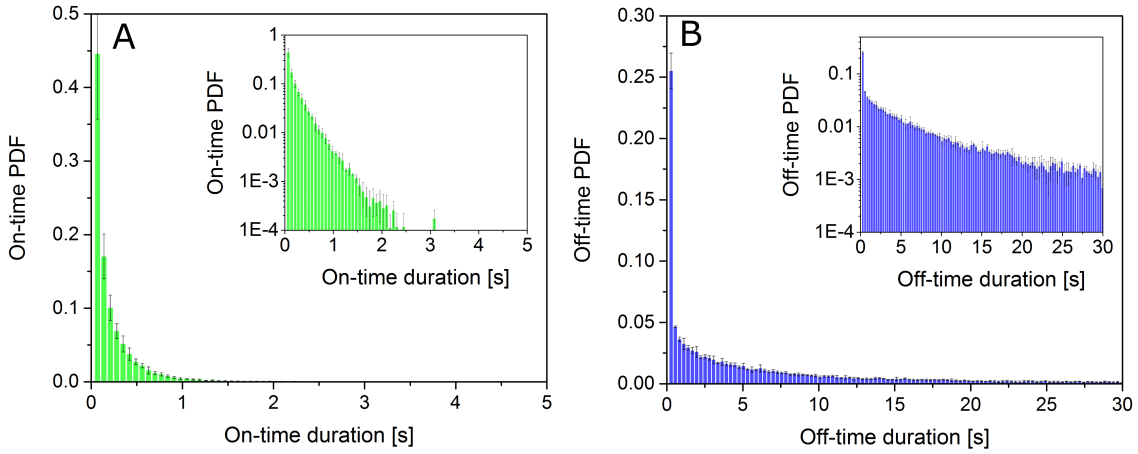

Figure 8.4: Examples of on- (A) and off-times (B) histograms extracted from in-vitro single-molecule datasets of mEos4b immobilised in PAA. Insets show the same histograms in logarithmic scale, which allows a better visualisation of the scarcely populated regions (long on- and off-times).

On to off rate determination

Fitting the on-times histogram (Figure 8.4 A) using a monoexponential model (as shown below) yields a global rate for the transition of the molecules from the fluorescent state to a non-fluorescent state.

$$y(t) = a_0.e^{-k.t}$$

With a_0 the amplitude of the function, k the rate, and t the on-time duration. The rate obtained includes transitions to dark-states as well as photobleaching, which cannot be distinguished here.

Off to on rates determination

Keeping in mind that our dataset is sparse enough to avoid the overlap of signals from different molecules, the off-times histogram (Figure 8.4 B) is only affected by the rate at which molecules recover from non-fluorescent states to the fluorescent state. More complex photophysical transitions can be described by linear combinations of exponential functions, as shown in the following equation:

$$y(t) = a_1.e^{-k_1.t} + a_2.e^{-k_2.t}$$

where k_1 and k_2 are the rate constants for the recovery from distinct dark-states to the fluorescent state. It is important to bear in mind that adding more exponential terms to the model can result in over-fitting. Furthermore, the recovery rates can only be directly deduced from such a model if the dark-states transition independently to and from the fluorescent state. In more complex systems where transitions between dark-states occur, the fitted rates cannot be simply related to the recovery rates, but will be combinations of different transitions.

Retrieving red mEos4b blinking-on rate from the long-lived dark-state

In chapter 10, we attempted to retrieve the blinking-on rate from the long-lived dark-state of red mEos4b by fitting single-molecule off-times histograms. We have however reported that the off-times histograms under sole 561-nm illumination are more complex than previously thought, and show a triphasic behaviour. They could be successfully fitted with a linear combination of three exponentials, but the resulting rates could not be easily related to light-induced recovery from the long-lived dark-state, probably due to transitions between dark-states, as mentioned above. The fastest fitted rate was however attributed to thermal recovery from the short-lived radical state previously reported in mEos2.

In order to retrieve rates that could be compared with the on-switching rates obtained from ensemble data, we used the single-molecule traces to reconstruct ensemble switching curves, as explained below.

In ensemble-level photoswitching experiments, a pool of FPs is in the red fluorescent state at the beginning of the experiment. They are then "switched-off" under 561-nm illumination, i.e. the system is brought to a steady state where FPs constantly exchange between dark and fluorescent states, but the macrosocpic population of each state stays constant. Some FPs exit the system through photobleaching, and a few enter it through photoconversion, although we have found this

effect to be limited in ensemble experiments and have therefore not included it in our model.

In single-molecule experiments, the initial pool of red FPs is very limited, but we rely on constant readout photoconversion to bring new molecules to the red state. This is an important difference with ensemble-level experiments, which can be overcome by synchronising the fluorescence traces relative to the photoconversion event. From these synchronised traces, summing the number of molecules in the fluorescent state over time will show their ensemble-level behaviour. This strategy is summarised in figure 8.5.

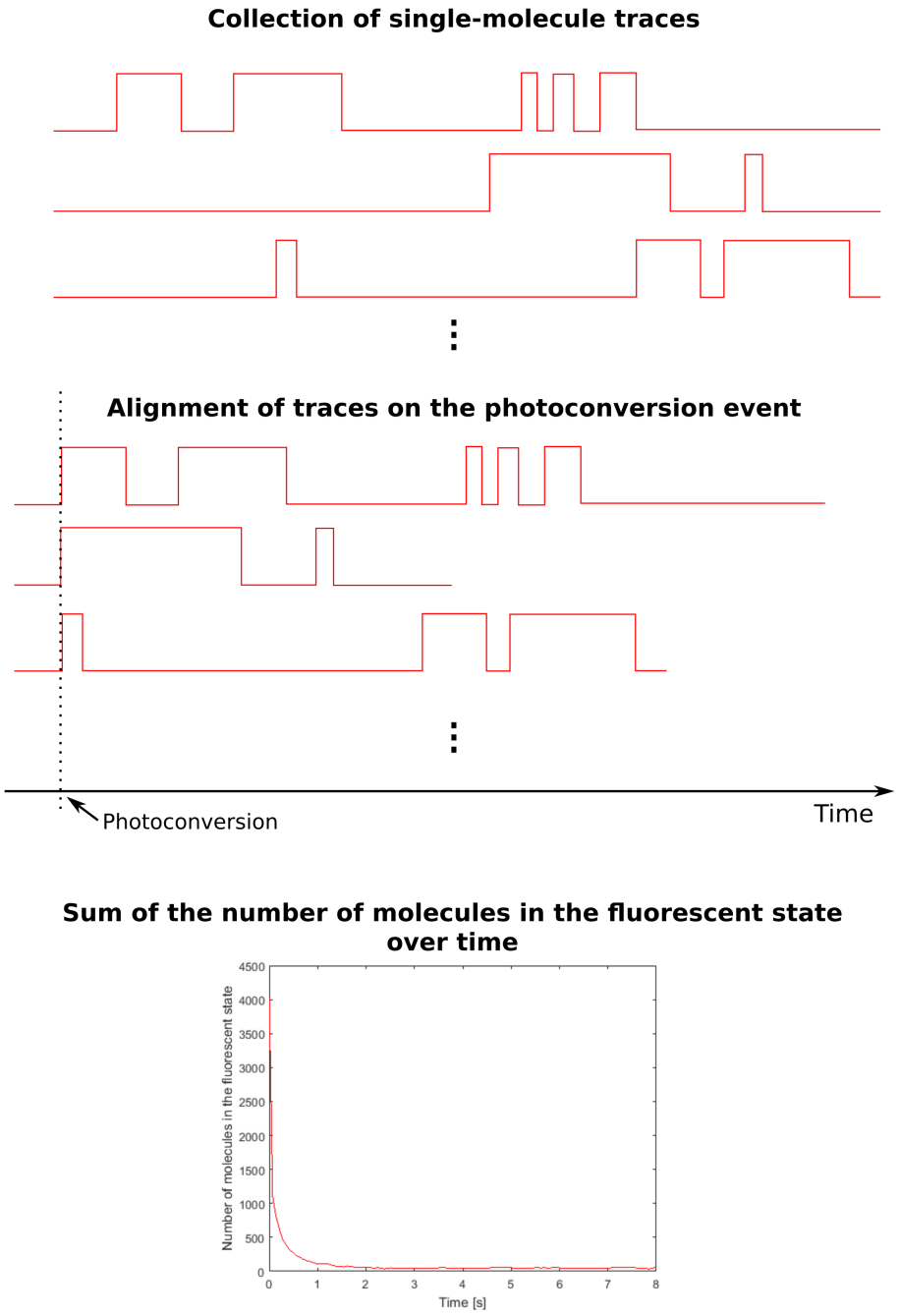

Figure 8.5: Strategy for reconstitution of ensemble fluorescence decays from single-molecule experiments. The fluorescence traces are synchronised relative to their first fluorescence emission, and the number of active molecules is summed over time to reveal their behaviour at the ensemble level.

Interestingly, we can still benefit from the original single-molecule information of the data: thanks to the fluorescence traces, when a molecule is non-fluorescent we know whether it is in a reversible dark-state, or whether it is irreversibly photobleached.[ii] Similarly to the way we summed the number of molecules in the fluorescent state over time, we can sum the number of molecules in dark-states and photobleached, and get access to ensemble-level behaviour about non-emissive states, that is not accessible in classical ensemble fluorescence experiments (as shown on Figure 8.6).

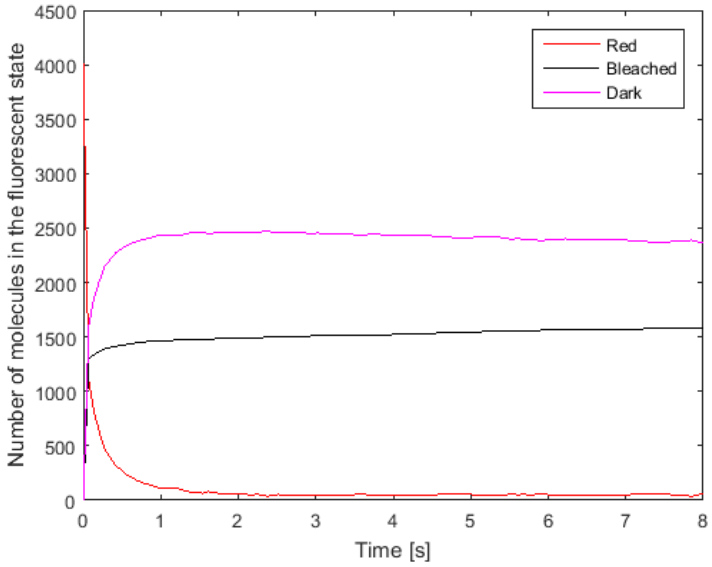

Figure 8.6: Ensemble fluorescence decay and population of dark and bleached states reconstituted from single-molecule data.

Showing all states in this way, it becomes apparent that the first point of the curve has an unexpected behaviour: a large population of red fluorophores appears to instantly transit to the bleached and dark states (whereas the transition happens with slower dynamics afterwards). We attributed this to spurious localisations in the dataset appearing as 1-frame fluorescence events, based on these unexpected effects that are not seen in ensemble-level experiments. We therefore excluded the first point of the curve from further analyses. It would however be interesting to investigate what proportion of the localisations these spurious events represent, and what is their origin (e.g. fluorescent impurities in the samples, or false positive detections by Thunderstorm).

Finally, we fitted the obtained decay curves with the same kinetic model as used for ensemble-level experiments. Even though this model included only two dark-states, it was able to fit reasonnably well the decay curves, which is discussed in more details in chapter 13. The fits allowed us to retrieve on-switching rates from the long-lived dark-state, as shown in chapter 10.

[ii] Molecules which did not recover fluorescence by the end of the single-molecule dataset were considered photobleached.

8.2.3 Cumulative photoconversion curves

A way of analysing the influence of green state photophysics on the photoconversion kinetics (chapter 9) was to plot cumulative photoconversion curves. These curves were built by summing the number of newly appearing molecules over the length of the dataset. Since FPs in the sample were sparse, we attributed all spatially close fluorescence events to the same FP (to avoid blinking-related biases).

The obtained curves were fitted with the same kinetic model as used for ensemble-level experiments on green mEos2, except that the fitting variable was not anymore the fraction of green fluorescent proteins, but the fraction of red proteins. Since the cumulative curves are not affected by the photobleaching of green FPs, the fitted rate corresponded solely to photoconversion, and did not take photobleaching into account.

Interestingly, rates for off- and on-switching were also present as fit parameters in the model. The off- and on-switching rates of the short-lived dark-state were fixed to the value derived from ensemble experiments to avoid over-fitting, while the rates associated to the long-lived dark-state were free fit parameters.

8.2.4 qPALM analysis

τ_c calibration curve

τ_c curves were generated either from simulated traces (thanks to the PALM simulation software mentioned below in section 8.3), or from monomers imaged in the same experimental conditions as for counting (for more details on the procedure, see the discussion in chapter 12).

In both cases, random traces were combined to build artificial oligomer traces with defined stoichiometries. These were processed with increasing τ_c values, and the optimal τ_c was defined as the smallest one that allowed retrieving the correct number of molecules from the trace. For each stoichiometry, a large number of reconstituted traces were generated (typically 1000) to account for stochasticity and obtain an average optimal τ_c value.

Processing of decamer datasets

Single-molecule localisation and filtering was performed according to the general workflow described above. Localisations were clustered thanks to a K-means algorithm, and the number of molecules per cluster was determined using the previously obtained τ_c curve. As described in section 5.2.4, this involved an iterative procedure to find the τ_c that would yield the correct number of molecules. This was done on all the clusters of a field of view (typically 200 to 400), and the count of the number of molecules per cluster was represented as a histogram.

8.3 Simulation of microscopy data

Ensemble-level data were simulated using kinetic models in Matlab. These models could be adjusted to integrate as many states and transitions between them as necessary. Even though the simulations had a high time resolution to be able to model fast processes (e.g. transitions to the

triplet state), the final curves could be binned to better reflect experimental curves, that are limited in resolution by the exposure time of the camera (usually a few tens of milliseconds). The generated data could be processed identically to the experimental ones.

At the single-molecule level, a custom Matlab script was developed by Dominique Bourgeois to perform detailed simulations of PALM experiments. A large number of parameters could be tuned in the simulations, including the number and nature of the fluorophores (and their photophysics), the laser illumination scheme, poissonian noise, or the detection efficiency of the microscopy setup. Using this script, we could generate stacks of images truthfully reproducing the quality of the ones obtained experimentally. These images were processed in the same way as experimental data.

Part III

Results

Preliminary remark on the fluorescent proteins used in this work

As mentioned earlier, this thesis work focused on the photophysical characterisation of FPs of the Eos family. Historically, mEos2 has been and still is one of the most used markers in PALM, which is why it was originally chosen as an object of study during the PhD work of Romain Berardozzi. However, new variants were then reported (mEos3.2 in 2012[59] and mEos4b in 2015[65]) that had improved properties, notably in terms of monomericity. We therefore estimated that research labs were likely to change their current FPs to these new versions in the near future, and hence the work of Elke De Zitter was conducted on mEos4b.

As a result, some of the following chapters deal with mEos2, and others with mEos4b. We however believe the photophysics of the two proteins to be extremely similar, since most mutations differentiating them are located on the outside of the β-barrel, and not in the chromophore pocket.[59,65] Furthermore, in all experiments that we performed on both mEos2 and mEos4b, we found extremely similar photophysical behaviour. A few experiments conducted on mEos3.2 (derived from mEos2 and parent of mEos4b) also showed identical behaviour.

Chapter 9

Photophysics of green mEos2

9.1 Introduction

The first theme of investigation of this thesis was the photophysics of the green state of PCFPs of the Eos family. Only little attention had been given to it thus far, since the red form of the protein is the one observed in PALM. However, the common observations of incomplete photoconversion and readout photoconversion point to a possible influence of green state photophysics on PALM experiments. Furthermore, from observations made in our lab, green mEos2 was seen to photobleach rapidly under 488-nm fluorescence excitation, which prompted us to investigate whether this could be due to a reversible photoswitching behaviour, as that present in mGeosM (an mEos2 variant engineered to display photoswitching but that cannot photoconvert).[136] This work was initiated by Romain Berardozzi, a previous PhD student who defended his thesis in 2016.

In this chapter, it will be shown that green mEos2 is able to undergo light-induced loss and recovery of fluorescence, suggesting that photoswitching is not limited to RSFPs, but rather a shared property between FPs. Furthermore, photoswitching of green mEos2 will be demonstrated not only using 488-nm light, but also intense 561-nm illumination, as is typically used in PALM. A quantitative evaluation of the photophysical processes taking place at both wavelengths and at different light intensities will allow us to propose a kinetic model, which successfully accounts for green mEos2 behaviour both at the ensemble fluorescence and single-molecule levels. Finally, single-molecule experiments will give an insight into how green-state photophysics affects PALM, which will be further discussed as a conclusion.

9.2 Characterisation at the level of ensemble fluorescence

Throughout this chapter, all ensemble-level experiments used the fluorescence readout scheme of Figure 7.3 (see materials and methods), combining weak 488-nm illumination (0.2 W/cm^2) for 5% of the time for fluorescence readout, and actinic illumination at 488, 561 or 405 nm for 90% of the time.[i] For clarity, only actinic illumination will be mentioned in the description of the experimental conditions, but readout light (at constant power) is always present.

[i] Actinic illumination is used to produce a photophysical effect on the FP, and not to excite fluorescence.

9.2.1 Reversible photoswitching of green mEos2

At first, we tested whether illumination at 488-nm (as typically used for fluorescence excitation) could induce photobleaching and/or reversible switching of green mEos2. Upon weak illumination at 488-nm (10 W/cm^2), the green fluorescence of mEos2 dropped to ∼10% of its initial value in a few tens of seconds (Figure 9.1). However, upon subsequent illumination at 405-nm, more than 80% of the fluorescence could be recovered, indicating that the loss of fluorescence was indeed due to a reversible switching behaviour, as observed with RSFPs such as Dronpa[128] or IrisFP.[66] The fraction of fluorescence that could not be recovered upon illumination at 405 nm was attributed to a mix of photobleaching and photoconversion by 488- or 405-nm light. Since these two processes are irreversible, they cannot be distinguished in this experiment.

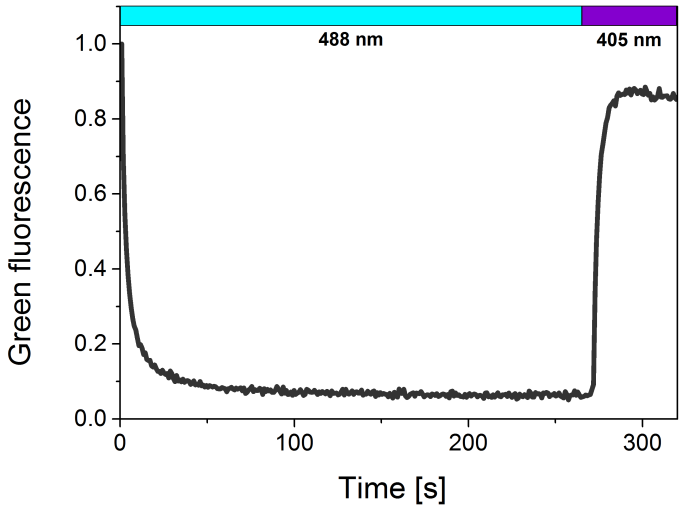

Figure 9.1: Reversible off-switching of PVA-embedded mEos2 under 488-nm illumination (10 W/cm^2) followed by fluorescence recovery upon illumination at 405 nm (0.03 W/cm^2). Figure representative of >3 experiments on different FP preparations.

After showing that green mEos2 was indeed able to undergo reversible switching, we wanted to check that Eos4b showed similar behaviour, and compare its switching speed to that of known RSFPs. In particular, we wanted to compare it to two other Eos variants engineered to display photoswitching, mGeosM and IrisFP. We also compared these to Dronpa, which is a well known and studied RSFP. Therefore, fluorescence decay under 488-nm light followed by recovery under 405-nm light was performed on these 4 proteins embedded in PAA, using identical experimental conditions. The resulting curves (Figure 9.2) indicated that mEos4b switches off significantly slower than IrisFP but on a very similar timescale (or slightly faster) than mGeosM. Both mEos4b and mGeosM showed slower off-switching than Dronpa. Fluorescence recovery occured at a similar level (>80% for all proteins). Of note, off-switching of mEos4b is slower here than for mEos2 on Figure 9.1 above, due to an ∼10 times lower 488-nm laser intensity, rather than to a difference between the proteins.

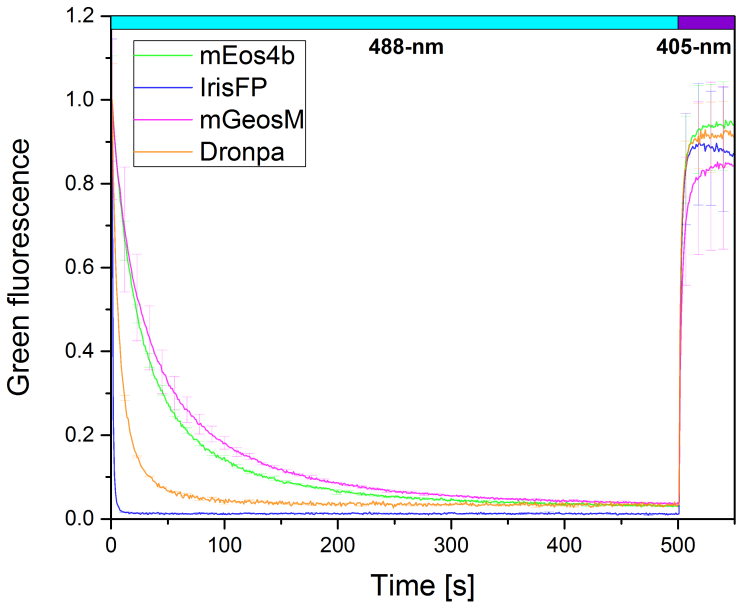

Figure 9.2: Reversible off-switching of mEos4b and 3 other fluorescent proteins in PAA under 488-nm illumination (1 W/cm^2) followed by fluorescence recovery under 405-nm light (0.25 W/cm^2). Curves shown as mean ± SD (n = 3 different FP preparations).

These findings show that photoswitching is an inherent property to photoconvertible Eos proteins (e.g. mEos2 and mEos4b), and that the engineering of mGeosM, although it succesfully impaired photoconversion as was intended,[136] did not modify much the photoswitching properties.

Notes on the notion of switching contrast

The "switching contrast" is defined as the residual level of fluorescence after off-switching, compared to the initial level. This residual level is due to the equilibrium between on- and off-switching events occuring under sole 488-nm illumination (due to residual absorbance of the off-state at this wavelength). The switching contrast of a protein is related to the achievable signal-over-noise ratio (SNR) in PALM or RESOLFT experiments using RSFPs, since residual fluorescence after off-switching will contribute to background in the images.[ii] As a consequence, differences in switching contrast that seem small (e.g. a few %) can result in a substantial change of the SNR.

The switching contrast is typically measured on switching curves, like the ones shown on Figure 9.2, by dividing the last point of the fluorescence decay curve by its first point (initial fluorescence). This method however does not take photobleaching into account: therefore, a poor switcher that

[ii] Of note, optimal SNR in PALM when using RSFPs requires both slow photoswitching (so the protein stays long enough in the on-state to be detected) and good contrast, two qualities which are often anti-correlated.

photobleaches quickly will appear to have a good switching contrast, whereas most molecules can actually not be brought back to the fluorescent state. Therefore, we propose to define two types of switching contrast, depending on the comparison to be made:

- The **apparent switching contrast**: calculated as stated above, by dividing the initial fluorescence level by the fluorescence signal after off-switching. Even though this does not account for photobleaching, it will represent the level of background fluorescence in a PALM experiment. A quickly photobleaching protein would present low background fluorescence, reflected by the good apparent switching contrast, with however a poor labelling efficiency (due to photobleaching).
- The **photophysical switching contrast** is meant as a more fundamental property of the FP, and can be defined as the ratio of the on- and off-switching rates under sole 488-nm illumination. Therefore, this photophysical switching contrast will not be increased if photobleaching is higher. It can be estimated from the switching curves of Figure 9.2 by dividing the signal after fluorescence recovery under 405-nm light (i.e. the total pool of proteins that are amenable to fluorescence emission) by the fluorescent signal after-off switching. Of note, a more precise way of determining this photophysical contrast would be performing a global fit of the whole photoswitching curve (including off- and on-switching).

As an example, table 9.1 shows the switching contrasts calculated from the switching curves of Figure 9.2, using both methods. IrisFP showed the best switching contrast, with little variation between calculation methods due to its efficient fluorescence recovery. mGeosM on the other hand had the worst apparent switching contrast, which was further degraded in terms of photophysical contrast due to its less efficient fluorescence recovery. Of note, differences between calculation methods are small here because all FPs recovered >80% of their fluorescence upon on-switching. Bigger differences can be observed in experimental conditions allowing only limited fluorescence recovery (e.g. very long off-switching times).

FP	**Apparent contrast (fold-change**	**Photophysical contrast (fold-change)**
mEos4b (green)	33 (± 10)	32 (± 9)
IrisFP (green)	90 (± 7)	81 (± 4)
mGeosM	27 (± 8)	23 (± 7)
Dronpa	32 (± 8)	30 (± 8)

Table 9.1: Comparison of apparent and photophysical switching contrasts of 4 different fluorescent proteins. Values are given as fold-change between fluorescence after off-switching and either fluorescence before off-switching (apparent contrast) or after on-switching (photophysical contrast).

Additionally, the apparent switching contrast can be biased if switching is too fast and sampling unsufficient. In the case of a fast-switching FP, the signal from the first camera frame will be an integration of fluorescence over the frametime, and therefore underestimated, leading in turn to an underestimated apparent switching contrast. Solutions to this problem include using lower laser intensities to slow down switching, or using devices that allow high acquisition rates such an an sCMOS camera, or a single-photon counter.

The photophysical switching contrast can also be biased if off-switching by the fluorescence readout laser (here at 488-nm) competes with on-switching by the fluorescence recovery laser (here at 405-nm). This would lead to an underestimated fluorescence recovery, and hence an underestimated photophysical switching contrast. To avoid this, the fluorescence readout light intensity should be kept as low as possible, to avoid having an influence on the photoswitching curves.

9.2.2 Intense 561-nm light induces photoswitching of green mEos2

Readout photoconversion is a commonly observed phenomenon in PALM, whereby molecules undergo photoconversion under sole 561-nm illumination, in the absence of 405-nm light. Although photoconversion by readout light occurs at a much slower rate than by 405-nm illumination, it points to the fact that 561-nm light must interact with green mEos2, despite its absorbance being extremely low at this wavelength (Figure 9.3 A). Indeed, intense illumination at 561 nm (a few kW/cm^2) as used in PALM experiments was able to induce off-switching of green mEos2 (Figure 9.3 B), in a similar manner as was observed under 488-nm illumination. Probing this behaviour was made possible by decoupling fluorescence excitation (by weak 488-nm light) and actinic illuminations (at 561 or 405 nm) as described in section 7.4.

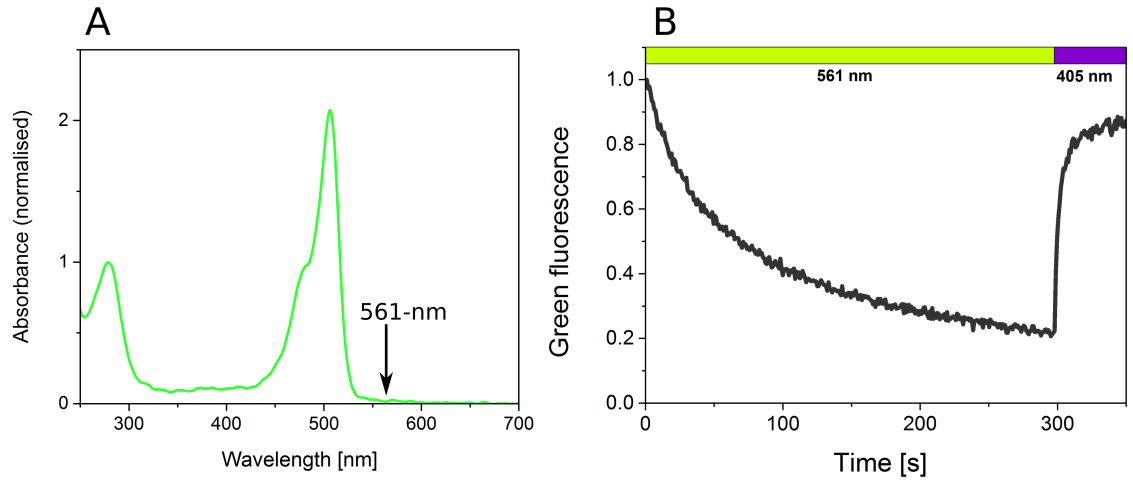

Figure 9.3: (A) Absorbance spectrum of the green state of mEos2 (normalised at 280 nm). The main absorbance peak is at 500 nm, and corresponds to the anionic chromophore. (B) Reversible off-switching of mEos2 under intense 561-nm illumination (2.4 kW/cm^2) followed by fluorescence recovery upon illumination at 405 nm (0.03 W/cm^2). Figure representative of >3 experiments on different FP preparations.

Since the wavelength of 561-nm light is longer than the 0-0 transition of the anionic chromophore, it is not expected to be able to affect the green state of the protein. The effects mentioned here could be due to the "hot band", or "Urbach tail" effect, through which molecules in a vibrationally excited state can be pumped into an electronically excited state.[137] This same effect has been successfully used to induce switching of diarylethylene dyes.[138,139]

9.2.3 Photophysical model for green mEos2

We next turned to quantifying the off-, on-switching and photobleaching rates under 488- or 561-nm illumination. To this aim, the fluorescence on-off switching curves of Figures 9.1 and 9.3 were fitted using a non-linear fit based on a kinetic model, as described in section 7.4.

The minimal working hypothesis for the fit was the transition of the green fluorescent form of the protein to a reversible dark-state, and to an irreversibly photobleached (or photoconverted) form (Figure 9.4, panel A). The resulting fits are shown on panels B and C of Figure 9.4 for switching under 488- and-561 nm light, respectively. The green curve shows the fitting variable (protein in the fluorescent state), whereas the other colored curves are the populations of the other states, extracted from the kinetic model.

From the overlay of the experimental and fitted curves, and the corresponding fit residuals, it appears that the model does not allow to accurately describe the kinetics of the fluorescence decay. Furthermore, the red form of mEos2 had previously been shown to enter two dark-states with distinct lifetimes,[74] so one could expect a similar behaviour in the green state. Hence a second model was tested, taking into account the presence of two reversible dark-states (Figure 9.4, panel D). This model allowed accurate fitting of the fluorescence decay curves (panels E and F), and yielded distinct lifetimes for the two dark-states, a long one (in the order of minutes) and a short one (in the order of seconds). Fitted rates as well as derived quantum yields (when applicable, using the extinction coefficient of green mEos2 at 488 nm, $\varepsilon = 79000\ M^{-1}.cm^{-1}$) are given in table 9.2.

Control experiments were performed to ensure that the shape of the fluorescence decays was not influenced by other parameters, such as dipole orientation, or laser beam heterogeneity (see section 9.4.1).

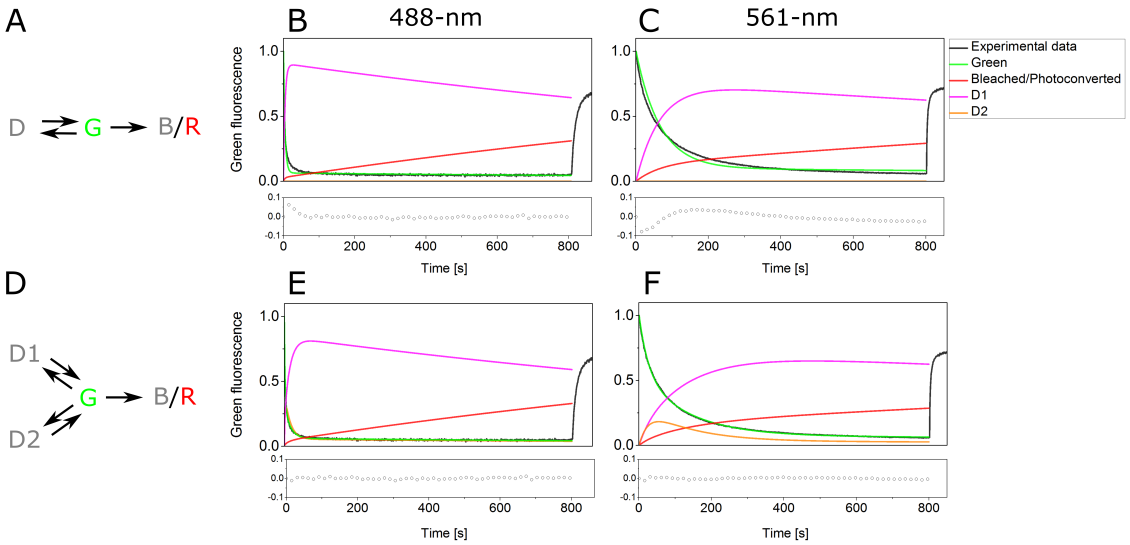

Figure 9.4: Fitting of the light-induced fluorescence decays of PVA-embedded green mEos2. Fluorescence decays were recorded under 488- or 561-nm illumination (10 and 2400 W/cm^2, respectively), and fitted with a model including irreversible photobleaching, and transition to one or two reversible dark-states (panels A and D). The simpler model with a single dark-state failed to accurately describe the experimental data (B, C), whereas the one with two dark-states provided a good quality fit (E, F). Fitting residuals are shown in the bottom panels.

		488-nm (10 W/cm^2)	**561-nm (2.4 kW/cm^2)**
long-lived dark-state	off-switching rate [s^{-1}]	$1.4 \times 10^{-1}(\pm 3.2 \times 10^{-2})$	$7.7 \times 10^{-3}(\pm 1.0 \times 10^{-3})$
	on-switching rate [s^{-1}]	$1.1 \times 10^{-2}(\pm 1 \times 10^{-3})$	$2.3 \times 10^{-3}(\pm 2.1 \times 10^{-4})$
	off-switching quantum yield [-]	2.6×10^{-5}	ND
	off-switching brightness [$M^{-1}.cm^{-1}$]	1.58	6.1×10^{-4}
	on-switching brightness [$M^{-1}.cm^{-1}$]	1.2×10^{-1}	1.9×10^{-4}
short-lived dark-state	off-switching rate [s^{-1}]	$1.6 \times 10^{-1}(\pm 3.6 \times 10^{-2})$	$9.5 \times 10^{-3}(\pm 2.9 \times 10^{-3})$
	on-switching rate [s^{-1}]	$1.8 \times 10^{-1}(\pm 2.1 \times 10^{-2})$	$4.2 \times 10^{-2}(\pm 6 \times 10^{-3})$
	off-switching quantum yield [-]	3×10^{-5}	ND
	off-switching brightness [$M^{-1}.cm^{-1}$]	1.78	7.6×10^{-4}
bleaching and photoconversion	combined rate [s^{-1}]	$1 \times 10^{-2}(\pm 5 \times 10^{-3})$	$1.3 \times 10^{-3}(\pm 2.5 \times 10^{-4})$

Table 9.2: Rates fitted from the switching curves of Figures 9.1 and 9.3, using the kinetic model of Figure 9.4, panel D (including two reversible dark-states). Quantum yields for on-off switching at 488 nm excitation could be derived based on the knowledge of the green mEos2 extinction coefficient at this wavelength. Switching brightness refers to the product (switching quantum yield x extinction coefficient). ND: not determined. Numbers given as mean ± SD (n=3 different FP preparations).

In order to test our model, we performed a titration of the 561-nm illumination intensity on mEos2 embedded in PVA. Switching rates were retrieved as previously for each condition (Figure 9.5), and were expected to show a linear dependence on laser intensity in the case of light-induced processes, or to remain constant over the titration in the case of thermal processes.

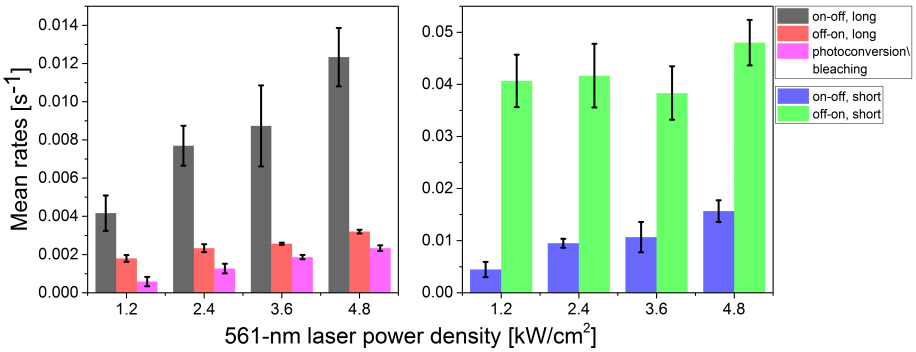

Figure 9.5: Switching rates of green mEos2 according to 561-nm illumination intensity. All rates evolve linearly, except the off-on switching from the short-lived dark-state, which is thus expected to result from a thermal process. Points represent mean ± SD (n=3 different FP preparations).

Whereas the on-switching rate from the long-lived dark-state evolved linearly with 561-nm illumination intensity, the one of the short-lived dark-state appeared to be independent of illumination intensity. This points to a thermal recovery of the short-lived dark-state, consistent with a non-absorbing chromophore, as previously observed for the redox-induced blinking of green IrisFP.[76]

9.2.4 Nature of the long-lived dark-state

The long-lived dark-state of green mEos4b was found to be stable in the dark for hours (Figure 9.6 A), opening the way to cryo-trapping of the dark-state in the crystalline form and solving its structure by X-ray crystallography. This was done by Elke De Zitter on mEos4b, in the frame of a collaboration with KU Leuven (manuscript in prep.). The structure (Figure 9.6 B) revealed an isomerised chromophore, in an unstable *trans* conformation.

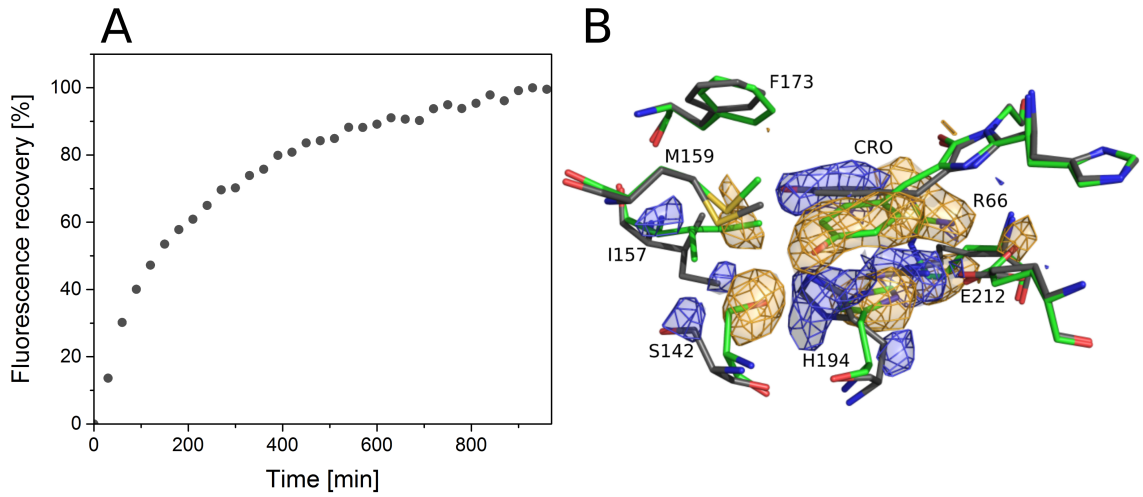

Figure 9.6: (A) Green mEos4b was illuminated with 488-nm light, and subsequently left in the dark at 37°C for 16 hours. During this period, fluorescence recovery was monitored by weak pulses of 488-nm light every 30 min. The recovery half-time was ∼2 hours. Figure representative of 2 experiments on different FP preparations. (B) Crystal structures of the green fluorescent (green model and yellow electron density) and dark (grey model and blue electron density) states of mEos4b, solved by Elke De Zitter. The structure of the dark state features a *trans* isomerised chromophore. Difference electron density maps contoured at 3 r.m.s.d.

The absorbance spectrum of green mEos4b after off-switching under 488-nm light showed a peak around 400 nm, characteristic of a protonated state (Figure 9.7). This state could be recovered to the anionic state by illumination at 405-nm, consistent with the fluorescence recovery shown on Figure 9.1.

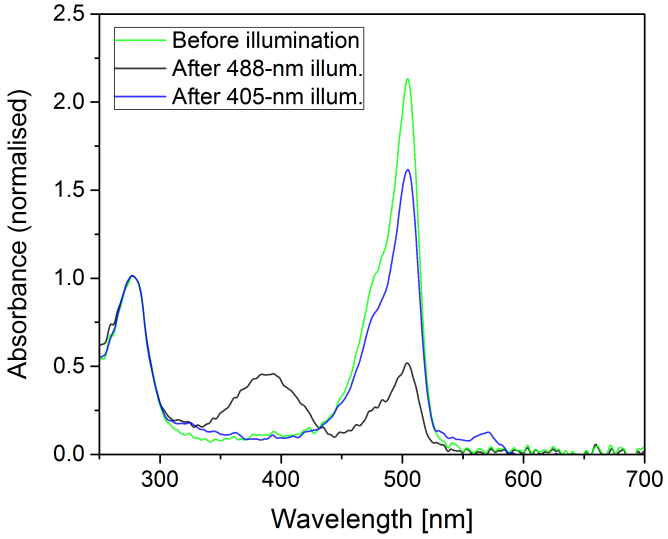

Figure 9.7: Evolution of the absorbance spectrum of green mEos4b upon photoswitching. Upon illumination at 488-nm, the anionic peak (∼500 nm) is depopulated, and a peak corresponding to the protonated chromophore appears around 400 nm. Upon illumination at 405 nm, the protonated peak is depopulated towards the anionic peak. Note a small population of red chromophores appearing at 570 nm after 405-nm illumination.

Taken together, these results show that mEos4b (and presumably mEos2) undergo a very similar process to photoswitching in RSFPs, with combined cis-trans isomerisation and protonation of the chromophore.[128,140] This highlights that photoswitching is not unique to RSFPs, but can be found in other FPs such as PCFPs.

Another finding of the crystallographic study, combined with molecular dynamics simulations, was that the off-switched chromophore of PCFPs is less stable than the one of RSFPs, which might explain their lower switching contrast (see for example the contrasts of mEos4b and IrisFP reported in table 9.1). This low stability of the off-state of PCFPs results in a lower population of chromophores in the off-state at equilibrium. Conversely, the more stable off-state of RSFPs allows it to be more populated at equilibrium. Of note, this finding is independent of the energy barrier between the on- and off-states, which will affect the speed at which equilibrium is reached, but not the steady-state populations.

9.3 Characterisation at the single-molecule level

9.3.1 Influence of green mEos2 photoswitching on the appearance of red single molecules

The fact that green mEos2 is able to undergo reversible switching under strong 561-nm illumination prompted us to check whether this phenomenon had an influence on single-molecule experiments on the red form of the protein. To this aim, we made cumulative plots of photoconverted molecules (as described in materials and methods, section 8.2.2), either under sole 561-nm light (readout photoconversion), or under combined 561- and 405-nm light, as is commonly done during PALM experiments (Figure 9.8).

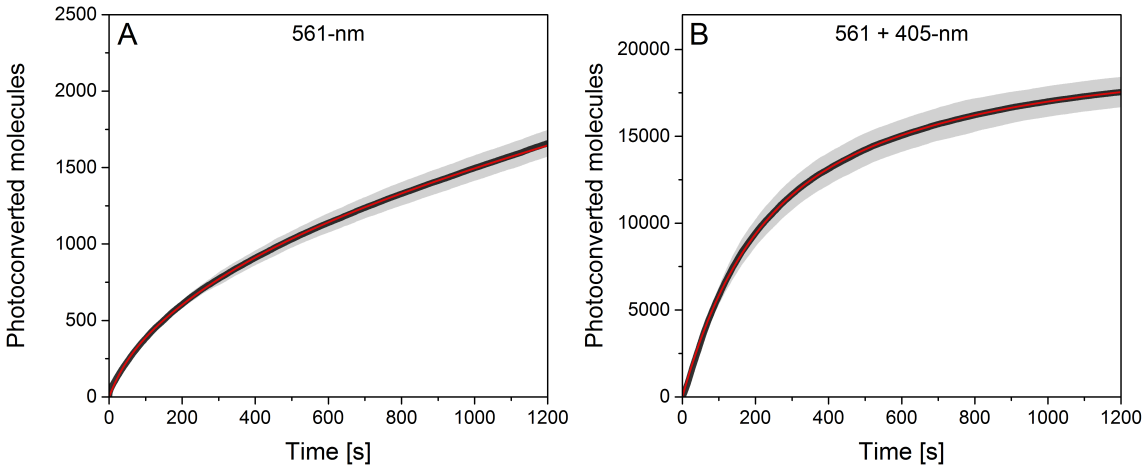

Figure 9.8: Cumulative plots of the number of photoconverted molecules during PALM experiments on mEos2 embedded in PVA, under (A) sole 561-nm illumination (2.4 kW/cm^2), or (B) with additional 405-nm illumination (0.8 W/cm^2). Whereas combined 561- and 405-nm illumination yields a close to monophasic curve, 561-nm illumination alone yields a strongly biphasic curve. Both curves were fitted (red lines) using the same kinetic model as shown on Figure 9.4, panel D. Note the difference in Y-scale between the two plots, outlining the higher efficiency of 405-nm light to induce photoconversion. Curves show mean ± SD (n=3 different FP preparations).

As expected, the addition of 405-nm light largely increased the photoconversion rate compared to sole 561-nm light (about 10 times more molecules photoconverted over the time span of the experiment). Furthermore, the shape of the cumulative curve was different with and without 405-nm illumination, showing a pronounced biphasic behaviour under sole 561-nm illumination, and a close to monophasic shape upon addition of 405-nm light. We attributed this biphasic behaviour to the shelving effect produced by photoswitching of the green state, after eliminating possible spurious effects (see control experiments in section 9.4.2). The cumulative curves could be well fitted using the kinetic model of Figure 9.4, yielding very similar rates for the long-lived dark-state to those extracted from ensemble experiments (as shown in Table 9.3).

	Rate [s^{-1}]	Ensemble level	Single-molecule level
long-lived dark-state	off-switching	$8.7 \times 10^{-3}(\pm 2.1 \times 10^{-3})$	$1.2 \times 10^{-2}(\pm 3 \times 10^{-4})$
	on-switching	$2.6 \times 10^{-3}(\pm 6 \times 10^{-5})$	$3 \times 10^{-3}(\pm 1.3 \times 10^{-4})$
short-lived dark-state	off-switching	$1.1 \times 10^{-2}(\pm 2.9 \times 10^{-3})$	Fixed to ensemble value
	on-switching	$3.8 \times 10^{-2}(\pm 5.1 \times 10^{-3})$	Fixed to ensemble value
bleaching and photoconversion	combined rate	$1.9 \times 10^{-3}(\pm 1.2 \times 10^{-4})$	ND
photoconversion	photoconversion rate	ND	$4.9 \times 10^{-4}(\pm 2.5 \times 10^{-5})$

Table 9.3: Comparison between rates fitted under sole 561-nm illumination (2.4 kW/cm^2) from ensemble-level experiments, and single-molecule experiments. The off- and on- switching rates for the long-lived dark-state are in good agreement between the two types of experiments. Single-molecule experiments additionally allow isolating the photoconversion rate. Numbers given as mean ± SD (n=3 different FP preparations).

Interestingly, cumulative photoconversion curves from single-molecule experiments gave access to the photoconversion rate. Since ensemble experiments provided a combined rate for bleaching and photoconversion, we were able to estimate that, under conditions of readout photoconversion, only 25% of the molecules may eventually reach the red state due to green state photobleaching. This indicates that 561-nm readout light has an important contribution to the limited photoconversion efficiency of mEos2 previously reported.[69]

9.3.2 Implications for PALM experiments

One of the direct conclusions from the previous results is that performing PALM experiments using readout photoconversion as the sole activation should be avoided, since it would cause massive photobleaching of the green proteins. However, PALM experiments are typically performed using 405-nm light to prompt photoconversion. In this case, the rate of depopulation of the long-lived dark-state is expected to be higher; nevertheless, shelving in dark states still produces a slowing down of photoconversion, as illustrated on Figure 9.9 for increasing 561-nm illumination intensities. As a consequence, the potential advantage of using a highly intense readout laser for faster PALM data collection is strongly offset by substantial shelving in dark-states.

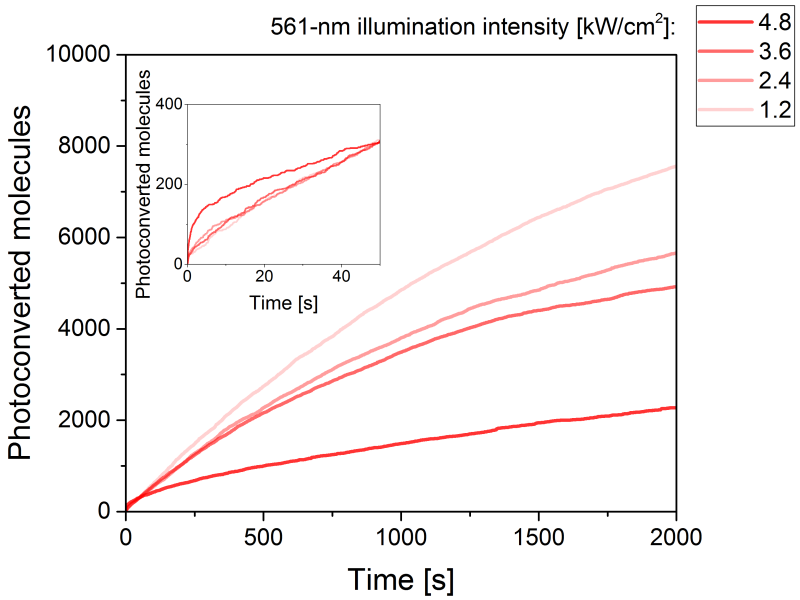

Figure 9.9: Influence of 561-nm illumination intensity on cumulative photoconversion curves in the presence of 405-nm light (0.03 W/cm^2). Stronger intensities of 561-nm light slow down photoconversion and increase the biphasic behaviour of the cumulative curves, which is particularly visible at short times at high 561-nm illumination intensity (inset). Curves correspond to single experiments.

Finally, photobleaching being a light-induced process, it is expected to increase with 561-nm illumination intensity. Thus, a more powerful readout laser will increase bleaching of the green state, reducing the apparent photoconversion efficiency, and the labelling density. Similarly, "pre-bleaching" by 561-nm light that is sometimes applied to eliminate the red molecules already present at the start of PALM experiments would cause important shelving and photobleaching of green molecules as well.

9.4 Control experiments

Several control experiments were performed to ensure that the behaviours observed at the ensemble and single-molecule levels were not due to spurious effects, such as heterogeneities in laser excitation, orientation of the molecules, or fluorescent impurities. These controls will be presented here in two parts, for ensemble-level and single-molecule experiments.

9.4.1 Ensemble level

In order to assess the effect of intense 561-nm illumination on the green state of mEos2, the laser scheme of Figure 7.3 was used, featuring a short pulse of weak 488-nm light for fluorescence readout, followed by a longer pulse of actinic light (e.g. at 561 nm). In order to check that the observed

switching was due to the actinic light, we performed experiments under sole readout light, and with varying intensities of 561-nm light (Figure 9.10).

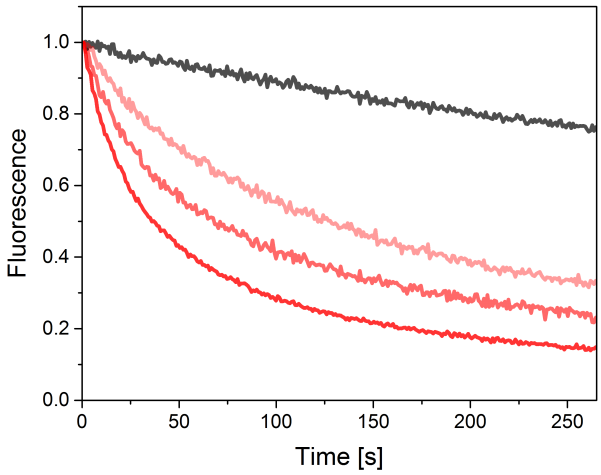

Figure 9.10: Ensemble fluorescence measurements under sole 488-nm readout light (grey curve, 0.2 W/cm^2, 5% duty-cycle), or with additional 561-nm actinic illumination (red curves, 1.2, 2.4 and 3.6 kW/cm^2, 90% duty-cycle). Curves correspond to single experiments.

The weak 488-nm readout light appears to induce a slow fluorescence decay; however, this decay is much more pronounced in the presence of actinic 561-nm light, and becomes sharper under increasing illumination intensity. Actinic light is therefore the main factor inducing fluorescence off-switching.

Finally, we wanted to check that the shape of the fluorescence decays, that led us to a two dark-states model (Figure 9.4) was not caused by spurious effects.

Laser beam profile heterogeneity was eliminated by conducting analysis on a small fraction of the field of view, where laser intensity was considered homogenous (as shown in materials and methods, section 8.1.1, Figure 8.1).
Another possible source of the observed shape of our fluorescence decay curves was heterogenous fixed orientations of mEos2 molecules in PVA, creating sub-populations absorbing different amounts of light. Hence, experimental data were fitted with a one dark-state model (as shown on Figure 9.4 A) taking into account the fixed, random orientation of fluorophores[134] (Figure 9.11). The difference in the fit is minor, so that the possibly anisotropic distribution of the fluorophores in PVA does not account for the observed shape of the fluorescence decay.

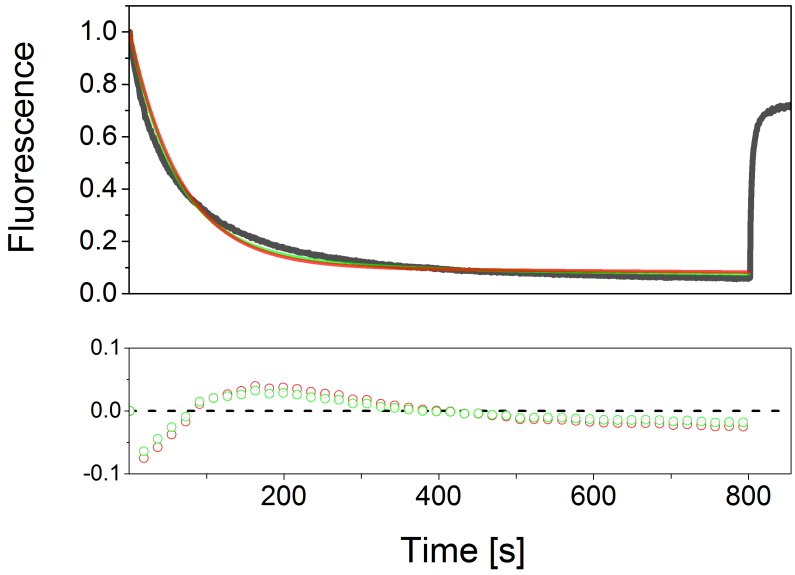

Figure 9.11: Fitting of green mEos2 off-switching under 561-nm illumination (2.4 kW/cm^2) with the model of Figure 9.4 A, either considering fluorophore rapid tumbling (red curve) or fixed fluorophores (green curve). The bottom panel shows the fitting residuals. Anisotropy generates only a small difference in the fit, that does not account for the deviation from the experimental data.

None of the spurious effects presented here were sufficient to account for the shape of the ensemble-level fluorescence decay curves, which comforted us in thinking that it actually reflected the underlying photophysical behaviour of the FP.

9.4.2 Single-molecule experiments

A similar question could be asked regarding cumulative photoconversion curves obtained from single-molecule experiments. We attributed the observed biphasic behaviour to shelving of green molecules by 561-nm light, but wanted to make sure that it was not in fact due to a spurious effect.

To assess the influence of fluorescent impurities in the PVA samples, we imaged PVA films with and without embedded mEos2 fluorophores. The cumulative photoconversion curves (Figure 9.12) show a very low noise level compared to the number of detected molecules when mEos2 was added to the PVA. We therefore conclude that the shape of the cumulative photoconversion curves was not affected by fluorescent impurities.

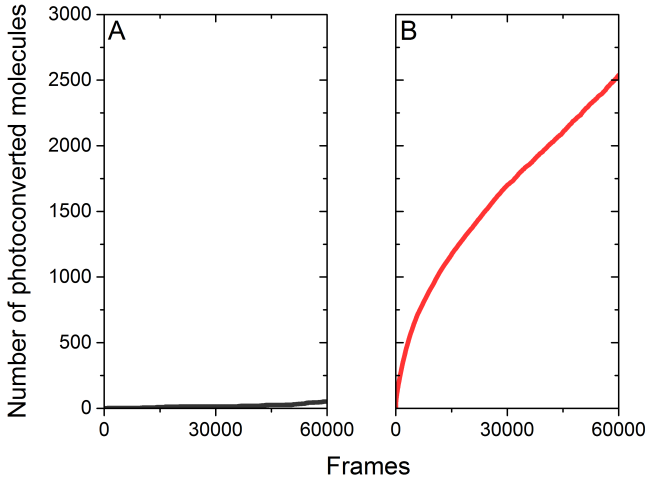

Figure 9.12: Single-molecule datasets were acquired on PVA films containing (B), or not (A), mEos2 fluorophores at nanomolar concentration. The low number of spurious detections in absence of mEos2 proteins suggests that these are unlikely to affect the shape of the cumulative photoconversion curves of Figure 9.8. Curves correspond to single experiments.

The effect of laser beam heterogeneity was also checked, by conducting different analyses on subregions of the field of view where laser intensity was considered homogenous (Figure 9.13 A). All cumulative photoconversion curves obtained showed a pronounced biphasic behaviour, indicating that this shape was not due to heterogeneities in laser intensity (Figure 9.13 B).

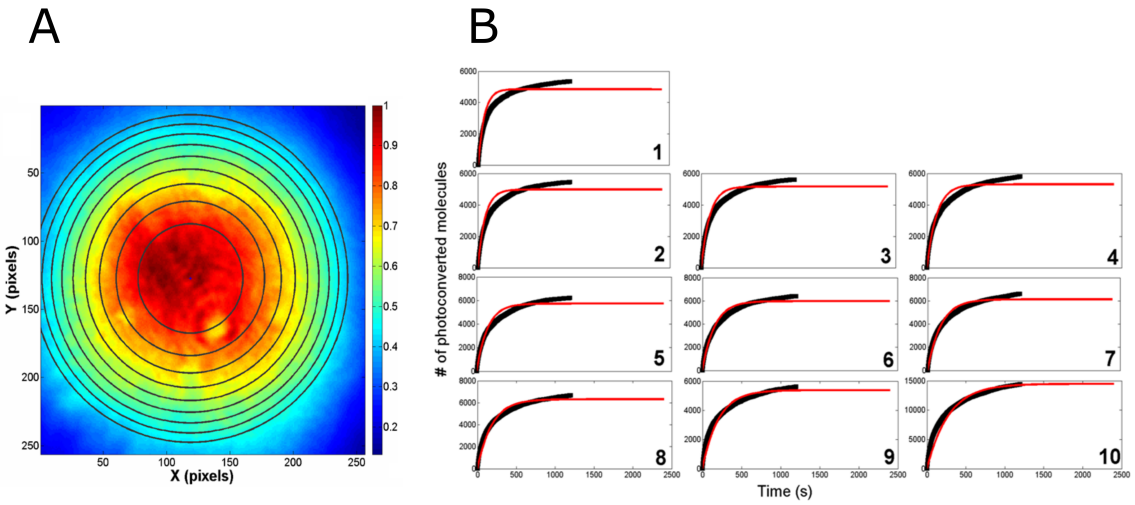

Figure 9.13: (A) Laser beam profile showing the 10 subregions of near-homogenous illumination intensity used for analysis. (B) Cumulative photoconversion curves from each region all display a strong biphasic behaviour, and cannot be fitted with a model that does not account for dark-state formation in the green form of the protein.

These controls point to the absence of spurious effects affecting our single-molecule data.

9.5 Conclusion: taking green state photophysics into account during PALM

In summary, we have shown in this chapter that green mEos2 and mEos4b present a behaviour very similar to that of RSFPs, in that their fluorescence can be switched-off under 488-nm light, and recovered by illumination at 405-nm. Careful analysis of the switching curves suggested the presence of two dark-states with different lifetimes, one of which was stable in the dark, allowing its trapping *in-cristallo* and structure solving. In combination to spectroscopic data, it showed that this dark state was of a similar nature to the off-state of RSFPs, featuring a *trans* isomerised, protonated chromophore.

Surprisingly, green mEos2 off-switching was also achieved by intense 561-nm light, with the direct consequence of delaying photoconversion in PALM experiments. Furthermore, 561-nm light also induced photobleaching of green mEos2, reducing the apparent photoconversion efficiency.

It therefore appears that PALM experiments where labelling density is a crucial parameter (e.g. qPALM) should use as low 561-nm light intensity as possible, to limit green state photobleaching and shelving in dark-states. 405-nm light can be used to limit shelving, and to speed up photoconversion, thus limiting green state photobleaching.

A few questions remain however concerning the short-lived dark-state hypothesised from the fitting

of fluorescence decay curves (see section 9.2.3). Even though a similar dark-state has been reported in the red state of mEos2,[74] its thermal recovery is much faster ($\sim$16 s^{-1}, against the 0.04 s^{-1} fitted here for the green state under 561-nm illumination). Furthermore, inconsistent values were found for its thermal recovery under 488- and 561-nm illumination (0.04 s^{-1} under 561-nm illumination and 0.2 s^{-1} under 488-nm illumination). Taken together, these results question the nature or the existence of this putative dark-state, as will be further discussed in chapter 13. Of note, the presence of a non-absorbing dark-state recovering at a rate of 16 s^{-1} (by analogy to the red state) cannot be excluded, since such a rapidly equilibrating state cannot be detected at the timescale used here for off-switching.

The next chapter will deal with photophysics of the red state of mEos4b, which is crucial for the proper interpretation of PALM experiments, notably sptPALM and qPALM.

Chapter 10

mEos4b blinking characterisation

10.1 Introduction

FP blinking (described in section 3.3) is commonly seen in PALM as the reversible loss of fluorescence of a single-molecule. These interruptions in fluorescence emission are a cause of artefacts in PALM images (see section 4.4.3), and for advanced PALM techniques such as sptPALM and qPALM (sections 5.1.3 and 5.2.2).

Blinking of Eos proteins has been characterised at the single-molecule level (mostly in mEos2) in several studies,[72,73] including in the lab.[74] They have reported two main blinking processes: one with short lifetime, probably a non-absorbing radical state, returning thermally to the fluorescent state in ∼50 ms; and one with longer lifetime (seconds), recovering through a light-induced process which was accelerated by illumination at 405-nm.[73,74] The resulting two-dark-states scheme is shown on Figure 10.1.

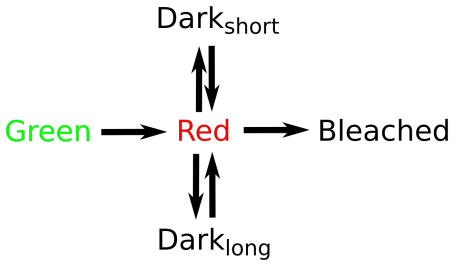

Figure 10.1: Photophysical scheme for red mEos2, as reported in refs.[72–74] Dark-states of the green state have been omitted for clarity.

Whereas short-lived fluorescence emissions are well handled by current SMLM processing software, longer interruptions are difficult to correct for, and therefore most detrimental to the quality of PALM datasets. In this context, understanding better the blinking behaviour of PCFPs is important, to design strategies to suppress it or account for it in data analysis. Notably, the precise nature of the long-lived dark-state was still unknown at the beginning of this work. Since it had

been reported to be sensitive to 405-nm light, the lab made the hypothesis that long-lived blinking was a light-induced process, and that the non-emissive state could be trapped in a crystal to solve its structure. We therefore engaged in a collaboration with researchers from KU Leuven (Elke De Zitter and Peter Dedecker), aiming at solving the crystal structure of the dark-state responsible for long-lived blinking in mEos4b.

Trapping a dark-state *in-cristallo* requires to be able to populate it at the ensemble level (since X-ray crystallography provides an average electron density for the molecules in the crystal). To show that this was possible, we conducted a photophysical study on red mEos4b, summarised in Figure 10.2. We investigated the dependence of ensemble-level photoswitching and single-molecule blinking lifetimes on the intensity of 561-nm light, to confirm that both phenomena stem from the same molecular process, and that recovery to the fluorescent state was light-driven.[i] Finally, assessing the thermal stability of the dark state and the possibility for the proteins to photoswitch within a crystal opened the door to freeze-trapping of the dark-state *in-cristallo*, and solving its structure by X-ray crystallography, which was achieved by Elke De Zitter.

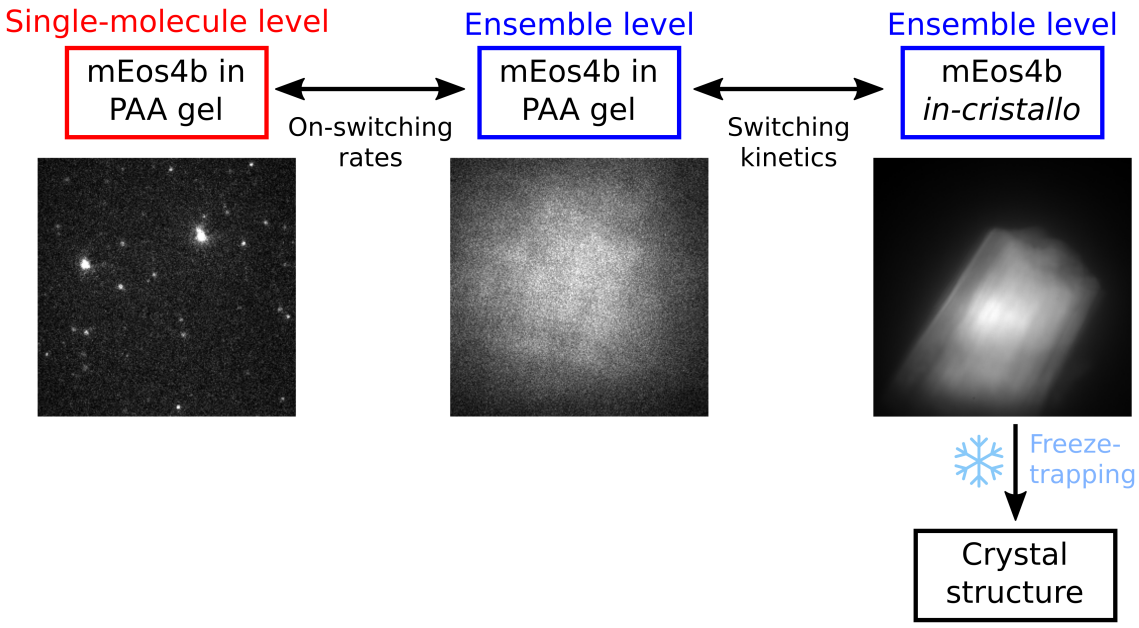

Figure 10.2: Strategy for solving the structure of the blinked state in red mEos4b.

[i] As in the previous chapter, rates of light-induced processes are expected to evolve linearly with laser intensity, while those of thermal processes stay constant.

10.2 Blinking and photoswitching arise from the same molecular process

As stated above, our working hypothesis for this work, based on previous knowledge in the lab, was that single-molecule blinking and ensemble-level photoswitching were two manifestations of a single phenomenon. This remained however to be proven, and so we set out to investigate (i) the light-dependence of recovery from the blinked and switched states to the fluorescent state, and (ii) the associated recovery rates. Matching results between single-molecule and ensemble-level experiments for these two points would validate this hypothesis, and light-dependence of recovery to the fluorescent state would enable us to later trap the dark-state *in-cristallo* (since it would stay populated after illumination).

10.2.1 Light-sensitivity of the long-lived dark-state from ensemble photoswitching experiments

To characterise photoswitching at the ensemble level, we performed experiments on PAA-embedded mEos4b at micromolar concentration. A pool of mEos4b molecules was photoconverted under 405-nm light, and fluorescence decay curves were recorded under varying 561-nm laser intensities (2 to 6000 W/cm^2). The curves were fitted using a kinetic model including two dark-states, a short-lived one (with fixed thermal recovery rate at 16 s^{-1}, in accordance with refs[73,74] and single-molecule data shown below) and a long-lived one. Off-switching rates to both dark states and on-switching rate from the long-lived dark-state were free parameters in the fits, whereas the photobleaching rate was manually adjusted to match the fluorescence recovery level observed unpon 405-nm illumination.

The power titration showed an expected linear dependence between the long-lived dark state on-switching rate and low 561-nm laser intensities (Figure 10.3, A). At higher intensities however (>1 kW/cm^2), a saturation behaviour was observed, up to a maximum recovery rate of $\sim$0.7 s^{-1} (Figure 10.3, B). Possible reasons for this unexpected behaviour will be discussed in section 10.4. Despite this, recovery from the long-lived dark-state appeared to be light-driven.

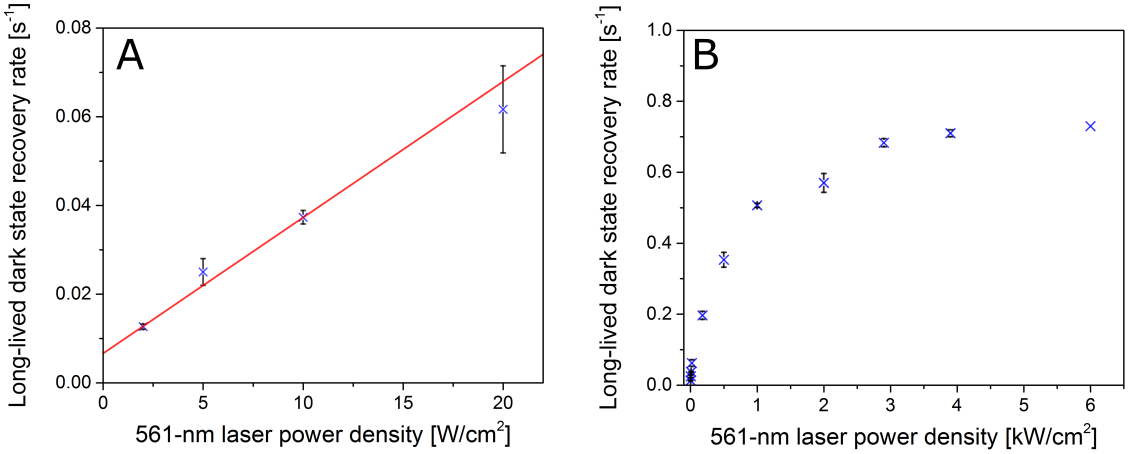

Figure 10.3: (A) At low 561-nm laser intensities (2 to 20 W/cm^2), the recovery rate from the long-lived dark-state follows a linear dependence to the 561-nm laser intensity (red line: linear fit, R^2=0.99). (B) At higher laser intensities (>1 kW/cm^2), a saturation behaviour is observed, with a maximum rate of $\sim$0.7 s^{-1}. Points are mean $\pm$ SD (n=3 different FP preparations).

10.2.2 Characterisation of long-lived blinking at the single-molecule level

In order to compare the dark-states giving rise to blinking at the single-molecule level and photoswitching at the ensemble level, we needed to retrieve single-molecule blinking-on rates, to compare them with the switching rates obtained at the ensemble-level. We performed single-molecule experiments on purified proteins embedded in PAA, under sole 561-nm illumination, at laser intensities ranging from 0.2 to 5.7 kW/cm^2.[ii] Molecules were photoconverted only through readout photoconversion, to avoid using 405-nm light that would modify the blinked-state recovery rate. Experiments were processed as described in materials and methods to retrieve fluorescence traces and off-times histograms (i.e. the time between the last appearance of a fluorophore and its reactivation). As reported in previous studies,[73,74,121] off-times histograms can be fitted to retrieve blinking-on rates. Typically, due to the presence of two dark-states with different lifetimes, off-times histograms had been reported to be biphasic, and thus fitted with a biexponential model. The coefficients of the two exponentials would yield the rates of recovery from the dark states to the fluorescent state (see section 8.2.2 for details).

However, a bi-exponential fitting of the histograms obtained from our single-molecule data did not account well for off-times longer than 1 second (Figure 10.4, A), which was particularly visible when plotting the histogram on a log scale. A tri-exponential function on the other hand allowed accurate fitting of the whole histograms (Figure 10.4, B).

[ii] Laser intensities could not be decreased as much as in ensemble-level experiments in order to enable single-molecule detection.

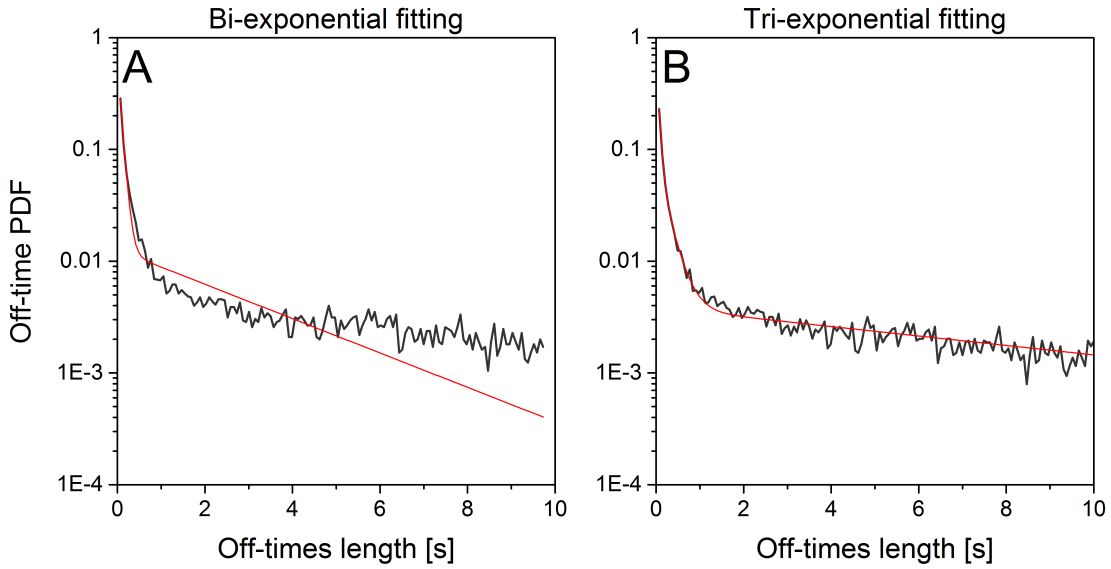

Figure 10.4: (A) The off-times histogram of red mEos4b under sole 561-nm light (0.5 kW/cm^2) displays more complex behaviour than a biphasic decay, and is therefore poorly fitted with a bi-exponential function. (B) Using a tri-exponential function allows to provide an accurate fit of the histogram. PDF: probability density function. Data are representative of >5 experiments on different FP preparations.

From the tri-exponential fits, the fastest rate (Figure 10.5 A) was not affected by laser intensity, and matched with the non-absorbing short-lived dark-state previously reported in mEos2. The other two fitted rates however (Figure 10.5 B, C) showed erratic behaviour upon increasing 561-nm laser intensity. This points to interconnections between dark-states, making the retrieval of rate constants non-trivial since the fitted rates must correspond to a combination of several transitions between states.

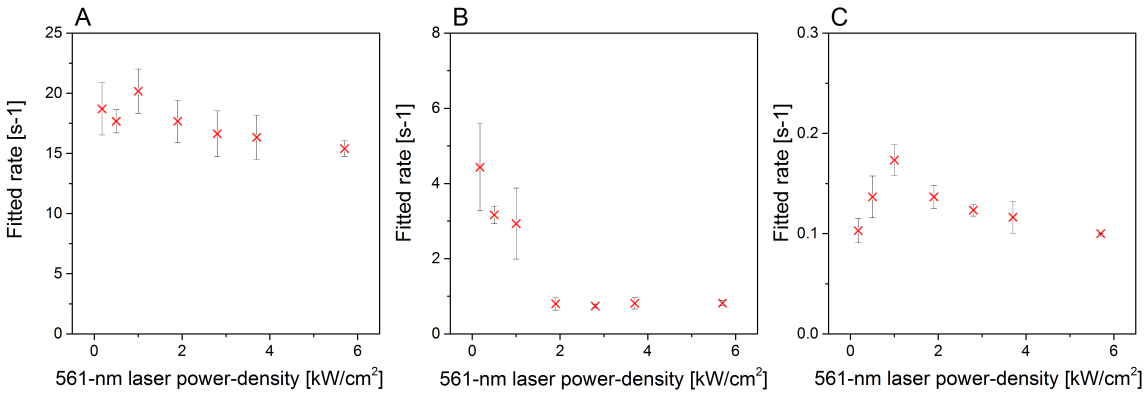

Figure 10.5: Rate constants retrieved from tri-exponential fitting of red mEos4b off-times histograms. Whereas the rate in panel A could be associated with recovery from the short-lived dark-state (reported to occur at 16 s^{-1} in mEos2), rates from panels B and C could not be simply associated with recovery from the long-lived dark-state.

The triphasic behaviour of the off-times histograms shown here had not been reported in previous studies of similar proteins, possibly because long-lived dark-states are relatively rare events, which therefore require important statistical sampling to be detected. Possible causes for this observed triphasic behaviour are discussed below, in section 10.4 and chapter 13.

Since the blinking rates were not easily obtainable, we could not yet confirm that blinking-on was a light-induced process. The fact that the rates fitted from the tri-exponential model showed an evolution with laser intensity (Figure 10.5), even though difficult to decipher, hints to a light-sensitivity of at least one of the involved states. This was confirmed by comparing ensemble-level and single-molecule experiments, as will be presented in the next section.

10.2.3 Comparison of dark-state recovery rates from ensemble-level and single-molecule experiments

Since the blinking-on rate from the long-lived dark-state was not easily obtainable from single-molecule data, and in order to make our comparison with ensemble-level data possible, we resorted to a different strategy, detailed in section 8.2.2. In brief, fluorescence decay curves were reconstituted from single-molecule data by counting for each timepoint how many fluorophores were in the on-state. The decay curves obtained were fitted with the same kinetic model as used for ensemble-level data processing, and on-switching rates plotted against 561-nm laser intensity (Figure 10.6). It is important to note that if the true photophysics of red mEos4b is indeed more complex than a two-dark-states model (as suggested by the triphasic off-times histograms and the saturation behaviour of ensemble-level on-switching rates), then the rates fitted from such a model must be incorrect. We however postulate that treating single-molecule experiments like ensemble-level data allows for a reliable comparison because (i) fluorescence off-switching curves are well-fitted by our two-dark-states model and (ii) rates obtained from the same physical process, using the same analysis method (albeit on different types of raw data) are still expected to match. A more in-depth discussion on why

ensemble-level curves can still be fitted by a simple two-dark-states model is proposed in chapter 13.

The rates obtained from single-molecule experiments for on-switching from the long-lived dark-state were very similar to those obtained from ensemble fluorescence data. Furthermore, they showed the same saturation behaviour at high 561-nm laser intensities, pointing that the underlying effect could be detected from both types of data.

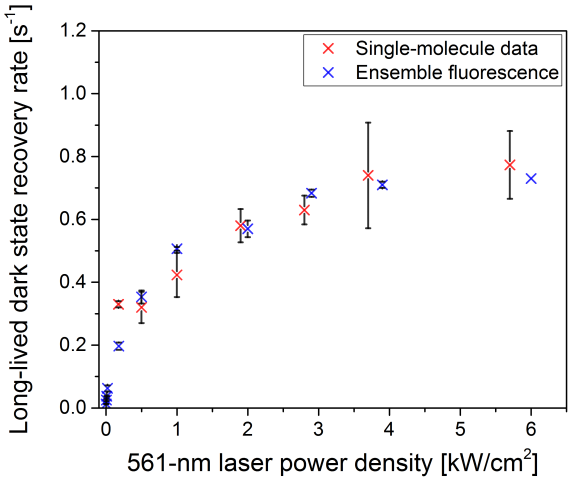

Figure 10.6: Comparison of on-switching rates from the long-lived dark-state from ensemble-level and single-molecule experiments. Both types of experiments yield very similar rates, showing the same saturation behaviour towards higher 561-nm laser intensity values. Points are mean ± SD (n=3 different FP preparations).

In conclusion, we have shown that the long-lived dark-state reached by red mEos4b during ensemble-level photoswitching experiments was likely to be the same as the one causing long-lived blinking in PALM. Furthermore, its rate of recovery to the fluorescent state depended on 561-nm illumination intensity, showing that the process was light induced.

10.3 Solving the structure of the long-lived blinked state

Freeze-trapping the long-lived dark-state *in-cristallo* required its thermal recovery to be slow enough, so that it would stay populated between the end of illumination and plunging in liquid nitrogen (i.e. a few seconds). Once flash-frozen, it was assumed that the dark-state could be kept in liquid nitrogen (77 K) for as long as needed, since molecular dynamics are essentially stopped below the glass-transition temperature (∼180 K).

Figure 10.7 shows the thermal recovery of red mEos4b from its long-lived dark-state to the fluorescent state.

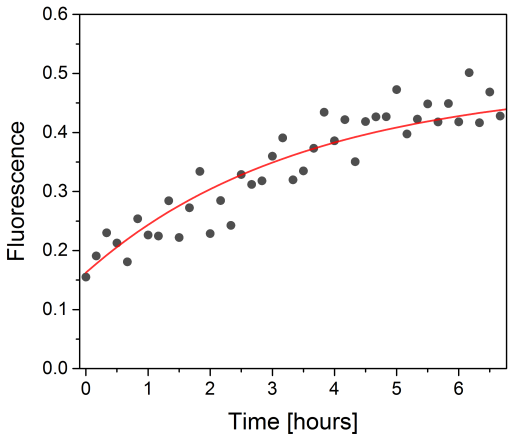

Figure 10.7: Thermal recovery of red mEos4b from the long-lived dark-state to the fluorescent state. After off-switching by 561-nm light (2 kW/cm^2) for 170 seconds, the protein was left in the dark for 6 hours, and fluorescence monitored by short pulses of 561-nm light (1 W/cm^2) every 10 min to avoid influencing fluorescence recovery. Fitting with a monoexponential model (red line) yielded a recovery half-time of ∼2 hours. Curve corresponding to a single experiment.

The fitted recovery half-time of 2 hours confirms that it is possible to trap the dark-state by flash-freezing, since this process only requires a few seconds.

Finally, to check that photoswitching was not prevented by the crystal packing, we performed photoswitching experiments on crystalline red mEos4b, and compared them to experiments performed on purified protein embedded in PAA (Figure 10.8). Both experiments were conducted on the same microscope, under similar illumination conditions, although the illumination intensities were changed to account for the high OD produced by FPs in the crystalline state.

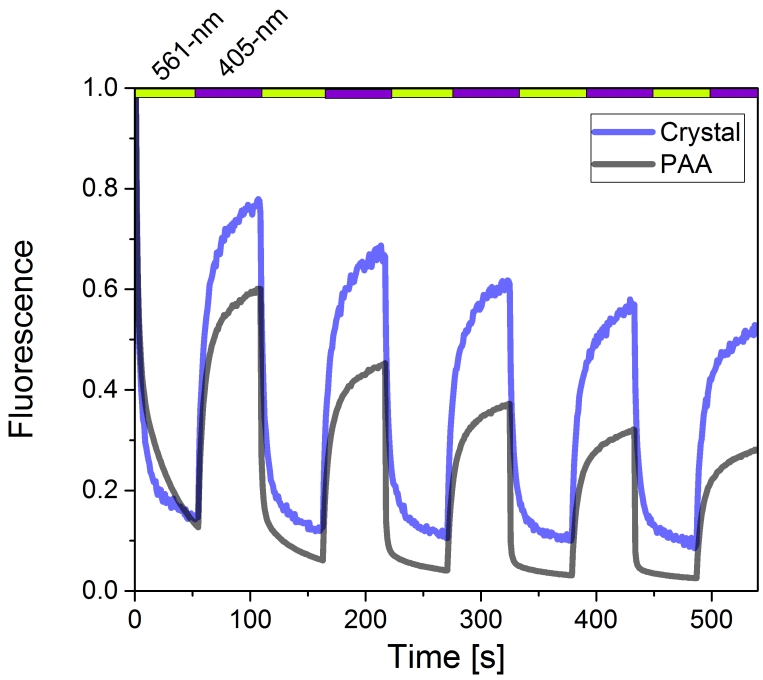

Figure 10.8: Reversible photoswitching of red mEos4b embedded in PAA (black curve) or *in-cristallo* (blue curve) under alternating 561- and 405-nm light (green and violet bar shown on top, respectively 70 and 0.3 W/cm^2 for *in-cristallo* data, and 25 and 1 W/cm^2 for PAA data). Data are representative of >3 crystals and PAA samples.

The switching behaviours are very similar between the two experimental conditions, confirming that the dark-state populated *in-vitro* can also be accessed *in-cristallo*. The precise switching kinetics are however slightly modified, which can be attributed to different factors:

- The density of proteins in a crystal is much higher than in a gel, giving rise to inner filtering effects. The high optical density creates heterogeneities, since proteins at the top of the crystal receive more photons than those at the bottom, which are shielded by the top layers. This will result in an slower apparent switching speed, since each new layer of switched proteins will uncover another non-switched layer.
- Another effect of crystal packing is that the chromophore dipoles are not randomly oriented, but have defined orientations. This can also create heterogeneities, with populations of favorably oriented chromophores efficiently absorbing light, and populations of unfavorably oriented chromophores showing reduced absorption. This effect, although not major here due to the number of orientations within space group $P2_12_12_1$, could produce small differences in switching kinetics.

Using this technique, Elke De Zitter was able to solve the structure of the dark-state (Figure 10.9), which revealed a very dynamical chromophore in a "frustrated" *trans* conformation. Furthermore, recording of absorbance spectra on the crystals during off-switching indicated that this off-state

possessed a protonated chromophore, similarly to what had been observed on the green form of the protein, and again reminiscent of photoswitching in RSFPs. The spectroscopic signature of the dark-state also brought interesting insights to limit blinking during PALM experiments, which will be discussed in the next chapter.

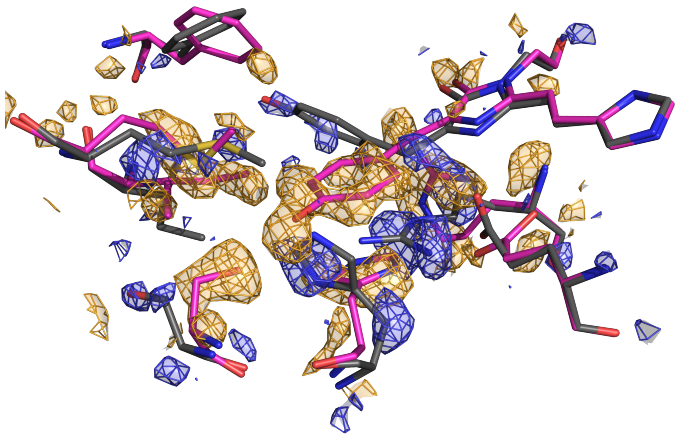

Figure 10.9: Crystal structures of the red fluorescent (magenta model and yellow electron density) and dark (grey model and blue electron density) states of mEos4b, solved by Elke De Zitter. The structure of the dark state features a *trans* isomerised chromophore. The poorly defined electron density around the Tyrosine of the dark-state chromophore is due to its high flexibility. Difference electron density maps contoured at 3 r.m.s.d.

10.4 Deviation of the photophysical behaviour from a two-dark-states model

On several occasions during this study of red mEos4b photophysics, deviations from the expected photophysical behaviour shown on Figure 10.1 have been observed, which might challenge our view of the light-induced reactions undergone by the protein.

Both ensemble-level and single-molecule experiments have shown a saturation behaviour of the long-lived dark-state recovery rate at high 561-nm laser intensity (Figure 10.6), in contradiction with the linear relationship expected from a direct dark-to-fluorescent conversion. Furthermore, a careful analysis of the single-molecule off-times histograms revealed a triphasic behaviour (Figure

10.4), again incoherent with the expected biphasic behaviour expected from two dark-states with differing recovery rates, and with the fitting of ensemble-level data using a two-dark-states model.

Such unexpected behaviours can either arise from spurious effects causing heterogeneities in the measurements, or reflect a genuine property of the FP, such as the presence of an additional, uncharacterised dark-state. This section will give an overview of the possible causes for the observed deviations from our original model.

10.4.1 Spurious effects

One of the main potential causes for heterogeneities in the observed behaviour is the gaussian profile of the laser beam used to illuminate the sample. To probe if this had an influence on the triphasic shape of the off-times histograms, we conducted an analysis of single-molecule data on a small region of the field of view (Figure 10.10 A) where laser power was considered homogenous. The resulting off-times histogram (Figure 10.10 B), despite increased noise due to reduced sampling, showed identical triphasic behaviour to the one obtained from the whole field of view. Conversely, an off-times histogram built from simulated data using a gaussian beam profile and a two-dark-states photophysical model could be well fitted using a bi-exponential function (Figure 10.10 C). Taken together, these results rule out illumination heterogeneity as the cause of the triphasic off-times histograms.

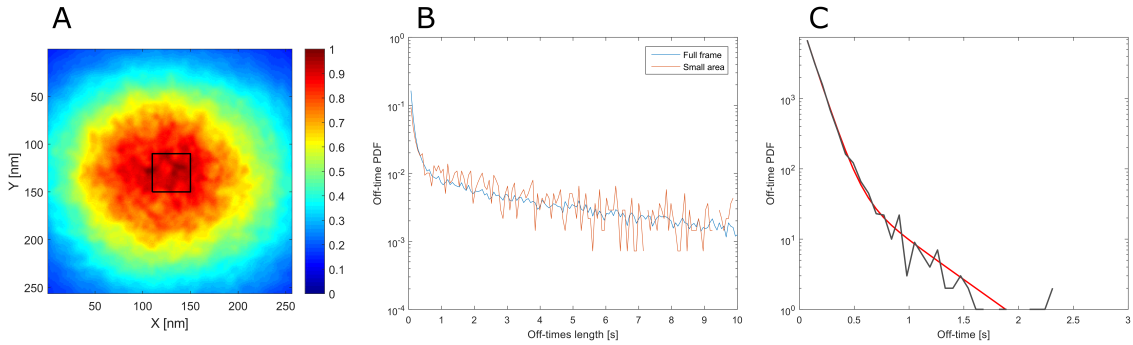

Figure 10.10: Influence of the gaussian laser beam profile on off-times histograms. (A) The intensity profile of the 561-nm laser used for fluorescence readout is gaussian over the field of view. (B) Off-times histograms of molecules from the whole field of view (blue line) or from the black square of panel A (orange line) show extremely similar behaviour. (C) A simulated off-times histogram using a gaussian beam profile and a two-dark-states photophysical model (black line) can be well fitted with a biexponential function (red line).

Despite considering other possible spurious effects such as limited accuracy of single-molecule detection and localisation, and after performing ensemble-level and single-molecule simulations, we could find none able to account for the observed behaviour. We therefore concluded that the photophysical behaviour of red mEos4b is indeed more complicated than we first envisioned.

10.4.2 Alternative photophysical models

Under the hypothesis that our experimental data are not biased by spurious effects, we must consider that they originate from more complex photophysics than was initially thought. Both the triphasic off-times histogram and the on-switching rate saturation suggest that a fraction of non-fluorescent fluorophores recovers to the fluorescent state slower than the light-induced recovery from the long-lived dark-state under 561-nm power-densities higher than 1 kW/cm^2.

This led us to introduce one more dark-state in our model (Figure 10.11). The nature of this putative dark-state is not known, nor are its exact transitions to and from the other states of the protein.

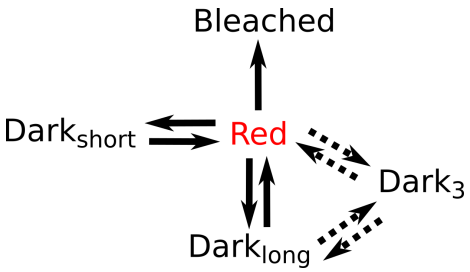

Figure 10.11: Kinetic model including an additional dark state Dark$_3$, which could be at the origin of the saturation behaviour of the on-switching rate, and the triphasic off-times histograms observed in single-molecule experiments.

A more in-depth discussion of the nature of this extra dark-state, and its relation to other states of the protein, will be given in chapter 13.

10.5 Conclusion

The main aim of this part of the thesis was to demonstrate that the non-emissive state of mEos4b responsible for blinking was the same as the one populated during photoswitching at the ensemble level, and could therefore be trapped *in-cristallo*. This study illustrates well the complexity of correlating informations obtained at the ensemble and single-molecule levels, due to the intrinsically different nature of the data collected.

In an unexpected manner, these experiments also brought new insights into the photophysics of red mEos4b, suggesting transitions of the protein to multiple dark-states, slowing down the recovery of the protein to the fluorescent state. These results would need to be reproduced, if possible on different microscopes to eliminate the possible bias linked to the setup and confirm the deviations from a two-dark-states model. If the existence of an additional dark-state is confirmed, further experiments should be conducted to assess its nature, and sensitivity to experimental conditions (laser illumination, pH, oxygen...).

Aside from the fundamental knowledge gained on PCFPs, such photophysical studies could provide substantial improvements to PALM experiments by allowing to adapt the experimental conditions

to minimise the influence of detrimental FP photophysics. The next chapter proposes to make use of the spectroscopic knowledge gained during this mechanistical study of mEos4b to reduce blinking-induced artefacts in PALM.

Chapter 11

Suppression of mEos4b long-lived blinking

11.1 Introduction

Blinking is detrimental to PALM experiments (as mentioned in section 4.4.3), and more particularly to sptPALM and qPALM (see sections 5.1.3 and 5.2.2). In sptPALM, fluorescence intermittences interrupt the tracking of fluorophores, hence effectively limiting the maximum amount of time a protein can be tracked for. In qPALM, long-lived blinking is an important source of counting error when attempting to determine the stoichiometry of protein complexes, since fluorescence reactivations are difficult to distinguish from new photoconversion events.

Among the different blinking processes that have been characterised so far, those leading to long-lived fluorescence intermittences hinder the most PALM experiments. One such process has been characterised in the previous chapter, and shown to result from combined *cis-trans* isomerisation and protonation of the chromophore.

In this chapter it will be shown how the spectroscopic characterisation of this long-lived dark-state led to the design of a simple strategy to reduce the duration of fluorescence intermittences in FPs of the Eos family. The simple addition of weak blue light (available on most PALM setups) allows to drastically reduce the occurrence of long intermittences (several seconds) during PALM acquisitions. Finally, we will show that this strategy does not deteriorate other imaging parameters (such as the signal-over-noise ratio), and conclude by an overview of how it enables improved sptPALM experiments.

11.2 Spectroscopic characterisation

As part of the characterisation of the long-lived dark-state presented in the previous chapter, a pool of mEos4b proteins was photoconverted to the red state, embedded in PVA, and absorbance and fluorescence spectra recorded under 561-nm illumination (Figure 11.1).

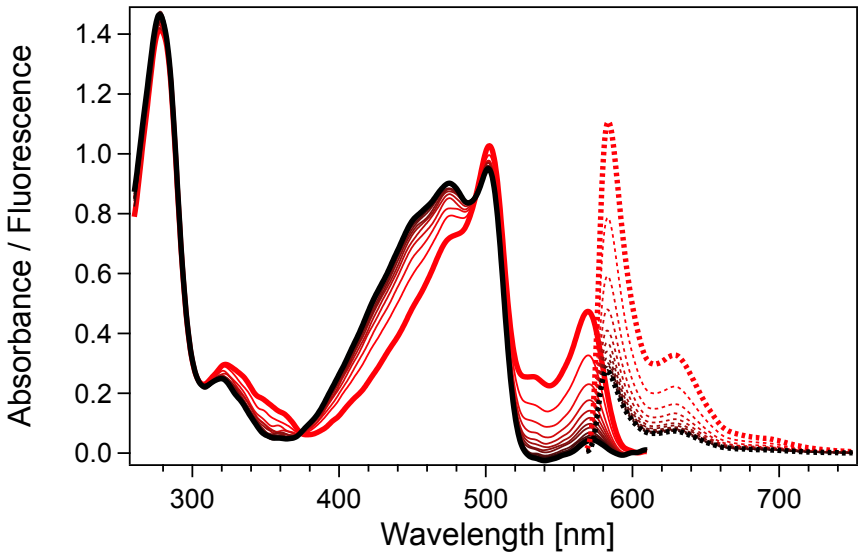

Figure 11.1: Evolution (red to black) of absorption (solid lines) and fluorescence emission (dashed lines) spectra of PVA-embedded mEos4b during 561-nm illumination. Upon illumination at 561 nm, the absorbance peak of the anionic red chromophore (570 nm) decreases, while a new absorbance peak appears at ∼475nm, corresponding to a long-lived dark state. Residual absorbance at 570 nm and fluorescence in the black spectrum arise from incomplete switching to the dark state.

The evolution of absorbance during 561-nm illumination shows depopulation of the 570 nm peak (corresponding to the anionic chromophore), and concomitant apparition of a peak at 475 nm. This blue shift hints at a protonated chromophore, and suggests that illumination at this wavelength might speed up recovery of the protein to the fluorescent state.

To test this hypothesis, ensemble-level fluorescence data were collected on mEos4b embedded in PAA. A pool of protein was photoconverted to the red state under 405-nm illumination, subsequently illuminated with 561-nm light (inducing fluorescence off-switching), and finally with 488-nm light, in the absorbance peak of the dark species (Figure 11.2).

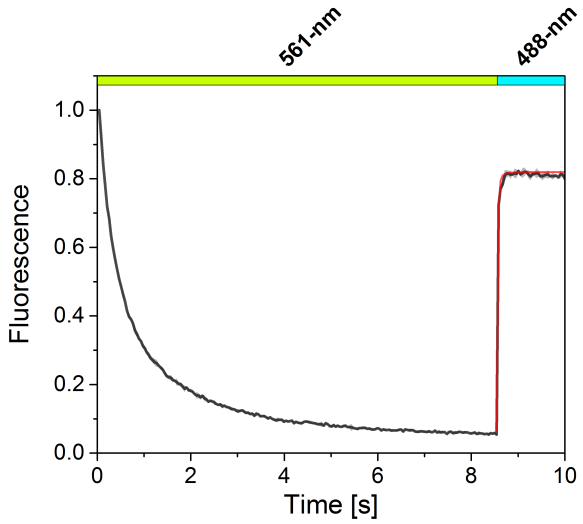

Figure 11.2: Ensemble photoswitching of red mEos4b under 561- and 488-nm light (80 and 5 W/cm^2, respectively). On illumination at 488nm, fluorescence recovery occurs in a few tens of milliseconds. The recovery could be fitted with a monoexponential model (red line), yielding a recovery rate of 45 s^{-1}. Curve shown as mean ± SD (n=3 different FP preparations).

As anticipated, 488-nm illumination produced rapid recovery of the off-switched proteins to the fluorescent state. This confirmation prompted us to add weak 488-nm illumination during PALM experiments, and to quantify the duration of off-times of single-molecules, which will be described in the next section.

11.3 Effect of 488-nm light on blinking during PALM

In order to test the effect of cyan light on the fluorescence off-times of mEos4b, weak 488-nm illumination was added to the PALM illumination scheme, either continuously, or in an interleaved manner (Figure 11.3 A, top and bottom panels, respectively). A drawback of using continuous 488-nm illumination can be an increased background due to excitation of green mEos4b.[i] The pulsed illumination scheme allowed avoiding this issue by temporally separating fluorescence readout and 488-nm illumination, as is commonly done with 405-nm illumination for similar reasons. Note that since the duration of the 488-nm laser pulses was shorter in this case (10% duty-cycle), the illumination intensity was raised accordingly, to reach the same dose as with the continuous scheme.

Sparse mEos4b embedded in PAA was illuminated in pulsed mode, and the fluorescence trace of each molecule reconstituted from the single-molecule data. The resulting off-times histograms (Figure 11.3 B) show a drastic reduction in intermittencies longer than 3 seconds, with for example a factor ∼10 between the number of intermittences lasting 10 seconds with and without 488-nm illumination. More generally, the fraction of intermittencies longer than 4 frames (which are typically difficult to correct for) is decreased from 75% to 40% using 488-nm light (120 W/cm^2, 10% duty-cycle).

[i] Although fluorescence emission of green mEos4b peaks at 517 nm, the emission spectrum extends to ∼600 nm.

Unfortunately, the fraction of long-offtimes did not decrease linearly with 488-nm laser intensity (Figure 11.3, inset), and a similar levels of off-times longer than 10 seconds was observed under all tested 488-nm intensities. This might be related to the complex photophysical scheme mentioned in chapter 10. If a third dark-state can indeed be accessed through the long-lived dark-state, it might prevent part of the molecules from recovering to the fluorescent state under 488-nm light.

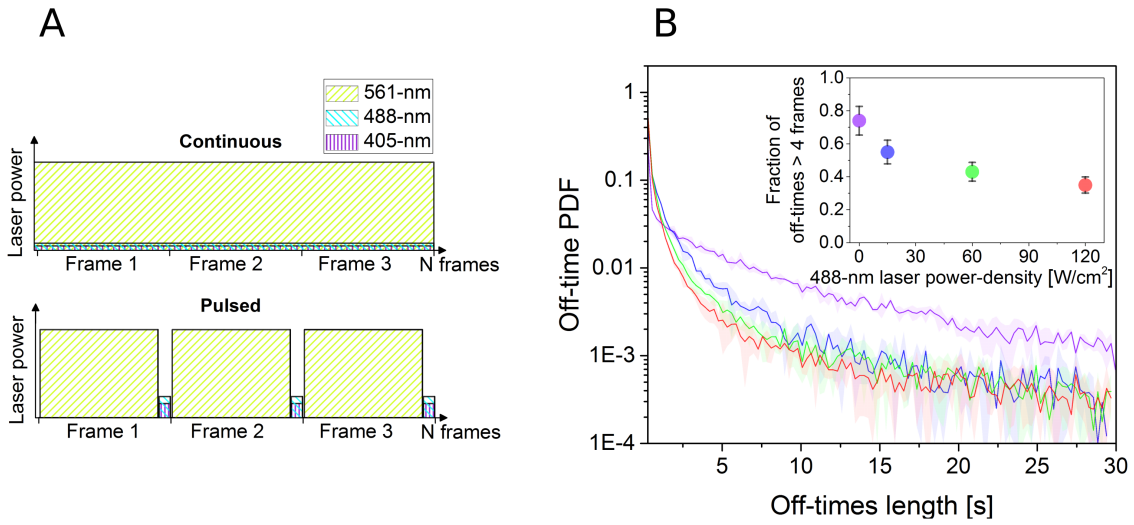

Figure 11.3: (A) Possible laser schemes for addition of 488-nm light during PALM experiments. (B) Off-times histograms of red mEos4b embedded in PAA, under sole 561-nm light (0.5 kW/cm^2, violet curve) or combined 561- and 488-nm light (15, 60, 120 W/cm^2, 10% duty-cycle, blue, green and red curves). The total fraction of off-times longer than 4 frames is largely decreased in the presence of 488-nm light (inset). Curves shown as mean ± SD (n=3 different FP preparations). PDF: probability density function.

Since the number of intermittencies longer than a few frames is significantly decreased in the presence of 488-nm light, the length of on-times (corrected for off-times shorter than 4 frames) is expected to increase accordingly. This was indeed the case, and increasing intensities of 488-nm illumination yielded higher fractions of long on-times (Figure 11.4 A). For example, the fraction of on-times longer than 2 seconds was increased by a factor 10 by 488-nm illumination (120 W/cm^2, 10% duty-cycle).

We compared this increase to the recently published photoactivatable Janelia Farm dye PA-JF549,[97] considered as one of the best options currently available for prolonged single-particle tracking. Even-though the length of the tracks obtained with this dye was still above what we could achieve with mEos4b, 488-nm illumination allowed bringing the track length of mEos4b to a close level, while retaining the advantages of FP labelling[ii]. It should be noted that for the sake of the comparison, experimental parameters were kept the same for experiments with JF dyes and FPs. However, the

[ii]Notably the high specificity of FPs, whereas dyes are expected to give rise to more unspecific binding and hence background fluorescence.

higher brightness of the dyes would probably allow decreasing the intensity of the 561-nm read-out laser, thus producing even longer tracks with a signal-over-noise ratio comparable to that of FPs.

Finally, we wondered if the same strategy was applicable to other FPs commonly used in PALM. We acquired single-molecule datasets in the presence and absence of 488-nm illumination and plotted the increase in mean on-time for each of them (Figure 11.4 B). All FPs of the Eos family showed a similar increase in mean on-time (∼2-fold), while the three other FPs tested showed no difference in mean on-time. Even though it seems probable that these FPs possess similar protonated dark-states to the one characterised in mEos4b (and therefore sensitive to 488-nm light), illumination at 488-nm might have other detrimental effects on them (e.g. accelerated photobleaching), preventing a net increase of on-times.

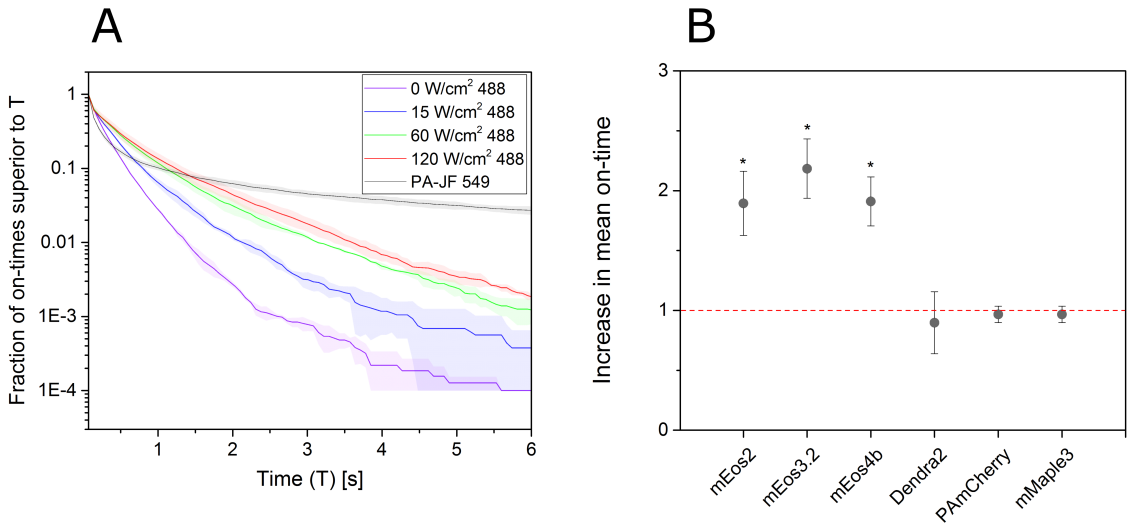

Figure 11.4: (A) Increase in mEos4b single-molecule on-times using 488-nm illumination (pulsed mode, 10% duty-cycle, 15, 60, 120 W/cm^2). The illumination scheme allows reaching similar track lengths to what is achievable using the PA-JF549 organic dye. (B) Increase in mean on-time due to 488-nm illumination on different popular PALM markers. Only FPs of the Eos family show an increase in on-times. Curves shown as mean ± SD (n=3 different FP preparations).

One of the side-effects of using 488-nm light during PALM experiments was a slight increase of the photoconversion rate of the FPs (Figure 11.5), resulting in ∼twice more photoconverted molecules than under sole 561-nm light, in the absence of 405-nm illumination.

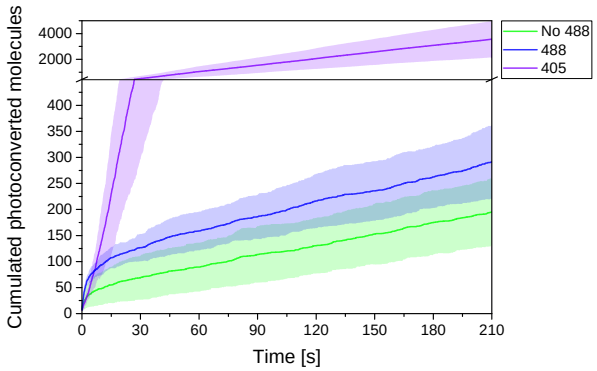

Figure 11.5: Using 488-nm light (120 W/cm^2, pulsed mode, 10% duty-cycle), the number of photoconverted molecules is slightly increased compared to sole 561-nm illumination (0.5 kW/cm^2). This increase is however still well below the one produced by 405-nm illumination (0.6 W/cm^2, pulsed mode, 10% duty-cycle), as typically used in PALM (note the break in Y-axis at 500). Curves shown as mean ± SD (n=3 different FP preparations).

The fact that illumination at 488-nm produces only little additional photoconversion is an important asset for blinking suppression. Indeed, 405-nm light had already been reported in the past to prompt fluorescence recovery from the long-lived dark-state, but its use often resulted in too dense activation of the molecules. The strategy proposed here allows decoupling blinking-suppression and photoconversion, hence effectively shortening off-times while keeping a molecule density compatible with single-molecule localisation.

Since 405- and 488-nm light both induce recovery from the long-lived dark-state, it can be reasonably expected that illumination at any wavelength in the absorption peak of the dark-state will have a similar effect. To probe this, fluorescence recovery from the long-lived dark-state was performed as in Figure 11.2, using either 405-, 473- or 488-nm light at equal power-density, and fitted using a monoexponential model from which the rate constants were extracted (Figure 11.6).

As expected, the different wavelengths all induced fluorescence recovery, and the rates scaled with the absorption of the dark-state at the corresponding wavelengths.

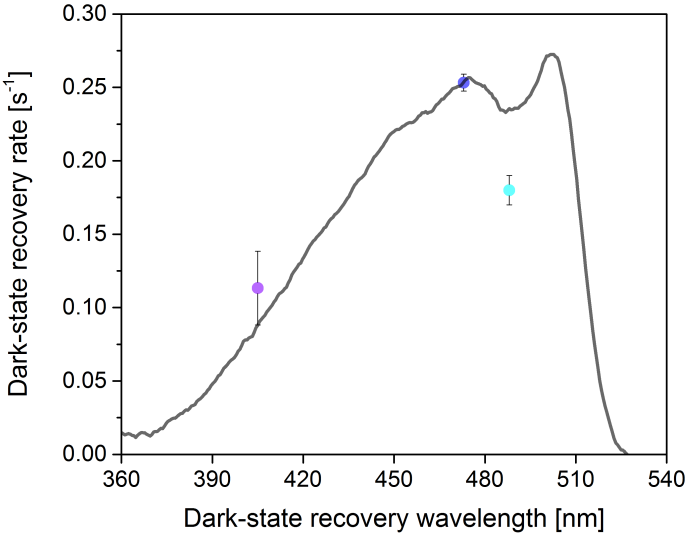

Figure 11.6: Recovery rates from the long-lived dark-state of red mEos4b upon illumination at different wavelengths, overlaid with the absorption spectrum of the dark-state (black spectrum of Figure 11.1). This spectrum corresponds to a mix of different states, mainly green anionic (peaking at 505 nm) and long-lived dark-state (peaking at around 470 nm). Therefore, the measured recovery rate at 488 nm matches well with the absorption of the long-lived dark-state, taking into account the contribution of the green anionic form to the absorbance spectrum at this wavelength. Points are mean ± SD (n=3 different FP preparations).

A 473-nm laser (sometimes found on PALM setup instead of the 488-nm laser) can therefore be used for blinking suppression. However, even though recovery is slightly faster at 473-nm than at 488-nm, the blue shift in wavelength is expected to cause more photoconversion, hence reducing the decoupling between the two processes.

11.4 Controls

After assessing the feasibility of our blinking suppression strategy by 488-nm light, we needed to make sure that it did not degrade other important metrics for the quality of PALM images, due to the following factors:

- Photobleaching of the red molecules could result in reduced brightness per localisation (and hence reduced localisation precision), and/or reduced photon budget per molecule.
- Photobleaching of green molecules would reduce the labelling efficiency.
- Creation of background signal by 488-nm light could reduce localisation precision.

First, we checked the effect of different 488-nm illumination intensities on localisation brightness and uncertainty. Both have been found to be unaffected by illumination at 488-nm (Figure 11.7 A, B). Additionally, localisation uncertainty was measured using different exposure times, in the presence and absence of 488-nm light. Again, no significant effect could be detected (Figure 11.7 C).

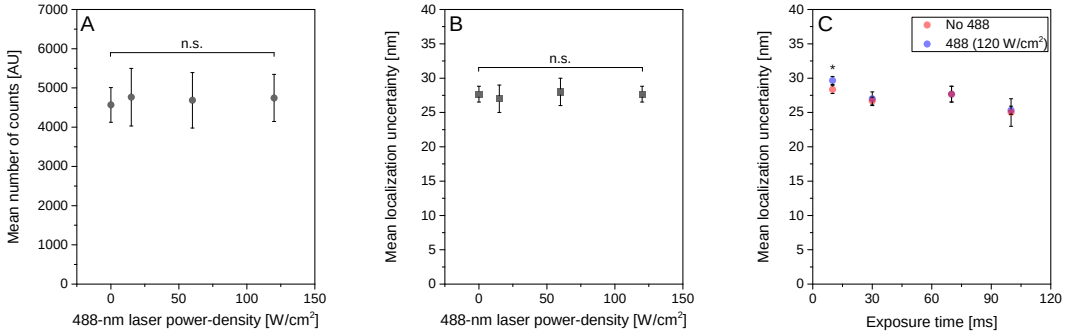

Figure 11.7: (A) Number of counts per localisation and (B) localisation uncertainty as a function of 488-nm laser power-density (0, 15, 60 and 120 W/cm^2, pulsed mode, 10% duty-cycle), at 70 ms exposure time. Illumination at 488 nm did not significantly affect either of these two metrics (n.s.: P$\geq$0.7, one-way ANOVA tests)(C) Localisation uncertainty as a function of exposure time. The addition of 488-nm illumination does not decrease the localisation uncertainty, except possibly at 10 ms exposure time (* P$<$0.05, one-way ANOVA tests) with however a difference of only 1 nm between the two illumination conditions. Points are mean $\pm$ SD (n=3 different FP preparations).

Similarly, controls on experiments performed with continuous 488-nm illumination showed no degradation of fluorophore brightness or localisation precision (Figure 11.8). It therefore appears that at these low intensities, 488-nm light does not generate significant background fluorescence.

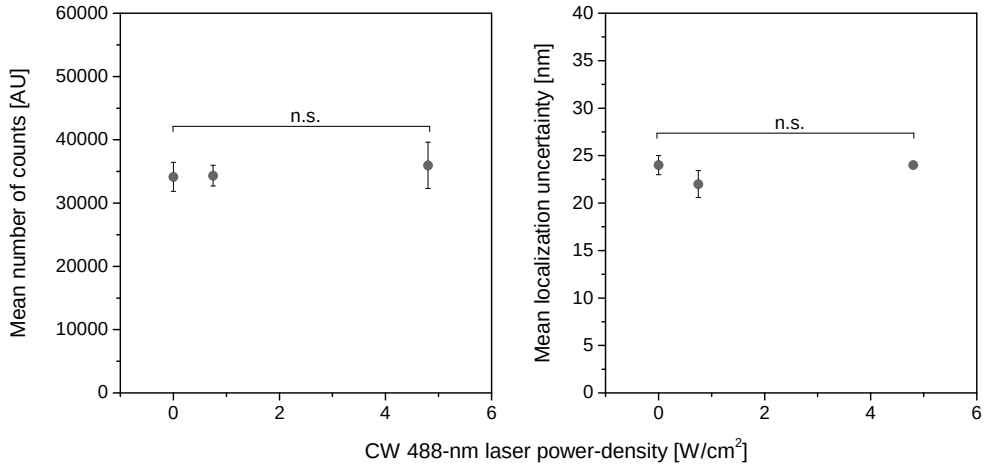

Figure 11.8: Continuous 488-nm illumination at 0.75 or 4.8 W/cm^2 on mEos4b in COS7 cells does not significantly affect localisation brightness (A) of precision (B). n.s.: non-significant, as supported by a one-way ANOVA test with confidence level 0.05. Points are mean ± SD (n=3 different cells).

Another concern when adding additional illumination during the experiment, is the increased photobleaching it might cause to the molecules. Here, attention should be given to potential increases in photobleaching on both the red and the green forms of the protein. Increased photobleaching of the red state will cause lower photon budgets per molecule, and hence lower resolution of the images and more missed detections. Green state photobleaching will contribute to incomplete photoconversion, reducing the labelling density.

To probe red state photobleaching, we imaged sparse PAA-embedded mEos4b in the presence and absence of 488-nm light, and compared the total number of photons collected per cluster of localisations (considered to each arise from a single molecule). 488-nm light was not found to significantly affect the total number of photons emitted per molecule (Figure 11.9).

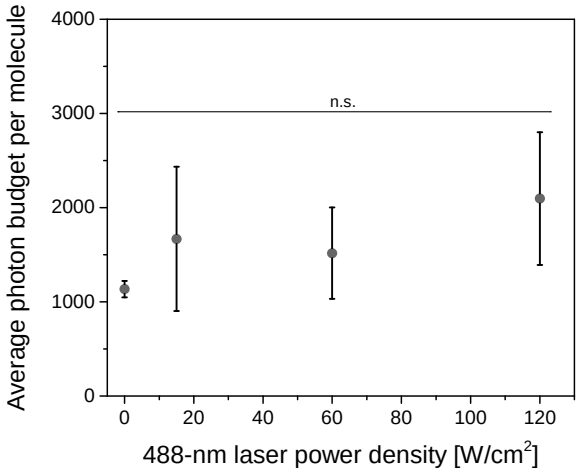

Figure 11.9: Measured average photon budget (over the total lifetime of a molecule), under 0.5 kW/cm^2 of 561-nm light and as a function of additional 488-nm illumination (10% duty cycle, pulsed mode). Increasing the 488-nm illumination intensity does not significantly affect the photon budget of red mEos4b molecules (n.s.: P$\geq$0.2, one-way ANOVA tests), showing that, at these intensity levels, and taking into account the unchanged photon counts per frame (Figure 11.7), 488-nm light does not increase substantially their photobleaching rate. Points are mean $\pm$ SD (n=3 different FP preparations).

To probe green state photobleaching, ensemble-level experiments were performed on PAA-embedded mEos4b, using a weak 488-nm readout light (15 W/cm^2), along with the same laser scheme and intensities as for PALM experiments. Photobleaching rates were fitted in the presence and absence of additional 488-nm light in the PALM illumination scheme (Figure 11.10). Even though the average photobleaching rate increased in the presence of more intense 488-nm light, this increase was found non-significant. This result however points out that care should be taken not to use too high intensities of 488-nm light during PALM, especially for experiments where photoconversion efficiency is important. Furthermore, rate determination from these experiments was not very precise, and the large resulting error bars might hide a significant influence of 488-nm illumination at these intensities on the photobleaching rate.

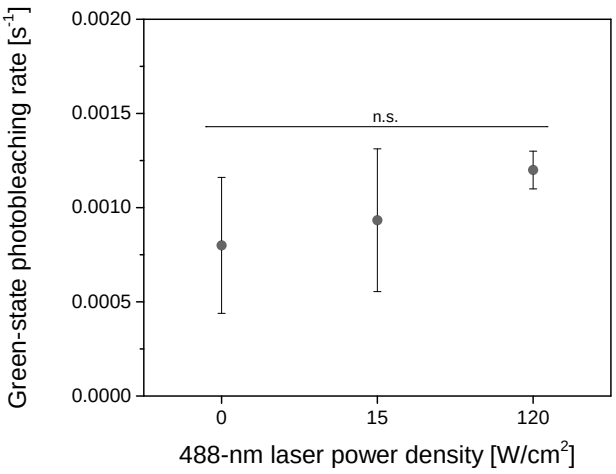

Figure 11.10: Ensemble fluorescence experiments were conducted on the green form of mEos4b using the laser scheme and power densities shown in Figure 11.3 A, and with short pulses of weak 488-nm light (15 W/cm^2 for 10 ms every second) for fluorescence readout. Green-state photobleaching rates were retrieved as described in section 8.1.2. Upon addition of 488-nm light, no significant increase of green-state photobleaching was observed upon raising the 488-nm laser power-density (n.s.: P$\geq$0.3, one-way ANOVA tests). Points are mean $\pm$ SD (n=3 different FP preparations).

In summary, our illumination scheme does not degrade the quality of PALM acquisitions under the tested 488-nm illumination intensities. No loss in localisation precision was observed, nor any significant photobleaching of green mEos4b. This last point should however be kept in mind, since high 488-nm illumination intensities are expected to eventually produce green state photobleaching, as described in chapter 9.

11.5 Conclusion: implications for tracking

Suppression of long-lived blinking during PALM acquisitions is an important improvement to the technique. In classic PALM imaging, it will allow reducing clustering artefacts (such as mentioned in ref[109]), and generally facilitate the interpretation of colocalisation patterns or protein distributions in cells, by making it easier to merge together localisations arising from the same emitter. An important improvement is also expected to take place in sptPALM, where long-lived blinking limits the achievable tracking length. The longer on-times reported here under 488-nm illumination should therefore be of particular use, allowing prolonged tracking of single molecules, and in turn the observation of more consecutive changes in diffusion behaviour.

This was indeed shown by our collaborators in KU Leuven, who conducted sptPALM experiments on single MAP4 (microtubule-associated protein 4) proteins fused to mEos4b in COS7 cells. In the presence of weak 488-nm light (4.8 W/cm^2, continuous mode), the number of long tracks was increased by 65% (Figure 11.11 A). This allowed gaining more informations from the tracks, for

example increasing the number of detected diffusion state changes per track (Figure 11.11 B). Of note, sptPALM experiments showed substantial improvement in track length even in the presence of very weak 488-nm illumination (0.75 W/cm^2, continuous mode). One of the reasons for this might be that the intensity of the 561-nm laser was set 10 times lower than in the in-vitro experiments (55 against 500 W/cm^2), largely reducing the on-off switching rate. Although this point might require more precise investigation, it suggests that our blinking-suppression strategy is most efficient at low 561-nm intensities.

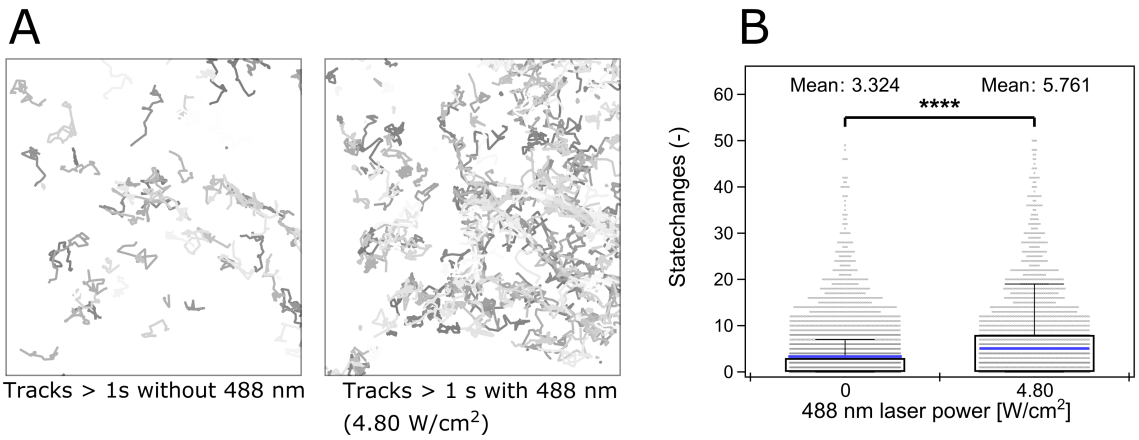

Figure 11.11: sptPALM experiments on MAP4-mEos4b in COS7 cells. (A) Upon addition of weak 488-nm light (4.8 W/cm^2, continuous mode), the number of long tracks (here >1 second) is increased. (B) The longer tracks allow the detection of a larger number of diffusion state changes per molecule. **** P$< 10^{-7}$, χ^2-test.

qPALM experiments are also largely hindered by long-lived blinking; therefore, the next chapter will focus on applying the blinking suppression scheme presented here to an *in-vitro* qPALM experiment, with the aim of improving the accuracy of molecular counting.

Chapter 12

Design of an experimental strategy for qPALM

12.1 Introduction

As mentioned in section 5.2.2, long-lived blinking is one of the major flaws preventing accurate stoichiometry determination of protein complexes by PALM. When using the technique proposed by Lee et al.[73] based on a threshold dark-time, shortening blinks with 488-nm light would reduce mixing of the fluorescent traces of different FPs, making counting easier and more reliable.

This chapter will present an attempt at setting up a qPALM experiment and demonstrating the effect of 488-nm illumination on counting accuracy. To test our method, we chose the inducible lysine decarboxylase (LdcI), a bacterial protein complex, as a molecular counting template of known stoichiometry. Important parameters for data acquisition and analysis will be discussed, and finally preliminary results on counting experiments performed on LdcI will be shown. We have not yet been able to perform accurate molecular counting, but the work is an important step towards establishing a reliable qPALM protocol in the lab, and outlines the difficulties associated with such experiments.

12.2 Using the inducible lysine decarboxylase (LdcI) as a counting template

12.2.1 Choosing a template for molecular counting

Demonstrating our strategy to improve molecular counting required a template of known stoichiometry. Several systems have been proposed so far to this purpose:

- Small oligomers (1-3 subunits) of membrane proteins, mostly used as models to demonstrate counting approaches based on the number of blinks per cluster (e.g. CD86, CTLA-4, CD80, VSVG).[117,124]

– Nuclear Pore Complexes (NPCs), recently proposed as gold standards to calibrate quantitative super-resolution approaches.[123]

– DNA origamis, that can be arranged in structures of different sizes and stoichiometries.[141]

– "Reconstituted" fluorescence traces of oligomers, made from concatenation of traces from monomers (this strategy was used by a few studies to benchmark their molecular counting approaches).[73,122]

These templates can be divided in three main categories, as shown on Figure 12.1.

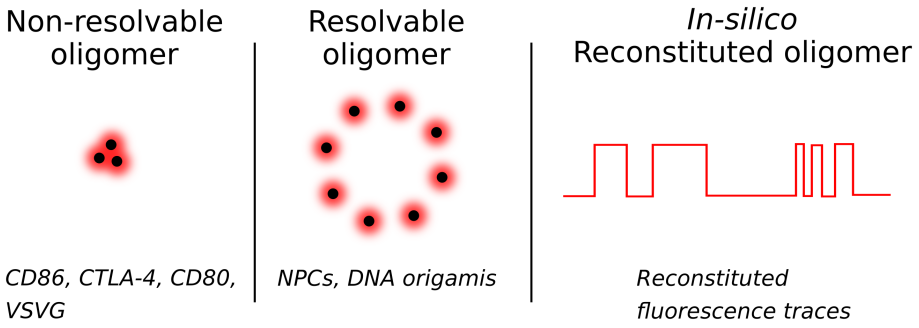

Figure 12.1: Templates for benchmarking of qPALM strategies.

Performing molecular counting on these templates shows an increasing difficulty from left to right. Most challenging - but representative of most quantification problems in biology - are the unresolvable oligomers. When used for benchmarking, their oligomeric state should be known with confidence; else it becomes difficult to assess if the counting method is performing well. Another possibility is to use complexes that are resolvable spatially. Counting is more straightforward in that case, and precise labelling efficiencies (or in the case of PCFPs, photoconversion efficiencies) can be determined. Furthermore, their fluorescence signal can be treated identically to the one of non-resolvable clusters to benchmark counting approaches. Finally, reconstituting fluorescence traces *in-silico* from traces of monomers is the least challenging because it does not take into account issues linked to photoconversion efficiency, and deals with traces of known stoichiometry. It can nevertheless be useful to test the performance of new algorithms.

For a first demonstration, we looked for a stable protein complex, and deemed it easier to first work on purified proteins rather than on fixed cells (which excluded the use of NPCs, since those have to be observed *in-cellulo*). We also ruled out using reconstituted fluorescence traces, since it would not account for some of the issues typically encountered in qPALM, such as limited photoconversion efficiency. Finally, we aimed for a number of subunits above 3 per complex, where we thought our blinking suppression strategy would have the most effect, by helping unmixing traces from different proteins.

For these reasons, we turned to the inducible lysine decarboxylase (LdcI), which has been studied for several years by the team of Irina Gutsche at IBS. They have shown that LdcI builds a stable complex, which can be easily purified from *E. coli*, and have characterised two main oligomeric

states depending on the pH: a dimeric state that forms at high pH (8 and above), and a decameric state that forms at more acidic pH (7 and below). Additionally, they reported that the protein was never observed in the monomeric state. Finally, they characterised fusions of the complex with FPs by negative-stain electron microscopy, and designed a construct where LdcI could be labelled with one FP per subunit, while retaining its native structure.

All these advantages make LdcI an attractive template for molecular counting. Furthermore, the change of oligomeric state with pH offered a possibility to test two different stoichiometries with the same protein in different conditions. We therefore generated an LdcI-mEos4b construct, that we transformed and purified from *E. coli* (as described in materials and methods, section 6.2.2).

12.2.2 Biological function of LdcI

LdcI is an endogenous *E. coli* enzyme, that uses the cofactor PLP to decarboxylate lysine into cadaverine. It is involved in acid stress response: upon decrease of the pH below 7, the enzyme is mainly found as a decamer, which is its active form (shown on Figure 12.2).

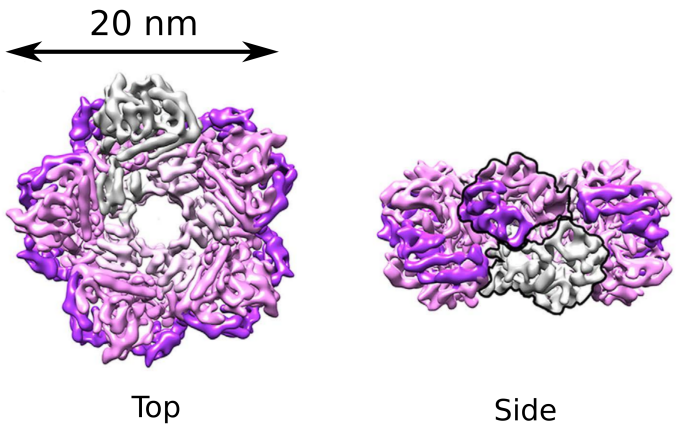

Figure 12.2: Structure of the inducible lysine decarboxylase (LdcI). The monomer is shown in grey; the decamer is formed by stacking of two pentamers.

The decarboxylation reaction (shown on Figure 12.3), removes the acid group of lysine to produce cadaverine and CO_2. The reaction consumes a proton, which decreases the pH inside the bacterium. Furthermore, LdcI is coupled to the lysine/cadaverine antiporter CadB, that imports lysine into the cell, and exports cadaverine. Together, these two proteins form the lysine-dependent acid resistance system (LDAR), that allows bacteria to survive in very acidic environments such as the stomach, or the urinary tract.[142]

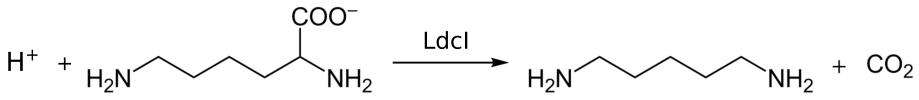

Figure 12.3: The inducible lysine decarboxylase (LdcI) removes the acid group of lysine to form cadaverine and CO_2.

12.2.3 Verification of the oligomeric state for microscopy experiments

After purification, a crucial step was to check whether the decamer was correctly assembled. Although the protein was reported never to be found monomeric, we wanted to assess the dimer/decamer ratio after purification (at pH 7), and verify that the FPs were not cleaved from the oligomer.

To check the presence of the decamer in our sample, we loaded the purified protein on a superose-6 10/300GL column, equilibrated with the same gel filtration buffer as during purification. The elution profile (Figure 12.4) showed a peak at 11 mL, corresponding to the decameric protein. Additionaly, smaller peaks were visible at higher elution volumes (14 to 24 mL), indicative of smaller proteins in the solution. These might include the dimeric form of LdcI, in equilibrium with the decamer.

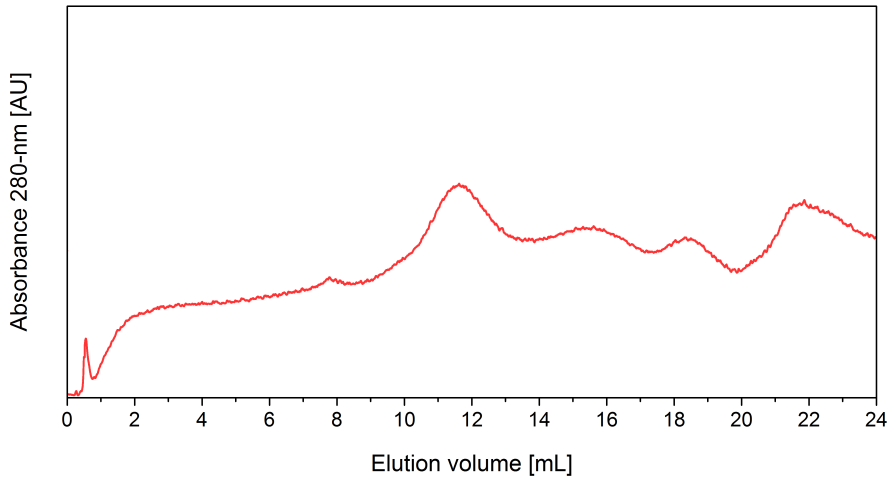

Figure 12.4: Gel filtration profile of purified LdcI-mEos4b. The peak eluting at 11 mL corresponds to the decameric protein, whereas peaks at higher elution volumes correspond to smaller proteins.

To confirm this result and obtain a more precise quantification of the proportion of decamers in the sample, we performed AUC. The resulting profile (Figure 12.5) shows a main peak at 15S (40% of the total signal), corresponding to the decameric protein, a smaller peak at 8S (6% of the signal) which could be attributed to the dimer, as well as a number of peaks between 20 and 45S, corresponding to bigger structures (e.g. aggregated protein). The low-weight proteins seen in the gel filtration profile (Figure 12.4) were not detected here, except dimeric LdcI. This led us to

the conclusion that these low-weight proteins are non-fluorescent protein impurities, which should therefore not impair microscopy experiments.

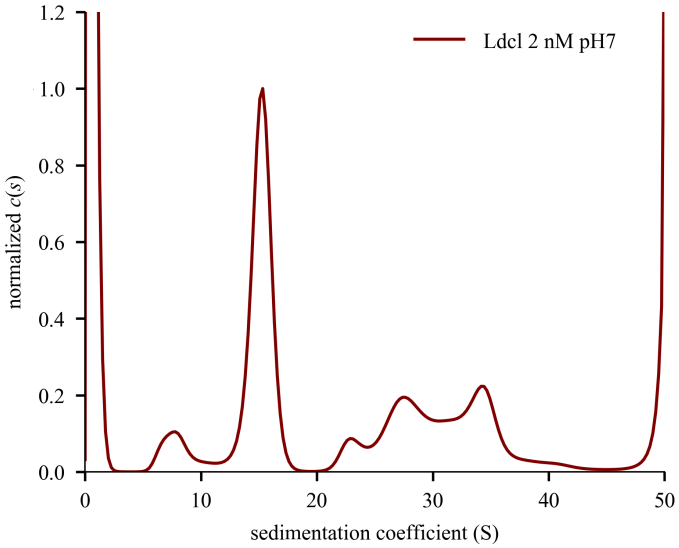

Figure 12.5: Analytical ultracentrifugation of purified LdcI-mEos4b. The profile shows clear peaks at 8 and 15S, matching with decameric and dimeric LdcI, respectively. Peaks above 20S correspond to bigger oligomers, possibly formed through aggregation.

Both experiments allowed us to confirm a significant pool of decameric LdcI, while also indicating the possible presence of other oligomeric forms such as dimers, or protein aggregates. The fact however that aggregates were only seen in AUC experiments and not by gel filtration points to an issue during the AUC experiment, rather than to significant aggregation in our samples.

Next, we wanted to verify that the linker between LdcI and mEos4b was not cleaved during purification or storage of the protein. Therefore, ESI-TOF (electrospray ionisation - time of flight) mass spectrometry was performed to confirm the mass of the LdcI-mEos4b fusion. A largely dominant species was found at a mass of 110504 ± 4.8 Da, in accordance with the predicted mass of 110500 Da obtained from the protein sequence. We were therefore able to conclude to an absence of cleavage of the FP from LdcI.

A last concern was the possibility that the decameric complex would dissociate upon the strong dilution applied for PALM experiments (final protein concentration $\sim$2 nM). To prevent this, we incubated aliquots of the protein prior to dilution with a cross-linker (glutaraldehyde, 1% v/v), to establish covalent links between the subunits of the complex. This strategy was inspired by GraFix, a protocol used to stabilise complexes for observation in electron-microscopy.[143]

12.3 Setting up a protocol for molecular counting

qPALM experiments have been made in many different ways in the various publications that exist in the field. There is so far little consensus on which experimental conditions should be used, and some of them depend on the system studied (cells or purified components, membrane or soluble proteins, type of data processing...). Finally, publications do not always describe in details the way experiments are performed.

We have found that performing molecular counting experiments was not as straightforward as it may seem at first, and have therefore set out to optimise a qPALM protocol based on the one proposed by Lee et al.[73] (described in section 5.2.4). Furthermore, we wanted to assess whether the blinking-suppression strategy described in chapter 11 could be beneficial to qPALM experiments. This section aims at giving an account on our progress in these different tasks, and highlights several points in data acquisition and processing that still require optimisation.

12.3.1 Immobilisation of the purified protein

Since we are working with purified proteins, the question arised of how to immobilise them on the coverslide for prolonged imaging. Among the available immobilisation methods in the lab were aqueous gels such as PVA and PAA; however, both allow limited control of buffer conditions. Notably, they require relatively high pH for polymerisation (8-9), whereas we initally wanted to acquire images at pH 7, to maximise the amount of decamers in the sample while retaining good fluorescence from mEos4b.[i] Of note, after using glutaraldehyde to cross-link the decamers, it would probably be possible to raise the pH without dissociating them, and hence use PAA as an immobilisation technique. Since we considered glutaraldehyde cross-linking only later in the course of the experiments, we did not have this option of using PAA to start with. Another possibility was to adsorb the proteins on UV-treated glass; but even though proteins adsorbed in this way seemed bound with high affinity (they could not be detached by rinsing, nor seen to diffuse under the microscope) we could not be fully sure that they would remain attached for the whole length of the experiments. Proteins detaching from the surface during acquisition would have led to important under-counting.

Due to the constraints mentioned above, we decided to use disuccinyl-suberate (DSS) cross-linking as an immobilisation method. This technique, previously developed in the lab by Virgile Adam, functionalises the surface of a glass coverslide with DSS (an amine cross-linker) on which proteins can be bound. The detailed protocol can be found in materials and methods, section 7.1.4. As a result, the proteins are covalently bound to the glass surface, and can be kept in any buffer, with the exception of buffers containing free amines (e.g. Tris), since those would saturate the DSS cross-linking sites. After protein cross-linking to the surface, the coverslide is incubated with fetal bovine serum (FBS) as an excess source of protein to detach any FPs that would be adsorbed to the glass and not covalently cross-linked (Figure 12.6).

[i] At pH below 7, protonation of the chromophore impairs fluorescence emission, making single-molecule detection less reliable.

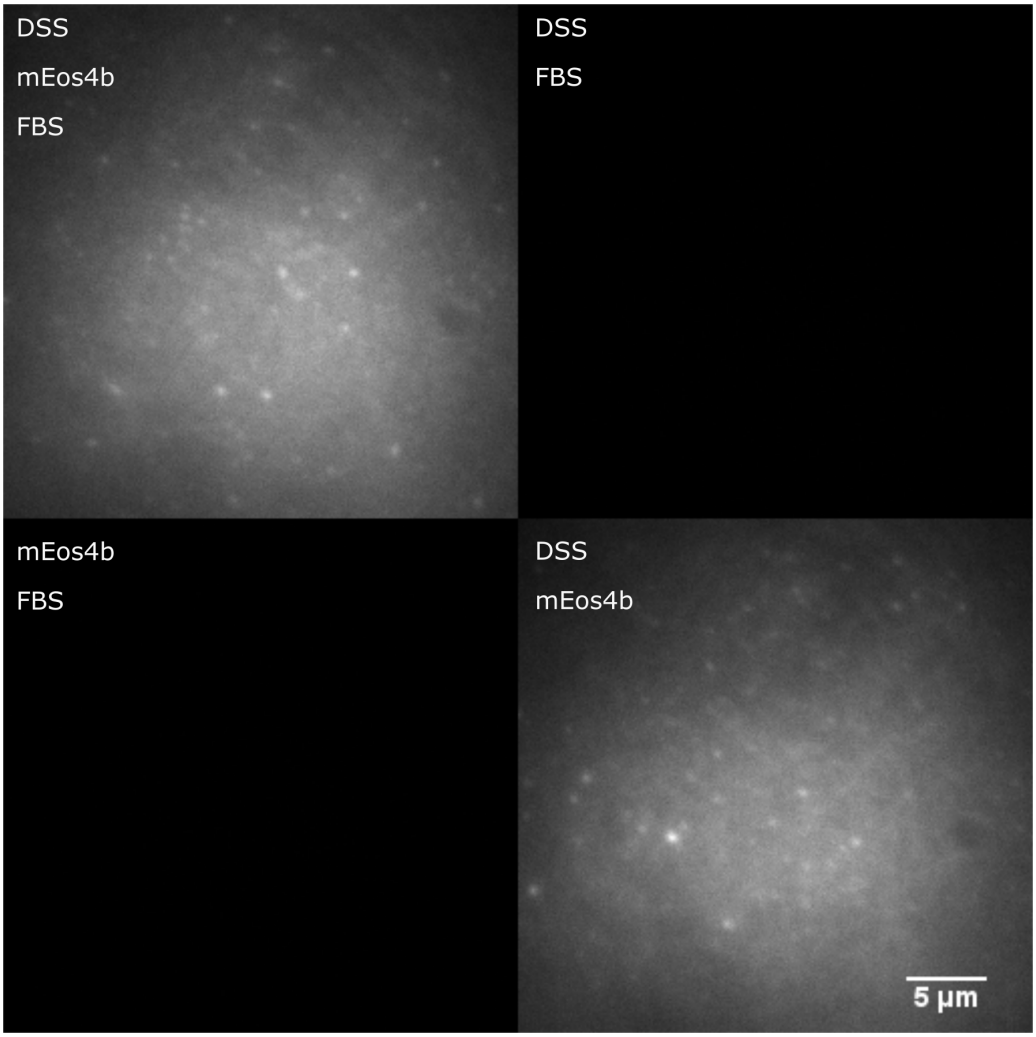

Figure 12.6: Control of the specificity of FP binding to glass by DSS. In the absence of DSS, mEos4b is detached from the glass by 30 min incubation at 37°C with FBS (bottom left). In the presence of DSS, mEos4b is retained to the glass (bottom right), and cannot be removed by incubation with FBS (top left). DSS and FBS do not produce significant background fluorescence (top right).

12.3.2 Fine-tuning laser illumination

As the previous results of this thesis have shown, carefully tuning laser illumination intensities is of primary importance for qPALM experiments with mEos variants, both for the green and red form of the protein. In general, the main parameters that will be affected by laser intensities are the signal-over-noise ratio (SNR), photobleaching of both green and red molecules, spreading of photoconversion events over the whole dataset, and modification of the blinking behaviour of the FPs. This section will detail how we fine-tuned illumination at different wavelengths to obtain the most

reliable molecular counting, and what modifications could be tested to bring further improvements.

Spreading out photoconversion events

In their original publication, Lee et al.[73] propose using a profile based on a Fermi function to control the intensity of the activation laser (405-nm) such that photoconversion events would be evenly spread out over the dataset. We therefore implemented a similar scheme, using the parameters given in the publication. Figure 12.7 shows the number of localisations obtained per 100 frames, overlaid with the intensity profile applied to the 405-nm laser.

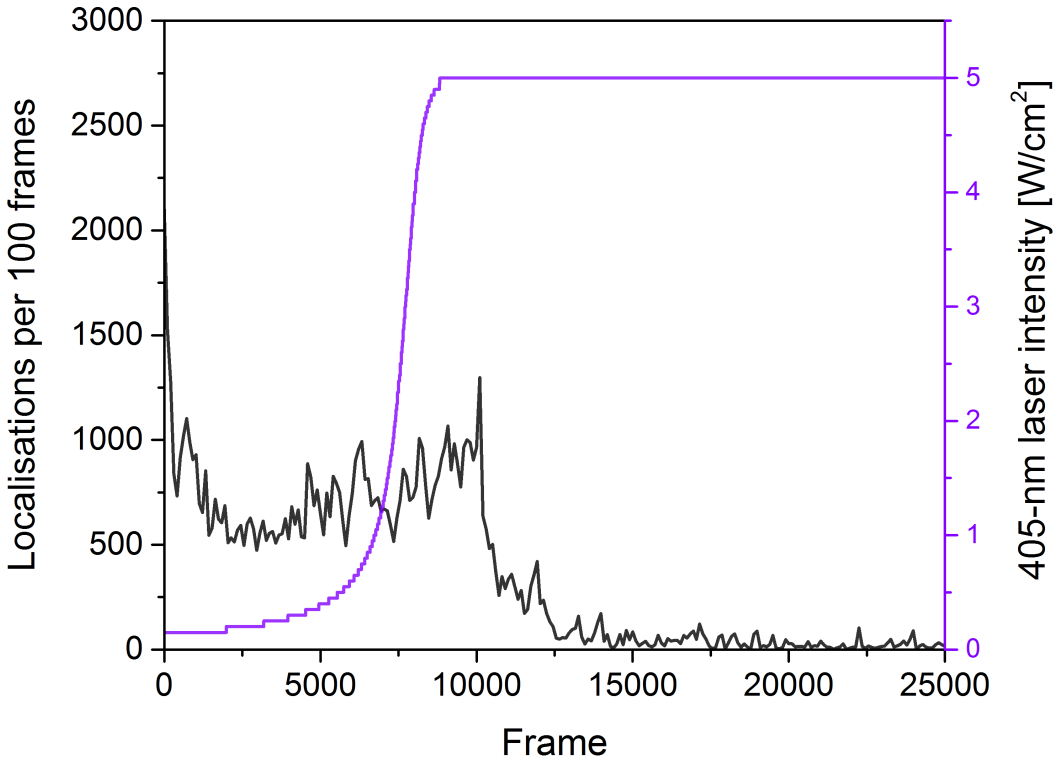

Figure 12.7: Application of a Fermi activation profile on LdcI-mEos4b fusion proteins. The maximum 405-nm laser intensity at the sample (reached after ∼10000 frames) was 5 W/cm^2.

The number of localisations remains relatively constant over the first 10000 frames, while laser intensity increases, and shows a clear drop when the laser has reached its maximal intensity (5 W/cm^2). The few localisations occurring between 10000 and 25000 frames can be either ascribed

to noise from impurities, or from mEos4b molecules undergoing late photoconversion.[ii] We consider the former most likely, since the number of localisations per 100 frames (∼50) is below the noise level recorded on a sample without FPs (150 localisations per 100 frames).

From this graph, it clearly appears that photoconversion events are not yet optimally spread over the 25000 frames of the experiment. Since the localisations occuring after 10000 frames appear to be noise, probably the activation profile needs to increase more slowly, and/or to a lower maximum laser intensity. Additionally, these localisations could be excluded from further analysis.

In any case, one should keep in mind that 405-nm light is phototoxic to FPs, and that its intensity should be minimised to reduce photobleaching and under-counting.

Avoiding green- and red-state photobleaching

Green- and red-state photobleaching have different influences on our qPALM experiment. In chapter 9, we have shown that green photobleaching could be caused by 488-nm or strong 561-nm light.[iii] As a consequence, the number of FPs per decamer that get photoconverted to the red state will be lower, leading to under-counting. Red-state photobleaching will decrease the total number of photons collected per molecule. This is not a very big impediment to the experiment - as long as we collect enough photons to detect the FPs. However, a high red state bleaching rate will lead to molecules bleaching before they have emitted enough photons to be reliably detected.

For these reasons, we tried to keep laser intensities as low as possible for the three lasers (561-, 488- and 405-nm). For the 561-nm laser, the minimum intensity was dictated by the signal-over-noise ratio of the localisations. In our case, we found an intensity of 0.5 kW/cm^2 to be the minimum achievable (using 70 ms exposure time). This came as a surprise, since other publications have reported much lower illumination intensities, for example our collaborators in KU Leuven who used 55 W/cm^2 at 40 ms exposure time to perform sptPALM experiments. We do not understand yet where this important difference comes from; hypotheses include an issue in our detection setup, or a wrong calibration of our power-density measurements. Furthermore, our signal-over-noise ratio histogram (Figure 12.8) suggest that lowering the 561-nm laser intensity (and hence brightness of the FPs) might be doable while maintaining good detection.

[ii] The photoconversion rate can differ between molecules depending on their orientation: a poorly oriented chromophore will absorb less photons, and therefore have a lower probability of photoconverting.

[iii] Even though we did not demonstrate it here, 405-nm light is also expected to have a photobleaching effect, since it is more energetic than 488-nm light.

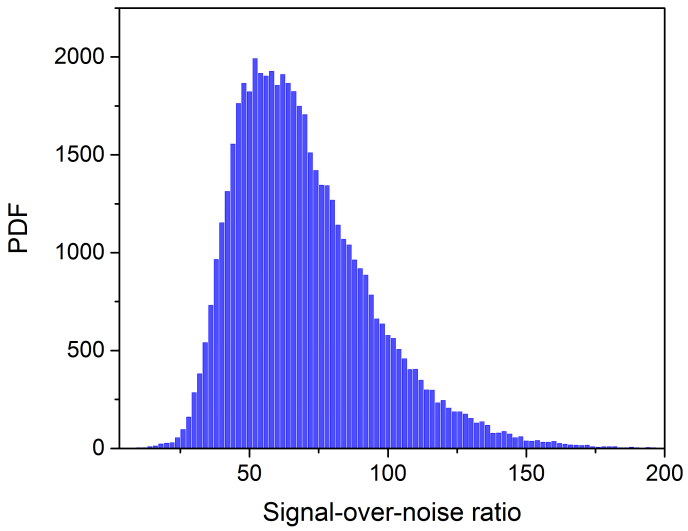

Figure 12.8: Signal-over-noise ratio histogram for a qPALM experiment. PDF: probability density function.

The intensity of the 405-nm laser was mostly dictated by the photoconversion properties of the FPs (as detailed in the above section), but was also minimised whenever possible. In experiments so far, we have used a ramping 405-nm intensity up to a few W/cm^2. Finally, for experiments using 488-nm light, 15 and 120 W/cm^2 (pulsed mode, 10% duty-cycle) were used, similarly to the results of chapter 11, but a further decrease of the intensity would be possible, should these cause too much green-state photobleaching.

Optimising blinking suppression by 488-nm light

It should be noted that 405- and 488-nm light have partially similar effects: 488-nm light can induce additional photoconversion (Figure 11.5), while 405-nm light can suppress blinking (Figure 11.6). Therefore, in datasets recorded in the presence of 488-nm illumination, it might be interesting to decrease the 405-nm illumination intensity, to keep a constant photoconversion rate and minimise the adverse effects of 405-nm light. Another possibility might be to modulate the intensity of the 488-nm laser inversely to that of the 405-nm laser. An example of such a modulation is presented on Figure 12.9. At the beginning of the dataset, 405-nm illumination intensity is low, so 488-nm light is needed to efficiently suppress blinking. On the other hand, at the end of the dataset where 405-nm illumination intensity is high, less 488-nm light is needed, since 405-nm light will suppress most of the long-lived blinking. 488-nm light can therefore be turned down to minimise green-state photobleaching. We have not yet implemented this scheme in a qPALM experiment, but it might allow increasing blinking suppression while limiting photobleaching effects.

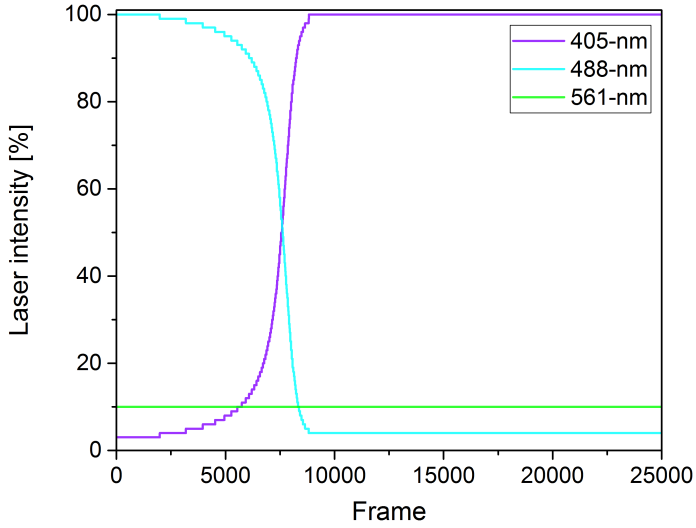

Figure 12.9: Alternative illumination profile for 488-nm light in qPALM. The 405- and 488-nm laser intensities are anti-correlated, since they share similar functions (although with different efficiencies). 561-nm readout light is set at constant intensity, as low as possible to limit photobleaching.

12.3.3 Data processing: localisation and filtering

The first step in processing qPALM experiments is the localisation of single-molecules. This step is performed using an intensity threshold, that allows separating molecules from noise. The threshold is set manually, and therefore subject to interpretation. A too low threshold will result in a high number of noise detections (false positives, causing over-counting) while a too high threshold will result in missed molecules (false negatives, causing under-counting). Furthermore, if the signal-over-noise ratio is low (as is typically the case with FPs), it is most likely impossible to find a threshold that completely avoids both error sources. A technique has been published recently to overcome this issue, which could be of great interest to minimise counting errors due to detection issues.[144] In short, the technique is based on computing the histogram of intensities from the fluorescence trace of each cluster of localisations in the dataset. The resulting histogram is bimodal, since it contains frames where a fluorophore is active (high intensity) and frames where no fluorophore is active (low intensity). A common strategy is to define the optimal threshold as the minimum value between the two peaks. The authors of the above-cited study propose a more elaborate scheme using two detection thresholds and a more elaborate photophysical model that includes "grey" states, where the fluorophore is ON but weakly emitting. This procedure allows them to more faithfully detect blinking events in their dataset.

For similar reasons, the table obtained from the localisation step is often filtered to remove noise, and if possible, process only the localisation clusters corresponding to oligomers. To this purpose, we attempted filtering of the clusters based on an image recorded in the green channel prior to the

PALM acquisition. We anticipated that decameric LdcI would be visible as bright spots due to the green fluorescence of mEos4b in its native state. Although the resulting image did show bright spots (Figure 12.10 A), they proved surprisingly difficult to match with corresponding localisations from the PALM image. 76% of the green spots matched with at least one localisation, but a large number of them matched with only a single localisation in the PALM image. Furthermore, a large number of localisations did not correspond to any signal in the green image. This absence of reliable correlation between the green and the red image is very surprising. We would normally expect that most molecules that produce a high green fluorescence also produce a large number of localisations in the red channel, and that most large localisation clusters in the PALM image could be matched to an intense green signal. Possible causes for this unexpected result could be chromatic aberrations shifting the position of green and red signals relatively to each other, or detachment and diffusion of the molecules during the PALM dataset. These two effects could be checked by:

1. Aligning images of fluorescent beads acquired in each channel and correcting for chromatic abberation.

2. Acquiring images in the green channel over a large range of time (1 or 2 hours) to check if molecules are diffusing on these timescales.

3. Additionally, since we work on complexes that are stabilised by glutaraldehyde cross-linking, we could immbobilise them in PAA, where diffusion would be more reliably stopped. Despite the associated raise in pH, the complex should stay assembled thanks to the cross-linking.

Despite this poor matching of green and red clusters, we attempted selection of red clusters based on the green image, to see if it could help filtering out noise localisations. In order to get a first estimation of the effect of this selection, we processed clusters from the complete PALM image and from the selection with an arbitrary cutoff time of 10 seconds (Figure 12.10 B, C). After selection, a small peak appears around 7 molecules per cluster, which could correspond to our decamer. This peak remains however minor, and the experiment would need to be repeated to confirm this result.

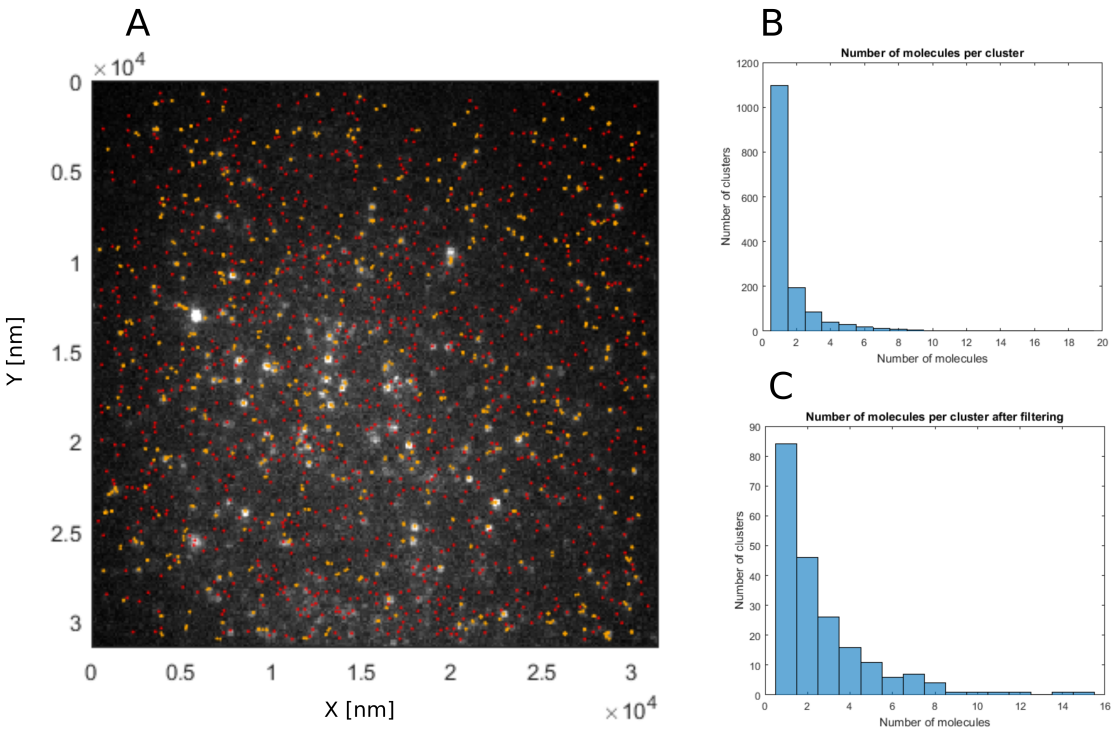

Figure 12.10: Filtering out noise localisation using the green fluorescence of mEos4b. Data processed with an arbitrary τ_c cut-off time of 10 seconds. (A) Image acquired in the green channel under 488-nm illumination (120 W/cm^2) overlaid with the localisations from the PALM image. Clusters composed of only 1 localisation are shown in red, and those composed of several localisations in orange. (B, C) Histograms of the number of molecules per cluster before and after selection, respectively (fixed τ_c, 10 sec).

As an alternative to using an image from the green channel, we also attempted manual picking of clusters from the reconstituted PALM image. This allowed sorting out noise clusters made of only a few localisations, and picking all clusters made of a large number of localisations. On average, 200 to 300 clusters were picked from each PALM image by manually selecting their centre of mass, and keeping all localisations within a user-defined radius.[iv] Figure 12.11 A shows the result of the filtering. Applying this strategy on the same dataset of Figure 12.10 with the same arbitrary τ_c of 10 seconds provided a similar result (Figure 12.11 B), with a small peak appearing around 6 molecules per cluster. It therefore seems that this technique was similarly successful to remove noise localisations, though again the results would need repetition to be statistically relevant.

[iv] A radius of 180 nm was used here, but it should be adapted depending on cluster size and density.

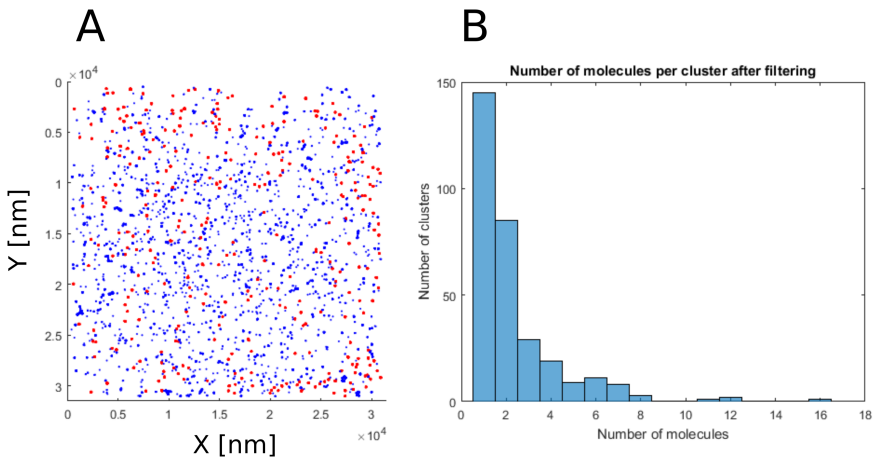

Figure 12.11: (A) Manual picking of clusters of localisations in a PALM image. Kept localisations are indicated in red, and discarded ones in blue. (B) Histogram of the number of molecules per cluster after manual picking.

The downside of this technique is however that it relies on the appreciation of the user to select clusters, which could result in significant bias of the analysis. A more automatised strategy for noise filtering would therefore be of great benefit to qPALM experiments.

12.4 Preliminary results

12.4.1 Reduction of off-times by 488-nm light

To check if 488-nm illumination does indeed suppress blinking in our qPALM experiments, we imaged monomeric mEos4b using the same experimental protocol as for molecular counting of LdcI decamers (i.e. with constant 561-nm readout light, increasing 405-nm light, and with or without 488-nm light). From these datasets, we built off-times histograms, similarly to Figure 11.3. The result, shown on Figure 12.12 shows identical histograms in the presence and absence of 488-nm light. This absence of influence of 488-nm light on off-times is probably due to the presence of 405-nm light during the acquisition, which has a similar blinking-suppression effect, as discussed above.

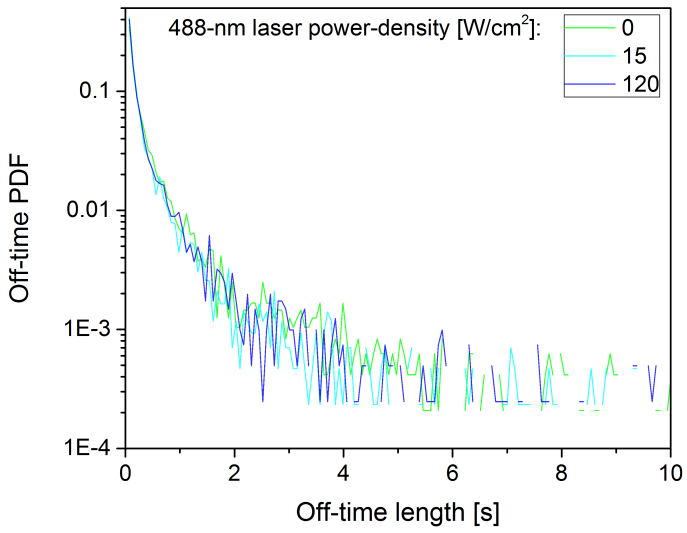

Figure 12.12: Off-times distribution of mEos4b molecules under our qPALM illumination scheme. Illumination at 488-nm does not have a significant effect on the off-times, probably due to the presence of 405-nm light during the acquisition.

Interestingly, this result does not mean that 488-nm illumination cannot be beneficial to qPALM experiments. Since it increases the photoconversion rate, it could for example allow using a lower intensity of the 405- and/or 561-nm lasers, which are both phototoxic to the FPs, while retaining good blinking behaviour. Therefore, a fairer comparison for the effect of 488-nm light on qPALM experiments might be using weaker 405-nm illumination when 488-nm light is present, to keep a constant localisation density over the dataset.

12.4.2 τ_c curve optimisation

In our case, one of the crucial steps for molecular counting is building the τ_c curve which will allow us to use a different dark-time to account for blinking depending on the number of FPs per cluster. In the original publication by Lee et al.,[73] oligomer fluorescence traces are built by combining traces of monomers. These monomer traces can be obtained in two ways, either experimentally or through simulations.

For the **experimental approach**, mEos4b monomers are imaged in the exact same conditions as the LdcI-mEos4b decamers. Fluorescence traces are built, and summed to reconstitute traces from oligomers. In that way, any bias due to spreading of photoconversion events (e.g. if many more molecules are activated at the beginning of the dataset) will be reflected in the reconstituted traces. For each oligomeric state, 1000 traces were generated and the smallest τ_c yielding the correct number of molecules was retrieved. Each point of the final τ_c curve is therefore an average over 1000 reconstituted traces.

For the **simulation approach**, traces from 2000 molecules were simulated, all of them photoconverting at frame 1. Oligomeric traces were then generated by combining several traces together, and shifting them in time, so that photoconversion events would be evenly distributed. In that sense, the simulated data reflect less well potential issues with photoconversion that might be encountered when recording fluorescence traces from decamers.

For both approaches, to **perform the counting** using the τ_c curve, the iterative algorithm orignally proposed by Lee et al. was applied. For each experimental cluster, the fluorescence trace was split with a τ_c equal to 0, yielding a large count of molecules. From this number of molecules a new τ_c value was retrieved, used to split the trace and retrieve a new number of molecules. This iteration was repeated until convergence, which typically happens after a few cycles.

We have attempted both calibration methods described above, yielding the τ_c curves of Figure 12.13 A, B, which show different responses of τ_c to the number of molecules per cluster. The curve obtained from simulated data finds shorter τ_c values than the one obtained from experimental fluorescence traces. This difference might be due to the even distribution of photoconversion events in the simulations.[v] Another notable difference is that the curve obtained from simulated traces is much "flatter" towards higher numbers of molecules, i.e. the optimal τ_c does not vary a lot for different oligomeric states. As a consequence, it becomes more difficult to distinguish oligomeric states using the iterative procedure since it will more likely converge early, at a large number of molecules.

We tested the two different τ_c curves on the same dataset as above, which yielded the histograms of Figure 12.13 C, D. Using the τ_c curve built from experimental monomer data does not show a peak that could correspond to decamers. This can be due to too high τ_c values leading to under-counting, or to an actual absence of decamers in our sample (which is however questioned by the previous analyses that tend to show a small population of decamers). As expected, the τ_c curve obtained from simulated data yielded much higher counts of molecules per cluster (due to the smaller τ_c values). A peak centred at 5 molecules per cluster was visible, that could correspond to decameric proteins. However, many clusters were clearly over-counted, with counts between 10 and 40 molecules per cluster.

[v] Experimentally, the photoconversion rate depends on many factors, such as 405- and 488-nm laser intensity, orientation of the FPs, or photoswitching in the green state.

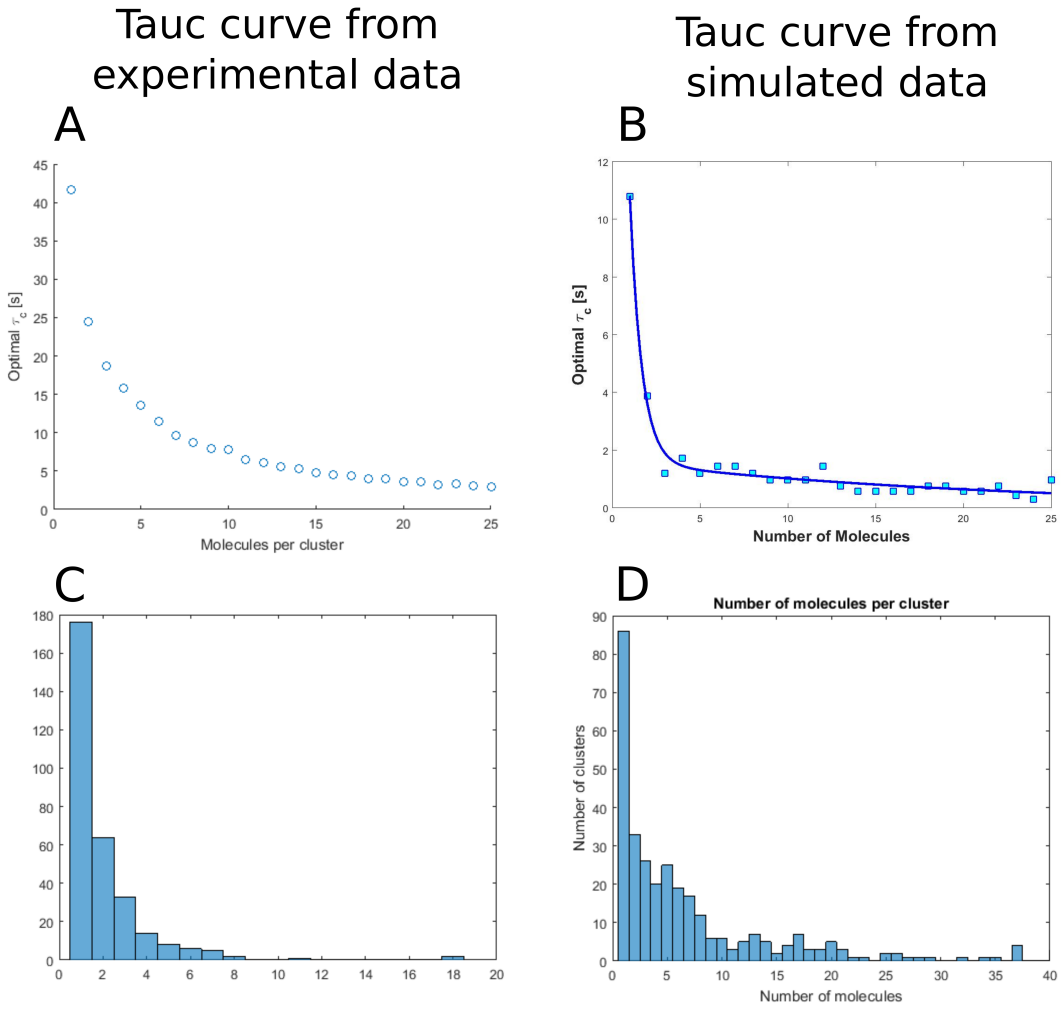

Figure 12.13: (A, B) τ_c curves generated from experimental monomer fluorescence traces, or from simulated fluorescence traces. (C, D) corresponding histograms obtained for the number of molecules per cluster.

A first conclusion to these results is that τ_c splitting is not as straightforward as it might seem, and that the τ_c curve itself depends heavily on the type of dataset used for calibration. As a consequence, the final results (i.e. the number of molecules per cluster) is also extremely variable.

Choosing between a τ_c curve made from experimental or simulated fluorescence traces, one may postulate that the former would be more accurate, since it was acquired in the exact same conditions as the subsequent qPALM experiment. This conclusion is however not obvious from our results, since the final histogram derived from the τ_c curve using simulated data shows more features, and seems to be able to detect a fraction of oligomers that is not seen using the calibration from

experimental data.

12.5 Conclusion

The preliminary results shown in this chapter are still incomplete, and thus difficult to interpret. All of them need to be performed in triplicates to acquire statistical significance, and most of the parameters listed above (detection threshold, filtering, τ_c-splitting...) need to be fine-tuned to obtain reliable data. I suggest to conduct these experiments along the following general guidelines, split in two main points:

1. Perform experiments on monomers in qPALM conditions. Monomers are easier to handle and immobilise than decamers, and have no issue of unknown maturation efficiency, varying stoichiometry or complex dissociation. Furthermore, they would still allow optimising parameters such as the detection threshold, spreading of photoconversion events, laser intensities, data filtering and τ_c curve building. As a first approach, it would also be possible to use them to produce "reconstituted" oligomer fluorescence traces, and benchmark our counting approaches and experimental conditions. Even though these traces might be easier to process than real oligomers, they would allow optimising the data processing workflow and some of the experimental parameters, without having to deal with uncertainties concerning the state of the decamer.

2. Perform experiments on decamers, using the knowledge acquired on the monomers in the previous step. This would allow to validate the technique developed on reconstituted fluorescence traces, refine it if needed, and tackle more specific issues such as maturation level or mixed oligomeric states.

Of note, it might also be interesting to test our approach on different types of oligomeric structures, to check that the method is not template-dependent, or limited in terms of number of FPs per cluster.

Concerning our primary aim of testing the effect of 488-nm illumination on molecular counting, preliminary results indicate an absence of effect. An important question remains however about the laser intensities used: could we lower the intensities of the 561- and 405-nm laser to reduce photobleaching effects and enhance photoconversion efficiency? If this is possible, 488-nm illumination might have a much more pronounced effect, and allow combining low photobleaching (in both the green and red state) and shortened blinking.

Chapter 13

Remaining questions on Eos proteins photophysics

The characterisation of mEos2 and mEos4b performed in chapters 9, 10 and 11 have significantly improved the understanding of the photophysical behaviour of these two proteins during PALM experiments. However, they raised at the same time several questions that we were not able to fully answer yet. This chapter is meant to give an overview of these open questions, along with preliminary data giving hints for further investigations, and to discuss the possible phenomena underlying the experimentally observed behaviours. The main points discussed here will be:

- The nature of the short-lived dark-state seen in mEos2 and mEos4b (chapter 9).
- Photophysical models that could explain the unexpected shape of off-times histograms for red mEos4b as well as the saturation behaviour of the recovery rate from the long-lived dark-state (chapter 10), in relation with the observed off-times under 488-nm illumination (chapter 11).
- The possibility for photoconversion from a non-emissive state of green mEos2 to the red state.

13.1 Nature of the short-lived dark-state in green mEos2 and mEos4b

Chapter 9 presents off-switching curves for mEos2, and argues that a two-dark-states model is required to explain the kinetics of the observed fluorescence decays, both under 488- and 561-nm light (Figure 9.4). The resulting model contained a long-lived dark-state, which structure could be solved by Elke De Zitter, and a short-lived dark-state recovering thermally to the fluorescent state. This hypothesis was backed by the previous characterisation in the lab of a similar short-lived dark-state in green IrisFP, due to a non-absorbing chromophore generated through redox chemistry.[76] A similar non-absorbing dark-state had also been observed in red mEos2.[74]

Here, we will amend and refine this view, and discuss the nature of this dark-state based on the different experiments we performed on the green state of mEos2 and mEos4b.

In chapter 9, we hypothesise that the short-lived dark-state recovers thermally to the fluorescent state, based on a titration of the 561-nm laser intensity (showing a constant recovery rate at 0.04 s^{-1}, Figure 9.5). This finding was however questioned by the higher recovery rate fitted under 488-nm illumination (0.2 s^{-1}, Table 9.2), pointing to a more complex behaviour than simple thermal recovery.

To gain further insight on this point, we performed photoswitching experiments on green mEos4b under increasing 488-nm laser intensity, and plotted the fitted recovery rates from the long- and short-lived dark-states (Figure 13.1).

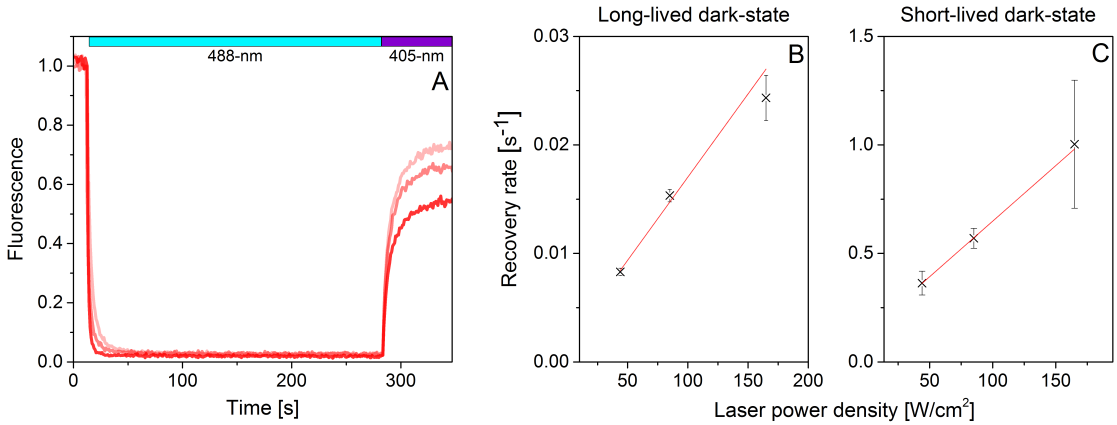

Figure 13.1: (A) Photoswitching curves of green mEos4b under increasing 488-nm laser intensities (45, 85 and 165 W/cm^2), followed by fluorescence recovery under 405-nm light (0.03 W/cm^2). (B) Fitted recovery rates from the long-lived dark-state (red line: linear fit, R^2=0.96). (C) Fitted recovery rates from the short-lived dark-state (red line: linear fit, R^2=0.99). Curves in (A) are representative of 3 experiments on different FP preparations. Points in (B) and (C) shown as mean ± SD (n=3 different FP preparations).

From panels B and C, it appears clearly that the fitted rates for both dark-states depend linearly on the 488-nm laser intensity. The value of 0.2 s^{-1} reported in Table 9.2 under 488-nm light at 10 W/cm^2 is consistent with this linear behaviour. This finding invalidates the hypothesis of the short-lived dark-state being a non-absorbing state.

The first observation that prompted us to think that fluorescence recovery from this state might be thermal was its constant rate under varying 561-nm illumination. In light of the new results presented above, we would like to propose a new interpretation as follows:

1. The short-lived dark-state does not thermally recover to the fluorescent state (or with a very slow rate)

2. It absorbs 488-nm light which accelerates its recovery to the fluorescent state, but not (or very weakly) 561-nm light.

3. It was observed to recover at a constant rate of 0.04 s^{-1} under 561-nm light due to the weak (and constant over the experiments) 488-nm light used for fluorescence readout.

Of note, we do not rule out the existence of a non-absorbing radical state in green mEos2/mEos4b. The corresponding state observed in red mEos2 was reported to recover with a rate of 16 s^{-1}; i.e. on a much shorter timescale than our ensemble photoswitching experiments, which were performed over minutes. This state could therefore exist but not be significantly populated at such low laser intensities. Figure 13.2 A, B shows the corresponding two photophysical models, including or not the radical state with a recovery rate of 16 s^{-1}. Panel B shows simulations of ensemble off-switching curves with these two models, which show that at the employed laser intensities, $D_{radical}$ in not populated as the ensemble level, and therefore does not affect the shape of the fluorescence decay curve (shown in green).

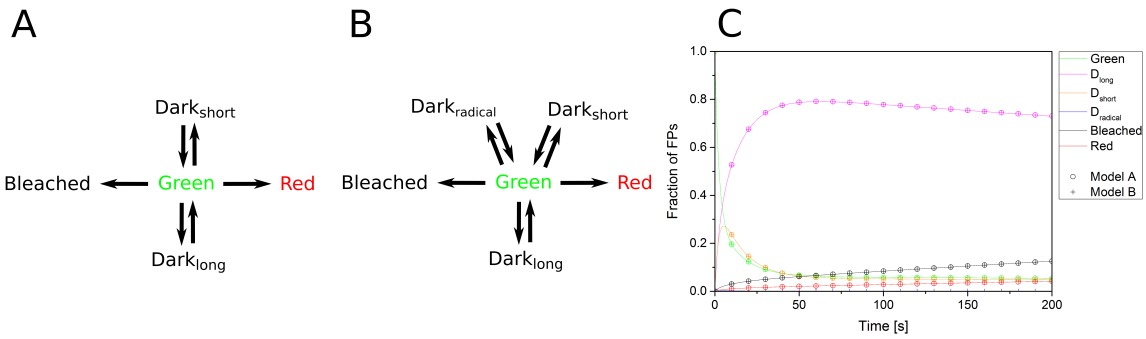

Figure 13.2: Influence of a short-lived radical state on green mEos2 off-switching curves. Photophysical model including (B) or not (A) a short-lived radical state recovering to the fluorescent state at 16 s^{-1} were used to simulate ensemble off-switching curves (C). Circles correspond to the simulation using model A, and crosses the one using model B. The simulation yields identical curves in both cases, because $D_{radical}$ is not populated at the ensemble level.

The precise nature of the short-lived dark-state observed here remains elusive. Sensitivity to 488- but not 561-nm light hints at a protonated state[i], which might be possible to test by performing experiments at different pH. An interesting possibility would be that this state corresponds to a stable isomerisation intermediate, as observed on the RSFP rsEGFP2.[64] It has recently been shown that access of the chromophore to this isomerisation intermediate depended on the constraining of the protein's β-barrel,[145] which might provide a way to probe similar behaviours on Eos proteins.

Another interesting question that remains open is whether a similar dark-state exists in green mEos4b as the putative one discussed in the next section of this chapter for red mEos4b. Extending the power-titration of Figure 13.1 to higher 488-nm laser intensities would allow assessing the presence or absence of a similar saturation behaviour in the long-lived dark-state recovery rate as observed on the red state.

[i] which would be expected to show blue-shifted absorption relative to the anionic state

13.2 A photophysical model for red mEos4b

Chapter 10 proposed a study of the blinking behaviour of red mEos4b under varying 561-nm laser intensity, and showed that single-molecule blinking and ensemble-level photoswitching arise from the same light-induced molecular process. These findings however came together with unexpected observations: off-times histograms obtained from single-molecule data were found to be tri-exponential (Figure 10.4), and recovery rates from the long-lived dark-state showed a saturation behaviour, instead of the linear dependency expected from a simple light-induced process (Figure 10.3). This saturation behaviour was also strongly reflected in the evolution of the single-molecule off-times histograms under increasing 561-nm laser intensity, as shown on Figure 13.3.

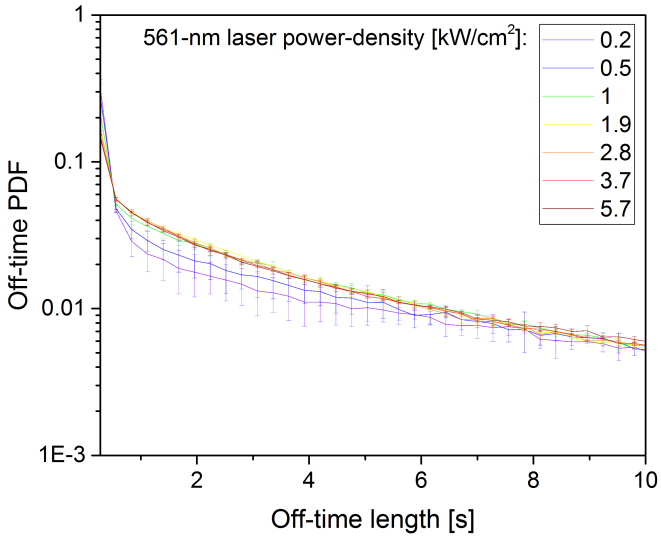

Figure 13.3: Evolution of off-times histograms under varying 561-nm illumination intensity (0.2 to 5.7 kW/cm^2).

The off-times histograms showed noticeable change between 0.2, 0.5 and 1 kW/cm^2, but remained nearly identical at higher laser intensities; this accurately reflects the saturation behaviour observed from the rates fitted from ensemble-level experiments, which reached a plateau at 561-nm illumination intensities higher than 1 kW/cm^2. We consider this strong concordance between ensemble and single-molecule level experiments to be a good indication that this behaviour is a real feature of the observed FP, and not a bias due to our experimental setup. Of note, ensemble-level off-switching curves could however still be fitted with a simple two-dark-states model: a reason for this could be that the phenomenon at play here does not have a strong enough influence on these ensemble-level curves to be detectable, since they result from more parameters (on- as well as off-switching rates, and photobleaching) than single-molecule off-times histograms.

Even though the single-molecule histograms could be well fitted with a tri-exponential model, the

rates retrieved (Figure 10.5) could not easily be matched to the recovery rates from two dark-states independently populated from the red state.[ii] This rather prompted us to think that the potential third dark-state could be populated through the already known long-lived dark-state. This hypothesis is further supported by the fact that long-lived off-times cannot be entirely suppressed by 488-nm light, as is visible on the histograms of Figure 11.3. Although weak 488-nm light (15 W/cm^2) produces a decrease of about a factor 10 in long off-times, increasing the illumination power to 120 W/cm^2 only marginally shortens the off-times duration. This is a hint that 488-nm illumination not only prompts recovery of the FPs to the fluorescent state, but also drives them to another, light-insensitive dark-state.

An interesting possibility would be that the long-lived dark-state could enter the triplet state, as is the case for the fluorescent state. Entry into the triplet state would then be an entry point to different non-absorbing states (e.g. radical states), that would only recover thermally to D_{long} or the red fluorescent state. Hence upon 488-nm illumination, the fraction of chromophores in these non-absorbing states would not be affected, and would generate long-lived off-times.

To test this hypothesis, we simulated ensemble-level experiments using the kinetic model of Figure 13.4 A, and fitted them with a two-dark-states model as for experimental data to retrieve on-switching rates from the long-lived dark-state. The retrieved rates (panel B) were in extremely good agreement with the rates retrieved from ensemble and single-molecule experimental data. The rates used in the simulations (summarised in the table of panel C) were on the same order of magnitude than the ones fitted from ensemble-level experiments. All rates of light-induced processes were scaled linearly with illumination intensity, whereas rates of thermal processes were assumed independent from illumination intensity. Panel D shows the evolution of all states of the model (under 561-nm illumination at 1 kW/cm^2). Panels E and F show the evolution of the D_{long} and D_3 dark-states respectively, depending on the intensity of the 561-nm laser. While at low intensity, D_{long} stays populated for a long time and D_3 is not very populated ($\sim$5% at most), as intensity increases the population of D_{long} is depleted more quickly, and that of D_3 becomes more important

[ii] In this case, the recovery rates would be expected to either remain constant (thermal process) or increase with laser power (light-induced process).

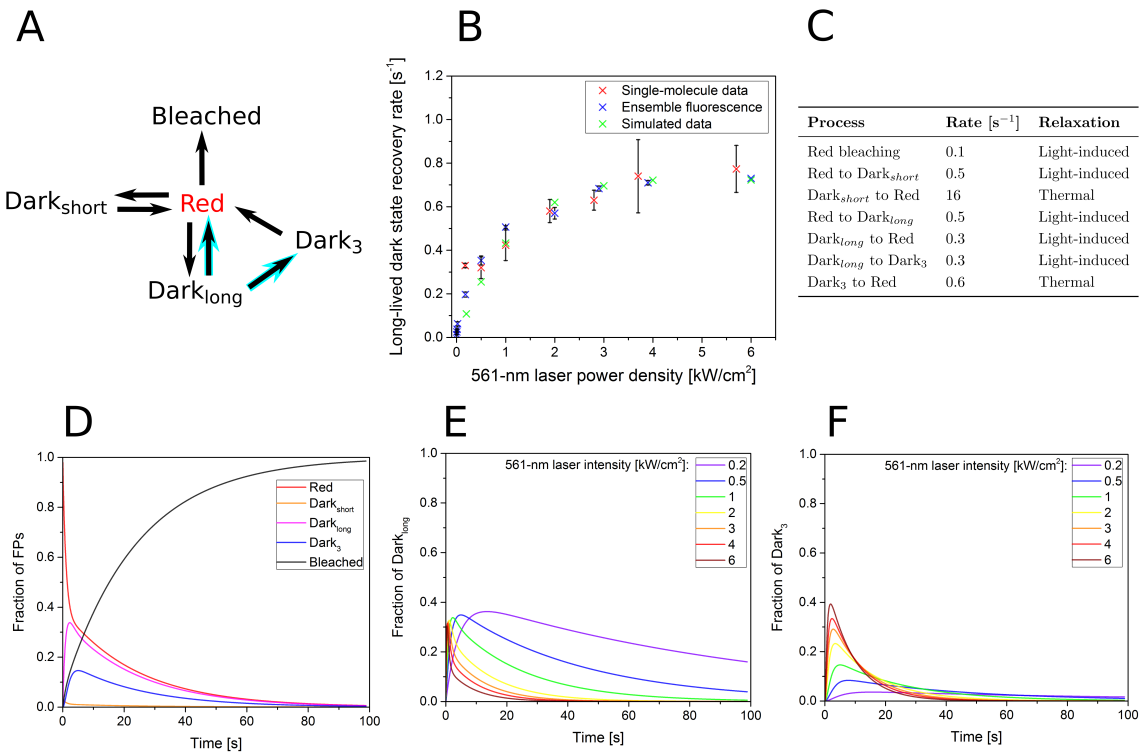

Process	Rate [s^{-1}]	Relaxation
Red bleaching	0.1	Light-induced
Red to Dark$_{short}$	0.5	Light-induced
Dark$_{short}$ to Red	16	Thermal
Red to Dark$_{long}$	0.5	Light-induced
Dark$_{long}$ to Red	0.3	Light-induced
Dark$_{long}$ to Dark$_3$	0.3	Light-induced
Dark$_3$ to Red	0.6	Thermal

Figure 13.4: (A) Kinetic model including an additional dark-state Dark$_3$, which could be at the origin of the saturation behaviour of the recovery rate. Cyan arrows represent the rates that would be increased by 488-nm illumination. (B) Ensemble-level data simulated using the kinetic model of panel A allows a faithful reproduction of the experimentally observed saturation behaviour. (C) Rate constants used in the simulation of panel B, given for an illumination intensity of 1 kW/cm^2. (D) Evolution of all states of the model during a simulated ensemble photoswitching experiment under 1 kW/cm^2. (E) Evolution of the population of D_{long} during the same experiment, as a function of 561-nm illumination intensity. (F) Evolution of D_3 as a function of 561-nm illumination intensity.

To further test our model, we simulated single-molecule off-times histograms (Figure 13.5). Although the model predicted long-lived off-times lasting up to 10 seconds, it did not reproduce the triphasic behaviour observed experimentally, and could still be well fitted by a biexponential model. The model also failed to generate the very long-lived dark-states ($>$ 10 seconds). This shows that our model, although a first step towards a better understanding of red mEos4b photophysics, is still incomplete and will need to be further refined in the future. The main questions that need to be addressed are the number of distinct states visited by the protein; the transitions that are possible between them; and the rates (light-induced or thermal) at which these processes occur.

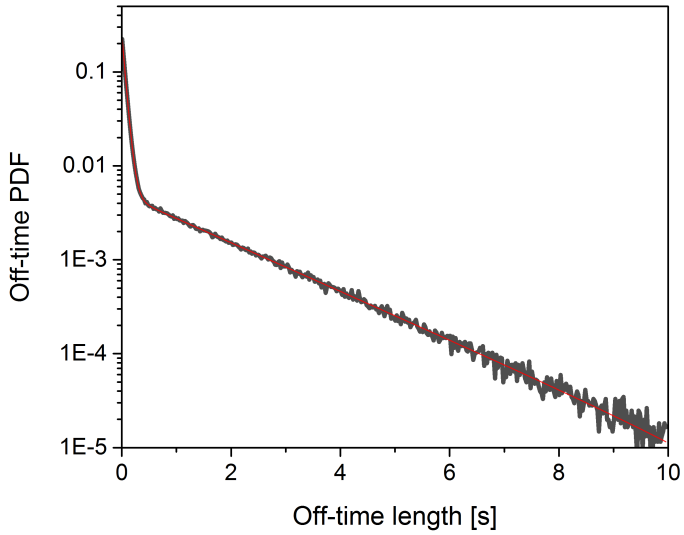

Figure 13.5: Simulated single-molecule off-times histogram using the model of Figure 13.4 A, and the rates of Figure 13.4 C. The simulated histogram (black line) can still be well fitted with a biexponential model (red line).

Another interesting observation is that off-times histograms from data acquired under 488-nm illumination cannot be fitted with a biexponential model (Figure 13.6). According to the model of Figure 13.4 A, 488-nm light should strongly depopulates D_{long}, hence making this state very short-lived and invisible in off-times histograms. The fact that this is not the case, and that despite 488-nm illumination, off-times histograms cannot be fitted with a biexponential model means that either (i) depopulation of D_{long} by 488-nm light is not efficient enough to make the associated off-times invisible in the histogram or (ii) that our model is not yet complete, and lacks elements that would explain this behaviour.

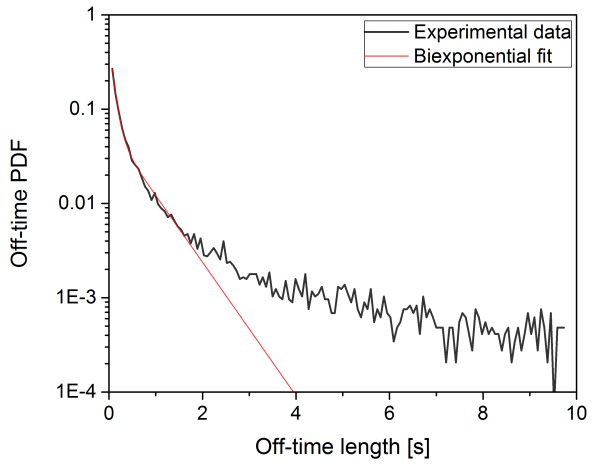

Figure 13.6: Off-times histograms from data acquired under 488-nm illumination (grey line) cannot be fitted by a bi-exponential model (red line).

As an additional insight, we performed single-molecule experiments under varying pH, in the presence or absence of 488-nm illumination (Figure 13.7). Varying the pH between 6 and 8 did not significantly influence the shape of the off-times histograms (panel A). Under 488-nm illumination however, increasing the pH tended to decrease the number of long off-times (panel B). It therefore appears that suppression of long off-times is more efficient at high pH (panel C), with more than 80% of the offtimes >3 seconds suppressed at pH 8, against 40 to 50% at pH 6. These results are unexpected, because at low pH, more chromophores should be in the protonated state, hence absorbing at 488-nm and more sensitive to light at this wavelength. More investigations are needed to clear out this seemingly incoherent result.

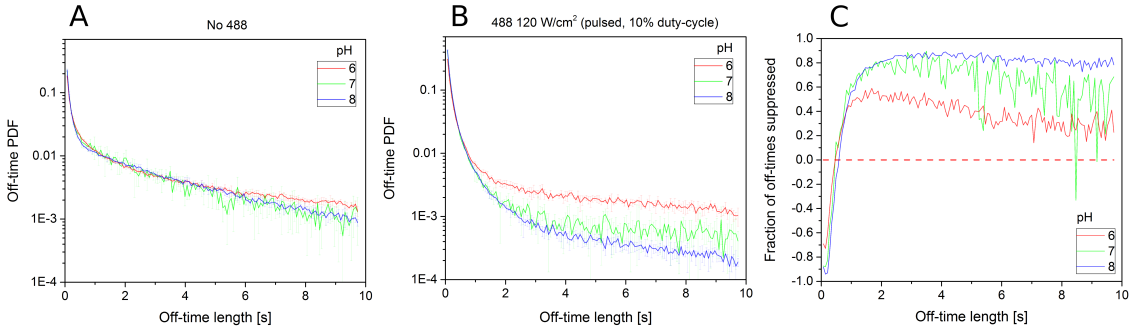

Figure 13.7: Off-times histograms from single-molecule experiments performed under varying pH (6, 7 or 8) in the absence (A) or presence (B) of 488-nm illumination (120 W/cm^2, pulsed mode, 10% duty-cycle). (C) Fraction of off-times suppressed by 488-nm illumination as a function of pH.

In conclusion, we have presented here strong evidence that the photophysics of red mEos4b is more

complex than was previously thought. Reversible switching to two distinct dark-states fails to account for the complex photophysical behaviour of the FP, observed from both ensemble-level and single-molecule data. This leads us to propose that the long-lived dark-state of mEos4b possesses a rich photochemistry, similarly to the red fluorescent state. Although conversion from the long-lived dark-state to further non-emissive states is difficult to assess, the effect is visible in PALM, and has the very practical consequence of generating long-lived fluorescence intermittencies (on the order of tens of seconds), detrimental to PALM experiments. Understanding the nature of these dark-states could drive the design of new experimental strategies to reduce the occurrence of long-lived off-times even further below the level achieved under 488-nm illumination.

13.3 Alternative photoconversion paths

It has previously been reported that violet light-induced photoconversion in green-to-red PCFPs occurs from the protonated *cis* state of the chromophore.[51] As part of our photophysical investigation of green mEos2, we therefore investigated whether photoconversion could also occur from the protonated *trans* chromophore (i.e. the long-lived dark-state). This study was further motivated by the observation made on the PCFP Kaede that very few newly appearing red molecules could be linked to a disappearing molecule in the previous image.[131]

To answer this question, we imaged PVA-embedded mEos2 using a two-color detection scheme. The protein was illuminated alternatively with 488- and 561-nm light at intensities sufficient for single-molecule detection, and with or without weak 405-nm light (0.03 W/cm^2). Since we had found 405-nm light to prompt recovery from the long-lived dark-state of green mEos2 to the fluorescent state, we hypothesised that illumination at this wavelength would allow us to detect more "direct photoconversion" events. For each newly appearing red molecule in the dataset, we examined the previous frame in the green channel to find an "ancestor" green molecule.

Similarly to what had been reported for Kaede, we found a low number of red molecules that had a green ancestor in the preceding frame ($\sim$15%) under conditions of sole readout photoconversion. When illuminated with 405-nm light, this proportion did not increase as expected, but dropped to $\sim$7%, in contradiction with the effect mentioned in the previous paragraph. To make sense of this result, we performed single-molecule simulations. The simulations did not include the possibility for photoconversion from the long-lived dark-state, and allowed us to test the effect of different parameters on the detection efficiency of green ancestors (Figure 13.8).

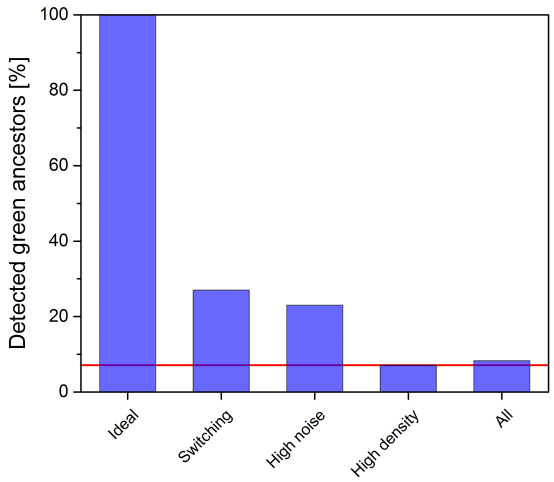

Figure 13.8: Influence of experimental parameters on the detection of green photoconversion ancestors. Red line: experimental level of detected ancestors (7%). In ideal experimental conditions, 100% of the green ancestors would be detected. This number drastically decreases when simulations take into account switching of molecules in the green form, high noise in the green channel, and high molecule density. Combined, these factors bring the level of detection of ancestors to 8%, close to the experimental value.

The simulation showed that several factors are liable to strongly decrease the proportion of detected ancestors, for example photoswitching of single-molecules, noisy detection, and high molecule density. The combination of these factors reproduces the experimentally detected fraction of ancestors. Figure 13.9 shows an example of detected or missed ancestors of red molecules, from experimental and simulated data.

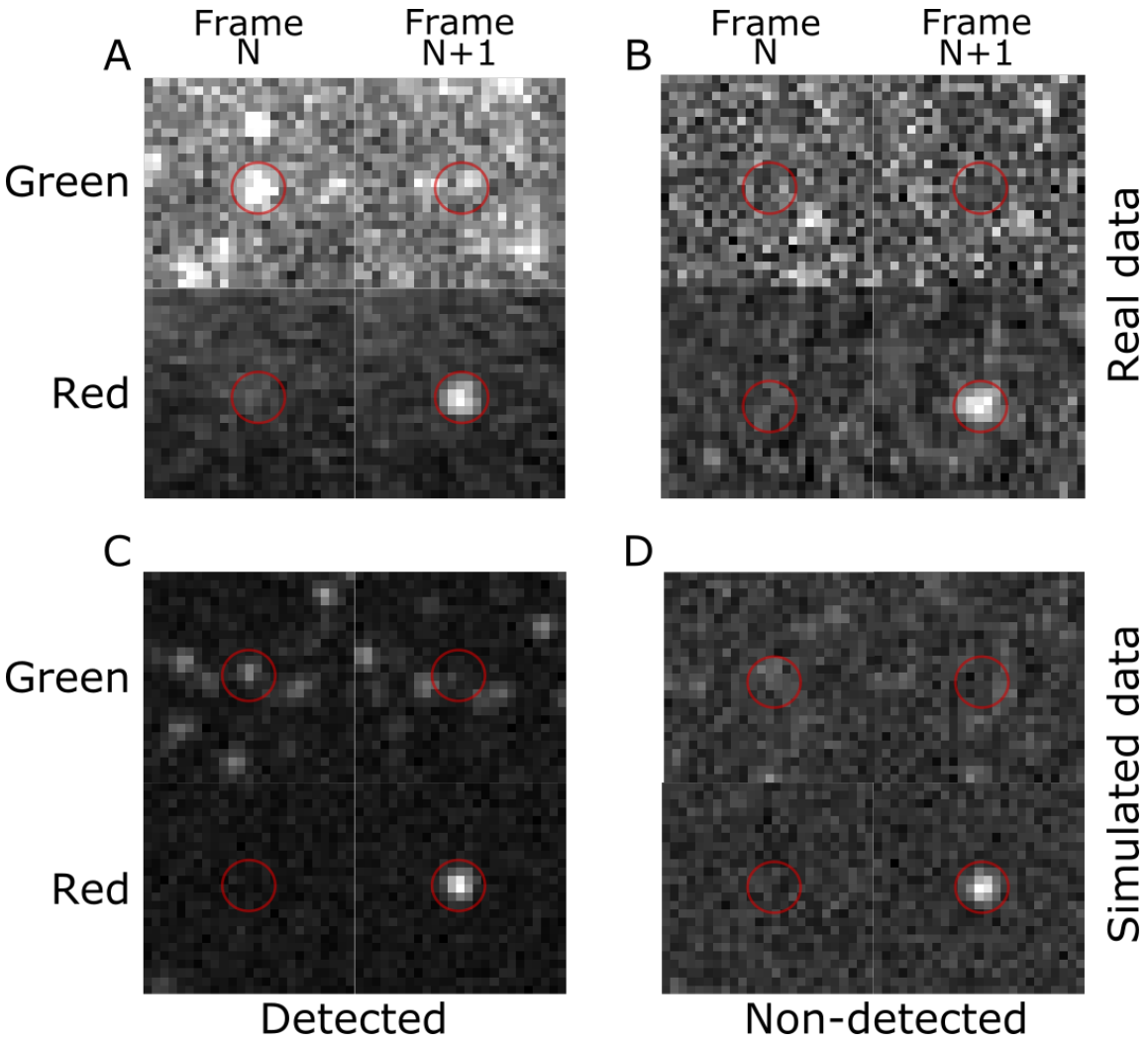

Figure 13.9: Examples of missed (B, D) and detected (A, C) ancestors from experimental (A, B) and simulated (C, D) data.

From examination of the experimental and simulated data, we concluded that our 2-color experiment was not sensitive enough to assess the presence or absence of photoconversion from the long-lived dark-state. Mainly, the poor switching contrast of green mEos2 was not sufficient to ensure reliable detection of the green single-molecules. Furthermore, using 405-nm light is expected to bring many dark molecules back to the green fluorescent state, which would further decrease their spatial separation. This might explain the lower number of ancestors detected upon 405-nm illumination.

The initial question therefore remains open to further investigation. From a chemical point of view, photoconversion from the long-lived dark-state seems plausible, since it is a protonated state, that

strongly absorbs at 405-nm. A hint might however come from the cumulative photoconversion curves recorded on mEos2 (Figure 9.8). We have attributed the biphasic shape of these curves under sole readout activation conditions to the shelving of green molecules in the long-lived dark-state delaying photoconversion. However if the molecules could equally well photoconvert from the dark-state as from the fluorescent state, no shelving would occur. This leads us to several hypotheses:

1. The biphasic shape of the photoconversion curves is not due to shelving of the green state. An alternative explanation for this inhomogenous behaviour would then need to be found, which I have not been able to do yet.

2. Photoconversion from the long-lived dark-state is possible, though at a slower rate than from the fluorescent state, thus still giving rise to a slow-down of photoconversion once most proteins are in the dark state.

3. Photoconversion from the long-lived dark-state is not possible; it would then be interesting to investigate why photoconversion would only be possible from the *cis* and not the *trans* conformation.

Part IV

Conclusion

Single-molecule localisation microsopy approaches are powerful tools for the sub-diffraction limit imaging of biological structures. More specifically, FPs enable observation with minimal perturbation of the system, and even *in-vivo* imaging. The strength of these techniques, compared to epifluorescence or confocal imaging, is not only their largely improved resolution, but also the informations that can be gathered from the observation of single molecules, which allow learning about the behaviour of proteins *in-situ*, and assessing for example their diffusion dynamics (using sptPALM) or oligomerisation state (qPALM). Unfortunately, such techniques are challenging to perform, largely because of the photophysics of the probes used - in the case of PALM, PTFPs. This work aimed at characterising PTFPs for advanced PALM imaging, and more particularly PCFPs of the Eos family, to understand the mechanisms that limit the extraction of informations from PALM datsets.

The main axis of the thesis was the photophysical characterisation of mEos2 and mEos4b *in-vitro*. Previous studies conducted in the lab and outside had set the bases used in this work: heterogenous blinking regimes of red mEos2,[72,74] triplet state-mediated photochemistry in FPs,[3] or reversible loss of fluorescence at the ensemble level in the green and red forms of mEos2 (from experiments conducted in the lab by Romain Berardozzi and unpublished at the time).

We continued this work, first with a study of the green state of these PCFPs, which we showed to photoswitch, on a slower timescale but through a similar mechanism than RSFPs. Of particular importance for PALM experiments, we showed that substantial photoswitching and photobleaching occurred in the green state under 561-nm illumination, causing a slowing-down of photoconversion and reduced photoconversion efficiency. Finally, in collaboration with Elke De Zitter who solved the structure of the green long-lived dark-state, we proposed an explanation for the lower switching contrast of PCFPs compared to RSPFs, which would be due to a less stable chromophore in the off-state. Questions remain as to the precise nature of the short-lived dark-state we observed in ensemble-level photoswitching experiments. A possible explanation could be the presence of two alternative trans conformations (as observed in some RSFPs).[145]

Another challenging work in this thesis was the characterisation of slow blinking in red mEos4b. We have been able to show that blinking and photoswitching arise from the same light-induced process; and this knowledge allowed Elke De Zitter to solve the structure of the long-lived dark-state, in the red form this time. This study was more complicated than we first envisioned, because of the complex photophysics of red mEos4b. We showed that the protein enters very long-lived dark-states (on the order of tens of seconds), which cannot be explained by the photophysical model accepted thus far for red mEos4b, and that included two dark-states in the red form. A further hint of complex photophysics was the saturation of recovery rates from the long-lived dark-state, indicating the presence of an as yet uncharacterised dark-state. The nature of this state is still very elusive, and we have not been able to characterise it yet. Although this characterisation would be challenging, it would be of great interest to reduce PCFP blinking. A promising direction for future investigations would be probing the influence of buffer composition, notably redox agents and triplet state quenchers, on the lifetime of this state.

This work on red mEos4b photophysics had the consequence of suggesting to us a new strategy to reduce long-lived blinking during PALM experiments. Thus we proposed addition of weak 488-nm light as an efficient way to drastically reduce slow blinking, and the artefacts it induces in PALM

images. We demonstrated this strategy *in-vitro*, and applied it to sptPALM in collaboration with Viola Mönkenmöller and Siewert Hugelier (KU Leuven). Addition of 488-nm light during sptPALM experiments with mEos4b was found to largely increase the tracking length, and hence the informations that can be derived from these experiments (such as changes in diffusion regimes during tracking). A point wort mentioning is that even if 488-nm light prompted rapid fluorescence recovery, it was not able to entirely suppress long-lived blinking. One can hypothesise that this is linked to the putative dark-state $Dark_3$ described during our photophysical study of red mEos4b. This makes the characterisation of $Dark_3$ particularly interesting, because it might suggest a strategy that, combined with 488-nm illumination, would bring long-lived blinking to an extremely low level - or eliminate it altogether.

Figure 13.10 below recapitulates our current views and hypotheses on mEos2/mEos4b photophysics, based on the crystal structures obtained by Elke De Zitter, and the photophysical characterisation performed in this work. Two main points are of importance to understand how we came to this scheme:

- The scheme is symmetrical for the green and red states: since photoconversion does not fundamentally change the chromophore environment, we expect that most processes taking place in one state of the protein can also take place in the other. This was confirmed in the case of the long-lived dark-states, for which crystal structures showed that isomerisation occurred in both the green and red states. Of note, even if similar processes occur in both states, their rates can differ (notably due to differences in absorption between the two states).
- We hypothesise that entry into the triplet state is possible not only from the fluorescent states, but from any state that can be excited by light (such as the trans-isomerised dark-states). Entry into the triplet state could then lead to formation of non-emissive radical states.

This scheme highlights the fact that triplet-state mediated chemistry might be of great importance to explain the blinking mechanisms of PCFPs, and an interesting topic for further investigations. Likewise, it would be interesting to probe the presence of alternative trans conformations in mEos4b. These conformations have not been seen so far in crystallography experiments, which could be due to a low ensemble-level population; but changing the environment of the FP might allow detecting them, as was done in ref.[145]

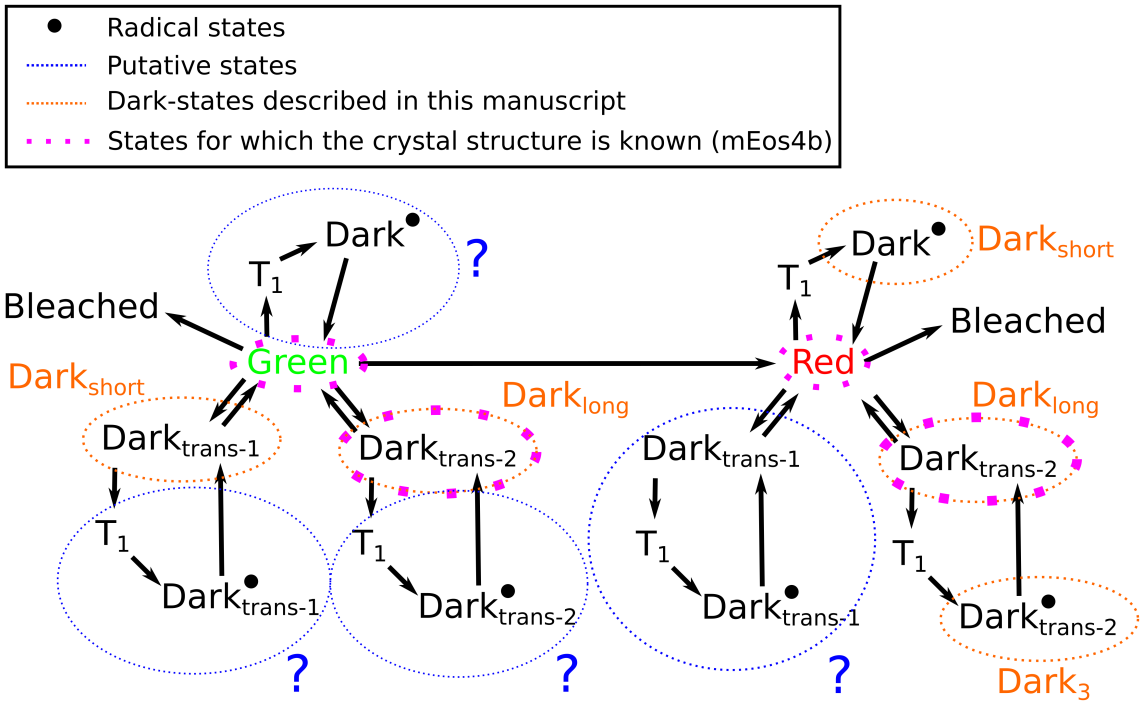

Figure 13.10: Photophysical scheme for mEos2 and mEos4b phototransformations. Black dots represent radical states, and trans-1 and trans-2 two alternative isomerised conformations. Orange circles and names show the states that were described in this manuscript. Blue circles show putative states for which we have no experimental evidence. Magenta circles show the states for which crystal structures are available (for mEos4b).

Finally, we have attempted to apply this newly gained knowledge to the challenging topic of stoichiometry determination in qPALM. Due to blinking and incomplete photoconversion, stoichiometry determination from PALM images is still a difficult task, and we hypothesised that by fine-tuning experimental conditions (notably laser illumination) and using our 488-nm illumination strategy, we could improve the counting accuracy. Our preliminary results have however shown that the strategy still requires optimisation before it can truly be used to confirm or determine *de novo* protein stoichiometries. The main points that require investigation and optimisation are:

- The correct assembly of our template decameric protein, with a sufficiently high proportion of decamers to be detectable.

- The reliable immobilisation of the protein on glass, to make sure that all or part of the proteins do not diffuse during the experiment.

- The laser intensities used, at 561-, 405- and 488-nm, to limit green-state photobleaching (that leads to under-counting), while ensuring good SNR, even distribution of photoconversion events accross the dataset, and blinking suppression to avoid over-counting.

– Filtering of data: how and how much should our data be filtered to eliminate false positives that would bias our counting.

– Application of the τ_c counting strategy: what is the best way to obtain a τ_c curve (from experimental or simulated data), and what is the range of stoichiometries that can be determined?

There are yet many obstacles to overcome until we can perform reliable molecular counting using FPs. However, the field will greatly benefit from new studies applying previously developed approaches. This collective experience, as much as cutting-edge developments, will contribute to eventually making qPALM a standard, trustable technique in biology labs.

Part V

Appendix

Guidelines for users of the AOTF control software

The two following documents were written as guidelines for the users of the Labview software controlling the AOTF of our microscope setup. The first document is meant as a user guide to the software, whereas the second one describes how the code functions and can be edited to introduce further developments.

Labview AOTF control v2.11
User guide

Daniel Thédié

December 10, 2018

Contents

AOTF control is a custom-made software that can be used to control the passage of lasers through the AOTF for modulation of illumination at the PALM microscope. It can also send trigger pulses to the EMCCD camera to synchronise image acquisition with laser illumination.

The software's main window is shown below on figure 1.

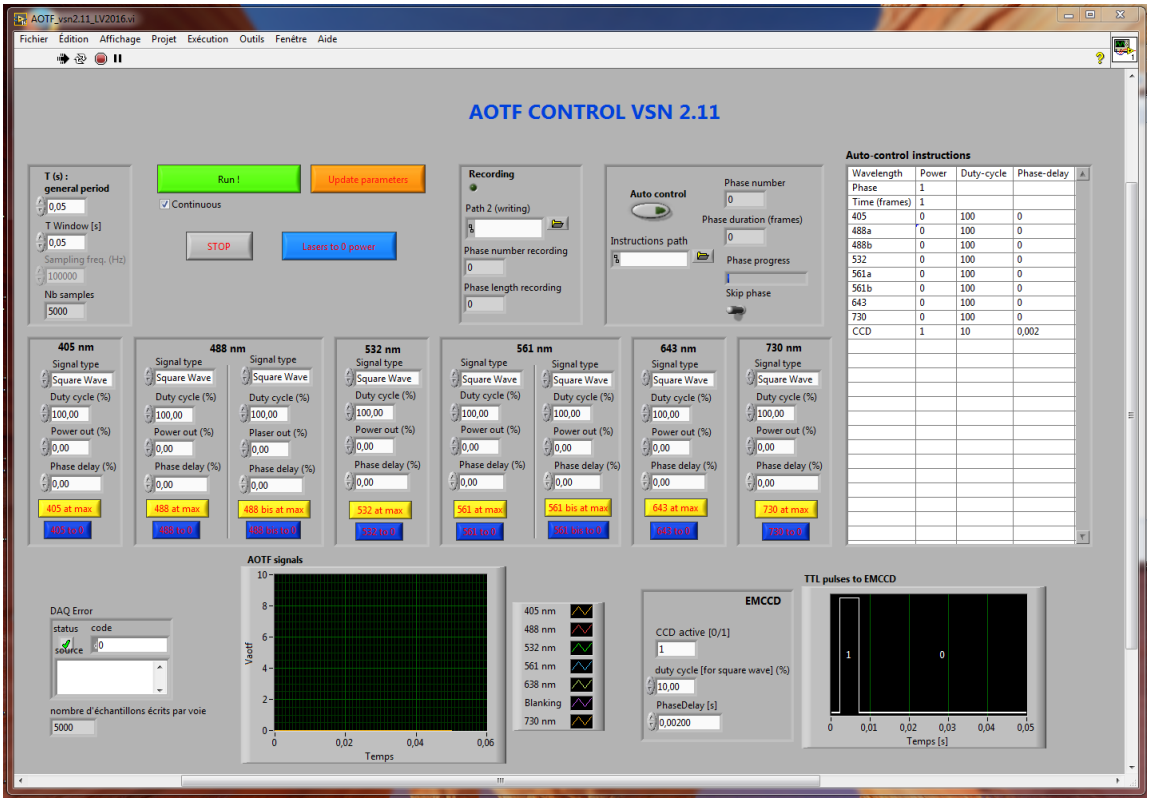

Figure 1: User interface of the AOTF control software (v2.11).

1 Continuous laser illumination

Available lasers are listed according to wavelength (405, 488, 532, 561, 643 and 730 nm).

- Enter a power output value between 0 and 100 in the field "Power out (%)".
- Check the "Continuous" box for continuous illumination, or leave it empty to produce a single laser pulse (length determined by the general period).
- Press the green "Run" button to start the laser illumination.

- If you change parameters *during* the run, press "Update parameters" (until then the changes will not be effective).

Note: values inferior to 1 can be entered. They are displayed as milli-units, so 0.1 will appear as 100m, 0.01 as 10m, etc. However at too low settings, the power response will stop behaving linearly (under approx. 0.1%). For lower illumination powers, use an optical density in front of the laser. You can also use the "Laser at max" and "Laser to 0" buttons to quickly set power output to 0 or 100. "Lasers to 0 power" sets all laser powers to 0.

2 Pulsed illumination

Pulsed illumination allows you to desynchronize different laser illuminations (e.g. excitation laser and 405-nm activation laser). This avoids the noise contribution of lasers other than the fluorescence excitation laser.

- Check the general period and T window (keep both equal). General period will define the length of the illumination cycles performed by the AOTF (represented on the AOTF signals graph).
- For each laser used, choose a duty cycle. This will define the duration of illumination per cycle, in percentage of the general period (e.g. a general period of 50 ms and duty cycle of 50% will result in 25 ms illumination per cycle).
- For each laser used, choose a phase delay. This will define when the illumination starts during the cycle, again in percentage of the general period (e.g. a general period of 50 ms and phase delay of 10% results in a 5 ms delay in each cycle before the laser illumination starts).
- Adjust the phase delay for the EMCCD, to trigger it synchronously with the fluorescence excitation laser. Note: there is a slight delay between lasers and EMCCD trigger, so if the laser starts at t = 0, the EMCCD phase delay should be set to 0.002 sec.

Figure 2 is an example of pulsed illumination to separate 643-nm fluorescence readout and 405-nm activation, with a frametime of 50 ms, and a general period of 80 ms.

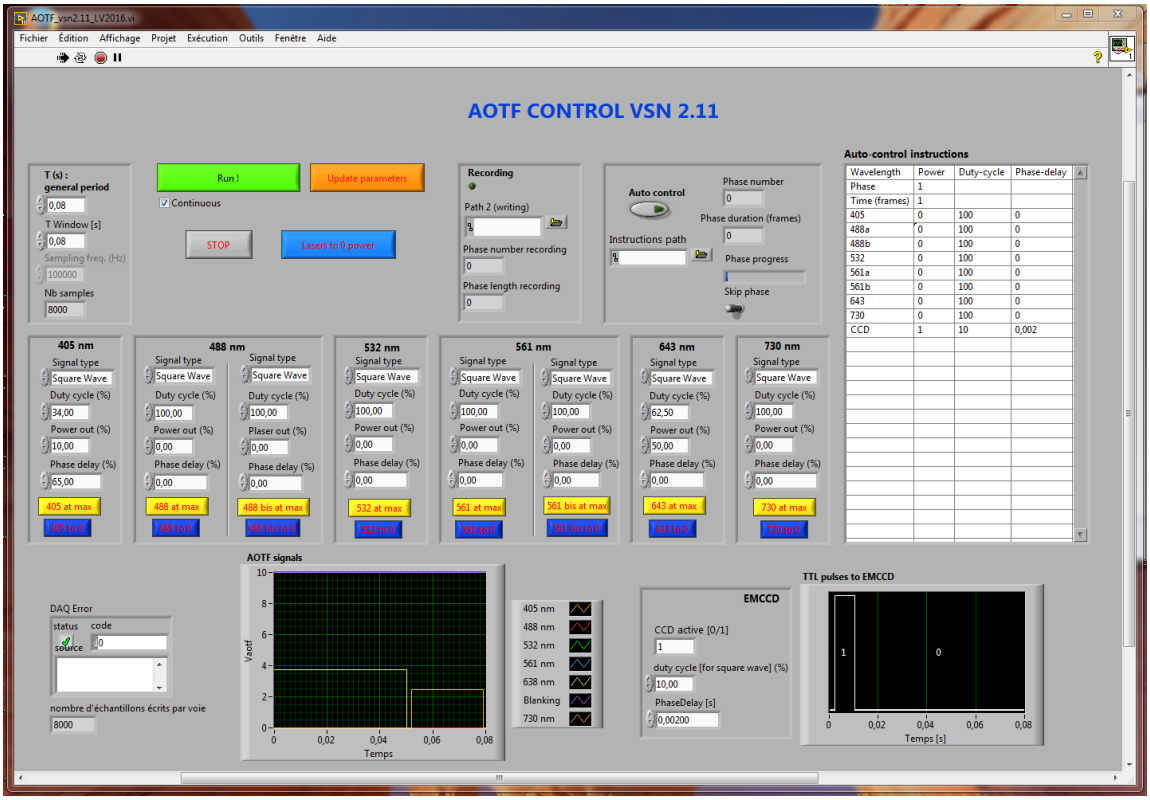

Figure 2: Example of configuration for pulsed illumination.

Furthermore, the 488- and 561-nm lasers are "duplicated" to allow creating two pulses at the same wavelength during the same cycle (can be used for example to create a weak 488-nm fluorescence readout followed by a strong 488-nm actinic illumination).

3 Recording illumination sequences

During an experiment, you might wish to change illumination conditions (e.g. gradually increase the power of the 405-nm laser). You can record the modifications you make in a text file.

To do so, enter a saving path in the "Recording" panel. The path can be one of an existing text file (will be over-written) or of an non-existing text file, in which case a new text file will be created.

Recording is automatically enabled if a valid path is entered. Once you press run, the recording will start, and the green diode will light up. If the diode stays off, then recording is not active.

The resulting text file is organized in "phases", which consist of consecutive cycles without changes in parameters (a new phase is created each time "Update parameters" is pressed). The length of the phase (i.e. number of cycles performed) is written under "Time (frames)", and for each laser, the power, duty-cycle and phase delay.

You can edit all parameters in the file manually for later use with auto-control (see next section). However, since we are running a french version of Labview, remember to use commas (",") as decimal separators, since points will not be recognized as such. You can also suppress phases, or add new ones by copy/pasting existing phases.

4 Using auto-control

Auto-control allows the software to read and execute a sequence of laser patterns from a text file (in the same format as produced by Recording). This can be used to replicate a previously recorded experiment, or apply the exact same sequence of illumination to different experiments.

To use auto-control, enter a path to a text file in the corresponding panel, and press the "auto-control" button (lights up green when activated). The table on the right gives you an overview of the contents of the text file. It can however not be edited (this has to be done directly on the text file). If you edit and save the text file, the changes should be immediately visible in Labview.

To start the experiment, press "Run". Phase number and duration are displayed in the auto-control panel, as well as a progression bar for the current phase. Note that if you are running in auto-control mode, you *cannot* manually modify lasers or EMCCD parameters. You can however stop the run before its end, or manually go to the next phase by pressing the "Skip phase" switch.

Labview AOTF control v2.11
Experimented user guide

Daniel Thédié

December 19, 2018

Contents

1 General description

Labview provides programming using a graphical interface (rather than written code lines). The code is therefore a diagram, variables are boxes whose values can be used by linking with threads, and operations are triangles or boxes. Figure 1 shows some of the basic elements which can be used. In Labview, a diagram is called a VI (Virtual Interface).

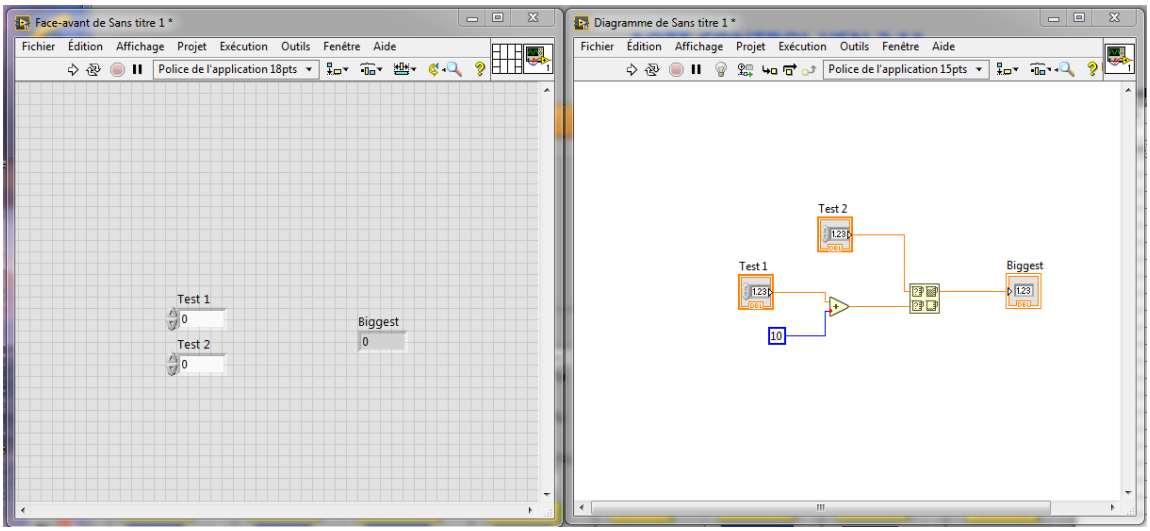

Figure 1: Example of a simple Labview code comparing the values of two manually entered variables.

To show the diagram of a code, go to the front panel and press Ctrl + E.

The AOTF control code consists of a main loop which runs continuously, which allows update the variables whenever the user modifies them. Inside this main loop, a "sequence" structure defines three main parts (figure 2):

- The initialization, which contain instructions for the "laser at max" and "laser to 0" buttons, writing of a new text file for "Recording", and reading the text file for "auto-control".
- The creation of the waveform (displayed as "AOTF signals" on the front panel). This part also contains the calibration function used to obtain a linear relation between input (user-specified value in the software) and output laser power (physical laser power delivered). All resulting waveforms are stored in a table.
- The execution of the waveforms. This uses three sub-VIs which should be included in the same folder as the main script: Setup.PreparePatterns, Setup.ExecutePatterns and Setup.TerminatePatterns.

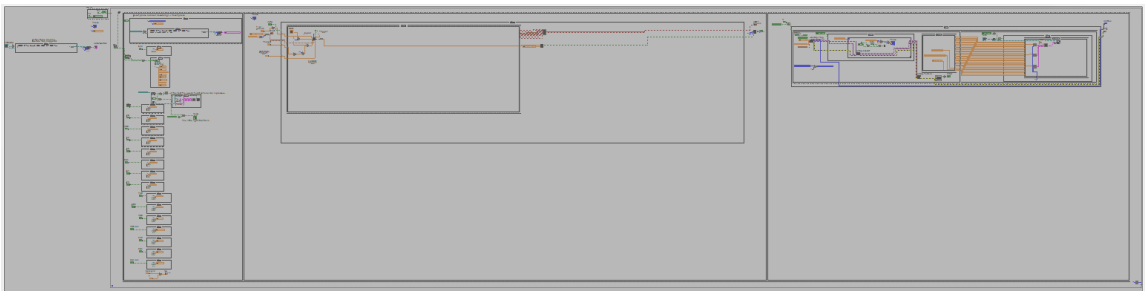

Figure 2: General overview of the diagram of the AOTF control software.

The following sections will explain in more details the functioning of each of the three parts of the diagram.

2 Initialization

Laser at max and laser to 0 Each laser has two "True/False" boxes, conditioned by the laser at max and laser to 0 buttons. They simply attribute the value 0 or 100 to the power of the corresponding laser.

Recording Conditions check if an existing path to a non-existing text file has been entered, and if "Run" has been pressed. If so, a new text file is created, with the header written (first line). A condition also lights up the diode if recording is active.

Auto-control If "Run" is *not* pressed, the text file is read. This is done continuously, so that updates made to the text file appear immediately in Labview. A condition gives a dummy instruction file to read if no path has been entered yet (note: it would also be possible to move the text file reading into this condition, and have nothing instead of the dummy).

3 Waveform generation

The main part of this section is duplicated with a condition depending on the auto-control (on or off). The only difference is where the parameters come from: either manual input, or auto-control instructions table.

Auto-control table reading The different parameters have to be fetched from the table, according to the phase we are in. An offset on the line to read is created according on the current

phase (figure 3). This is directly used to read the phase duration, and then for each laser the power, duty-cycle and phase delay.

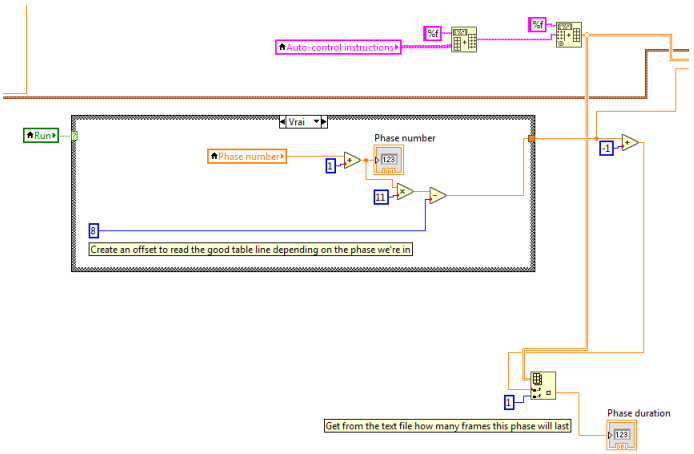

Figure 3: Offset calculation to read the parameters corresponding to the present phase.

Once laser parameters have been retrieved, duty-cycle and phase delay are directly used to create the waveform, whereas power is converted in voltage input thanks to a calibration function (figure 4) of the form $y(x) = a * \frac{\log(x+e^k)}{1-x+e^k} + b * x^l + c$. This function was found to best fit the response curve of the AOTF to the input voltage. The parameters a, b, c, e, k and l are determined experimentally.

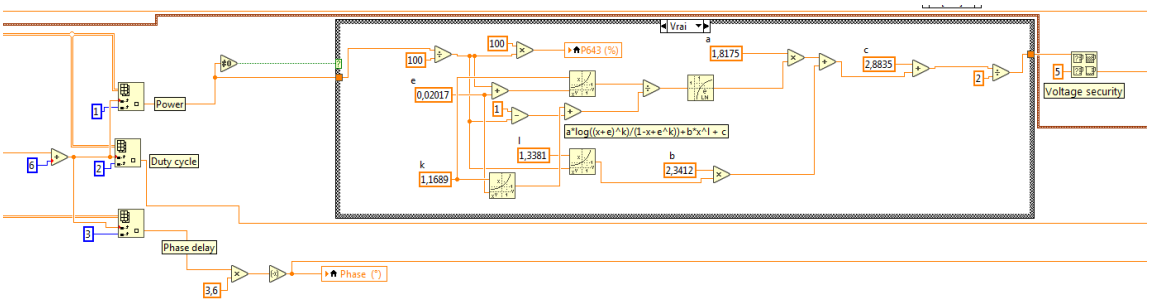

Figure 4: Mathematical function converting the input laser power (in % of max power) to voltage delivered to the AOTF.

The obtained voltage is filtered through a voltage security, which avoids sending a voltage superior to 5V to the AOTF. The waveforms are then created, and stored in a table.

Note: the duplication of the 488 and 561 lasers happens here: the two different inputs are used to

create two different waveforms, with a security to make sure that the sum of the two signals does not go over 100% power.

One panel is dedicated to the creation of the EMCCD waveform, and one to the creation of the blanking waveform. The blanking is used by the AOTF for auto-calibration, and should be 0 when no laser is activated, and 10V when at least one laser is activated.

4 Waveform execution

The waveform table "AOTF signals" is first passed to Setup.PreparePatterns. The pattern is then executed in a while loop, until "Update parameters" is pressed. This avoids performing the waveform creation steps at every cycle, which creates dead-times during acquisitions. Here, waveforms are only generated when a parameter is changed. Phase length recording is updated here. If auto-control is activated, the while loop is replaced by a for loop with the number of iterations depending on phase duration. Once the loop is broken, the pattern is closed in Setup.TerminatePatterns.

The last steps (figure 5) are used to write the recorded parameters (if Recording is active) to the text file. This needs to be done line by line (and therefore laser by laser).

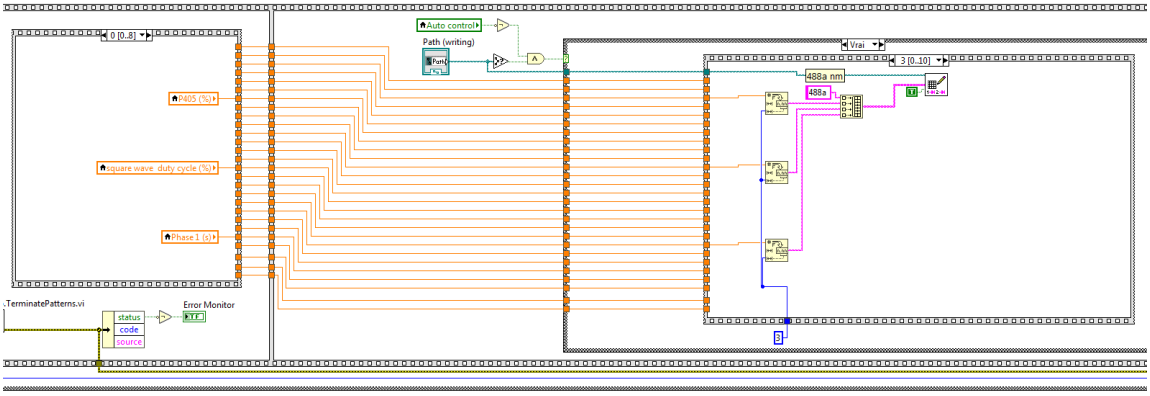

Figure 5: Recovery of recorded parameters, and writing into a text file.

Bibliography

[1] E. Abbe, "Beiträge zur Theorie des Mikroskops und der mikroskopischen Wahrnehmung," *Archiv für Mikroskopische Anatomie*, vol. 9, pp. 413–418, dec 1873. 14

[2] C. P. Toseland, "Fluorescent labeling and modification of proteins.," *Journal of chemical biology*, vol. 6, pp. 85–95, apr 2013. 15

[3] M. Byrdin, C. Duan, D. Bourgeois, and K. Brettel, "A Long-Lived Triplet State Is the Entrance Gateway to Oxidative Photochemistry in Green Fluorescent Proteins," *Journal of the American Chemical Society*, vol. 140, pp. 2897–2905, feb 2018. 15, 20, 39, 164

[4] O. SHIMOMURA, "The discovery of aequorin and green fluorescent protein," *Journal of Microscopy*, vol. 217, pp. 3–15, jan 2005. 16

[5] J. G. Morin and J. W. Hastings, "Energy transfer in a bioluminescent system," *Journal of Cellular Physiology*, vol. 77, pp. 313–318, jun 1971. 16

[6] M. Ormö, A. B. Cubitt, K. Kallio, L. A. Gross, R. Y. Tsien, and S. J. Remington, "Crystal Structure of the Aequorea victoria Green Fluorescent Protein," *Science*, vol. 273, pp. 1392–1395, sep 1996. 17, 21

[7] F. Yang, L. G. Moss, and G. N. Phillips, "The molecular structure of green fluorescent protein," *Nature Biotechnology*, vol. 14, pp. 1246–1251, oct 1996. 17, 22

[8] K. Brejc, T. K. Sixma, P. A. Kitts, S. R. Kain, R. Y. Tsien, M. Ormö, and S. J. Remington, "Structural basis for dual excitation and photoisomerization of the Aequorea victoria green fluorescent protein.," *Proceedings of the National Academy of Sciences of the United States of America*, vol. 94, pp. 2306–11, mar 1997. 17, 18

[9] . Jian Dong, . Kyril M. Solntsev, *, , . Olivier Poizat, and . Laren M. Tolbert*, "The Meta-Green Fluorescent Protein Chromophore," 2007. 17

[10] D. P. Barondeau, C. D. Putnam, C. J. Kassmann, J. A. Tainer, and E. D. Getzoff, "Mechanism and energetics of green fluorescent protein chromophore synthesis revealed by trapped intermediate structures.," *Proceedings of the National Academy of Sciences of the United States of America*, vol. 100, pp. 12111–6, oct 2003. 17

[11] S. J. Remington, "Fluorescent proteins: maturation, photochemistry and photophysics," *Current Opinion in Structural Biology*, vol. 16, pp. 714–721, dec 2006. 17

[12] A. B. Cubitt, R. Heim, S. R. Adams, A. E. Boyd, L. A. Gross, and R. Y. Tsien, "Understanding, improving and using green fluorescent proteins," *Trends in Biochemical Sciences*, vol. 20, pp. 448–455, nov 1995. 17

[13] R. Y. Tsien, "THE GREEN FLUORESCENT PROTEIN," *Annual Review of Biochemistry*, vol. 67, pp. 509–544, jun 1998. 17, 18

[14] Liping Zhang, Hetal N. Patel, , Jason W. Lappe, and R. M. Wachter*, "Reaction Progress of Chromophore Biogenesis in Green Fluorescent Protein," 2006. 17, 18

[15] M. Chattoraj, B. A. King, G. U. Bublitz, and S. G. Boxer, "Ultra-fast excited state dynamics in green fluorescent protein: multiple states and proton transfer.," *Proceedings of the National Academy of Sciences of the United States of America*, vol. 93, pp. 8362–7, aug 1996. 18

[16] M. V. Matz, A. F. Fradkov, Y. A. Labas, A. P. Savitsky, A. G. Zaraisky, M. L. Markelov, and S. A. Lukyanov, "Fluorescent proteins from nonbioluminescent Anthozoa species," *Nature Biotechnology*, vol. 17, pp. 969–973, oct 1999. 19, 21

[17] A. Salih, A. Larkum, G. Cox, M. Kühl, and O. Hoegh-Guldberg, "Fluorescent pigments in corals are photoprotective," *Nature*, vol. 408, pp. 850–853, dec 2000. 19

[18] S. Kawaguti, "Effect of the green fluorescent pigment on the productivity of the reef corals," *Micronesica*, vol. 5, no. 313, p. 121, 1969. 19

[19] D. Schlichter, H. W. Fricke, and W. Weber, "Light harvesting by wavelength transformation in a symbiotic coral of the Red Sea twilight zone," *Marine Biology*, vol. 91, no. 3, pp. 403–407, 1986. 19

[20] P. J. Cranfill, B. R. Sell, M. A. Baird, J. R. Allen, Z. Lavagnino, H. M. de Gruiter, G.-J. Kremers, M. W. Davidson, A. Ustione, and D. W. Piston, "Quantitative assessment of fluorescent proteins," *Nature Methods*, vol. 13, pp. 557–562, jul 2016. 19

[21] C. Duan, V. Adam, M. Byrdin, J. Ridard, S. Kieffer-Jaquinod, C. Morlot, D. Arcizet, I. Demachy, and D. Bourgeois, "Structural Evidence for a Two-Regime Photobleaching Mechanism in a Reversibly Switchable Fluorescent Protein," *Journal of the American Chemical Society*, vol. 135, pp. 15841–15850, oct 2013. 20

[22] V. Adam, R. Berardozzi, M. Byrdin, and D. Bourgeois, "Phototransformable fluorescent proteins: Future challenges," *Current Opinion in Chemical Biology*, vol. 20, pp. 92–102, jun 2014. 20, 30, 32, 33

[23] R. Heim, A. B. Cubitt, and R. Y. Tsien, "Improved green fluorescence," *Nature*, vol. 373, pp. 663–664, feb 1995. 21

[24] B. P. Cormack, R. H. Valdivia, and S. Falkow, "FACS-optimized mutants of the green fluorescent protein (GFP)," *Gene*, vol. 173, pp. 33–38, jan 1996. 21

[25] J. P. Levy, R. R. Muldoon, S. Zolotukhin, and C. J. Link, "Retroviral transfer and expression of a humanized, red-shifted green fluorescent protein gene into human tumor cells," *Nature Biotechnology*, vol. 14, pp. 610–614, may 1996. 21

[26] D. S. Bindels, L. Haarbosch, L. van Weeren, M. Postma, K. E. Wiese, M. Mastop, S. Aumonier, G. Gotthard, A. Royant, M. A. Hink, and T. W. J. Gadella, "mScarlet: a bright monomeric red fluorescent protein for cellular imaging," *Nature Methods*, vol. 14, pp. 53–56, jan 2017. 21

[27] R. Heim, D. C. Prasher, and R. Y. Tsien, "Wavelength mutations and posttranslational autoxidation of green fluorescent protein.," *Proceedings of the National Academy of Sciences of the United States of America*, vol. 91, pp. 12501–4, dec 1994. 21, 33

[28] R. E. Campbell, O. Tour, A. E. Palmer, P. A. Steinbach, G. S. Baird, D. A. Zacharias, and R. Y. Tsien, "A monomeric red fluorescent protein.," *Proceedings of the National Academy of Sciences of the United States of America*, vol. 99, pp. 7877–82, jun 2002. 22

[29] N. C. Shaner, "The mFruit Collection of Monomeric Fluorescent Proteins," *Clinical Chemistry*, vol. 59, pp. 440–441, feb 2013. 22

[30] D. Shcherbo, I. I. Shemiakina, A. V. Ryabova, K. E. Luker, B. T. Schmidt, E. A. Souslova, T. V. Gorodnicheva, L. Strukova, K. M. Shidlovskiy, O. V. Britanova, A. G. Zaraisky, K. A. Lukyanov, V. B. Loschenov, G. D. Luker, and D. M. Chudakov, "Near-infrared fluorescent proteins," *Nature Methods*, vol. 7, pp. 827–829, oct 2010. 22

[31] G. S. Filonov, K. D. Piatkevich, L.-M. Ting, J. Zhang, K. Kim, and V. V. Verkhusha, "Bright and stable near-infrared fluorescent protein for in vivo imaging," *Nature Biotechnology*, vol. 29, pp. 757–761, aug 2011. 22

[32] D. A. Zacharias, J. D. Violin, A. C. Newton, and R. Y. Tsien, "Partitioning of lipid-modified monomeric GFPs into membrane microdomains of live cells.," *Science (New York, N.Y.)*, vol. 296, pp. 913–6, may 2002. 22

[33] D. C. Prasher, V. K. Eckenrode, W. W. Ward, F. G. Prendergast, and M. J. Cormier, "Primary structure of the Aequorea victoria green-fluorescent protein," *Gene*, vol. 111, pp. 229–233, feb 1992. 22

[34] M. Chalfie, Y. Tu, G. Euskirchen, W. W. Ward, and D. C. Prasher, "Green fluorescent protein as a marker for gene expression.," *Science (New York, N.Y.)*, vol. 263, pp. 802–5, feb 1994. 22

[35] J. Lippincott-Schwartz and C. L. Smith, "Insights into secretory and endocytic membrane traffic using green fluorescent protein chimeras," *Current Opinion in Neurobiology*, vol. 7, pp. 631–639, oct 1997. 23

[36] D. M. Raskin and P. A. de Boer, "MinDE-dependent pole-to-pole oscillation of division inhibitor MinC in Escherichia coli.," *Journal of bacteriology*, vol. 181, pp. 6419–24, oct 1999. 23

[37] P. van Roessel and A. H. Brand, "Imaging into the future: visualizing gene expression and protein interactions with fluorescent proteins," *Nature Cell Biology*, vol. 4, pp. E15–E20, jan 2002. 23

[38] T. Förster, "Zwischenmolekulare Energiewanderung und Fluoreszenz," *Annalen der Physik*, vol. 437, pp. 55–75, jan 1948. 24

[39] L. Stryer and R. P. Haugland, "Energy transfer: a spectroscopic ruler.," *Proceedings of the National Academy of Sciences of the United States of America*, vol. 58, pp. 719–26, aug 1967. 24

[40] D. E. Clapham, "Calcium signaling," *Cell*, vol. 80, pp. 259–268, jan 1995. 24

[41] J. M. Kendall and M. N. Badminton, "Aequorea victoria bioluminescence moves into an exciting new era," *Trends in Biotechnology*, vol. 16, pp. 216–224, dec 1998. 24

[42] A. Miyawaki, J. Llopis, R. Heim, J. M. McCaffery, J. A. Adams, M. Ikura, and R. Y. Tsien, "Fluorescent indicators for Ca2+based on green fluorescent proteins and calmodulin," *Nature*, vol. 388, pp. 882–887, aug 1997. 24

[43] B. G. Oscar, W. Liu, Y. Zhao, L. Tang, Y. Wang, R. E. Campbell, and C. Fang, "Excited-state structural dynamics of a dual-emission calmodulin-green fluorescent protein sensor for calcium ion imaging," *Proceedings of the National Academy of Sciences*, vol. 111, pp. 10191 LP – 10196, jul 2014. 24

[44] Y. Qian, K. D. Piatkevich, B. Mc Larney, A. S. Abdelfattah, S. Mehta, M. H. Murdock, S. Gottschalk, R. S. Molina, W. Zhang, Y. Chen, J. Wu, M. Drobizhev, T. E. Hughes, J. Zhang, E. R. Schreiter, S. Shoham, D. Razansky, E. S. Boyden, and R. E. Campbell, "A genetically encoded near-infrared fluorescent calcium ion indicator," *Nature Methods*, vol. 16, pp. 171–174, feb 2019. 24

[45] R. Bizzarri, M. Serresi, S. Luin, and F. Beltram, "Green fluorescent protein based pH indicators for in vivo use: A review," *Analytical and Bioanalytical Chemistry*, vol. 393, pp. 1107–1122, feb 2009. 25

[46] R. M. Dickson, A. B. Cubitt, R. Y. Tsien, and W. E. Moerner, "On/off blinking and switching behaviour of single molecules of green fluorescent protein," *Nature*, vol. 388, pp. 355–358, jul 1997. 30, 37, 39, 42

[47] M. B. Elowitz, M. G. Surette, P.-E. Wolf, J. Stock, and S. Leibler, "Photoactivation turns green fluorescent protein red," *Current Biology*, vol. 7, pp. 809–812, oct 1997. 30

[48] A. M. Bogdanov, A. S. Mishin, I. V. Yampolsky, V. V. Belousov, D. M. Chudakov, F. V. Subach, V. V. Verkhusha, S. Lukyanov, and K. A. Lukyanov, "Green fluorescent proteins are light-induced electron donors," *Nature Chemical Biology*, vol. 5, pp. 459–461, jul 2009. 30

[49] R. Ando, H. Mizuno, and A. Miyawaki, "Regulated fast nucleocytoplasmic shuttling observed by reversible protein highlighting.," *Science (New York, N.Y.)*, vol. 306, pp. 1370–3, nov 2004. 31, 33

[50] R. Ando, H. Hama, M. Yamamoto-Hino, H. Mizuno, and A. Miyawaki, "An optical marker based on the UV-induced green-to-red photoconversion of a fluorescent protein.," *Proceedings of the National Academy of Sciences of the United States of America*, vol. 99, pp. 12651–6, oct 2002. 31, 33, 34

[51] J. Wiedenmann, S. Ivanchenko, F. Oswald, F. Schmitt, C. Röcker, A. Salih, K.-D. Spindler, and G. U. Nienhaus, "EosFP, a fluorescent marker protein with UV-inducible green-to-red fluorescence conversion," *Proceedings of the National Academy of Sciences*, vol. 101, pp. 15905–15910, nov 2004. 31, 33, 34, 159

[52] G. H. Patterson and J. Lippincott-Schwartz, "A photoactivatable GFP for selective photolabeling of proteins and cells.," *Science (New York, N.Y.)*, vol. 297, pp. 1873–7, sep 2002. 31

[53] F. V. Subach, G. H. Patterson, S. Manley, J. M. Gillette, J. Lippincott-Schwartz, and V. V. Verkhusha, "Photoactivatable mCherry for high-resolution two-color fluorescence microscopy," *Nature Methods*, vol. 6, pp. 153–159, feb 2009. 33

[54] M. Andresen, A. C. Stiel, J. Fölling, D. Wenzel, A. Schönle, A. Egner, C. Eggeling, S. W. Hell, and S. Jakobs, "Photoswitchable fluorescent proteins enable monochromatic multilabel imaging and dual color fluorescence nanoscopy," *Nature Biotechnology*, vol. 26, pp. 1035–1040, sep 2008. 33

[55] T. Brakemann, A. C. Stiel, G. Weber, M. Andresen, I. Testa, T. Grotjohann, M. Leutenegger, U. Plessmann, H. Urlaub, C. Eggeling, M. C. Wahl, S. W. Hell, and S. Jakobs, "A reversibly photoswitchable GFP-like protein with fluorescence excitation decoupled from switching," *Nature Biotechnology*, vol. 29, pp. 942–947, oct 2011. 33

[56] T. Grotjohann, I. Testa, M. Leutenegger, H. Bock, N. T. Urban, F. Lavoie-Cardinal, K. I. Willig, C. Eggeling, S. Jakobs, and S. W. Hell, "Diffraction-unlimited all-optical imaging and writing with a photochromic GFP," *Nature*, vol. 478, pp. 204–208, oct 2011. 33

[57] T. Grotjohann, I. Testa, M. Reuss, T. Brakemann, C. Eggeling, S. W. Hell, and S. Jakobs, "rsEGFP2 enables fast RESOLFT nanoscopy of living cells," *eLife*, vol. 1, dec 2012. 33

[58] M. El Khatib, A. Martins, D. Bourgeois, J.-P. Colletier, and V. Adam, "Rational design of ultrastable and reversibly photoswitchable fluorescent proteins for super-resolution imaging of the bacterial periplasm," *Scientific Reports*, vol. 6, p. 18459, may 2016. 33

[59] M. Zhang, H. Chang, Y. Zhang, J. Yu, L. Wu, W. Ji, J. Chen, B. Liu, J. Lu, Y. Liu, J. Zhang, P. Xu, and T. Xu, "Rational design of true monomeric and bright photoactivatable fluorescent proteins," *Nature Methods*, vol. 9, pp. 727–729, jul 2012. 34, 35, 88

[60] S. A. McKinney, C. S. Murphy, K. L. Hazelwood, M. W. Davidson, and L. L. Looger, "A bright and photostable photoconvertible fluorescent protein," *Nature Methods*, vol. 6, pp. 131–133, feb 2009. 34, 35

[61] D. M. Chudakov, S. Lukyanov, and K. A. Lukyanov, "Tracking intracellular protein movements using photoswitchable fluorescent proteins PS-CFP2 and Dendra2," *Nature Protocols*, vol. 2, pp. 2024–2032, aug 2007. 34

[62] A. L. McEvoy, H. Hoi, M. Bates, E. Platonova, P. J. Cranfill, M. A. Baird, M. W. Davidson, H. Ewers, J. Liphardt, and R. E. Campbell, "mMaple: A Photoconvertible Fluorescent Protein for Use in Multiple Imaging Modalities," *PLoS ONE*, vol. 7, p. e51314, dec 2012. 34

[63] M. Byrdin and D. Bourgeois, "The CAL(AI)2DOSCOPE: a microspectrophotometer for accurate recording of correlated absorbance and fluorescence emission spectra," *Spectroscopy Europe*, vol. 28, no. 6, pp. 14–17, 2016. 34

[64] N. Coquelle, M. Sliwa, J. Woodhouse, G. Schirò, V. Adam, A. Aquila, T. R. M. Barends, S. Boutet, M. Byrdin, S. Carbajo, E. De la Mora, R. B. Doak, M. Feliks, F. Fieschi, L. Foucar, V. Guillon, M. Hilpert, M. S. Hunter, S. Jakobs, J. E. Koglin, G. Kovacsova, T. J. Lane, B. Lévy, M. Liang, K. Nass, J. Ridard, J. S. Robinson, C. M. Roome, C. Ruckebusch, M. Seaberg, M. Thepaut, M. Cammarata, I. Demachy, M. Field, R. L. Shoeman, D. Bourgeois, J.-P. Colletier, I. Schlichting, and M. Weik, "Chromophore twisting in the excited state of a photoswitchable fluorescent protein captured by time-resolved serial femtosecond crystallography," *Nature Chemistry*, vol. 10, pp. 31–37, jan 2018. 34, 153

[65] M. G. Paez-Segala, M. G. Sun, G. Shtengel, S. Viswanathan, M. A. Baird, J. J. Macklin, R. Patel, J. R. Allen, E. S. Howe, G. Piszczek, H. F. Hess, M. W. Davidson, Y. Wang, and L. L. Looger, "Fixation-resistant photoactivatable fluorescent proteins for CLEM," *Nature Methods*, vol. 12, pp. 215–218, mar 2015. 35, 88

[66] V. Adam, M. Lelimousin, S. Boehme, G. Desfonds, K. Nienhaus, M. J. Field, J. Wiedenmann, S. McSweeney, G. U. Nienhaus, and D. Bourgeois, "Structural characterization of IrisFP, an optical highlighter undergoing multiple photo-induced transformations.," *Proceedings of the National Academy of Sciences of the United States of America*, vol. 105, pp. 18343–8, nov 2008. 36, 90

[67] J. Fuchs, S. Böhme, F. Oswald, P. N. Hedde, M. Krause, J. Wiedenmann, and G. U. Nienhaus, "A photoactivatable marker protein for pulse-chase imaging with superresolution," *Nature Methods*, vol. 7, pp. 627–630, aug 2010. 36

[68] B. Moeyaert, N. Nguyen Bich, E. De Zitter, S. Rocha, K. Clays, H. Mizuno, L. van Meervelt, J. Hofkens, and P. Dedecker, "Green-to-Red Photoconvertible Dronpa Mutant for Multimodal Super-resolution Fluorescence Microscopy," *ACS Nano*, vol. 8, pp. 1664–1673, feb 2014. 36

[69] N. Durisic, L. Laparra-Cuervo, Á. Sandoval-Álvarez, J. S. Borbely, and M. Lakadamyali, "Single-molecule evaluation of fluorescent protein photoactivation efficiency using an in vivo nanotemplate," *Nature Methods*, vol. 11, pp. 156–162, feb 2014. 36, 100

[70] P. Schwille, S. Kummer, A. A. Heikal, W. E. Moerner, and W. W. Webb, "Fluorescence correlation spectroscopy reveals fast optical excitation-driven intramolecular dynamics of yellow fluorescent proteins.," *Proceedings of the National Academy of Sciences of the United States of America*, vol. 97, pp. 151–6, jan 2000. 37

[71] N. V. Klementieva, A. I. Pavlikov, A. A. Moiseev, N. G. Bozhanova, N. M. Mishina, S. A. Lukyanov, E. V. Zagaynova, K. A. Lukyanov, and A. S. Mishin, "Intrinsic blinking of red fluorescent proteins for super-resolution microscopy," *Chemical Communications*, vol. 53, pp. 949–951, jan 2017. 37

[72] P. Annibale, M. Scarselli, A. Kodiyan, and A. Radenovic, "Photoactivatable Fluorescent Protein mEos2 Displays Repeated Photoactivation after a Long-Lived Dark State in the Red Photoconverted Form," *The Journal of Physical Chemistry Letters*, vol. 1, pp. 1506–1510, may 2010. 37, 107, 164

[73] S.-H. Lee, J. Y. Shin, A. Lee, and C. Bustamante, "Counting single photoactivatable fluorescent molecules by photoactivated localization microscopy (PALM)," *Proceedings of the*

National Academy of Sciences, vol. 109, no. 43, pp. 17436–17441, 2012. 37, 39, 53, 56, 75, 107, 109, 110, 133, 134, 138, 140, 147

[74] R. Berardozzi, V. Adam, A. Martins, and D. Bourgeois, "Arginine 66 Controls Dark-State Formation in Green-to-Red Photoconvertible Fluorescent Proteins," *Journal of the American Chemical Society*, vol. 138, no. 2, pp. 558–565, 2016. 37, 38, 39, 68, 69, 94, 106, 107, 109, 110, 151, 164

[75] V. Adam, P. Carpentier, S. Violot, M. Lelimousin, C. Darnault, G. U. Nienhaus, and D. Bourgeois, "Structural Basis of X-ray-Induced Transient Photobleaching in a Photoactivatable Green Fluorescent Protein," *Journal of the American Chemical Society*, vol. 131, pp. 18063–18065, dec 2009. 37

[76] A. Roy, M. J. Field, V. Adam, and D. Bourgeois, "The nature of transient dark states in a photoactivatable fluorescent protein," *Journal of the American Chemical Society*, vol. 133, no. 46, pp. 18586–18589, 2011. 37, 39, 97, 151

[77] F. Malvezzi-Campeggi, M. Jahnz, K. G. Heinze, P. Dittrich, and P. Schwille, "Light-Induced Flickering of DsRed Provides Evidence for Distinct and Interconvertible Fluorescent States," *Biophysical Journal*, vol. 81, pp. 1776–1785, sep 2001. 39

[78] U. Endesfelder, S. Malkusch, B. Flottmann, J. Mondry, P. Liguzinski, P. J. Verveer, M. Heilemann, U. Endesfelder, S. Malkusch, B. Flottmann, J. Mondry, P. Liguzinski, P. J. Verveer, and M. Heilemann, "Chemically Induced Photoswitching of Fluorescent ProbesA General Concept for Super-Resolution Microscopy," *Molecules*, vol. 16, pp. 3106–3118, apr 2011. 39

[79] T. N. Baldering, M. S. Dietz, K. Gatterdam, C. Karathanasis, R. Wieneke, R. Tampé, and M. Heilemann, "Synthetic and genetic dimers as quantification ruler for single-molecule counting with PALM," *Molecular Biology of the Cell*, vol. 30, pp. 1369–1376, jun 2019. 39

[80] J. Vogelsang, R. Kasper, C. Steinhauer, B. Person, M. Heilemann, M. Sauer, and P. Tinnefeld, "A Reducing and Oxidizing System Minimizes Photobleaching and Blinking of Fluorescent Dyes," *Angewandte Chemie International Edition*, vol. 47, pp. 5465–5469, jul 2008. 39

[81] M. Heilemann, S. vandeLinde, M. Schüttpelz, R. Kasper, B. Seefeldt, A. Mukherjee, P. Tinnefeld, and M. Sauer, "Subdiffraction-Resolution Fluorescence Imaging with Conventional Fluorescent Probes," *Angewandte Chemie International Edition*, vol. 47, pp. 6172–6176, aug 2008. 39

[82] A. Jiménez-Banzo, S. Nonell, J. Hofkens, and C. Flors, "Singlet Oxygen Photosensitization by EGFP and its Chromophore HBDI," *Biophysical Journal*, vol. 94, pp. 168–172, jan 2008. 39

[83] W. P. Dempsey, L. Georgieva, P. M. Helbling, A. Y. Sonay, T. V. Truong, M. Haffner, and P. Pantazis, "In vivo single-cell labeling by confined primed conversion," *Nature Methods*, vol. 12, pp. 645–648, jul 2015. 40

[84] M. A. Mohr, A. Y. Kobitski, L. R. Sabater, K. Nienhaus, C. J. Obara, J. Lippincott-Schwartz, G. U. Nienhaus, and P. Pantazis, "Rational Engineering of Photoconvertible Fluorescent Proteins for Dual-Color Fluorescence Nanoscopy Enabled by a Triplet-State Mechanism of

Primed Conversion," *Angewandte Chemie International Edition*, vol. 56, pp. 11628–11633, sep 2017. 40

[85] E. Betzig and J. K. Trautman, "Near-field optics: microscopy, spectroscopy, and surface modification beyond the diffraction limit.," *Science (New York, N.Y.)*, vol. 257, pp. 189–95, jul 1992. 41

[86] R. Heintzmann and C. G. Cremer, "Laterally modulated excitation microscopy: improvement of resolution by using a diffraction grating," vol. 3568, pp. 185–196, International Society for Optics and Photonics, jan 1999. 41

[87] M. G. L. Gustafsson, "Surpassing the lateral resolution limit by a factor of two using structured illumination microscopy.," *Journal of Microscopy*, vol. 198, pp. 82–87, may 2000. 41

[88] S. W. Hell and J. Wichmann, "Breaking the diffraction resolution limit by stimulated emission: stimulated-emission-depletion fluorescence microscopy," *Optics Letters*, vol. 19, p. 780, jun 1994. 41

[89] E. Betzig, G. H. Patterson, R. Sougrat, O. W. Lindwasser, S. Olenych, J. S. Bonifacino, M. W. Davidson, J. Lippincott-Schwartz, and H. F. Hess, "Imaging Intracellular Fluorescent Proteins at Nanometer Resolution," *Science*, vol. 313, pp. 1642–1645, sep 2006. 41, 42

[90] S. T. Hess, T. P. Girirajan, and M. D. Mason, "Ultra-High Resolution Imaging by Fluorescence Photoactivation Localization Microscopy," *Biophysical Journal*, vol. 91, pp. 4258–4272, dec 2006. 41, 42

[91] W. E. Moerner and L. Kador, "Optical detection and spectroscopy of single molecules in a solid," *Physical Review Letters*, vol. 62, pp. 2535–2538, may 1989. 42

[92] M. Orrit and J. Bernard, "Single pentacene molecules detected by fluorescence excitation in a p-terphenyl crystal," *Physical Review Letters*, vol. 65, pp. 2716–2719, nov 1990. 42

[93] H. Nyquist, "Certain Topics in Telegraph Transmission Theory," *Transactions of the American Institute of Electrical Engineers*, vol. 47, pp. 617–644, apr 1928. 42

[94] M. J. Rust, M. Bates, and X. Zhuang, "Sub-diffraction-limit imaging by stochastic optical reconstruction microscopy (STORM)," *Nature Methods*, vol. 3, pp. 793–796, oct 2006. 42

[95] A. Sharonov and R. M. Hochstrasser, "Wide-field subdiffraction imaging by accumulated binding of diffusing probes," *Proceedings of the National Academy of Sciences*, vol. 103, pp. 18911–18916, dec 2006. 42

[96] M. Heilemann, S. vandeLinde, M. Schüttpelz, R. Kasper, B. Seefeldt, A. Mukherjee, P. Tinnefeld, and M. Sauer, "Subdiffraction-Resolution Fluorescence Imaging with Conventional Fluorescent Probes," *Angewandte Chemie International Edition*, vol. 47, pp. 6172–6176, aug 2008. 42

[97] J. B. Grimm, B. P. English, H. Choi, A. K. Muthusamy, B. P. Mehl, P. Dong, T. A. Brown, J. Lippincott-Schwartz, Z. Liu, T. Lionnet, and L. D. Lavis, "Bright photoactivatable fluorophores for single-molecule imaging," *Nature Methods*, vol. 13, pp. 985–988, dec 2016. 42, 50, 124

[98] T. Dertinger, R. Colyer, G. Iyer, S. Weiss, and J. Enderlein, "Fast, background-free, 3D super-resolution optical fluctuation imaging (SOFI).," *Proceedings of the National Academy of Sciences of the United States of America*, vol. 106, pp. 22287–92, dec 2009. 44

[99] D. T. Burnette, P. Sengupta, Y. Dai, J. Lippincott-Schwartz, and B. Kachar, "Bleaching/blinking assisted localization microscopy for superresolution imaging using standard fluorescent molecules.," *Proceedings of the National Academy of Sciences of the United States of America*, vol. 108, pp. 21081–6, dec 2011. 44

[100] S. J. Holden, S. Uphoff, and A. N. Kapanidis, "DAOSTORM: an algorithm for high- density super-resolution microscopy," *Nature Methods*, vol. 8, pp. 279–280, apr 2011. 44

[101] F. Huang, S. L. Schwartz, J. M. Byars, and K. A. Lidke, "Simultaneous multiple-emitter fitting for single molecule super-resolution imaging," *Biomedical Optics Express*, vol. 2, p. 1377, may 2011. 44

[102] S. Cox, E. Rosten, J. Monypenny, T. Jovanovic-Talisman, D. T. Burnette, J. Lippincott-Schwartz, G. E. Jones, and R. Heintzmann, "Bayesian localization microscopy reveals nanoscale podosome dynamics," *Nature Methods*, vol. 9, pp. 195–200, feb 2012. 44

[103] L. Zhu, W. Zhang, D. Elnatan, and B. Huang, "Faster STORM using compressed sensing," *Nature Methods*, vol. 9, pp. 721–723, jul 2012. 44

[104] N. Gustafsson, S. Culley, G. Ashdown, D. M. Owen, P. M. Pereira, and R. Henriques, "Fast live-cell conventional fluorophore nanoscopy with ImageJ through super-resolution radial fluctuations," *Nature Communications*, vol. 7, p. 12471, nov 2016. 44

[105] R. J. Marsh, K. Pfisterer, P. Bennett, L. M. Hirvonen, M. Gautel, G. E. Jones, and S. Cox, "Artifact-free high-density localization microscopy analysis," *Nature Methods*, vol. 15, pp. 689–692, sep 2018. 44

[106] J. MacQueen, "Some methods for classification and analysis of multivariate observations," in *Proceedings of the fifth Berkeley symposium on mathematical statistics and probability*, vol. 1, pp. 281–297, Oakland, CA, USA, 1967. 45

[107] M. Ester, H.-P. Kriegel, J. Sander, and X. Xu, "A Density-Based Algorithm for Discovering Clusters in Large Spatial Databases with Noise," in *Proceedings of the 2nd International Conference on Knowledge Discovery and Data Mining*, 1996. 45

[108] Q. Du, V. Faber, and M. Gunzburger, "Centroidal Voronoi Tessellations: Applications and Algorithms," *SIAM Review*, 2005. 45

[109] P. Annibale, S. Vanni, M. Scarselli, U. Rothlisberger, and A. Radenovic, "Identification of clustering artifacts in photoactivated localization microscopy," *Nature Methods*, vol. 8, pp. 527–528, jul 2011. 45, 131

[110] S. Manley, J. M. Gillette, G. H. Patterson, H. Shroff, H. F. Hess, E. Betzig, and J. Lippincott-Schwartz, "High-density mapping of single-molecule trajectories with photoactivated localization microscopy," *Nature Methods*, vol. 5, pp. 155–157, feb 2008. 46

[111] D. Alcor, G. Gouzer, and A. Triller, "Single-particle tracking methods for the study of membrane receptors dynamics," *European Journal of Neuroscience*, vol. 30, pp. 987–997, sep 2009. 46, 48, 49

[112] A. N. Kapanidis, S. Uphoff, and M. Stracy, "Understanding Protein Mobility in Bacteria by Tracking Single Molecules," *Journal of Molecular Biology*, may 2018. 46

[113] A. Kusumi, T. A. Tsunoyama, K. M. Hirosawa, R. S. Kasai, and T. K. Fujiwara, "Tracking single molecules at work in living cells," *Nature Chemical Biology*, vol. 10, pp. 524–532, jul 2014. 49

[114] D. Calebiro, F. Rieken, J. Wagner, T. Sungkaworn, U. Zabel, A. Borzi, E. Cocucci, A. Zürn, and M. J. Lohse, "Single-molecule analysis of fluorescently labeled G-protein-coupled receptors reveals complexes with distinct dynamics and organization.," *Proceedings of the National Academy of Sciences of the United States of America*, vol. 110, pp. 743–8, jan 2013. 49

[115] J. Elf, G.-W. Li, and X. S. Xie, "Probing transcription factor dynamics at the single-molecule level in a living cell.," *Science (New York, N.Y.)*, vol. 316, pp. 1191–4, may 2007. 49

[116] K. A. K. Tanaka, K. G. N. Suzuki, Y. M. Shirai, S. T. Shibutani, M. S. H. Miyahara, H. Tsuboi, M. Yahara, A. Yoshimura, S. Mayor, T. K. Fujiwara, and A. Kusumi, "Membrane molecules mobile even after chemical fixation," *Nature Methods*, vol. 7, pp. 865–866, nov 2010. 50

[117] F. Fricke, J. Beaudouin, R. Eils, and M. Heilemann, "One, two or three? Probing the stoichiometry of membrane proteins by single-molecule localization microscopy," *Scientific Reports*, vol. 5, p. 14072, nov 2015. 52, 53, 54, 133

[118] P. Annibale, S. Vanni, M. Scarselli, U. Rothlisberger, and A. Radenovic, "Quantitative Photo Activated Localization Microscopy: Unraveling the Effects of Photoblinking," *PLoS ONE*, vol. 6, p. e22678, jul 2011. 53, 55

[119] C. Coltharp, R. P. Kessler, and J. Xiao, "Accurate Construction of Photoactivated Localization Microscopy (PALM) Images for Quantitative Measurements," *PLoS ONE*, vol. 7, p. e51725, dec 2012. 53

[120] E. M. Puchner, J. M. Walter, R. Kasper, B. Huang, and W. A. Lim, "Counting molecules in single organelles with superresolution microscopy allows tracking of the endosome maturation trajectory.," *Proceedings of the National Academy of Sciences of the United States of America*, vol. 110, pp. 16015–20, oct 2013. 53

[121] S. Avilov, R. Berardozzi, M. S. Gunewardene, V. Adam, S. T. Hess, and D. Bourgeois, "In cellulo evaluation of phototransformation quantum yields in fluorescent proteins used as markers for single-molecule localization microscopy," *PloS One*, vol. 9, no. 6, p. e98362, 2014. 53, 58, 110

[122] G. C. Rollins, J. Y. Shin, C. Bustamante, and S. Pressé, "Stochastic approach to the molecular counting problem in superresolution microscopy.," *Proceedings of the National Academy of Sciences of the United States of America*, vol. 112, pp. E110–8, jan 2015. 53, 134

[123] J. V. Thevathasan, M. Kahnwald, K. Cieśliński, P. Hoess, S. K. Peneti, M. Reitberger, D. Heid, K. C. Kasuba, S. J. Hoerner, Y. Li, Y.-L. Wu, M. Mund, U. Matti, P. M. Pereira, R. Henriques, B. Nijmeijer, M. Kueblbeck, V. J. Sabinina, J. Ellenberg, and J. Ries, "Nuclear pores as versatile reference standards for quantitative superresolution microscopy," *bioRxiv*, p. 582668, mar 2019. 53, 134

[124] G. Hummer, F. Fricke, and M. Heilemann, "Model-independent counting of molecules in single-molecule localization microscopy," *Molecular Biology of the Cell*, vol. 27, pp. 3637–3644, nov 2016. 53, 133

[125] T. N. Baldering, M. S. Dietz, K. Gatterdam, C. Karathanasis, R. Wieneke, R. Tampé, and M. Heilemann, "Synthetic and genetic dimers as quantification ruler for single-molecule counting with PALM," *Molecular Biology of the Cell*, vol. 30, pp. 1369–1376, jun 2019. 53

[126] D. G. Gibson, L. Young, R.-Y. Chuang, J. C. Venter, C. A. Hutchison, and H. O. Smith, "Enzymatic assembly of DNA molecules up to several hundred kilobases," *Nature Methods*, vol. 6, pp. 343–345, may 2009. 65

[127] M. Cotlet, J. Hofkens, F. Köhn, J. Michiels, G. Dirix, M. Van Guyse, J. Vanderleyden, and F. C. De Schryver, "Collective effects in individual oligomers of the red fluorescent coral protein DsRed," *Chemical Physics Letters*, vol. 336, pp. 415–423, mar 2001. 67

[128] S. Habuchi, R. Ando, P. Dedecker, W. Verheijen, H. Mizuno, A. Miyawaki, and J. Hofkens, "Reversible single-molecule photoswitching in the GFP-like fluorescent protein Dronpa.," *Proceedings of the National Academy of Sciences of the United States of America*, vol. 102, pp. 9511–6, jul 2005. 67, 90, 98

[129] N. Limpan, T. Prodpran, S. Benjakul, and S. Prasarpran, "Properties of biodegradable blend films based on fish myofibrillar protein and polyvinyl alcohol as influenced by blend composition and pH level," *Journal of Food Engineering*, vol. 100, pp. 85–92, sep 2010. 67

[130] R. M. Dickson, D. J. Norris, Y.-L. Tzeng, and W. E. Moerner, "Three-Dimensional Imaging of Single Molecules Solvated in Pores of Poly(acrylamide) Gels," *Science*, vol. 274, no. 5289, pp. 966–968, 1996. 68

[131] S. Schäfer, P. Dittrich, E. Petrov, and P. Schwille, "Single molecule fluorescence imaging of the photoinduced conversion and bleaching behavior of the fluorescent protein Kaede," *Microscopy Research and Technique*, vol. 69, no. 3, pp. 210–219, 2006. 68, 159

[132] S. Caglio and P. G. Righetti, "On the pH dependence of polymerization efficiency, as investigated by capillary zone electrophoresis," *Electrophoresis*, vol. 14, pp. 554–558, jan 1993. 68

[133] T. Mizutani, "Decreased Activity of Proteins Adsorbed Onto Glass Surfaces with Porous Glass as a Reference," *Journal of Pharmaceutical Sciences*, vol. 69, pp. 279–282, mar 1980. 68

[134] J. T. Fourkas, "Rapid determination of the three-dimensional orientation of single molecules," *Optics Letters*, vol. 26, p. 211, feb 2001. 77, 102

[135] M. Ovesný, P. Kížek, J. Borkovec, Z. Švindrych, and G. M. Hagen, "ThunderSTORM: a comprehensive ImageJ plug-in for PALM and STORM data analysis and super-resolution imaging," *Bioinformatics*, vol. 30, no. 16, pp. 2389–2390, 2014. 79

[136] H. Chang, M. Zhang, W. Ji, J. Chen, Y. Zhang, B. Liu, J. Lu, J. Zhang, P. Xu, and T. Xu, "A unique series of reversibly switchable fluorescent proteins with beneficial properties for various applications.," *Proceedings of the National Academy of Sciences of the United States of America*, vol. 109, pp. 4455–60, mar 2012. 89, 91

[137] F. Urbach, "The Long-Wavelength Edge of Photographic Sensitivity and of the Electronic Absorption of Solids," *Physical Review*, vol. 92, no. 5, p. 1324, 1953. 93

[138] B. Roubinet, M. Weber, H. Shojaei, M. Bates, M. L. Bossi, V. N. Belov, M. Irie, and S. W. Hell, "Fluorescent Photoswitchable Diarylethenes for Biolabeling and Single-Molecule Localization Microscopies with Optical Superresolution," *Journal of the American Chemical Society*, vol. 139, no. 19, pp. 6611–6620, 2017. 93

[139] Y. Arai, S. Ito, H. Fujita, Y. Yoneda, T. Kaji, S. Takei, R. Kashihara, M. Morimoto, M. Irie, and H. Miyasaka, "One-colour control of activation, excitation and deactivation of a fluorescent diarylethene derivative in super-resolution microscopy," *Chemical Communications*, vol. 53, no. 29, pp. 4066–4069, 2017. 93

[140] M. Andresen, A. C. Stiel, S. Trowitzsch, G. Weber, C. Eggeling, M. C. Wahl, S. W. Hell, and S. Jakobs, "Structural basis for reversible photoswitching in Dronpa," *Proceedings of the National Academy of Sciences*, 2007. 98

[141] F. C. Zanacchi, C. Manzo, A. S. Alvarez, N. D. Derr, M. F. Garcia-Parajo, and M. Lakadamyali, "A DNA origami platform for quantifying protein copy number in super-resolution," *Nature Methods*, vol. 14, pp. 789–792, aug 2017. 134

[142] U. Kanjee and W. A. Houry, "Mechanisms of Acid Resistance in Escherichia coli," *Annual Review of Microbiology*, vol. 67, no. 1, pp. 65–81, 2013. 135

[143] B. Kastner, N. Fischer, M. M. Golas, B. Sander, P. Dube, D. Boehringer, K. Hartmuth, J. Deckert, F. Hauer, E. Wolf, H. Uchtenhagen, H. Urlaub, F. Herzog, J. M. Peters, D. Poerschke, R. Lührmann, and H. Stark, "GraFix: sample preparation for single-particle electron cryomicroscopy," *Nature Methods*, vol. 5, pp. 53–55, jan 2008. 137

[144] A. Mukherjee, K. K. Ray, C. Phadnis, A. Layek, S. Bera, and A. Chowdhury, "Insights on heterogeneity in blinking mechanisms and non-ergodicity using sub-ensemble statistical analysis of single quantum-dots," *The Journal of Chemical Physics*, vol. 151, p. 084701, aug 2019. 143

[145] J. Chang, M. Romei, and S. Boxer, "Structural Evidence of Photoisomerization Pathways in Fluorescent Proteins," aug 2019. 153, 164, 165

Acknowledgements

Cette thèse fut un voyage passionnant dans le mondes des protéines fluorescentes et de la microscopie, qui a été rendu possible par un grand nombre de personnes.

Tout d'abord, je tiens à remercier Dominique pour sa bienveillance, son attitude toujours positive et ses remarques toujours pertinentes ; c'est grâce à toi que durant ces trois ans j'ai pu prendre plaisir à découvrir la photophysique, et à me creuser la tête sur toutes les questions passionnantes que l'on a pu aborder. Tu m'as appris à regarder derrière les questions apparemment insolubles, et à toujours chercher les détails, jusqu'au "clic" de compréhension. Merci !

Un grand merci aussi à l'équipe Pixel : Virgile, Joël, Sasha, Martin, Ninon, sans qui mes journées n'auraient pas été les mêmes; merci pour vos conseils, votre soutien, et les éclats de rire au bureau ! Et merci à tout le groupe Dynamop, pour votre présence et votre gentilesse.

This thesis would also not have been the same without our scientific collaborators, so many thanks to Elke De Zitter, Viola Mönkenmöller, Siewert Hugelier and Peter Dedecker, for your patience, and for all the work done; I'm really proud of the work we've achieved. Vielen dank auch zu Jörg Enderlein, wer mir zweimal in Göttingen wilkommen hat; es war immer ein Vergnügen und wirklich interessant, in deinem Labor zu arbeiten!

La recherche ne fait pas tout dans une thèse, et j'ai été très heureux de pouvoir également enseigner ; et pour a je voudrais vraiment remercier Claire Durmort, qui m'en a donné la possibilité, et Pierre Cavailles, Véronique Frachet et Cécile Batandier pour leur aide, leurs conseils et leur bonne humeur. Merci aussi à Pascale Chauvet de m'avoir permis de venir parler à ses élèves le temps d'un cours, ça a été une expérience vraiment nouvelle et enrichissante.

Rien n'aurait non plus été pareil si je n'avais pas rencontré ici des gens fantastiques avec qui parler de plein de choses le soir autour d'une bière ou d'un pho; merci en particulier à Joyce, Quentin, Raleb, Ana et Muge !

Et enfin, merci à Lisa pour ton soutien, and cheers to new adventures coming soon! Chapeau !